Aerodynamic and acoustic investigation of automotive fan-driven cooling systems

Alessandro Zarri

N° d'ordre NNT: 2021LYSEC23

THÈSE de DOCTORAT DE L'UNIVERSITÉ DE LYON
opérée au sein de l'École Centrale de Lyon et
de l'Institut von Karman de Dynamique des Fluides

École Doctorale N° 162
Mécanique Énergétique Génie Civil Acoustique

Spécialité de doctorat: Acoustique

Soutenue publiquement le 28/06/2021, par

Alessandro Zarri

Aerodynamic and acoustic investigation of automotive fan-driven cooling systems

---

Superviseurs:

Schram, Christophe	Professeur, von Karman Institute for Fluid Dynamics, Codirecteur de thèse
Christophe, Julien	Docteur Ingénieur, von Karman Institute for Fluid Dynamics

Devant le jury composé de:

Carolus, Thomas	Professeur, Universität Siegen	Rapporteur
Sanjose, Marlène	Professeur, ÉTS Montréal	Rapporteur
Bailly, Christophe	Professeur, École Centrale de Lyon	Examinateur
Grilliat, Julien	Docteur Ingénieur, ebm-papst	Examinateur
Herr, Michaela	Docteure Ingénieure, DLR	Examinatrice
Henner, Manuel	Docteur Ingénieur, Valeo	Examinateur
Moreau, Stéphane	Professeur, Université de Sherbrook	Examinateur
Roger, Michel	Professeur, École Centrale de Lyon	Directeur de thèse

Thesis submitted by Alessandro Zarri
in fulfillment of the requirements to achieve the Ph.D.
(Doctoral Degree of Philosophy) in Engineering Sciences.

Academic year 2020-2021.

von Karman Institute for Fluid Dynamics
Environmental and Applied Fluid Dynamics Department

Waterloosesteenweg 72, 1640 Sint-Genesius-Rode
Phone: +32 359 96 11, https://www.vki.ac.be

D/2021/0238/743, T. Magin, Editor-in-Chief
Published by the von Karman Institute for Fluid Dynamics with permission.

ISBN 978-2-87516-173-4

A mio nonno Mario Zarri,
per esserci sempre stato

To my grandfather Mario Zarri,
for having always been there

Contents

List of Figures

List of Tables

Nomenclature

Roman Letters

A, P	area and perimeter of the grid triangular radiator element
A_0	area of the heat exchanger
a_{ij}	anisotropy stress tensor
B	number of fan blades
b	half-chord aligned with U_0
b'	rotated half-chord aligned with x'
b_c	Corcos model constant
C	contraction rate
c	chord
C_p	pressure coefficient
c_0	sound velocity
C_L	lift coefficient
C_ν	vena-contracta factor
d	characteristic dimension, Appendix A
D_a	antenna diameter
d_p, ρ_p	diameter and density of the particle
d_{a-ss}	distance between antenna and fan suction side
d_{fan}	fan diameter
e	trailing-edge thickness
$E[-]$	Fresnel Integral
E_r	error estimation
F	equation defining the surface S and its kinematics, Chapter 2

F	transfer function, Chapter 3
f	frequency
F'	fluctuating force amplitude
F_0	steady aerodynamic force
f_0	resonance frequency
f_e	electric network frequency
f_n	n^{th} one-third octave band mid-frequency
f_v	vortex shedding frequency
$f_{1/3}$	one-third octave frequency band
$f_\#$	aperture of the camera objective
f_{BPF}	blade passing frequency
$f_{h.o.}$	harmonic-oscillating frequency
f_{min}	minimum frequency band
f_{sh}	frequency shift
G	Green's function
G_0	free-field Green's function
I_S	steady-loading noise intensity
I_U	unsteady-loading noise intensity
j	imaginary unit, Appendix A
J_0, J_1	first kind Bessel functions of zero and first orders
k	Shear number, Appendix A
$\bar{K_x}$, $\bar{K_y}$	dimensionless longitudinal and in-plane transversal wavenumbers, Chapter 4
$\mathbf{K}$	wavenumber vector
k_1, k_2	wavenumbers in the 1 and 2 directions, Chapter 2
k_a	acoustic wavenumber
K_c'	convective wavenumber parallel to x'
k_e	average wavenumber of the energy-containing eddies
K_r	kurtosis or flatness

k_t	turbulent kinetic energy
K_x, K_y	longitudinal and in-plane transversal wavenumbers, Chapter 4
K'_x	aerodynamic wavenumber parallel to x'
K'_y	aerodynamic wavenumber parallel to y'
k_ω	convective wavenumber ω/U_c
L	span length
$\mathcal{L}^{LE}$	leading-edge aeroacoustic transfer function
$\mathcal{L}^{TE}$	trailing-edge aeroacoustic transfer function
L'	rotated span of a strip aligned with y'
L_0	flow characteristic length
L_B	radial blade length
L_c	air cavity depth, Appendix A
L_p	sound pressure level
l_y	spanwise correlation length of wall-pressure fluctuations
$L_{p,1/3}$	one-third octave frequency band SPL
M	hydraulic diameter of the radiator grid size
m	multiple of the rotational frequency, Chapter 2
$\boldsymbol{M}$	vectorial Mach number
m, n	Butterworth filter order coefficients, Chapter 5
M_i	Mach number projected along the i^{th} direction
M_r	relative Mach number
m_{in}	internal reactance
M_{MPP}	acoustic reactance of an MPP
N	number on independent measurements
n	band number, Chapter 2
$\boldsymbol{n}$	unit normal to the surface S, Chapter 2
N_{im}	number of images
p	pressure

p_∞	laboratory pressure reference
ΔP	pressure difference, Chapter 3
Δp	pressure difference across the orifice, Appendix A
$\mathbf{P}$	net force on surface element
p'	pressure fluctuation
p_0	mean background pressure
P_D	dipolar acoustic power
P_i	i^{th} component of the net force on surface element
P_Q	quadrupolar acoustic power
p_{ij}	stress tensor
p_{ref}	reference pressure
p_{rms}	root-mean-square of the pressure fluctuations
p_{up}	upstream acoustic pressure
Q	generic source distribution
$\langle q^2 \rangle$	twice the size of TKE
q_m	airflow rate
R	absolute distance between listener and source, Chapter 2
R	fan radial distance, Chapter 5
R	minimum resolvable source separation, Chapter 3
r	hole radius, Appendix A
$\boldsymbol{R}$	vectorial distance between listener and source
R_0	fan radius, Chapter 2
r_0	first zero crossing of the correlation function
r_1, r_2	longitudinal and transversal separations, Chapter 4
R_i	distance between listener and source along the i^{th} direction
R_S	surface resistance
R_T	ratio of timescales of pressure
$R_{\alpha\alpha}$	two-points correlation function

r_{in}	internal resistance
R_{MPP}	acoustic resistance of an MPP
r_{n-l}	non-linear contribution to the MPP resistance
r_{tip}	fan tip radius
Re_c	chord-based Reynolds number
S	discontinuity surface, Chapter 2
S	infinite plane surface, Appendix A
St_t	Strouhal number based on the tip chord length, Chapter 3
S_0	listener's corrected distance
S_k	skewness
S_r	Strouhal number
S_t	Stokes number
S_{pp}	one-sided auto PSD of p
S_{pp}^{Ψ}	single-strip sound PSD
S_{pp}^{LE}	single-strip LE noise PSD
S_{pp}^{TE}	single-strip TE noise PSD
T	period of time
t	MPP thickness, Appendix A
t	time
t'	emission time
t_c	characteristic time
T_q	turbulence intensity
T_q^{va}	vertical average of T_q
T_{ij}	Lighthill's tensor
U	boundary-layer velocity, Chapter 5
U	mean streamwise velocity component, Chapter 4
u	particle velocity, Appendix A
u	streamwise velocity component, Chapter 4

$\bar{u}$	cross-sectional averaged velocity, Appendix A
$\overline{u^2}$	mean square of the velocity fluctuations
$\boldsymbol{u}$	aerodynamic velocity vector field
u'	streamwise velocity fluctuation, Chapter 4
U^{va}	vertical average velocity
U_0	flow velocity
U_0	local entrainment velocity, Chapter 5
U_c	convection velocity
U_e	external boundary-layer velocity
U_f	reference flow velocity, Chapter 4
u_h	velocity within a hole, Appendix A
U_p	particle velocity
U_S	tangential velocity amplitude
U_x	rotated velocity component parallel to x'
U_y	rotated velocity component parallel to y'
U_{max}	boundary-layer maximum velocity
u_{rms}	r.m.s of the streamwise velocity component
u_{tip}	fan tip velocity
V	fixed volume of fluid, Chapter 2
V	mean in-plane crosswise velocity component, Chapter 4
v	in-plane crosswise velocity component, Chapter 4
$\mathcal{V}$	generic volume of space
$\mathcal{V}_e$	external volume
$\mathcal{V}_i$	internal volume
$\boldsymbol{v_s}$	velocity of S, Chapter 2
$\boldsymbol{V}$	absolute velocity field of a solid surface
$\boldsymbol{v}$	flow velocity, Chapter 2
v'	in-plane velocity fluctuation, Chapter 4

V_0	characteristic velocity
v_i	i^{th} velocity component, Chapter 2
V_n	velocity component normal to the surface S
v_{rms}	r.m.s of the in-plane crosswise velocity component
v_{tip}	absolute velocity tangential component
W	mean out-of-plane crosswise velocity component, Chapter 4
w	out-of-plane crosswise velocity component, Chapter 4
w	velocity disturbance, Chapter 2
w'	out-of-plane velocity fluctuation, Chapter 4
W_ν	power dissipation
w_{rms}	r.m.s of the out-of-plane crosswise velocity component
(x, y, z)	local reference frame with x axis aligned with U_0
(x', y', z)	rotated local reference frame with y' parallel to the LE and TE edges
$\mathbf{x}$	listener position
x_{1c}, x_{2c}, x_{3c}	turbulence-state characteristic positions on invariant maps
x_c	strip-chord distance parallel to c
x_i	i^{th} space coordinate
$\mathbf{y}$	vectorial location of the noise source
y^+	boundary-layer dimensionless wall distance
y_c	boundary-layer vertical distance
Z_1	single-hole impedance
z_c	confidence critical value
z_{ex}	external relative impedance
z_{in}	internal relative impedance
Z_{MPP}	controlled complex impedance of an MPP

Greek Letters

α	U_0/U_c factor, Chapter 5
α	statistical quantity, Chapter 4

α, α_g, β, δ	empirical coefficients, Appendix A
α_{MPP}	absorption coefficient
β_0	compressibility factor, Chapter 5
β_c	constant in exponential correction to the von Kármán model, Chapter 4
β_i	compressibility factor based on i^{th} mean velocity component
δ	Dirac delta function
δ	boundary-layer thickness, Chapter 5
δ^*	boundary-layer displacement thickness
δ_g	mass end correction with grazing flow
δ_{ij}	Kronecker delta
ϵ	turbulent kinetic energy dissipation rate
η	Kolmogorov length scale
$\boldsymbol{\eta}$	Lagrangian coordinate system
η_2	spanwise length
Γ	Gamma function
$\mathbf{\Gamma}$	acceleration field of a solid surface
Γ_0	centripetal acceleration
γ_c	correlation function
Γ_i	acceleration field i^{th} component
Λ	integral length scale
λ	acoustic wavelength
λ_0	wavelength at the resonance frequency
Λ_f	turbulent integral length scale
λ_i	i^{th} eigenvalue
Λ_u	streamwise integral length scale
Λ_v	in-plane crosswise integral length scale
$\Lambda_{i,j}$	integral length scale of the i^{th} component along the j^{th} direction
μ	air dynamic viscosity

ν	air kinematic viscosity
Ω	fan velocity rotation
ω	angular frequency
ω_e	source-emitted frequency
Ω_r	relative angular velocity
φ	scalar field variable
ϕ_{pp}	single-point frequency spectrum of wall-pressure fluctuations
Φ_{ww}	two-dimensional wavenumber spectrum of velocity fluctuations w
Φ_{ww}^{exp}	2D turbulence experimental spectrum
Φ_{ww}^{Pao}	exponentially corrected 2D von Kármán spectrum
Φ_{ww}^{VK}	2D von Kármán spectrum
Π_0	one-wavenumber-frequency spectral density of wall-pressure fluctuations
Ψ	fan azimuthal position
ψ	sweep angle defined between x and x', Chapter 5
ρ	density
ρ'	density fluctuation
ρ_0	density of a fluid at rest
ρ_∞	laboratory density reference
σ	porosity, Appendix A
σ	principal stress, Chapter 4
σ	source signal, Chapter 3
σ_U	standard deviation of the streamwise component
σ_x, σ_y, σ_z	normal Reynolds stresses
τ_e	emission time
τ_v	time lag
τ_w	wall-shear stress across the boundary layer
Θ	directivity angle in the X-Z plane, Chapter 5
θ	boundary-layer momentum thickness, Chapter 5

θ	directivity angle, Chapter 3
$\boldsymbol{\xi}'$	velocity of a moving source
$\boldsymbol{\xi}$	time-dependent position
ξ, ν	normalized longitudinal and in-plane transversal axes, Chapter 4

Acronyms

ALCOVES	Aeroacoustic Lab for Cooling and Ventilation Systems
B&K	Bruel and Kjaer
BPF	Blade Passing Frequency
CAD	Computer-Aided Design
DNS	Direct Numerical Simulation
FA	Fan Alone
FFT	Fast Fourier Transform
FM	Full Module
FOV	Field Of View
FWH	Ffowcs-Williams and Hawkings
HE	Heat Exchanger
HIT	Homogeneous and Isotropic Turbulence
HVAC	Heat Ventilation and Air Conditioning
IHD	Ischaemic Heart Disease
ISO	International Organization for Standardization
LBM	Lattice Boltzmann Method
LE	Leading Edge
LES	Large Eddy Simulation
MPP	Micro Perforated Plate
OP	Operating Point
PDF	Probability Density Function
PIV	Particle Image Velocimetry
PM	Particulate Matter

PR	Panel and Radiator
PSD	Power Spectral Density
PTU	Programmable Timing Unit
QWR	Quarter-Wave Resonator
r.m.s	root mean square
RA	Radiator Alone
RANS	Reynolds Averaged Navier-Stokes
ROSI	Rotating Source Identifier
S-PIV	stereoscopic particle image velocimetry
SG	Scanning Grid
SPL	Sound Pressure Level
TE	Trailing Edge
TKE	Turbulent Kinetic Energy
UdeS	Université de Sherbrooke
VKI	von Karman Institute
VLES	Very Large Eddy Simulations
VRA	Virtual Rotating Array
WHO	World Health Organization

Others

$(\cdot)^*$	quantity normalized by the semi-chord $c/2$, Chapter 2
$(\cdot)'$	sweep-angle rotation, Chapter 5
$[\cdot]_{(1)}^{(2)}$	jump of a quantity between regions 2 and 1
$\hat{(\cdot)}$	normalization by k_e
$\langle\cdot\rangle$	ensemble average
$\overline{(\cdot)}$	normalization by the rotated half chord, b'
I, II, III	first, second, and third invariant

Summary

The mitigation of urban noise pollution, due to automobiles among other things, is a growing international concern, as exposure to noise at high levels or for long periods of time can lead to physical and mental health problems. This research work focuses on broadband noise emitted by fan cooling modules, used for engine temperature control. Several mechanisms responsible for noise generation are present in such applications due to the aerodynamic interaction between the airflow and the fan blades. Three broadband noise mechanisms dominating the acoustic spectra are identified in the literature review, namely: trailing-edge noise, turbulence-interaction noise, and tip-clearance noise. First, this work proposes to estimate the relative importance between these mechanisms, especially in the presence of the radiator upstream of the propeller. Indeed, its influence on the modification of the flow through the radiator and on the resulting aerodynamic sound sources is not yet clearly defined. Direct sound measurement and rotating acoustic beamforming techniques are being implemented at the von Karman Institute for Fluid Dynamics in Belgium and at the University of Sherbrooke in Canada. The obtained sound-localization maps indicate that the radiator has a negligible effect on the source position, which is always located at the leading edge of the blade tip when the operating conditions of the fan used vary. This experimentally validates the high-fidelity simulations available in the literature and extends the importance of the tip-clearance noise to high frequencies. Since the effect of the radiator is not restricted to its influence on the acoustics, an experimental campaign was conducted to characterize the turbulent flow downstream of the fan, exploiting a stereoscopic PIV technique. For the analyzed cases, a maximum turbulence intensity production of about 15% is measured, decreasing to 6% at the position corresponding to the fan location. Significant levels of anisotropy and non-homogeneity are found here, requiring an analysis of the applicability of the isotropy-based von Kármán turbulence model, typically used in noise prediction methods. The results indicate that this model approaches reasonably well the two-dimensional turbulence spectra in most cases. In the second part of the thesis, a review of previous work shows that high-fidelity simulations, although accurate, are still too expensive when aeroacoustics is taken into account in industrial pre-design optimization processes. A low-order technique capable of predicting the broadband noise of fans is developed here. In order to understand the influence of the blade curvature on the acoustic prediction, the case of the isolated fan is chosen to be studied numerically. Stationary 3D RANS simulations are computed as input data for a semi-analytical approach, based on Amiet's theory, adapted to the rotational case, and extended to include blade sweep effects. The results obtained are in agreement with the experimental data at high frequencies. However, the stationary approach used does not allow the simulation of the large turbulent structures that develop at the tip of the blade, thus underestimating the low and medium frequencies. The sweep angle is a parameter that should be considered in the early stages of design, as it attenuates the noise emissions and changes the dominant sources along the blade.

Keywords: aeroacoustics, turbulence, broadband fan noise, automotive cooling system, rotating source localization, stereoscopic PIV, Amiet's theory, sweep angle.

Résumé

L'atténuation de la pollution sonore urbaine, causée entre autres par les automobiles, est une préoccupation internationale croissante, car l'exposition au bruit à des niveaux élevés ou pendant de longues périodes peut conduire à des problèmes de santé physique et mentale. Ce travail de recherche se concentre sur le bruit à large bande émis par les modules de refroidissement par ventilateur, utilisés pour la régulation de la température du moteur. Plusieurs mécanismes responsables de la génération de bruit sont présents dans de telles applications en raison de l'interaction aérodynamique entre le flux d'air et les pales du ventilateur. Trois mécanismes sonores à large bande dominant les spectres acoustiques sont identifiés dans la revue de la littérature, à savoir : le bruit de bord de fuite, le bruit d'interaction de turbulence et le bruit de jeu en bout de pale. Dans un premier temps, ce travail se propose d'estimer l'importance relative entre ces mécanismes, notamment en présence du radiateur en amont de l'hélice. En effet, son influence sur la modification de l'écoulement qui traverse le radiateur et sur les sources sonores aérodynamiques résultantes ne sont pas encore clairement définies. Des techniques de mesure directe du son et d'antennerie acoustique en rotation sont mises en œuvre à l'Institut von Karman de dynamique des fluides, en Belgique, et à l'Université de Sherbrooke, au Canada. Les cartographies de localisation sonore obtenues indiquent que le radiateur a un effet négligeable sur la position des sources, demeurant au bord d'attaque de l'extrémité de la pale lorsque les conditions de fonctionnement du ventilateur utilisé varient. Ceci valide expérimentalement les simulations haute-fidélité disponibles dans la littérature et étend l'importance du bruit de jeu en bout de pale aux hautes fréquences. L'effet du radiateur n'étant pas restreint à son influence sur l'acoustique, une campagne expérimentale a été menée pour caractériser l'écoulement turbulent en aval du ventilateur, en exploitant une technique de PIV stéréoscopique. Pour les cas analysés, une production maximale d'intensité de turbulence d'environ 15% est mesurée, diminuant à 6% à la position correspondant au ventilateur. Des niveaux significatifs d'anisotropie et de non-homogénéité sont retrouvés ici, nécessitant une analyse de l'applicabilité du modèle de turbulence de von Kármán, habituellement utilisé dans les méthodes de prédiction de bruit et étant basé sur l'isotropie de l'écoulement. Les résultats indiquent que ce modèle approche raisonnablement bien les spectres de turbulence bidimensionnelle dans la plupart des cas. Dans la deuxième partie de la thèse, une revue des travaux précédents montre que les simulations haute-fidélité bien que précises, restent encore trop onéreuses lorsque l'aéroacoustique est prise en compte dans les processus d'optimisation industrielle de préconception. Une technique d'ordre inférieur capable de prédire le bruit large bande des ventilateurs est ici développée. Afin de comprendre l'influence de la courbure des pales sur la prédiction acoustique, le cas du ventilateur isolé est choisi pour être étudié numériquement. Des simulations RANS 3D stationnaires sont utilisées comme données d'entrée d'une approche semi-analytique, basée sur la théorie d'Amiet, adaptée au cas de la rotation et étendue pour inclure les effets de flèche de la pale. Les résultats obtenus sont en accord avec les données expérimentales aux hautes fréquences. Cependant, l'approche stationnaire utilisée ne permet pas de simuler les grandes structures turbulentes qui se développent à l'extrémité de la pale, sous-estimant dès lors les basses et moyennes fréquences. L'angle de flèche est un paramètre qui mérite d'être pris en compte dès les premières étapes de

la conception, car il atténue les émissions sonores et modifie les sources dominantes le long de la pale.

Mots-clés : aéroacoustique, turbulence, bruit de ventilateur à large bande, système de refroidissement automobile, localisation des sources rotatives, PIV stéréoscopique, théorie d'Amiet, angle de flèche.

Acknowledgments

I would like to acknowledge the support of the European Commission's Framework Program "Horizon 2020", through the Marie Skłodowska-Curie Innovative Training Networks (ITN) "SmartAnswer - Smart mitigation of flow-induced acoustic radiation and transmission" grant agreement No. 722401 to the present research project. I would like to thank the members of the jury for offering me their valuable time. Thanks to Professor Thomas Carolus and Professor Marlène Sanjose for correcting and writing up the reports: their suggestions were very helpful. Many thanks to Professor and Thesis Director Michel Roger for hosting me at the École Centrale de Lyon and for following and advising me throughout my Ph.D. Lots of thanks to Professor Stéphane Moreau, for welcoming me to the Université de Sherbrooke during the secondment and for always being a huge source of knowledge to appeal to in times of need. Likewise, thanks to Dr. Manuel Henner for providing the automotive module, for always answering all my questions (way too many!) and curiosities, and for welcoming me to his amazing team at Valeo during the secondment. From that period, sincere thanks are due to Maxime Laurent for his unrelenting patience in answering all my doubts. Heartfelt thanks from the bottom of my heart go to the best supervisors in the world, Prof Christophe Schram and Dr. Julien Christophe. Thank you for choosing me, for always believing in me, for giving me the possibility to follow my dream of becoming a researcher. I have always looked up to you as I admire you as people and as scientists. Many thanks to the students who collaborated with me, especially Orestis Amoiridis and Miguel Baena Botana. Their hard work contributed to the research goals achieved in this manuscript. I would like to thank all the guys in the SmartAnswer group, unique people with whom it was great to share a hundred happy moments around Europe. So many grateful thanks also go to all the wonderful friends I met in Belgium, especially Francisco Torres Herrado, Dr. Simon Demange, Andrea Attavino, Dr. Ivan Padilla, Vincent Fitzgerald Giangaspero, Zoé Jardon, Dr. Maria Faruoli, Michele Capriati, Dr. Charline Fouchier, Adriana Enache, Dr. Daniel Guariglia, Dr. Stefania D'Aria, Dr. Lionel Hirschberg, Dr. Florian Danvin, Rebecca Torpey, Domenico Fiorini. I have precious memories with each of you that I hold on to. Thanks to all the members of our fantastic aeroacoustics team at VKI: especially to Dr. Yakut Cansev Kucukosman, Dr. Georgios Bampanis, Joachim Dominique, Kartik Venkatraman, for the many conversations and advice. A special thank you goes to the most important member of the ZaZa Team, Dr. Riccardo Zamponi. I have a thousand memories with you, from travels around the world to office chats, shared dreams, and (unfortunately!) shared beds. Thank you very much for all this.

Grazie agli amici che ho lasciato in Italia, nonostante la lontananza continuate ad essere fondamentali per me. In particolare, grazie a Matteo Gaidano, Rosario Valentino, Maria Grazia Lugano, Alberto Faravelli, Marco Oddone. Grazie infinite a tutta la mia famiglia, in particolare ai nonni ed a mio papà Giovanni Zarri, a mia mamma Angela Longo ed alla mia sorellina Elisa Zarri. Voi mi avete accompagnato lungo tutta la mia vita, avete creduto in me ed appoggiato la difficile scelta di andare a studiare lontano. Vi sarò per sempre debitore e vi porterò per sempre con me ovunque andrò. Un grazie senza fine va alla mia Elena Nicoleta Grof. Per aver lasciato tutto in Italia e

deciso di inseguire i miei sogni. Per aver sopportato le tante ore di lavoro, stress e fatica. Grazie di aver dato tutto per starmi vicino sempre. Grazie per tutti i momenti felici negli ultimi 12 anni. Sono orgoglioso della vita che abbiamo costruito insieme.

Brussels, June 2021
Alessandro Zarri

List of Publications

Journal Papers

1. **A. Zarri**, J. Christophe, S. Moreau, C. Schram, "Influence of swept blades on low-order acoustic prediction for axial fans", Acoustics 2020, 2(4), 812-832, doi: 10.3390/acoustics2040046.

2. O. Amoiridis, **A. Zarri**, R. Zamponi, Y. Pasco, G. Yakhina, J. Christophe, S. Moreau, and C. Schram. "Sound localization and quantification analysis of an automotive engine cooling module". Journal of Sound and Vibration, 517:116534, doi: 10.1016/j.jsv.2021.116534.

3. **A. Zarri**, M. Baena Botana, J. Christophe, C. Schram, "Aerodynamic investigation of the turbulent flow past a radiator". Manuscript in preparation to be submitted to Experiments in Fluids.

Conference Papers

1. **A. Zarri**, J. Christophe, C. Schram, "Low-order aeroacoustic prediction of low-speed axial fan noise", AIAA Aviation 2019, 25th AIAA/CEAS Aeroacoustics Conference, Delft University of Technology (NL), AIAA paper 2019-2760, doi: 10.2514/6.2019-2760.

2. O. Amoiridis, **A. Zarri**, R. Zamponi, J. Christophe, C. Schram, G. Yakhina, S. Moreau, "Experimental analysis of the sound radiated by an automotive cooling module working at different operational conditions", AIAA Aviation 2020, 26th AIAA/CEAS Aeroacoustics Conference, online event, AIAA paper 2020-2598, doi: 10.2514/6.2020-2598.

3. O. Amoiridis, R. Zamponi, **A. Zarri**, J. Christophe, C. Schram, "Localization and characterization of rotating noise sources on axial fans by means of an irregularly shaped microphone array", Journal of Physics: Conference Series 1909 012003, May 2021, doi: 10.1088/1742-6596/1909/1/012003.

4. **A. Zarri**, J. Christophe, S. Moreau, C. Schram, "Sweep-angle effect on low-order acoustic prediction for low-speed fans", Journal of Physics: Conference Series 1909 012005, May 2021, doi: 10.1088/1742-6596/1909/1/012005.

1 Introduction

Aerodynamic noise emitted by rotating machinery is a critical concern in several industrial sectors. Often, these machines are used to cool combustion engines [1, 2] or electric batteries [3] as in the case of the ground transportation sector; to regulate the temperature inside civil buildings or industrial plants (HVAC sector) [4, 5], or to cool electronic components [6–8], such as laptops and desktops. In the aeronautical field [9, 10], rotating machines are typically used to propel airplanes and helicopters, whereas wind turbines exploit the force of the wind to produce electrical power through the rotation of the blades [11, 12]. Although most of the sound measurement and prediction techniques developed in this manuscript are extendable to several of the aforementioned areas, in this work we focus on the flow-induced noise emitted by fans typically used to cool automotive engines. As reported in [13] and in Figure 1.1, fan noise is of primary importance with respect to other sources of the vehicle overall noise like the engine, transmission, tire, mechanical, or exhaust contributions. In traffic idle conditions it can become the most dominant [14]. Furthermore, also in railways noise investigations [15, 16], in standstill and acceleration cases, the fan and engine noise must be accounted for. In the context of urban noise pollution, transport vehicles are the main source of noise. There is an increasing tightening of international regulations due to studies linking noise pollution to health problems. In [17, 18], traffic noise was reported as the second highest environmental risk for mental and physical health after air pollution, becoming of great concern to policy-makers in Europe. Noise-related sleep disturbance and annoyance[1] are the most common symptoms of physical and psychological stress, as reported by Ouis [19]. A relationship between ischaemic heart disease (IHD) and traffic noise exposure has been reported with high-quality epidemiological evidence by van Kempen *et al.* [21]. The study shows an increased risk of 1.08% per $10\,\mathrm{dB}$ increase of noise, with a 95% confidence level. Other investigations on cardiovascular diseases, in particular about the incidence of stroke [22–24], identified an augmented risk of 1.14% per $10\,\mathrm{dB}$ noise increase, with a 95% confidence level. In 2018, the World Health Organization (WHO) Regional Office for Europe [25], decided to adhere to a 5% as the relevant risk increase for IHD and 10% for hypertension. These risks are impressive when compared to the WHO air quality guidelines for fine particulate matter ($PM_{2.5}$) [26] which consider an increased risk of IHD

[1] Noise annoyance is described as a feeling of a nuisance, irritation, displeasure caused by long-exposure to unwanted sounds.

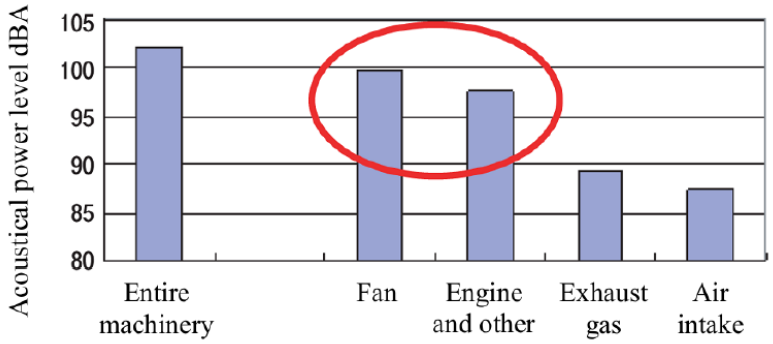

Figure 1.1: Noise sources in construction machinery: analysis taken from [20].

incidence of the same order of magnitude 5-10%. A thorough summary of European and global noise regulations can be found in [27]. Hereafter, we report only two of the recommendations given by the WHO Regional Office for Europe [25]. Regarding road traffic noise, they strongly recommended that, in case of average noise exposure, the sound levels must be kept below 53 dB in order to avoid adverse health effects. This value is further reduced to 45 dB during night time. These tight requirements can be mitigated by reducing the noise exposure of people by means of anti-propagation or insulation measures. Nevertheless, most of the European regulations focus on the mitigation of the acoustic source [27]. This is because at-source measures have the greatest potential to reduce exposure to urban acoustic pollution [28] and are generally more cost-effective than those designed to hamper the noise propagation [29]. As a result, automotive manufacturers have a great interest in producing vehicles whose design has taken acoustics into account. In addition to international regulations, ground vehicles manufacturers are careful to evaluate other factors that make their products more appealing to potential customers. These include, for example, reliability, safety, styling, ecological impact, and performance. Vehicle noise and vibration are some of the key factors that customers are interested in evaluating when they intend to purchase an automobile [30]. This is because customers associate the level of noise and vibration with driving comfort and product quality and reliability. Hence, we comprehend that there is a keen incentive to mitigate urban traffic noise, both for clinical and regulatory reasons and because of the comfort and quality of the product to be sold. As such, we are motivated to investigate and quantify the sound generation mechanisms that characterize such cooling units, given that in some conditions the engine fan is the major source of noise of the vehicle.

The automotive cooling modules are located in the underhood compartment of the car, as Figure 1.2[2](a) shows, and are typically composed of a low-speed cooling fan used to cool down a heat exchanger or radiator by extracting hot air out of it. Low speed because the blade tip angular velocity is highly subsonic (Mach number is usually below 0.1) and the chord-based Reynolds number falls within the range $10^4 \leq Re_c \geq 5 \times 10^5$. As a consequence, the flow is incompressible and partially or totally transitional over the whole span of the blade. Since it is necessary to optimize the heat extraction over the radiator surface, we are more interested in moving a large airflow rather than increasing pressure. Axial fans are generally used for this purpose [31]. These are typically molded from plastic, so as to allow more freedom in shapes. Unlike turbofans, for example, these ventilators are unducted and have low solidity, i.e., the blades hardly overlap. This

[2]These images were taken from the presentation of the work by Henner *et al.* from Valeo at the ISROMAC Conference, Online Event, 2020.

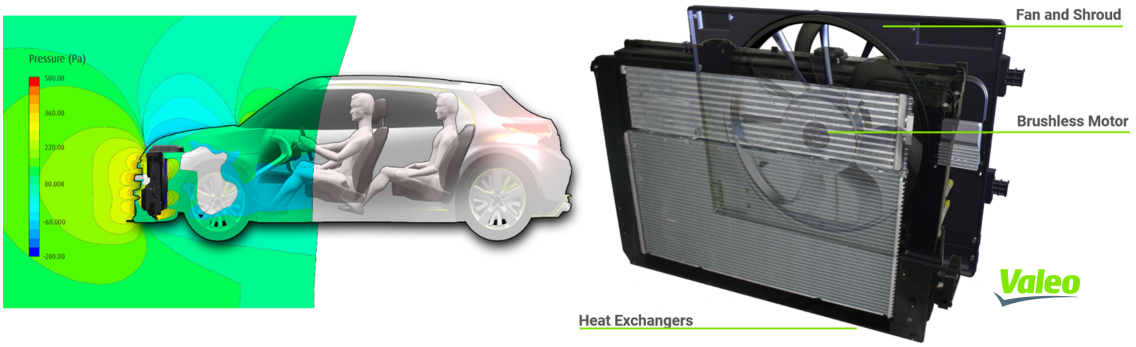

Figure 1.2: The automotive module is located in the underhood compartment of the car (a). It is composed of a fan, held by its shroud and by an upstream heat exchanger stack (b).

causes secondary flows to occur, e.g., the flow recirculation at the tip of the blades, which are crucial in noise generation. As a consequence, several sound generation mechanisms such as, e.g., the fan self-noise, the fan tip noise, the sound generated by the flow distortion caused by the shroud converging section can occur[3]. Cooling systems are thus very interesting to study from an aeroacoustic point of view. Also, fans are typically located at the suction-side of a radiator (or a radiator stack [32]) in a puller configuration. Radiators are made up of a metal core that consists of cooling pipes where the refrigerant fluid flows and fins (or slats, or lamellas) that facilitate the heat transfer. The latter is then further enhanced by the presence of louvers triggering the turbulence within the radiator core. As such, the upstream presence of the radiator affects the type of flow that impinges on the fan, particularly the degree of flow distortion and turbulence intensity. As discussed later in Section 2.6, turbulence-interaction noise is one of the dominant sound mechanisms in these systems [33]. Although there have been many research studies examining the sound generation mechanisms for fan-alone configurations, both numerical and experimental, few have focused on the modifying effect of acoustic sources due to the installation of an upstream radiator. The installation effects caused by the heat exchanger on the noise generation in different fan operating conditions is a matter of study in this manuscript.

In addition to the experimental study of fan sound sources, in this work, we are also interested in their prediction and modeling. Aeroacoustic prediction problems through numerical simulation are globally divisible into two categories [34]: direct methods and hybrid methods. The former allows solving the acoustic and flow fields simultaneously while solving the compressible flow equations. The Direct Numerical Simulation (DNS) approach, which solves even the smallest flow scales, or the Large-Eddy Simulation (LES) approach, which models the smallest scales and solves the largest, both have a very high and usually prohibitive computational cost. The axial fans investigated here have high Reynolds numbers and low Mach numbers. Consequently, there is a great disparity between turbulent scale amplitudes and acoustic wave numbers, making it necessary to use extremely fine and adaptable meshes. Concurrently, when the receiver is located far from the sound source, the computational domain widens and the computational cost increases dramatically. Thus, direct approaches are typically impractical for engineering purposes. As explored in more detail in Chapter 2, out of this category, only Lattice Boltzmann methods have

[3]The sound generation mechanisms concerning low-speed fans are addressed in detail in chapter 2.

found employment and will be increasingly popular in the future. The alternative to the direct approach is the hybrid approach, i.e., splitting the flow computation in the near-field, followed by the propagation of the acoustic sources in the far-field. The main assumption of this methodology is that the sound field has no influence on the flow field, yet it is from the latter that the noise sources are generated. A clear advantage of this decoupling is the opportunity to use an incompressible approach to solve the near-field of highly subsonic flows. Furthermore, it is unnecessary to extend the computational domain to the far-field to include the receiver within it. Hybrid approaches thus have a much lower computational cost than direct methods. In the industrial pre-design phases, there is a tendency to use multiphysics approaches with as little reliance on trial and error testing as possible. This is in order to speed up the conception and development phase of a product such as an automotive cooling module. There is great interest in including also acoustic field calculations in design optimization cycles. Since aeroacoustic calculations are typically expensive in terms of computation time, here we are interested in developing low-order methodologies that can be used in the industrial conception chain of a low-speed cooling fan. In particular, a hybrid approach will be implemented exploiting three-dimensional RANS steady-state computations to compute the sound sources. It will be coupled with semi-analytical methods, originally developed to predict the broadband sound emitted by steady airfoils. This approach has already been adopted [35] in order to predict turbulence-interaction noise and self-noise. However, in this work, we will include the blade sweep angle in the prediction methodology. Swept blades have been employed in previous work as a technique for alleviating fan noise [36] by phase-shift canceling the noise generated at different blade radial stations [37]. Moreover, sharp reductions concerning the turbulence-interaction noise obtained with swept blades in dirty inflow environments are achieved in [38, 39]. The sweep angle is considered a key factor whose acoustic and aerodynamic effect needs to be known from the early stages of development, where the detailed geometry of the final fan design has not yet been made available. In this work we exploit recent analytical developments in the treatment of turbulence-impingement noise [40] and self-noise [41] on steady swept profiles, implementing them in the proposed fan noise prediction methodology.

1.1 Objectives and outline of the thesis

We can state explicitly the three main objectives that this thesis aims at achieving:

1. Determine the influence that the upstream radiator has on sound sources and sound propagation. In particular, we are interested in experimentally characterizing the turbulent flow downstream of the radiator.

2. Identify and quantify the sound generation mechanisms that characterize the automotive cooling module in real application conditions and at varying operating points.

3. Develop a low-order acoustic prediction methodology that accounts for blade sweep angle and predicts turbulence-interaction and self-noise.

   This by coupling three-dimensional steady RANS simulations with semi-analytical Amiet theory, properly modified to take into account blade rotation via a strip approach.

In Chapter 2, the literature review concerning the study of fan noise is conducted, focusing on the mechanisms of broadband sound generation, as well as the experimental, numerical, and analytical investigation techniques that are used to study this type of system. In addition, the characteristics of the ALCOVES anechoic laboratory and the fan-driven automotive cooling system studied hereafter are presented. In Chapter 3, we conduct an experimental acoustic analysis using direct and rotating-beamforming sound measurements in order to investigate the influence of the radiator on the acoustic field under varying fan operating conditions. Furthermore, the dominant sound mechanisms will be identified and quantified by comparing acoustic measurements obtained from different experimental campaigns. Chapter 4 characterizes the turbulent flow produced downstream of the radiator through a stereoscopic particle image velocimetry (stereo-PIV) experimental campaign. The applicability of the von Kármán turbulence spectrum model will be discussed along with the characterization of the level of isotropy and homogeneity of the flow produced past the radiator. In Chapter 5, the low-order hybrid aeroacoustic methodology is developed to analyze the effect of sweep angle on the modeling of trailing- and leading-edge noise emitted by the fan. A complementary sensitivity study gives an indication of the importance of key parameters typically used in this type of hybrid approach. Ultimately, general conclusions and future perspectives are discussed in Chapter 6.

References

[1] Min-Jun Park and Duck-Joo Lee. *Sources of broadband noise of an automotive cooling fan*. Applied Acoustics, 118:66–75, 2017.

[2] Manuel Henner, Bruno Demory, Mohamed Alaoui, Maxime Laurent, and Benjamin Behey. *Effect of Blade Curvature on Fan Integration in Engine Cooling Module*. Acoustics, 2(4):776–790, October 2020.

[3] Antoine Minard, Adrien Vidal, Christophe Lambourg, and Patrick Boussard. *Sound synthesis of fan noise and modelling of its perception in car passenger compartment*. 04 2015.

[4] Wenhua Chen, Shichao Liu, Yunfei Gao, Hui Zhang, Edward Arens, Lei Zhao, and Junjie Liu. *Experimental and numerical investigations of indoor air movement distribution with an office ceiling fan*. Building and Environment, 130:14–26, February 2018.

[5] Rebecca Schäfer and Martin Böhle. *Validation of the Lattice Boltzmann Method for Simulation of Aerodynamics and Aeroacoustics in a Centrifugal Fan*. Acoustics, 2(4):735–752, September 2020.

[6] Lixi Huang and Jian Wang. *Acoustic analysis of a computer cooling fan*. Journal of The Acoustical Society of America, 118:2190–2200, 10 2005.

[7] Jeff Defoe and Colin Novak. *Review of computational aeroacoustics for application in electronics cooler noise*. 34, 09 2006.

[8] Sven Münsterjohann, Jens Grabinger, Stefan Becker, and Manfred Kaltenbacher. *CAA of an Air-Cooling System for Electronic Devices*. Advances in Acoustics and Vibration, 2016:1–17, October 2016.

[9] Stéphane Moreau and Michel Roger. *Advanced noise modeling for future propulsion systems*. International Journal of Aeroacoustics, 17(6-8):576–599, November 2018.

[10] Stéphane Moreau. *Turbomachinery Noise Predictions: Present and Future*. Acoustics, 1(1):92–116, January 2019.

[11] Stefan Oerlemans. *Reduction of wind turbine noise using blade trailing edge devices*. In 22nd AIAA/CEAS Aeroacoustics Conference, Lyon, France, May 2016.

[12] W.Y. Liu. *A review on wind turbine noise mechanism and de-noising techniques*. Renewable Energy, 108:311–320, 2017.

[13] Robert C. Chanaud and Douglas Muster. *Aerodynamic noise from motor vehicles*. The Journal of the Acoustical Society of America, 58(1):31–38, July 1975.

[14] Julien Christophe, Korcan Kucukcoskun, and Christophe Schram. *Tonal and Broadband sound prediction of a locomotive cooling unit*. In 19th AIAA/CEAS Aeroacoustics Conference, Berlin, Germany, May 2013. American Institute of Aeronautics and Astronautics.

[15] A. Frid, S. Leth, C. Högström, and J. Färm. *Noise control design of railway vehicles–Impact of new legislation*. Journal of Sound and Vibration, 293(3-5):910–920, June 2006.

[16] M.G. Dittrich and X. Zhang. *The Harmonoise/IMAGINE model for traction noise of powered railway vehicles*. Journal of Sound and Vibration, 293(3-5):986–994, June 2006.

[17] Frank Theakston and WHO, editors. *Burden of disease from environmental noise: quantification of healthy life years lost in Europe*. World Health Organization, Regional Office for Europe, Copenhagen, 2011.

[18] Otto Hänninen, Anne B. Knol, Matti Jantunen, Tek-Ang Lim, André Conrad, Marianne Rappolder, Paolo Carrer, Anna-Clara Fanetti, Rokho Kim, Jurgen Buekers, Rudi Torfs, Ivano Iavarone, Thomas Classen, Claudia Hornberg, Odile C.L. Mekel, and the EBoDE Working Group. *Environmental Burden of Disease in Europe: Assessing Nine Risk Factors in Six Countries*. Environmental Health Perspectives, 122(5):439–446, May 2014.

[19] D. Ouis. *Annoyance from Road Traffic Noise: a Review*. Journal of Environmental Psychology, 21(1):101–120, March 2001.

[20] Sabry Allam and Mats Åbom. *Noise Reduction for Automotive Radiator Cooling Fans*. FAN2015 Conference, Lyon, France, 2015.

[21] Elise van Kempen, Maribel Casas, Göran Pershagen, and Maria Foraster. *WHO Environmental Noise Guidelines for the European Region: A Systematic Review on Environmental Noise and Cardiovascular and Metabolic Effects: A Summary*. International Journal of Environmental Research and Public Health, 15(2):379, February 2018.

[22] Mette Sørensen, Martin Hvidberg, Barbara Hoffmann, Zorana J Andersen, Rikke B Nordsborg, Kenneth G Lillelund, Jørgen Jakobsen, Anne Tjønneland, Kim Overvad, and Ole Raaschou-Nielsen. *Exposure to road traffic and railway noise and associations with blood pressure and self-reported hypertension: a cohort study*. Environmental Health, 10(1), December 2011.

[23] Mette Sørensen, Zorana Andersen, Rikke Baastrup, Anne Tjønneland, O. Raaschou-Nielsen, K.G. Lillelund, Jorgen Jakobsen, and K. Overvad. *Road traffic noise and risk for stroke and myocardial infarction*. 41st International Congress and Exposition on Noise Control Engineering 2012, INTER-NOISE 2012, 7:6001–6008, 01 2012.

[24] Mette Sørensen, Pernille Lühdorf, Matthias Ketzel, Zorana J. Andersen, Anne Tjønneland, Kim Overvad, and Ole Raaschou-Nielsen. *Combined effects of road traffic noise and ambient air pollution in relation to risk for stroke?* Environmental Research, 133:49–55, August 2014.

[25] Regional Office for Europe World Health Organisation. *Environmental noise guidelines for the European Region*. 2018. OCLC: 1059293643.

[26] World Health Organization. *Air quality guidelines - global update 2005. Geneva.* 2006.

[27] University of Kragujevac, Faculty of Engineering, Danijela Miloradović, Jasna Glišović, University of Kragujevac, Faculty of Engineering, Jovanka Lukić, and University of Kragujevac, Faculty of Engineering. *Regulations on road vehicle noise -trends and future activities*. Mobility and Vehicle Mechanics, 43(1):57–72, March 2017.

[28] L. C. Den Boer and A. Schroten. *Traffic Noise Reduction in Europe. CE Delft, Netherlands.* March 2007.

[29] L. E. Larsen. *Cost-benefit analysis on noise-reducing pavements*. 2005.

[30] Mohamad S. Qatu, Mohamed Khalid Abdelhamid, Jian Pang, and Gang Sheng. *Overview of automotive noise and vibration*. International Journal of Vehicle Noise and Vibration, 5(1/2):1, 2009.

[31] Alain Guédel. *Acoustique des ventilateurs*. PYC Livres, Villeurbanne, France, 1999.

[32] Gerhard Dankowski. *Compact Cooling System for - Automotive Cooling Vehicles*, U.S. Patent 4 063 432 Dec. 1977.

[33] Stéphane Moreau and Michel Roger. *Competing Broadband Noise Mechanisms in Low-Speed Axial Fans*. AIAA Journal, 45(1):48–57, January 2007.

[34] J. Christophe. *Application of hybrid methods to high frequency aeroacoustics*. PhD thesis, Université libre de Bruxelles, 2011.

[35] Marlène Sanjosé and Stéphane Moreau. *Fast and accurate analytical modeling of broadband noise for a low-speed fan*. The Journal of the Acoustical Society of America, 143(5):3103–3113, May 2018.

[36] T. Wright and W. E. Simmons. *Blade Sweep for Low-Speed Axial Fans*. Journal of Turbomachinery, 112(1): 151-158, January 1990.

[37] Donald B. Hanson. *Near-field frequency-domain theory for propeller noise*. AIAA Journal, 23(4):499–504, April 1985.

[38] E. Kerschen and E. Envia. *Noise generation by a finite span swept airfoil*. In 8th Aeroacoustics Conference, Atlanta, GA, U.S.A., April 1983. American Institute of Aeronautics and Astronautics.

[39] E. Envia and E. Kerschen. *Noise produced by the interaction of a rotor wake with a swept stator blade*. In 9th Aeroacoustics Conference, Williamsburg,VA,U.S.A., October 1984. American Institute of Aeronautics and Astronautics.

[40] Michel Roger, Christophe Schram, and Stéphane Moreau. *On vortex–airfoil interaction noise including span-end effects, with application to open-rotor aeroacoustics*. Journal of Sound and Vibration, 333(1):283–306, January 2014.

[41] Gabriele Grasso, Michel Roger, and Stéphane Moreau. *Effect of sweep angle and of wall-pressure statistics on the free-field directivity of airfoil trailing-edge noise*. In 25th AIAA/CEAS Aeroacoustics Conference, Delft, The Netherlands, May 2019.

2

Fan-driven automotive module noise

The aim of this chapter is to introduce the reader to the noise emitted by low-speed cooling fans, as well as its measurement and modeling. We will first discuss the fundamental equations describing the fan aerodynamic noise and the most influential noise generating mechanisms; then we will go through the literature review concerning previous experimental, numerical, and analytical works on these cooling systems.

2.1 What is a fan?

According to the definition given by the ISO 13349:2010 norm [1], a fan is a rotary-bladed machine receiving mechanical energy and using it by means of one or more impellers fitted with blades to maintain a continuous flow of air passing through it and whose pressure rise does not exceed $30\,\mathrm{kPa}$ for a volumetric mass flow of $1.2\,\mathrm{kg\,m^{-3}}$. This upper limit has been chosen to distinguish fans from compressors, which must exert a greater work per unit mass on the flow (conventionally greater than $25\,\mathrm{kJ\,kg^{-1}}$) since their main task is to compress it by changing its density. The prime function of a fan is, instead, moving large volumes of air at pressures sufficient to exceed the resistance of the systems to which they are connected [2]. Several types of ventilators have been developed and are employed industrially for different purposes; examples are given in Figure 2.1. Among those, we identify the centrifugal fans, suitable for low flow rates and high pressure. Here, the flow enters the impeller parallel to the rotation axis and exits it radially. They are used to air condition buildings or vehicles, as well as heaters or home appliances. The tangential or cross-flow fans, used for very high flow rates encountering minimal resistance, work by maintaining a vortex with its axis parallel to the shaft and its position close to the impeller circumference. The outward portion of this air vortex is discharged through an outlet diffuser, thus the air has to traverse twice the blade passage before exiting the system. These fans are valued for their ease of integration and used in indoor air conditioning units and domestic ovens. Nevertheless, in this work, we are particularly interested in studying the axial fans (or propellers), where the

airflow remains fairly parallel to the rotation axis of the impeller[1]. In fact, the major component of the blade force is here directed axially from the inlet to the outlet side, producing a pressure rise across the fan. These machines are typically used to displace large air volumes for medium pressure ratios. For this reason, they are suited to cool automotive radiators: for this application, the required pressure difference across the fan never exceeds $1000\,\mathrm{Pa}$ [4].

Figure 2.1: Three typologies of fans produced by the ebm-papst manufacturer group are shown. This work is focused on the axial fans for automotive engine-cooling applications.

2.2 How to measure sound?

When considering the concept of sound in physiology [5], we intend not only the pressure fluctuations that propagate as waves, but also the perception of this signal through the auditory system and its interpretation by the brain. In fact, humans' hearing system has an uncanny ability to detect pressure waves with amplitudes ranging from $20\,\mu\mathrm{Pa}$ to $200\,\mathrm{Pa}$, before reaching the pain threshold. This corresponds in the air to an impressive wavelength variation from $17\,\mathrm{mm}$ to $17\,\mathrm{m}$. Therefore, the sensitivity of the ear can be based on a logarithmic scale, and it is measured on the decibel scale. One can define the Sound Pressure Level (SPL) as [6]:

$$\mathrm{SPL} = 10\log_{10}\left(p_{rms}^2/p_{ref}^2\right), \tag{2.1}$$

function of the ratio between the root mean square of the fluctuating pressure time history p_{rms} and a reference pressure $p_{ref} = 20\,\mu\mathrm{Pa}$, which is a value typically used when the propagation medium is air. The root mean square pressure p_{rms} corresponds to the time-averaged square of the pressure fluctuations: if we denote by $p(t)$ the pressure at a point in the fluid, the pressure fluctuation is defined with respect to the mean background pressure p_0 as $p'(t) = p(t) - p_0$. Thus, we can write:

$$p_{rms} = \sqrt{\frac{1}{2T}\int_{-T}^{T}\left(p(t)-p_0\right)^2 dt}, \tag{2.2}$$

where the integration period T must be large enough to include even the lowest frequencies contained in the signal. As the human ear discerns sounds in a logarithmic way, typically differences below $1\,\mathrm{decibel}$ are not perceived. It is convenient to group the frequency content by summing the

[1] It is not unusual though, especially at high pressure, to find relevant centrifugal forces in these machines, yielding the fan wake to become radial [3].

sound into one-third octave bands, which appear as equal-spaced intervals on a logarithmic scale. An octave band in acoustics is the interval between one frequency and another with double its frequency. Consequently, a third-octave band is the sum of the frequencies f on a band whose upper limit is $2^{1/3}$. The one-third octave band mid-frequencies can be written as $f_n = 1000 \times 2^{(n-30)/3}$, with n as given band number. Thus we can introduce an alternative definition of the SPL, useful in the following, linking it to $S_{pp}(f)$, i.e., the one-sided auto-power spectral density of p:

$$\mathrm{SPL}\,(f_n) = 10 \log_{10} \frac{\int_{f_n-\Delta f/2}^{f_n+\Delta f/2} S_{pp}(f)\mathrm{d}f}{p_{ref}^2}, \tag{2.3}$$

where Δf is the frequency bandwidth.

2.3 Electromagnetic and mechanical noise

The aerodynamic noise is by far the predominant component of fans' acoustic emissions in most cases and is the one studied in this manuscript. Nevertheless, we must mention other components like electromagnetic motor noise and mechanical noise. The former is associated with the force variations due to the variation of the motor magnetic field between the rotor and the stator [4]. These cause vibrations of the stator and the casing, which emit noise. This kind of noise is tonal with peaks corresponding to multiple frequencies of the rotation frequency as well as to harmonics of the double frequency of the electric network $2 \cdot f_e$ (where $f_e = 50\,\mathrm{Hz}$ in Europe). The mechanical noise can arise due to an unbalance of the rotor (tonal noise at the rotation frequency and harmonics), to the sliding of the bearings in case they have been badly lubricated, or to a bad coupling between the rotor and the motor. These non-aerodynamic sound-producing mechanisms may only be relevant at very low speeds and away from the typical operating conditions of axial fans. If any of these mechanisms were dominant at nominal rotational speeds, this would be indicative of a malfunction of the fan system itself.

2.4 Ffowcs-Williams and Hawkings Analogy

In this section, we report the relevant derivation steps of the Ffowcs-Williams and Hawkings aeroacoustic analogy in order to describe the sound-producing aerodynamic mechanisms and assess the ones of most interest in the context of low-speed cooling fans. The pioneering work of Lighthill [7], in which the exact equations of fluid dynamics are reformulated, allowed the distinction between acoustic sources and sound propagation and focused on the sound generated by a turbulent jet [8]. The unsteady stream fluctuations are represented by a distribution of quadrupole sources in the same volume. Replacing the flow fluctuations with equivalent acoustic sources is what Lighthill defined as an analogy. Curle [9] extended Lighthill's analogy by taking into account the effects of solid stationary surfaces while making use of the Kirchhoff boundary solution to the homogeneous wave equation. It is in fact possible to predict aerodynamic noise from wall-bounded flows by solving the wave equation together with relevant boundary conditions imposed on the wall surfaces. Ffowcs-Williams and Hawkings [10] further extended Lighthill-Curle's theory by introducing moving surfaces. The key idea is that fluid motion and moving bodies are replaced by equivalent sources radiating into undisturbed homogeneous and stagnant air. We write the exact equations of motion of fluid under no external forces in the form suggested by

Lighthill [7]:

$$\left.\begin{aligned} \frac{\partial \rho}{\partial t} + \frac{\partial}{\partial x_i}\left(\rho v_i\right) = 0, \\ \frac{\partial}{\partial t}\left(\rho v_i\right) + \frac{\partial}{\partial x_j}\left(\rho v_i v_j + p_{ij}\right) = 0, \end{aligned}\right\} \tag{2.4}$$

where ρ is the density, p_{ij} is the stress tensor, c_0 is the sound velocity in a fluid at rest, v_i is the velocity component in direction x_i, with $i = 1, 2, 3$ [2]. The first of Eq. (2.4) is the continuity equation, whereas the second is the momentum equation, and both are written in Cartesian form. As shown in Figure 2.2, consider a fixed volume of fluid V and suppose it is divided into regions

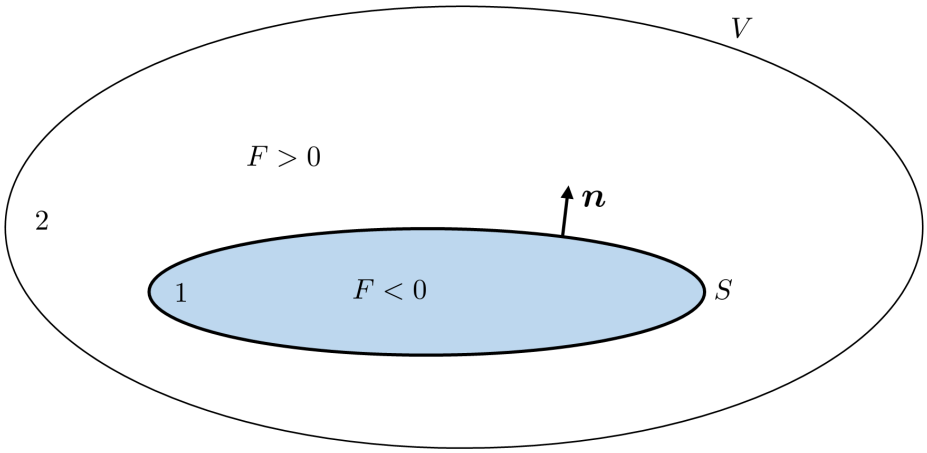

Figure 2.2: The moving surface S is defined where $F = 0$ within the volume V, dividing the regions 1 *and* 2.

1 and 2 by a surface of discontinuity S moving within region 2 with velocity $\boldsymbol{v_s}$. If an equation $F(\mathbf{x}, t) = 0$ defines the surface S and its kinematics, and is such that $F < 0$ in region 1 and $F > 0$ in region 2, it is possible to re-write Eq. (2.4) in the sense of generalized functions:

$$\left.\begin{aligned} \frac{\partial \rho}{\partial t} + \frac{\partial}{\partial x_i}\left(\rho v_i\right) = \left[\rho\left(v_i - v_{si}\right)\right]_{(1)}^{(2)} \delta(F) \frac{\partial F}{\partial x_i}, \\ \frac{\partial}{\partial t}\left(\rho v_i\right) + \frac{\partial}{\partial x_j}\left(\rho v_i v_j + p_{ij}\right) = \left[\rho v_i\left(v_j - v_{sj}\right) + p_{ij}\right]_{(1)}^{(2)} \delta(F) \frac{\partial F}{\partial x_j}, \end{aligned}\right\} \tag{2.5}$$

introducing the jump of a quantity $[-]_{(1)}^{(2)}$ between regions 2 and 1. The one-dimensional delta function $\delta(F)$ is zero everywhere except where $F = 0$. The unit normal to the surface pointing from region 1 to region 2 is defined as $\boldsymbol{n} = \boldsymbol{\nabla} F / |\boldsymbol{\nabla} F|$ and depicted in Figure 2.2. Inside V the fluid is at rest and so the density reduces to ρ_0 and the pressure to p_0. The flow velocity $\boldsymbol{v}$ becomes equal to $\boldsymbol{v_s}$ approaching the surface S from the outside, considering an impermeable surface S. Eq. (2.5) are general forms of the equations governing the unbounded fluid and they are valid everywhere. In fact, with no discontinuities such as the surface S, the mass and momentum sources vanish, leading back to Eq. (2.4). The wave equation is obtained through the same steps

[2] Einstein notation is adopted where indices are repeated.

of Lighthill's analogy [7], yielding:

$$\begin{aligned}\frac{\partial^2\rho}{\partial t^2} - c_0^2\frac{\partial^2\rho}{\partial x_i^2} = \frac{\partial^2}{\partial x_i \partial x_j}\left(\rho v_i v_j + p'_{ij} - c_0^2\rho\delta_{ij}\right) \\ - \frac{\partial}{\partial x_i}\left(p'_{ij}\delta(F)\frac{\partial F}{\partial x_j}\right) + \frac{\partial}{\partial t}\left(\rho_0 v_{si}\delta(F)\frac{\partial F}{\partial x_i}\right),\end{aligned} \tag{2.6}$$

with p'_{ij} as the difference of the stress tensor from its mean value $p_0\delta_{ij}$. Lighthill's tensor $T_{ij} = \rho v_i v_j + p'_{ij} - c_0^2\rho_0\delta_{ij}$ can be recognized as the first source term. The terms ρ and T_{ij} in Eq. (2.6) are intended as generalized functions, i.e., that they are valid throughout V being equal to zero within it and respectively equal to the density fluctuations and to the Lighthill's tensor outside S. The first source term on the right-hand side of Eq. (2.6) has a quadrupolar nature and represents the noise due to the mixing and distortions around the solid bodies. The second source term is referred to as loading noise, representing the dipolar sound emitted by the divergence of a vector field. The third source term, characterized by a time derivative of a scalar quantity, has a monopolar nature and is named thickness noise.

2.4.1 Wave equation solution using Green's functions

The formalism of Green's functions, briefly summarized below, can be used to solve the linear wave equation. More details can be found in [6], for instance. Considering a uniform stationary medium where the acoustic propagation is determined by the linear wave equation for the scalar field variable φ:

$$\Delta\varphi - \frac{1}{c_0^2}\frac{\partial^2\varphi}{\partial t'^2} = Q, \tag{2.7}$$

where a generic source distribution $Q(\mathbf{y}, t')$ is given radiating in a volume of space $\mathcal{V}(t')$, in which moving surfaces $\mathcal{S}(t')$ are present. Since the problem is linear, we are able to see the continuous source as a combination of impulses emitted at a certain instant. For this, we employ the Green's function $\mathrm{G}(\mathbf{x}, t \mid \mathbf{y}, t')$, defined as being the solution to the inhomogeneous equation:

$$\Delta\mathrm{G} - \frac{1}{c_0^2}\frac{\partial^2\mathrm{G}}{\partial t'^2} = -\delta(\mathbf{x}-\mathbf{y})\delta\left(t-t'\right), \tag{2.8}$$

where the functions on the right-hand side of Eq. (2.8) represent Dirac delta functions.
$\mathrm{G}(\mathbf{x}, t \mid \mathbf{y}, t')$ gives the relationship between the acoustic field at $\mathbf{x}$ and t, due to an impulsive source of sound at $\mathbf{y}$ and t'. Considering periodic or stationary random processes, we ignore the effect of initial conditions and we write the formal solution of the scalar field, as proposed in [11]:

$$\begin{aligned}\varphi(\mathbf{x}, t) = -\int_{-\infty}^{\infty}\int_{\mathcal{V}(t')} \mathrm{G}\left(\mathbf{x}, t \mid \mathbf{y}, t'\right) Q\left(\mathbf{y}, t'\right) \mathrm{d}\mathbf{y}\mathrm{d}t' \\ - \int_{-\infty}^{\infty}\int_{\mathcal{S}(t')} \left\{\mathrm{G}\left(\frac{\partial}{\partial n} + \frac{V_n}{c_0^2}\frac{\partial}{\partial t'}\right)\varphi - \varphi\left(\frac{\partial}{\partial n} + \frac{V_n}{c_0^2}\frac{\partial}{\partial t'}\right)\mathrm{G}\right\} \mathrm{d}\mathcal{S}_y\, \mathrm{d}t'.\end{aligned} \tag{2.9}$$

In Eq. 2.9 the volume integral represents the direct radiation of the source distribution, whereas the surface integral represents all effects of reflection and diffraction by the surfaces. The Green's function is not unique and depends on the boundary conditions of the specific problem. As such, its expression must be known to explicitly solve Eq. (2.9). Employing the free-field Green's function G_0, defined as:

$$\mathrm{G}_0\left(\mathbf{x}, t \mid \mathbf{y}, t'\right) = \frac{\delta\left(t' - t + R/c_0\right)}{4\pi R}, \tag{2.10}$$

where $R = |\boldsymbol{R}| = |\mathbf{x} - \mathbf{y}|$, the surface integral vanishes for sources emitting in free space because no boundaries are present. In the Ffowcs Williams and Hawkings' analogy the solid surfaces are, in fact, considered as equivalent sources, rather than boundary conditions. This leads to the general free-field solution assumed in the following:

$$\varphi(\mathbf{x}, t) = -\int_{-\infty}^{\infty} \int_{\mathcal{V}(t')} \mathrm{G}_0 \left(\mathrm{x}, t \mid \mathrm{y}, t'\right) Q \left(\mathbf{y}, t'\right) \mathrm{d}\mathbf{y}\mathrm{d}t'. \tag{2.11}$$

Using the properties of the delta function, it is possible to reduce the time integral, yielding the solution:

$$\varphi(\mathbf{x}, t) = -\int_{\mathcal{V}(t')} \frac{Q\left(\mathbf{y}, t + R/c_0\right)}{4\pi R} \mathrm{d}\mathbf{y} = -\int_{\mathcal{V}(t')} \frac{[Q]}{4\pi R} \mathrm{d}\mathbf{y}, \tag{2.12}$$

with the quantity $t' = t - R/c_0$ is the emission time or retarded time of the source at point $\mathbf{y}$, which is corresponding to a contribution at point $\mathbf{x}$ and at time t. The square brackets in Eq. (2.12) are conventionally used to indicate a quantity evaluated at a retarded time.

2.4.2 Formal solution of the FWH's equation

We make use of the free-field Green's function 2.10 in order to solve Eq. (2.6) in an unbounded medium at rest, as proposed by Ffowcs Williams and Hawkings [10]. With solid surfaces, it is possible to write the formal solution after having made use of the general properties of convolution products. Moreover, it is convenient to introduce a Lagrangian coordinate system $\boldsymbol{\eta}(\mathbf{y}, t')$, which moves so that the surface $\mathcal{S}(t')$ remains fixed in the $\boldsymbol{\eta}(\mathbf{y}, t')$ coordinate space [11]. The acoustic density fluctuation at point $\mathbf{x}$ and time t is written as:

$$\begin{aligned} c_0^2 \rho'(\mathbf{x}, t) = & \frac{\partial^2}{\partial x_i \partial x_j} \int_{-\infty}^{+\infty} \int_{\mathcal{V}} T_{ij}\left(\boldsymbol{\eta}, t'\right) \frac{\delta\left(t' - t + R/c_0\right)}{4\pi R} \mathrm{d}\boldsymbol{\eta}\mathrm{d}t' \\ & - \frac{\partial}{\partial x_i} \int_{-\infty}^{+\infty} \int_{\mathcal{V}} \left(p'_{ij} \delta(f) \frac{\partial f}{\partial y_j}\right)\left(\boldsymbol{\eta}, t'\right) \frac{\delta\left(t' - t + R/c_0\right)}{4\pi R} \mathrm{d}\boldsymbol{\eta}\mathrm{d}t' \\ & + \frac{\partial}{\partial t} \int_{-\infty}^{+\infty} \int_{\mathcal{V}} \rho_0 \left(V_{si} \delta(f) \frac{\partial f}{\partial y_i}\right)\left(\boldsymbol{\eta}, t'\right) \frac{\delta\left(t' - t + R/c_0\right)}{4\pi R} \mathrm{d}\boldsymbol{\eta}\mathrm{d}t', \end{aligned} \tag{2.13}$$

where $R = |\mathbf{x} - \mathbf{y}\left(\boldsymbol{\eta}, t'\right)|$. We can reduce the time integral exploiting the delta function properties, as done in Section 2.4.1, obtaining:

$$\begin{aligned} c_0^2 \rho'(\mathbf{x}, t) = & \frac{1}{4\pi} \frac{\partial^2}{\partial x_i \partial x_j} \int_{\mathcal{V}_e} \left[\frac{T_{ij}}{R\,|1 - M_r|}\right] \mathrm{d}\boldsymbol{\eta} \\ & - \frac{1}{4\pi} \frac{\partial}{\partial x_i} \int_{\mathcal{S}} \left[\frac{P_i}{R\,|1 - M_r|}\right] \mathrm{d}\boldsymbol{\eta} \\ & + \frac{1}{4\pi} \frac{\partial}{\partial t} \int_{\mathcal{S}} \left[\frac{\rho_0 V_n}{R\,|1 - M_r|}\right] \mathrm{d}\boldsymbol{\eta}, \end{aligned} \tag{2.14}$$

where the quantities enclosed within square brackets are evaluated at the retarded time by integrating over the external volume $\mathcal{V}_e$ and the body surfaces $\mathcal{S}$. In Eq. (2.14), the net force exerted on the fluid from each surface element is indicated with $\mathbf{P}$, whereas $V_n = \mathbf{v_s} \cdot \boldsymbol{n}$ is the normal of the velocity field on the surfaces. The factor $1 - M_r$ accounts for the Doppler effect related to the projected motion on the line connecting the source to the observer $M_r = \boldsymbol{M} \cdot \boldsymbol{R}/R$, with the

vectorial Mach number $\boldsymbol{M}$. Eq. (2.14) presents a singularity for supersonic cases when $M_r = 1$, discussed for instance in [12], hereafter ignored because we are interested in highly subsonic blade tip velocities. We can notice that the third integral on the right-hand side of Eq. (2.14) has a monopolar nature due to the time variation of ρV_n over the surface $\mathcal{S}$. Since we consider a solid surface, this fluid displacement source can be nonzero only due to a time-varying surface velocity at the emission time. Hence, this source is zero for a body in linear motion traveling at subsonic speeds towards the listener, and sound is emitted only by virtue of retarded-time differences between the monopoles. Another expression, mathematically equivalent to Eq. (2.14), was introduced in [10, 11] to write this monopolar term by means of volume integrals of dipoles and quadrupoles over the inner volume $\mathcal{V}_i$ of the surfaces:

$$\begin{aligned} c_0^2 \rho'(\mathbf{x}, t) = & \frac{1}{4\pi} \frac{\partial^2}{\partial x_i \partial x_j} \int_{\mathcal{V}_e} \left[\frac{T_{ij}}{R\,|1 - M_r|} \right] \mathrm{d}\boldsymbol{\eta} \\ & - \frac{1}{4\pi} \frac{\partial}{\partial x_i} \int_{\mathcal{S}} \left[\frac{P_i}{R\,|1 - M_r|} \right] \mathrm{d}\boldsymbol{\eta} \\ - \frac{1}{4\pi} \frac{\partial}{\partial x_i} \int_{\mathcal{V}_i} & \left[\frac{\rho_0 \Gamma_i}{R\,|1 - M_r|} \right] \mathrm{d}\boldsymbol{\eta} + \frac{\partial^2}{\partial x_i \partial x_j} \int_{\mathcal{V}_i} \left[\frac{\rho_0 V_i V_j}{R\,|1 - M_r|} \right] \mathrm{d}\boldsymbol{\eta}, \end{aligned} \tag{2.15}$$

where $\boldsymbol{V}$ and $\boldsymbol{\Gamma}$ are, respectively, the absolute velocity and acceleration fields of the solid surface motion. One can notice that if the surface $\mathcal{S}$ is stationary, $\boldsymbol{\Gamma} = \boldsymbol{M} = \boldsymbol{V} = 0$, and $\boldsymbol{\eta} = \mathbf{y}$. Consequently, Eq. (2.15) reduces to Curle's analogy equation derived in [9] for solid stationary surfaces.

2.5 Far-field sound radiation and usual approximations

We introduce the approximations usually applied for subsonic flows in order to determine the dominant contributors to the far-field noise of the FWH's equation 2.15.

1. For low-Mach numbers and high Reynolds numbers, we consider Lighthill's approximation $T_{ij} \approx \rho_0 u_i u_j$, where $\boldsymbol{u}$ only involves the aerodynamic velocity, without taking into account the acoustic motion. For such a case, Lighthill showed [7] that the quadrupolar acoustic power is $P_Q \propto \rho_0 U_0^8 c_0^{-5} L_0^2$, where U_0 and L_0 are, respectively, characteristic velocity and length of the flow. Additionally, Curle showed [9] that in presence of a solid stationary body, the acoustic power due to the dipolar term $P_D \propto \rho_0 U_0^6 c_0^{-3} L_0^2$. Therefore, the ratio $P_Q / P_D \propto M_0^2$, where $M_0 = U_0 / c_0$ is the Mach number. It follows that for highly subsonic flows, the contribution of the dipolar source term is greater than the quadrupolar one, which can be neglected.

2. In Eq. (2.15), the contributions of the integrals over the inner volume $\mathcal{V}_i$ tend to zero when $\mathcal{V}_i$ tends to zero. For this reason, this mechanism is called thickness noise: if the blade thickness is reduced, so is the thickness noise. For thin blades, this contribution is negligible and it only becomes important at tip speeds with Mach numbers greater than 0.7 [6].

3. In the second source term of Eq. (2.15), $\boldsymbol{P}$ represents the contact forces exerted from the surfaces onto the fluid and does not account for the scattering and diffraction effects. This can be only accepted if the source is acoustically compact, i.e., when its characteristic size is much smaller than the acoustic wavelength $L_0 / \lambda \ll 1$. In this case, the source region can be approximated as a single point source, where the retarded time differences are negligible. Since we consider the listener point $\mathbf{x}$ to be in the far-field, we take advantage of

the far-field approximation which makes it possible to commute the space derivatives into time derivatives and only account for the terms with spherical attenuation, as reported by Goldstein [11].

Considering the aforementioned points and knowing that the acoustic pressure is defined as $p' = c_0^2 \rho'$, Eq. 2.15 can be written:

$$p'(\mathbf{x},t) \simeq \frac{1}{4\pi} \int_{\mathcal{S}} \left[\frac{R_i}{R^2 c_0 \left(1 - M_r\right)} \left(\frac{\partial}{\partial t'} \left(\frac{P_i}{1 - M_r} \right) \right) \right] \mathrm{d}\boldsymbol{\eta}, \tag{2.16}$$

where only the noise produced by the forces, henceforth referred to as loading noise, is taken into account as it is dominant over the quadrupolar and monopolar sources for subsonic fans. From Eq. (2.16) we deduce that unsteady phenomena are a necessary condition for sound propagation to the far-field. As such, we focus on the loading-noise source term to thoroughly comprehend the role of the unsteadiness [13]. By developing the time derivative in Eq. (2.16), one can write:

$$\frac{\partial}{\partial t'} \left(\frac{P_i}{1 - M_r} \right) = \frac{1}{1 - M_r} \frac{\partial P_i}{\partial t'} - \frac{P_i}{\left(1 - M_r\right)^2} \frac{\partial \left(1 - M_r\right)}{\partial t'},$$

from which we notice that the far-field noise has two origins: the intrinsic unsteadiness of the source term (in the Lagrangian reference frame following the surface), and the unsteadiness due to the motion expressed by the Doppler factor. It is possible to develop also the Doppler factor derivative, obtaining two contributions:

$$\frac{\partial \left(1 - M_r\right)}{\partial t'} = \frac{M_i}{R} \left(V_i - \frac{R_i R_j}{R^2} V_j \right) - \frac{R_i}{R c_0} \Gamma_i,$$

where the first term on the right-hand side must be neglected as a near-term in the far-field approximation, whereas the second is due to the acceleration of the source. Hence, the far-field acoustic pressure can be approximated as:

$$p'(\mathbf{x},t) \simeq \frac{1}{4\pi} \int_{\mathcal{S}} \left[\frac{R_i}{R^2 c_0 \left(1 - M_r\right)} \left(\frac{1}{1 - M_r} \frac{\partial P_i}{\partial t'} + \frac{P_i}{\left(1 - M_r\right)^2} \frac{R_i}{R c_0} \Gamma_i \right) \right] \mathrm{d}\boldsymbol{\eta}, \tag{2.17}$$

from which we deduce that for a body with a uniform velocity, the unsteady aerodynamic loading is the only physical phenomenon generating noise, whereas steady forces do produce noise in the far-field if the body acceleration is nonzero.

2.5.1 Dimensional Analysis

We follow the dimensional analysis proposed in [13] for an acoustically compact segment of lifting surface to discern the relative importance of the sound-producing phenomena of Eq. (2.17), respectively due to unsteady and steady loading. Considering a fan blade segment rotating at a constant speed Ω at a radius R_0, the characteristic velocity is $V_0 = \Omega R_0$, whereas the corresponding centripetal acceleration can be written as $\Gamma_0 = V_0^2 / R_0$. We assume to have a chord length c with a spanwise dimension of the same order of magnitude. The steady aerodynamic force, from with the steady-loading noise is dependent, is $F_0 \simeq C_L c^2 \rho_0 V_0^2 / 2$, considering a given lift coefficient C_L. Referring to Sears' theory [14], the fluctuations around the average force F_0 are dependent on the velocity disturbances w. In particular, the fluctuating force amplitude is $F' \simeq \pi \rho_0 c^2 w V_0$; therefore its time derivative is:

$$\left| \frac{\partial F'}{\partial t'} \right| \propto m \rho_0 c^2 w V_0^2 / R_0,$$

with m as a multiple of the rotational frequency. Considering that $\partial M_r/\partial t' \propto V_0^2/(c_0 R_0)$, we introduce the acoustic far-field intensities for the steady-loading noise I_S and for the unsteady-loading noise I_U, yielding the dimensional evaluations:

$$I_S \propto \frac{\rho_0 c^4 V_0^8}{R_0^2 c_0^5 R^2 (1-M_0)^6}, \quad I_U \propto m^2 \frac{\rho_0 (w/V_0)^2 c^4 V_0^6}{R_0^2 c_0^3 R^2 (1-M_0)^4},$$

where R is the distance from the listener. We recognize the typical dipolar trend describing the unsteady-loading noise intensity that scales with the sixth power of a characteristic flow speed. On the contrary, steady-loading noise scales with the eighth power of the characteristic flow speed, yielding the ratio:

$$\frac{I_S}{I_U} \propto \frac{1}{m^2} \left(\frac{V_0}{w}\right)^2 \left(\frac{M_0}{1-M_0}\right)^2,$$

where the disturbance rate V_0/w is considered constant in this analysis. We infer that for fan blades rotating at low Mach numbers, steady-loading noise can be ignored because the fluctuating forces on the moving bodies are the most efficient sound sources and so the unsteady-loading noise is the most dominant in most applications.

2.6 Unsteady-loading noise mechanisms

In Section 2.4 the sound source terms resulting from the Ffowcs-Williams and Hawkings equation [10] have been examined. It is possible to observe in Figure 2.3 the aerodynamic noise mechanisms and remind that the monopolar and quadrupolar sound sources can be neglected, just as the steady-loading noise. In fact, for fans at low Mach numbers and high Reynolds numbers, unsteady

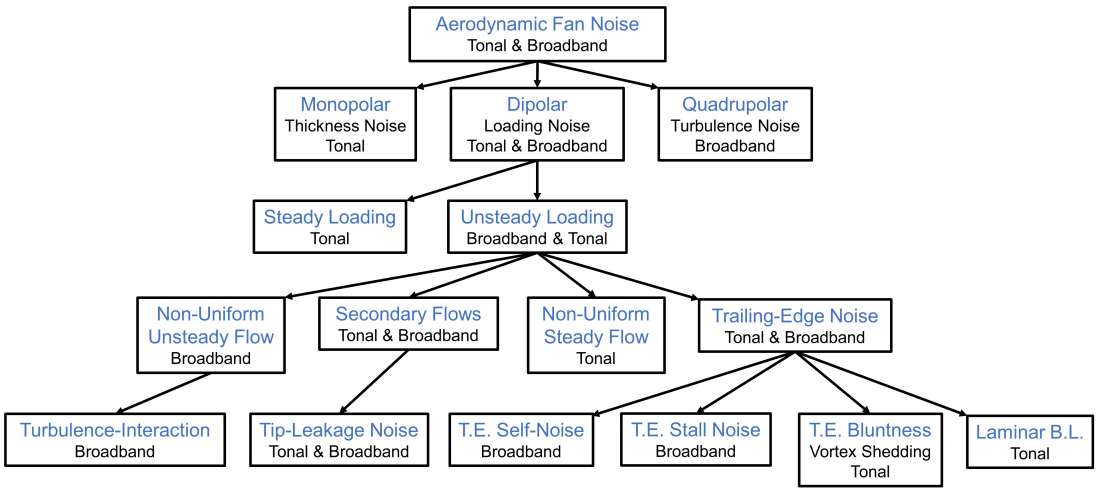

Figure 2.3: Aerodynamic fan noise mechanisms of broadband and tonal nature.

loading noise is the dominant sound-producing mechanism in most applications and particularly in the case of low-speed cooling fans. Nonetheless, several phenomena can occur yielding unsteady loads on the fan blades, as depicted in Figure 2.4. In the following, we analyze the typical ones.

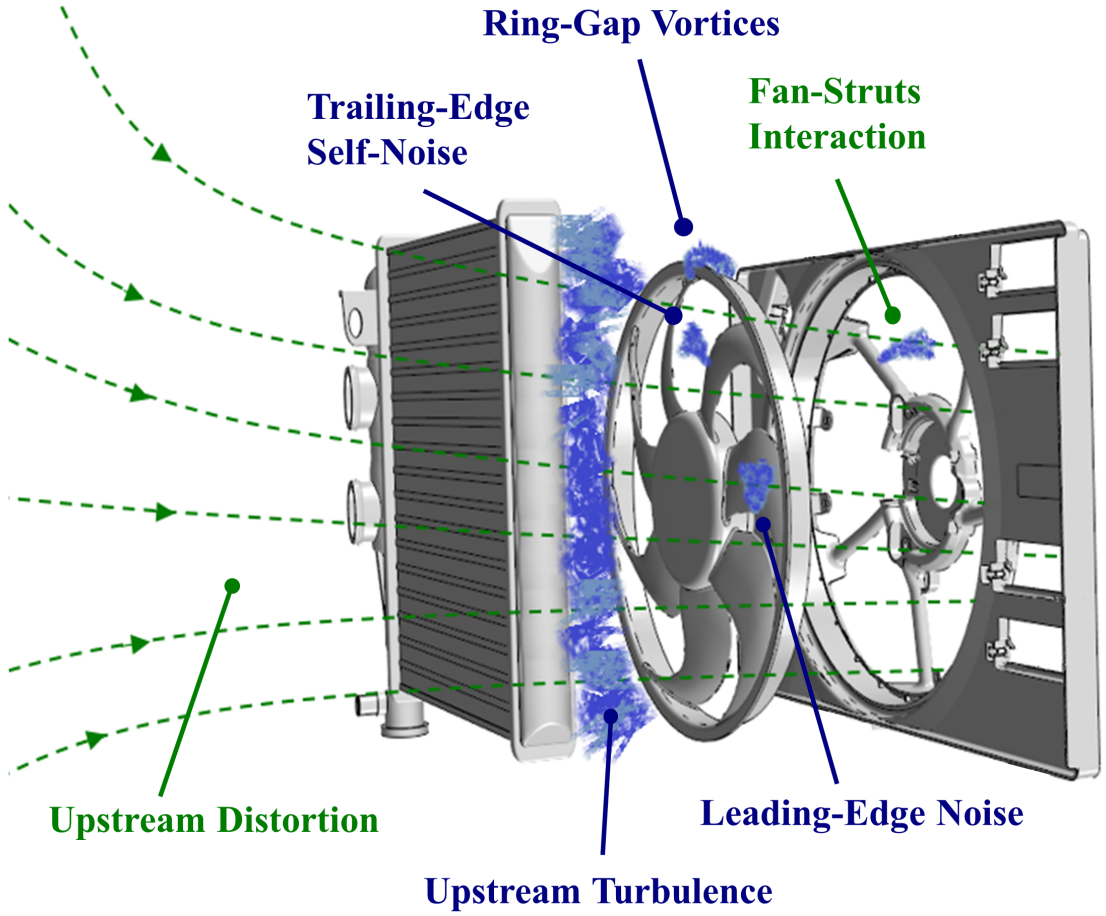

Figure 2.4: Common noise mechanisms in automotive cooling modules: tonal mechanisms in green and broadband mechanisms in blue.

2.6.1 Non-uniform steady-flow noise

The non-uniform steady-flow noise often referred to as periodic loading noise, is due to periodic velocity changes that the blades encounter cyclically during their rotation. These changes are typically due to the presence of obstacles at the inlet or outlet of the impeller which induce a non-uniform distribution of the velocity field along the circumference of the fan. It results in a change of the airfoil velocity triangle of the blades, thus varying the angle of attack and consequently the aerodynamic load. For this reason, this sound mechanism is tonal in nature, the sound peaks here being emitted at the blade passing frequency (BPF) and its harmonics. We define the BPF as $f_{BPF} = B\Omega/60$, where B is the number of blades and Ω is the rotational speed in revolutions per minute (rpm). These tonal peaks can be observed on a typical axial fan spectrum in Figure 2.5. We can distinguish the so-called viscous interaction of the downstream blade wake with any obstacles, such as motor support struts. In addition, there is tonal noise due to a so-called potential interaction that occurs with obstacles or deviations of the upstream flow due to rapid changes in geometry, such as the transition from the rectangular section of the casing to the circular section of the impeller. The potential interaction is more efficient at emitting than the viscous interaction, as suggested in [4]. However, its influence decreases more rapidly as one moves away from obstacles:

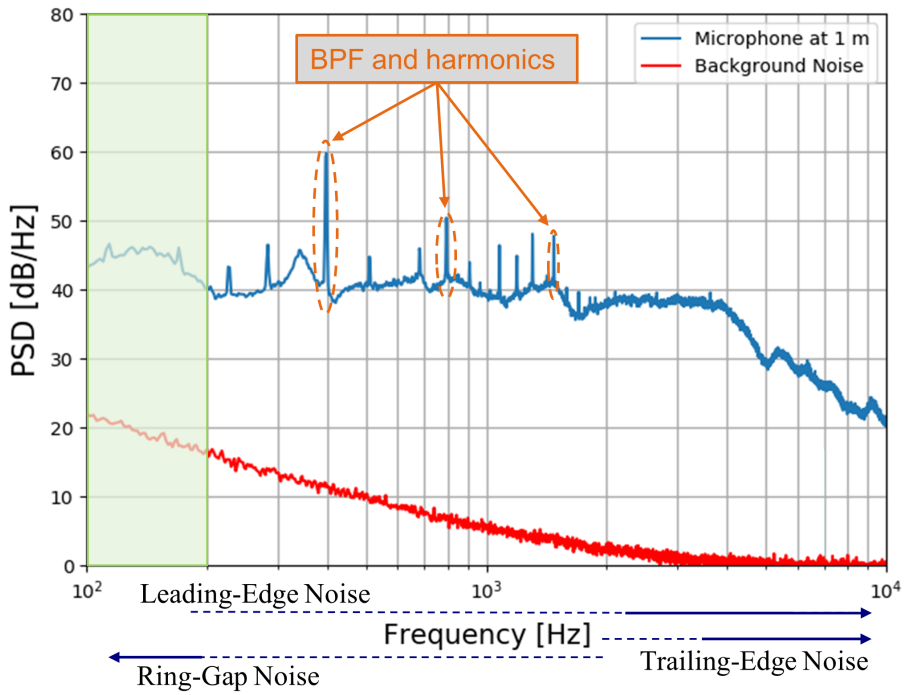

Figure 2.5: Example of noise frequency spectrum measured in an anechoic laboratory with a cut-off frequency equal to 200 Hz. *The tonal peaks due to the BPF and harmonics are indicated with orange ellipsoids, whereas the background noise is plotted in red.*

typically for distances greater than $3c$, where c is the length of the blade chord, the contribution of the viscous interaction overcomes that of the potential interaction [15].

2.6.2 Turbulence-interaction noise

Turbulence-interaction noise or turbulence-impingement noise is due to non-uniform turbulent inflow conditions. These might be caused by the presence of upstream obstacles such as the heat exchanger core that produces a turbulent flow impinging on the blade leading edge. The breakdown of oncoming vorticity induces a random variation of the blade angle of attack, yielding an unsteady modification of the blade lift as depicted in Figure 2.6 (a). In fact, an inflow turbulence increase can affect profoundly the broadband noise, as confirmed by Schneider [16]. In the sense of the analogy, this is like having equivalent acoustic sources distributed on the leading edge of the blades. For this reason, this noise mechanism is also known as leading-edge noise. It has been extensively studied experimentally from steady airfoils immersed in a distorted incoming flow. Its contribution to the frequency spectrum depends on the type of turbulent length scale the distorted flow is made of. For this reason, different incoming turbulent flows have been studied. In particular, turbulence is typically generated by an upstream circular cross-sectional rod [17, 18] or an upstream turbulence grid [19–21]. The leading-edge noise has been analytically modeled via Amiet's airfoil noise theory [22], whose mathematical elegance and physical relevance represent a milestone in the world of aeroacoustics. Some of the fundamental steps of this analytical approach are given below in order to understand what are the key parameters on which turbulence-interaction noise depends. By considering tiny perturbations on a thin, lightly loaded airfoil, it is possible to decouple steady-state aerodynamics from unsteady phenomena. Airfoil parameters

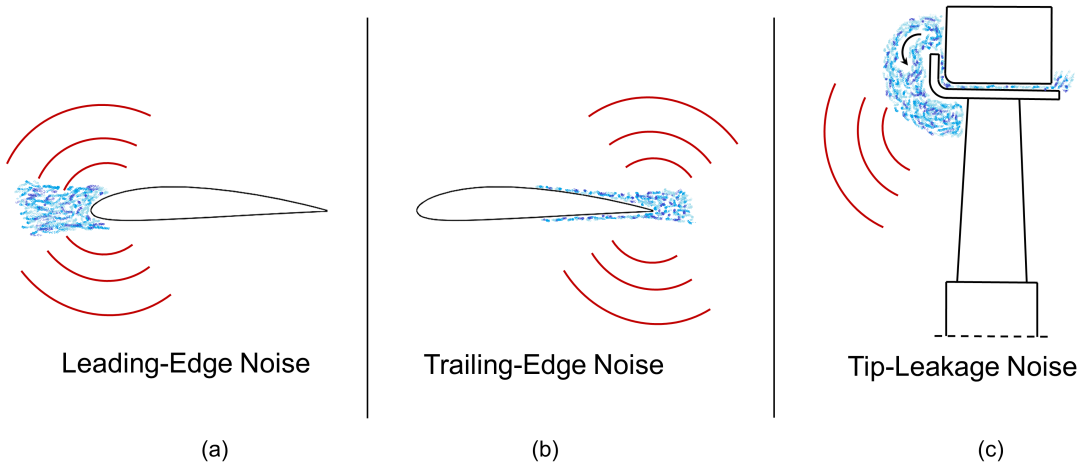

Figure 2.6: Most relevant broadband noise emitted by an axial fan rotating at the nominal condition: (a) turbulence-interaction or leading-noise; (b) trailing-edge or self-noise; (c) tip-leakage or ring-gap noise.

such as thickness, camber, and angle of attack depend on the former. Instead, the fluctuations around the mean lift depend on the chord c and on the component of fluctuating velocity normal to the chord line. Thus, it is possible to assimilate the airfoil to a rigid flat plate and assume that the incoming turbulence is frozen, i.e., the interaction with the flat plate is much faster than the evolution time of the turbulent eddies. We further represent the turbulence in terms of a continuous set of its spectral wavenumber components k_1 and k_2, as depicted in Figure 2.7. The frozen tur-

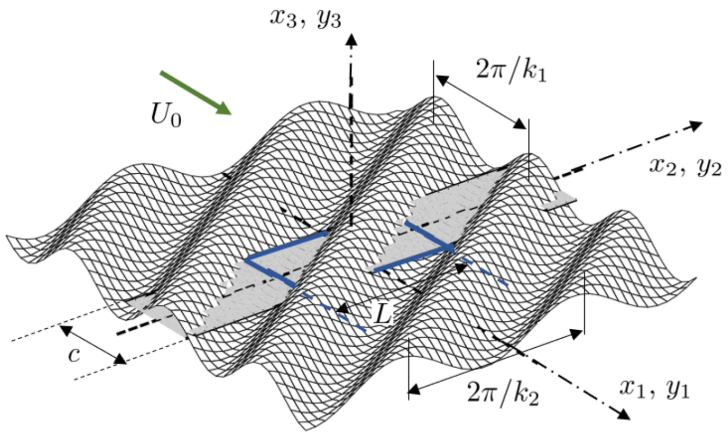

Figure 2.7: Two-dimensional sinusoidal gust impinging over a flat plate over which the Cartesian reference frame is defined with the coordinates of the sources y_i and the listener x_i; image is taken from [13].

bulence assumption determines the streamwise wavenumber $k_1 = \omega/U_0$, where ω is the angular frequency and U_0 is the flow speed. The first step in Amiet's theory is to derive the lift fluctuations induced by a single gust on the flat plate that is extended infinitely along the span direction. The far-field noise is then calculated by integrating the lift fluctuations over the actual rectangular

extent of the airfoil:

$$S_{pp}^{LE}(\mathbf{x},\omega) = \left(\frac{k_a \rho_0 c x_3}{2S_0^2}\right)^2 \pi U_0 \frac{L}{2} \int_{-\infty}^{\infty} \left[\Phi_{ww}\left(\frac{\omega}{U_0}, k_2\right) \times \left|\mathcal{L}^{LE}\left(x_1, \frac{\omega}{U_0}, k_2\right)\right|^2 \frac{\sin^2\left[\left(\frac{k_a x_2}{S_0} - k_2\right)\frac{L}{2}\right]}{\pi \frac{L}{2}\left(\frac{k_a x_2}{S_0} - k_2\right)^2}\right] \mathrm{d}k_2, \tag{2.18}$$

where a statistical approach is used to link S_{pp}^{LE} to the statistics of the upstream turbulent velocity field. This is represented by the two-dimensional wavenumber spectrum Φ_{ww}. It is possible to simplify Eq. (2.18) with an approximated expression valid for large-span airfoils, such that the aspect ratio $L/c \rightarrow \infty$. Exploiting the equivalence of the sine-cardinal function with Dirac's delta function, we write:

$$S_{pp}^{LE}(\mathbf{x},\omega) = \left(\frac{\rho_0 k_a c x_3}{2S_0^2}\right)^2 \pi U_0 \frac{L}{2} \Phi_{ww}\left(k_1, \frac{k_a x_2}{S_0}\right) \left|\mathcal{L}^{LE}\left(x_1, k_1, \frac{k_a x_2}{S_0}\right)\right|^2, \tag{2.19}$$

where a specific listener-dependent spanwise wavenumber is selected as $k_2 = \omega x_2 / c_0 S_0$. In Eq. (2.19), we understand that in addition to the flow-dependent terms and the relative geometric position between the source and the listener, and besides the aeroacoustic transfer function $\mathcal{L}^{LE}$ [3], the choice of Φ_{ww} is of high relevance. Typically, turbulence models that assume isotropic and homogeneous flow behavior are used, e.g. the Liepmann model or the von Kármán model; their mathematical formulation can be found in Chapter 5. However, in real-application cases, the turbulent flow produced by an upstream obstacle is not necessarily homogeneous and isotropic. This motivates the study done in Chapter 4, where we are going to experimentally characterize the turbulence of the flow downstream of an automotive radiator.

2.6.3 Trailing-edge noise

Under the trailing-edge noise classification, several sound mechanisms are often included that always develop at the trailing edge of the blade.

1. When the angle between the blade and the incident flow increases significantly, the blade may stall. This phenomenon can be local and followed by reattachment of the boundary layer on the airfoil as a result of a negative longitudinal pressure gradient on the blade. Or the stall may be complete and in this case, a characteristic low-frequency broadband noise appears. Under nominal operating conditions, this noise mechanism does not occur on the fan blades.

2. In the case of blunt trailing-edge blades, a tonal sound mechanism is produced as the airfoil establishes a von Kármán street in the near wake. This mechanism is called vortex shedding sound and is centered on a frequency f_v such that the Strouhal number is $f_v e / U_0 \approx 0.2$, where e is the trailing-edge thickness. Axial fan blades are generally sharpened so that e is less than about one-third of the displacement thickness of the boundary layer, which eliminates this sound source [4].

[3] The aeroacoustic transfer function has been derived mathematically by Amiet and the details of its derivation are given in the original paper [22].

3. In the case where the boundary layer remains laminar up to the trailing edge, laminar instability waves, known as Tollmien-Schlichting waves, can establish and cause a tonal sound mechanism. These waves convected by the flow, interact with the trailing edge resulting in acoustical feedback that strongly amplifies discrete high frequencies [23]. This sound mechanism can be deactivated by either using tripping devices, increasing the angle of incidence, or accelerating the transition to turbulence.

4. Self-noise, often directly referred to as trailing-edge noise, is the most relevant broadband sound mechanism in the study of axial fans among those generated at the trailing edge. This is because it is generated even in clean inflow conditions as a result of the turbulent boundary layer that, when encountering the discontinuity of the trailing edge, scatters acoustic waves (see Figure 2.6 (b)). This broadband mechanism is relevant especially at high frequencies because of the small turbulent scales that develop in the boundary layer. However, this mechanism is physically similar to leading-edge noise, which is why it was treated analytically by Amiet [24] in a similar manner. The main difference is that the incident wall-pressure fluctuations at the trailing edge are used as input; more details can be found in [25]. The wall pressure is expanded into a set of pressure gusts, convected at a speed U_c smaller than the external flow velocity. It is then possible to derive the aeroacoustic response to a single gust, exploiting Kutta's condition, and writing the power spectral density (PSD) as:

$$S_{pp}^{TE}(\mathrm{x},\omega) = \left(\frac{k_a x_3 L c}{4\pi S_0^2}\right)^2 \frac{2}{c}\int_{-\infty}^{\infty} \Pi_0\left(\frac{\omega}{U_c}, k_2^*\right) \times \frac{\sin^2\left\{\frac{L}{c}\left(k_2^* - k^*\frac{x_2}{S_0}\right)\right\}}{\left\{\frac{L}{c}\left(k_2^* - k^*\frac{x_2}{S_0}\right)\right\}^2} \left|\mathcal{L}^{TE}\left(\frac{\omega c}{2U_c}, k_2^*\right)\right|^2 \mathrm{d}k_2^*, \tag{2.20}$$

as a function of dimensionless variables with respect to the half-chord and denoted by stars. The aeroacoustic transfer function $\mathcal{L}^{TE}$ includes the main trailing-edge scattering term and also the back-scattering correction, derived from Roger and Moreau [25]. Analogously to Section 2.6.2, we introduce the large-span approximation, giving:

$$S_{pp}^{TE}(\mathbf{x},\omega) = \left(\frac{k_a x_3 c}{2\pi S_0^2}\right)^2 \pi\frac{L}{2}\left|\mathcal{L}^{TE}\left(\frac{\omega c}{2U_c}, k^*\frac{x_2}{S_0}\right)\right|^2 \Pi_0\left(\frac{\omega}{U_c}, k^*\frac{x_2}{S_0}\right), \tag{2.21}$$

from which one can notice that in addition to terms related to the flow and the relative position between the listener and the source, the important input is the wavenumber spectrum of the wall-pressure fluctuations:

$$\Pi_0\left(\frac{\omega}{U_c}, k_2^*\right) = \frac{1}{\pi}\Phi_{pp}(\omega)\ell_y\left(\omega, k_2^*\right), \tag{2.22}$$

where $\ell_y\left(\omega, k_2^*\right)$ is the correlation length related to the correlation function γ_c between two spanwise locations separated by η_2. This can be written as:

$$\ell_y\left(\omega, k_2^*\right) = \int_0^{\infty} \sqrt{\gamma_c^2\left(\eta_2,\omega\right)}\cos\left(k_2\eta_2\right)\mathrm{d}\eta_2. \tag{2.23}$$

The wall-pressure PSD Φ_{pp} is the one induced upstream near the trailing edge by the incident turbulence alone. These two quantities can vary significantly depending on the type of turbulent boundary layer and are therefore of high interest to whoever intends to simulate the

sound of rotating machines. Since it is very expensive to obtain fully resolved simulations of the wall-pressure statistics, semi-empirical models are often used for industrial purposes. In Chapter 5, we will use three different models, in order to compare them for what concerns the modeling of the fan trailing-edge noise. Similarly, for the spanwise correlation length, a generalization of the Corcos model, proposed by Caiazzo *et al.* [26], will also be employed and investigated.

2.6.4 Tip-leakage noise

Depending on the fan geometry, secondary flows such as recirculation bubbles near the blade trailing edge [27] or turbulent flows near the motor hub [28] can contribute to overall noise emissions. However, the main contribution is tip-leakage or tip-clearance noise. As proposed in 1978 by Longhouse [29], typically, these fans consist of an L-shaped ring that is used to join the blades together (increasing their structural stiffness), and to enhance aerodynamic efficiency, as the space between the tip of the blades and the stationary shroud is reduced. Nevertheless, the pressure rise across the impeller convects part of the tip flow upstream through the gap between the rotating ring and the steady shroud, hereafter referred to as ring gap or tip labyrinth. In this region shown in Figure 2.6 (c), large vortical structures [30] are produced and re-ingested by the propeller, interacting with the tip edges of the blades. However, the type of tip flow, which can reach 6% of the nominal flow through the fan [3], depends on various parameters such as the length and geometry of the tip labyrinth, the fan rotational speed, and the aerodynamic load on the blades. Furthermore, dealing with fans made of polymeric materials, there is a noticeable axial deflection due to a combination of centrifugal forces and blade loading, the so-called umbrella effect. A wider tip clearance induces larger tip vortices and more turbulent structures in the ring gap [31]. In order to differentiate it from the tip-leakage noise emitted by free-tip fans, we propose to refer to this mechanism as ring-gap noise, hereafter used alternatively. The studies related to this sound source are few and summarized by Grilliat in [32]. Only very recently though, high-fidelity compressible LBM/VLES simulations have allowed the generation and development of tip-leakage flow to be investigated. A general increase of sound emissions from low to medium frequencies due to tip-leakage noise is reported. However, the most striking effect of this noise mechanism is the appearance of subharmonic humps in the frequency spectrum that have a quasi-tonal behavior. In the tip labyrinth, the tangential velocity of the flow is reduced due to the friction of the flow with the shroud. As a result, the vortical structures impinging on the blades rotate at a lower angular velocity than that of the fan, giving rise to the subharmonic humps [33, 34]. In 2019, Canepa *et al.* [30] used two-dimensional Laser Doppler Velocimetry and PIV to study the leakage flow evolution for different operating conditions. Changing these, large-scale periodic eddies leaving the ring gap are reingested either wrapping around the rotating ring or flowing radially outwards, forming a broad recirculating bubble. If we suppose that the interaction between the sub-harmonics periodic structures with one blade is occurring at the tip, the frequency shift f_{sh} contributing to the sound spectrum with respect to the BPF and harmonics can be written as:

$$f_{sh} = \frac{1}{2\pi}\frac{u_{tip} - v_t}{r_{tip}} = \frac{1}{2\pi}\frac{u_{tip}}{r_{tip}}\left(1 - \frac{v_t}{u_{tip}}\right) = \frac{\Omega}{60}\left(1 - \frac{v_t}{u_{tip}}\right) \tag{2.24}$$

with v_t as the value of the tangential component of the absolute velocity at which the strictures are convected, whereas r_{tip}, and u_{tip} are the fan tip radius and the velocity of the tip, respectively. They found out that in addition to the periodic large vortical structures responsible for the subharmonic humps at low frequencies, non-periodic structures are always present in the flow leaving

the gap or may rise from the ripping of the periodic ones. Dealing with a highly unsteady three-dimensional flow, a fully accepted mathematical modeling of this source term is yet to be derived to the author's knowledge and this aspect will not be tackled in this manuscript. Nevertheless, in Chapter 3, we will infer that the dominant sources at high frequencies are likely coming from the ring-gap turbulent region.

2.7 Literature review

In the present section, some of the relevant previous publications concerning automotive low-speed cooling fan noise are reported. The aim is not to cover all the work done in the past, but rather to exploit studies relevant to the research presented in the subsequent chapters of this manuscript. This will focus primarily on the study of broadband noise. Indeed, tonal noise caused by rotating blades is associated with periodic interactions, corresponding to perfectly correlated interfering sources. It has already been the subject of numerous studies and mitigation strategies have been proposed. Screens can, for example, be used to minimize the inlet flow non-homogeneity [35, 36], as well as an asymmetric blade distribution can redistribute the acoustic energy on rotational harmonics [37]. Moreover, periodic flows can typically be simulated using relatively low-cost numerical techniques. In contrast, broadband noise needs very expensive numerical methods to solve the unsteady velocity and wall-pressure fluctuations [31], which are often unattainable in engineering development contexts. Thus, low-order semi-analytical techniques are often unavoidable in this case. We introduce at first the typical experimental approaches used in the past to study and measure the fan noise, then the numerical and analytical methods to simulate and model the acoustic sources and their propagation. In addition, we will focus on the acoustic installation effects related to the heat exchanger and fan coupling.

2.7.1 Experimental works

Canepa *et al.* [38] studied the tip-leakage noise generated by an L-shaped ring fan. An experimental campaign was carried out in a semi-anechoic chamber for 2 different operating points (nominal and high flow rate) at constant rotational speed and during speed ramps. In order to modify the operating conditions, the tip gap size, and the inlet configurations (ducted and unducted), a test plenum has been utilized according to ISO 10302 [39]. The spectral decomposition method has been used to separate the noise-generating mechanisms from the acoustic propagation effects. The acoustic response function has been compared with the velocity-scaled, constant-Strouhal-number SPL. By so doing it was possible to identify the ring-gap noise components and their relation with the upstream geometry. It was highlighted that even a strong reduction of the tip-gap could not eliminate this noise mechanism and that the upstream geometry influenced the radiated noise significantly. The authors observed that the main effect of the tip flow is to increase the broadband noise level and the emergence of wide peaks at Strouhal numbers preceding slightly the BPF and harmonics.

Rozenberg *et al.* [40] validated experimentally the analytical self-noise modeling dedicated to free-field low-speed cooling fans that will be extended and used in Chapter 5. This investigation is based on the rotating noise modeling *via* strip-approach firstly derived by Schlinker and Amiet [41] for helicopter blades, followed by Moreau and Roger [42] who adapted it to subsonic fan cases[4]. To do so, the authors instrumented a two-bladed fan, shown in Figure 2.8 (a), with wall-pressure

[4]More details on the implementation of this theory are provided in Chapter 5.

sensors and used a microphone to measure the radiated noise in the far-field. The sets of small-size

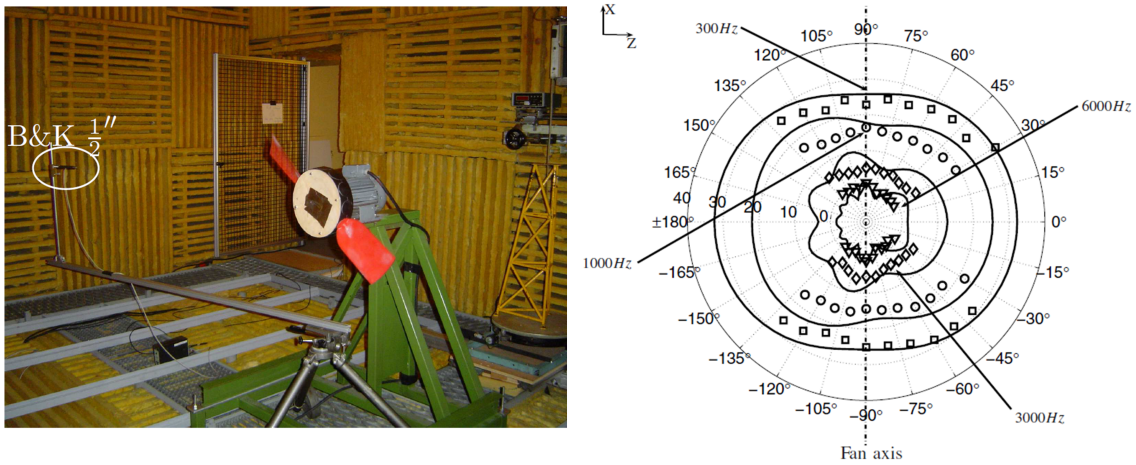

Figure 2.8: (a) Two-bladed instrumented fan produced by CETIAT and used by Rozenberg in [43]. (b) Validation of the trailing-edge noise Amiet's theory, adapted to rotation, with respect to the far-field noise directivity measurements [40].

microphones (2.5 mm diameter) are distributed at two stations of the blade: at the midspan and at the tip. The ones in the streamwise direction provide information on the turbulent eddies convection speed, whereas the ones aligned along the span measure the spanwise correlation length. This is in order to avoid the modeling of the wall-pressure statistics, as typically done when using this technique to predict the broadband noise. The far-field single microphone was mounted on a moving support, able to measure the directivity pattern at several locations and for four discrete frequencies, as depicted in Figure 2.8 (b). Despite some overestimation when the listener is near the fan axis, a global agreement is achieved between the analytical prediction and the far-field measurements.

The research published by Zenger *et al.* [44] in 2016 focused on the sound source localization on a generic axial fan at 5 diverse operating conditions. The fan was designed and manufactured at the University of Erlangen-Nuremberg: it has 9 unskewed blades with free tips, it was installed in a short duct, and was always exposed to clean inflow conditions. This investigation is among the first ones to apply successfully a frequency-based microphone-array algorithm to an axial fan for several working points. Their findings indicate that at low volumetric flow, the sound from the fan blade leading edges is the dominant mechanism, whereas for high flow rates the trailing edges become the main emitters, likely due to the vortex shedding sound. Thus, the operating point is strongly influencing the main contributing mechanisms.

Herold *et al.* [45], working in the same laboratory, continued the previous work [44] focusing on the influence of the skew of fan blades on noise emissions. They also implemented a virtual rotating array method, with subsequent beamforming and deconvolution algorithms, to generate the sound localization maps. Nonetheless, three fans with backward-skewed, unskewed, and forward-skewed blades are investigated here (all of them with free blade tips). The noise generation of the forward-skewed fan is always at the leading edge of the blade, close to the tip, regardless of the operating point. On the contrary, this is not the case for the unskewed and backward-skewed fans,

the trailing-edge noise dominates at high flow rates and at high frequencies. Hence, not only the operating point is of critical importance in defining the dominant noise mechanisms, but also the blade skewness is a key parameter to account for. This is why the curvature of the blade needs to be taken into account in low-order prediction methodologies, as highlighted in Chapter 5.

We want to emphasize that microphone array methods allow the localization and quantification of the sound sources, whereas other experimental tools classically employed are limited to methods for characterizing the flow properties and evaluating the fan spectrum as a whole. This aspect is beneficial in getting more insights into the aeroacoustic phenomena occurring with rotating machinery. For this reason, a rotating beamforming campaign will be carried out and discussed in Chapter 3 to identify the sound sources at varying operating conditions.

2.7.2 Numerical works

Pérot *et al.* [46] published for the first time in 2010 the prediction of the aeroacoustic sources *via* a direct, three-dimensional, unsteady, compressible computational approach based on the LBM [47]. Instead of discretizing the macroscopic continuum equation, i.e., the Navier-Stokes equations, the LBM exploits the "mesoscopic" kinetic equations, namely, the Boltzmann equation, to simulate the macroscopic fluid dynamics. An axial fan with 9 forward-skewed blades and a rotating L-shaped ring has been used in the simulation[5]. Not only does the simulated mean and fluctuating flow compare well to experiments, but also the acoustic power radiated is in good agreement with measurements. This work constitutes an early attempt to link the instantaneous flow topology between the turbulent eddies and the related sound mechanisms. The early findings point to the tip clearance and the internal hub ribs as likely areas where the vortical structures dominating the sound spectrum are generated.

As a continuation to the latter work discussed [46], three LBM simulations have been performed by Sanjosé *et al.* [52] on the same fan and large plenum setup. The focus was on the mesh refinement effect of the rotor and tip-gap regions. The secondary flows, at the hub and tip regions, are well resolved with the finer mesh setup, as Q-criterion iso-surfaces illustrate in Figure 2.9 (a). Here the tip-leakage flow structures are visualized and a hub flow detachment near the blade cusp is noticed. Hence, it was highlighted that the sound spectrum is dominated by the turbulence-interaction noise, namely, the secondary flows such as the tip flow and the hub corner recirculation, whereas it is only above 1-2 kHz that the self-noise contributes to the overall emissions.

Magne *et al.* [34] proposed to study the subharmonic tonal noise generated by the tip eddies of the same fan (see [46], for instance) with clean inflow *via* hybrid methodologies. In particular, a compressible unsteady-RANS approach is employed to resolve the flow field and identify the sound sources. Two methods are used to propagate the noise sources: a Ffowcs-Williams and Hawkings analogy in the time domain and an analytical model based on the compact rotating dipole formulation in the frequency domain. Despite the hybrid approach, the coherent vortical structures at the tip, found to be the greatest source of unsteadiness, are fairly well captured as Figure 2.9 (b) illustrates. The subharmonic tonal peaks are predicted by the time-domain FWH analogy and are in good agreement with experiments. Moreover, the frequency-domain compact dipole model was found to be a quick tool able to predict not only the BPF and harmonics peaks

[5]This particular fan, whose reference number is H380EC1, has been extensively studied both numerically and experimentally [27, 31, 34, 48–51].

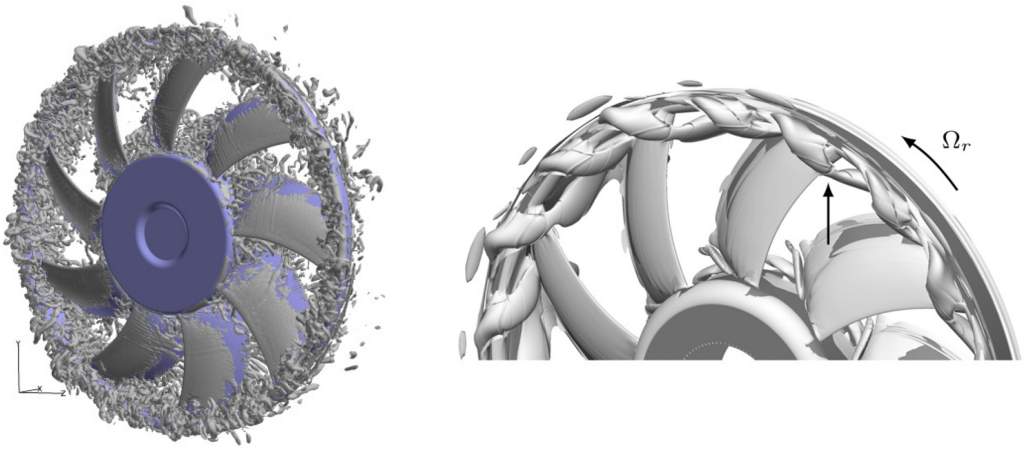

Figure 2.9: Q-factor iso-surfaces in the rotor frame of reference carried out with an LBM solver in [52] (a), and obtained with a 3D unsteady RANS approach (where Ω_r is the relative angular velocity between the fan rotation and the backflow) in [34] (b).

but also the subharmonic tones related to the large eddies interaction in the tip region. Similar results in this region have been obtained also on a different fan setup, employing an analogous hybrid approach (unsteady RANS coupled to a time-domain FWH analogy) by Park and Lee [53].

Sanjosé and Moreau in 2018 [27] investigated the broadband sound sources on a clean inflow low-speed fan (the same fan model as in [46]) with a hybrid low-order methodology based on steady RANS, exploring several flow rates at constant rpm. The sound propagation was carried out with Amiet's theory for rotating sources in free-field [41], exploiting the flow input parameters computed with the RANS approach. The blade noise emissions in a circular motion can be approximated by the contribution of the blade segments translating in rectilinear motion if the source frequencies are higher than the rotation frequency [54]. We point out that at low flow rates the inherent unsteadiness of the tip-gap flow is critical and cannot be captured by a steady-state method; the prediction can only be improved by switching to unsteady techniques, as highlighted in [31], especially at low frequencies. The uncertainty quantification related to this methodology is analyzed by Christophe *et al.* [50] and is indeed mostly due to the tip region. Nevertheless, the simulations are able to describe the turbulence kinetic energy evolution within the ring gap and at the blade corners near the fan hub. Results show that the leading-edge and trailing-edge noise are functions of the flow rate. Up to the design point, the former dominates over the latter, whereas for higher flow rates the opposite occurs. Overall, the analytical model yielded a good agreement of the acoustic spectra levels and shapes, measured in a reverberant room, but also with respect to the flow rate variation.

To conclude this section concerning previous numerical works found in the literature to simulate low-speed cooling fans with clean inflow conditions, we can summarize that only direct methods mainly based on LBM simulations have the possibility to capture strongly unsteady phenomena such as the tip-leakage flow. However, as of today, they remain very expensive in terms of computation, complicating their inclusion in industrial optimization phases in which acoustic prediction would play a role from the early stages of design and development. Therefore, in Chap-

ter 5 the focus is put on a low-order approach that deepens the work done in [27] by including the blade sweep-angle effect in the noise prediction methodology.

2.7.3 Distortion effects induced by the radiator

Piellard and Coutty [33] carried out a direct aeroacoustic simulation, using the unsteady and compressible LBM-based solver PowerFLOW, in order to predict the sound emissions of a complete automotive module, including the low-speed fan with a motor, a shroud, and a series of heat exchangers clamped on the fan suction side. The core of the radiators is modeled as an equivalent fluid region having porosity equal to one, in order to provide the correct pressure loss measured on the actual one. The porous medium was not validated for acoustic prediction but it proved to work well [51, 55]. Nevertheless, with this approach, the turbulence produced by the flow passing through the heat exchanger core and convected towards the fan inlet is neglected. Considering that the results are in very good agreement (with discrepancies less than 0.5 dB(A)) with the experimental ones, either this turbulence is dissipated before impinging on the fan blades or other noise mechanisms dominate the noise spectrum. The authors highlighted, in fact, that the tip region develops coherent annular vortices wrapped around the rotating fan ring having a relevant impact over a quite large frequency range (later confirmed on full modules also in [56]).

Zenger et al. [57] experimentally investigated the sound emissions of six free-tip axial fans (three of them with forward-skewed blades and three with backward-skewed ones) under distorted inflow conditions. These were imposed by means of four different grids: two of them to provide an arithmetically increasing or parabolic velocity profile at the cross-section of the inlet. The third was a fine rectangular grid yielding approximately the same turbulence intensity increase as the former two, whereas the fourth was a coarse rectangular one, to enhance substantially the inflow turbulence. The former two lead to non-uniform inlet velocity, affecting the tonal sound emission at the BPF and harmonics (see Section 2.6.1). The rectangular grids, when the integral length scale is smaller than the blade length, are expected to enhance the broadband contribution. With these, it was possible to vary the turbulence intensity in a range between 9% and 18.5%, yielding an impact on both tonal and broadband noise sources. Such an influence varies according to the blade design, in particular, being greater on forward-skewed fans. This evidence can be observed in Figure 2.10 where a significant increase at low frequencies occurs, especially for the coarse grid (up to ≈ 15 dB).

A second experimental study on the sound generation in forward- and backward-skewed fans with turbulent inflow has been published by Zenger *et al.* [58]. An upstream turbulence grid allowed to reach 28% of turbulence intensity and the investigation was conducted by means of a frequency-based microphone array method. We have to consider that the fans studied here do not have an L-shaped rotating ring and thus, the tip aerodynamics might differ from that case. Nonetheless, for free-inflow conditions, the sound-localization maps locate the sources either on the trailing edge or on the leading edge, depending on the considered frequency band and blade curvature. The distorted-inflow sound maps showed a clear impact of the ingested turbulence on the tonal and broadband sound emissions. For all third-octave bands, the sources tend to redistribute exclusively over the leading edge at the blade tip, confirming that the turbulence-interaction noise constitutes the dominant mechanism and that the inflow conditions have to be considered when designing a new system.

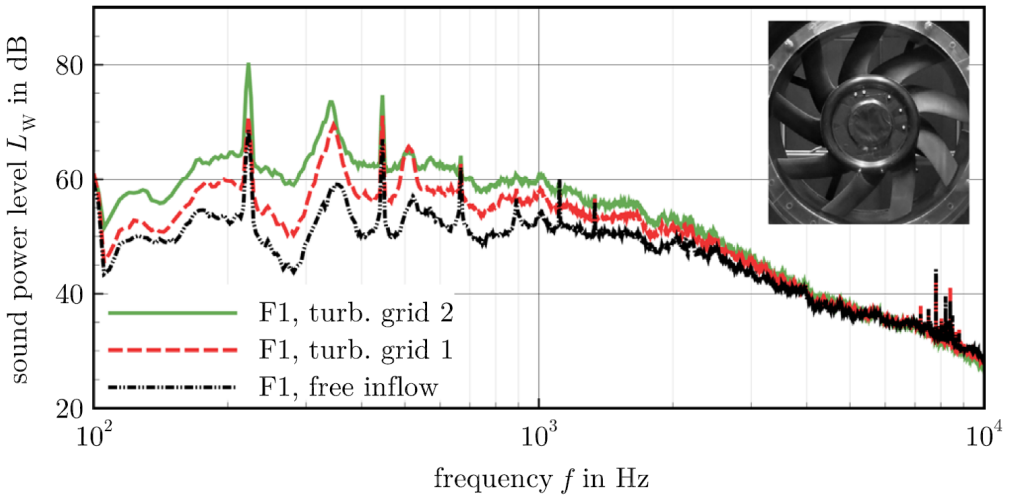

Figure 2.10: Sound power spectra of one of the forward-skewed fans exposed to inflow distortions using turbulence grids achieved and plotted in [57]. Grid 1 is the fine rectangular grid, whereas grid 2 is the coarse one.

Christophe *et al.* [59] published a work that deals with the measurement of acoustic and aerodynamic installation effects among a protection grid, a heat exchanger, and a low-speed fan. The former two are combined with a 90-degrees turning of the mean flow direction. This turning angle imposed by the mock-up geometry affects mostly the tonal noise component (see Section 2.6.1). On the other hand, the presence of the protection grid and the heat exchanger have an effect on the broadband contribution, probably related to the modification of the turbulent eddies ingested by the fan. The authors highlighted the need for more investigation concerning these vortical structures. They pointed out that a more accurate model should correctly describe the alteration of turbulence parameters (such as the turbulent intensity and turbulent integral length scale) through the narrow channels of such heat exchangers.

Allam & Åbom [60] focused on noise reduction by transmission path modification, aiming at characterizing the heat exchanger damping properties and investigating the employment of micro-perforated plates (MPPs) and quarter-wave resonators (QWRs) to control the near-field noise. The authors characterized the radiator-alone acoustics, showing a transmission loss of up to 4-5 dB at high frequencies, depending on the flow speed. Furthermore, MPPs were used to replace part of the shroud and to cover a back-plate installed on the fan pressure side. This configuration yielded sound reduction from 1.5 to 4.5 dB(A), depending on the MPPs covered area and on the fan speed. An MPP damper (namely, a combination of back-plate and QWRs) showed an even better absorption of 6 dB(A). Tuning MPPs is seen as a promising technique to be further investigated. Theoretically, MPP pipes could even be optimized to replace the louvered ones within the heat exchanger core. MPPs have also been successfully employed by Lee & Bolton [61] within the tip-gap region to reduce the tip-clearance noise.

To summarize what has been analyzed in this section, high-fidelity simulations predict very well the far-field sound emitted by complete automotive modules. However, there is still no clarity on the turbulence production due to an automotive heat exchanger nor on the type of vortical

structures reaching the fan inlet. This motivates the work presented in Chapter 4. Given that the heat exchanger may present an acoustic transmission loss, it is interesting to verify if it is possible to reconstruct the sound source maps using a microphone array through the heat exchanger core (see Chapter 3). The MPPs are have not been employed in this manuscript although they are recognized to be a promising technology to mitigate the cooling fan noise. Only some fundamentals related to their modeling are deepened in appendix A.

References

[1] International Organization for Standardization. *Fans — Vocabulary and definitions of categories*. ISO 13349:2010, July 2010.

[2] W. T. W. Cory. *Fans and ventilation: a practical guide ; the practical reference book and guide to fans, ventilation and ancillary equipment with a comprehensive buyers' guide to worldwide manufacturers and suppliers*. Elsevier, 2005. OCLC: 255419165.

[3] Manuel Henner, Bruno Demory, Mohamed Alaoui, Maxime Laurent, and Benjamin Behey. *Effect of Blade Curvature on Fan Integration in Engine Cooling Module*. Acoustics, 2(4):776–790, October 2020.

[4] Alain Guédel. *Acoustique des ventilateurs*. PYC Livres, Villeurbanne, France, 1999.

[5] Stephen McAdams and Emmanuel Bigand, editors. *Thinking in sound: The cognitive psychology of human audition.* Thinking in sound: The cognitive psychology of human audition. Clarendon Press/Oxford University Press, New York, NY, US, 1993.

[6] Stewart Glegg and William Devenport. *Aeroacoustics of Low Mach Number Flows*. Academic Press, 2017.

[7] J. Lighthill. *On sound generated aerodynamically I. General theory*. Proceedings of the Royal Society of London. Series A. Mathematical and Physical Sciences, 211(1107):564–587, March 1952.

[8] J. Lighthill. *On sound generated aerodynamically II. Turbulence as a source of sound*. Proceedings of the Royal Society of London. Series A. Mathematical and Physical Sciences, 222(1148):1–32, February 1954.

[9] N. Curle. *The influence of solid boundaries upon aerodynamic sound*. Proceedings of the Royal Society of London. Series A. Mathematical and Physical Sciences, 231(1187):505–514, September 1955.

[10] J. E. Ffowcs Williams and D. L. Hawkings. *Sound Generation by Turbulence and Surfaces in Arbitrary Motion*. Philosophical Transactions of the Royal Society of London. Series A, Mathematical and Physical Sciences, 264(1151):321–342, 1969.

[11] Marvin Goldstein. *Unified approach to aerodynamic sound generation in the presence of solid boundaries*. The Journal of the Acoustical Society of America, 56(2):497–509, August 1974.

[12] F. Farassat. *The prediction of the noise of supersonic propellers in time domain - New theoretical results*. Atlanta,GA,U.S.A., April 1983. American Institute of Aeronautics and Astronautics.

[13] Michel Roger, Georgios Bampanis, and Stéphane Moreau. *Advanced Concepts for the Reduction of Flow-Induced Noise Generation, Propagation and Transmission.* von Karman Institute for Fluid Dynamics Lecture Series Notes, November 2020, Sint-Genesius-Rode, Belgium.

[14] Th. von Kármán and W. Sears. *Airfoil Theory for Non-Uniform Motion*. Journal of the Aeronautical Sciences, 5:379–390, 1938.

[15] J. M. Tyler and T. G. Sofrin. *Axial Flow Compressor Noise Studies*. January 1962.

[16] M. Schneider. *Der Einfluss der Zuströmbedingungen auf das breitbandige Geräusch eines Axialventilators*. PhD thesis, Universität Siegen, Lyon, France, 2005.

[17] Marc Jacob, Jérôme Boudet, Damiano Casalino, and Marc Michard. *A rod-airfoil experiment as a benchmark for broadband noise modeling*. Theoretical and Computational Fluid Dynamics, 19:171–196, 07 2005.

[18] Riccardo Zamponi, Sutharsan Satcunanathan, Stéphane Moreau, Daniele Ragni, Matthias Meinke, Wolfgang Schröder, and Christophe Schram. *On the role of turbulence distortion on leading-edge noise reduction by means of porosity*. Journal of Sound and Vibration, 485:115561, 10 2020.

[19] R. Paterson and R. Amiet. *Acoustic radiation and surface pressure characteristics of an airfoil due to incident turbulence*. In 3rd Aeroacoustics Conference, Palo Alto,CA,U.S.A., July 1976. American Institute of Aeronautics and Astronautics.

[20] W. Olsen and J. Wagner. *Effect of thickness on airfoil surface noise*. AIAA Journal, 20(3):437–439, March 1982.

[21] William Devenport, Joshua Staubs, and Stewart Glegg. *Sound radiation from real airfoils in turbulence*. Journal of Sound and Vibration, 329:3470–3483, 08 2010.

[22] R.K. Amiet. *Acoustic radiation from an airfoil in a turbulent stream*. Journal of Sound and Vibration, 41(4):407–420, August 1975.

[23] Gyuzel Yakhina, Michel Roger, Stéphane Moreau, Lap Nguyen, and Vladimir Golubev. *Experimental and Analytical Investigation of the Tonal Trailing-Edge Noise Radiated by Low Reynolds Number Aerofoils*. Acoustics, 2(2):293–329, 2020.

[24] R.K. Amiet. *Noise due to turbulent flow past a trailing edge*. Journal of Sound and Vibration, 47(3):387–393, August 1976.

[25] Michel Roger and Stéphane Moreau. *Back-scattering correction and further extensions of Amiet's trailing-edge noise model. Part 1: theory*. Journal of Sound and Vibration, 286(3):477–506, September 2005.

[26] A. Caiazzo, R. D'Amico, and W. Desmet. *A Generalized Corcos model for modelling turbulent boundary layer wall pressure fluctuations*. Journal of Sound and Vibration, 372:192–210, June 2016.

[27] Marlène Sanjosé and Stéphane Moreau. *Fast and accurate analytical modeling of broadband noise for a low-speed fan*. The Journal of the Acoustical Society of America, 143(5):3103–3113, May 2018.

[28] Manuel Henner, Bruno Demory, Mohamed Alaoui, Maxime Laurent, and Benjamin Behey. *Effect of Blade Curvature on Fan Integration in Engine Cooling Module*. Acoustics, 2(4):776–790, October 2020.

[29] R.E. Longhouse. *Control of tip-vortex noise of axial flow fans by rotating shrouds*. Journal of Sound and Vibration, 58(2):201–214, May 1978.

[30] Edward Canepa, Andrea Cattanei, Fabio Mazzocut Zecchin, and Davide Parodi. *Large-scale unsteady flow structures in the leakage flow of a low-speed axial fan with rotating shroud*. Experimental Thermal and Fluid Science, 102:1–19, April 2019.

[31] Stéphane Moreau and Marlène Sanjosé. *Sub-harmonic broadband humps and tip noise in low-speed ring fans*. The Journal of the Acoustical Society of America, 139(1):118–127, January 2016.

[32] J. Grilliat. *Contribution à l'étude aéroacoustique des écoulments de jeu*. PhD thesis, École Centrale de Lyon, Lyon, France, 2009.

[33] M. Piellard, B. Coutty, V. Le Goff, F. Pérot, and V. Vidal. *Direct Aeroacoustics Simulation of Automotive Cooling Fan System: Effect of Upstream Geometry on Broadband Noise.* In 20th AIAA/CEAS Aeroacoustics Conference, AIAA 2014-2455 paper, Atlanta, GA, June 2014.

[34] Stéphan Magne, Stéphane Moreau, and Alain Berry. *Subharmonic tonal noise from backflow vortices radiated by a low-speed ring fan in uniform inlet flow*. The Journal of the Acoustical Society of America, 137(1):228–237, January 2015.

[35] Marlène Sanjosé and Stéphane Moreau. *Direct noise prediction and control of an installed large low-speed radial fan*. European Journal of Mechanics - B/Fluids, 61:235–243, 2017. Rotating Flows.

[36] M Sturm, M Sanjosé, S Moreau, and T Carolus. *Application of Analytical Noise Models Using Numerical and Experimental Fan Data*. Proceedings of 11^{th} European Conference on Turbomachinery Fluid dynamics & Thermodynamics. Madrid, Spain, March 2015.

[37] Andrea Cattanei, Riccardo Ghio, and Alessandro Bongiovı'. *Reduction of the tonal noise annoyance of axial flow fans by means of optimal blade spacing*. Applied Acoustics, 68(11):1323–1345, 2007.

[38] Edward Canepa, Andrea Cattanei, Fabio Mazzocut Zecchin, Gabriele Milanese, and Davide Parodi. *An experimental investigation on the tip leakage noise in axial-flow fans with rotating shroud*. Journal of Sound and Vibration, 375, August 2016.

[39] International Organization for Standardization. *Acoustics — Measurement of airborne noise emitted and structure-borne vibration induced by small air-moving devices — Part 1: Airborne noise measurement*. ISO 10302-1:2011, January 2011.

[40] Yannick Rozenberg, Michel Roger, and Stéphane Moreau. *Rotating Blade Trailing-Edge Noise: Experimental Validation of Analytical Model*. AIAA Journal, 48(5):951–962, May 2010.

[41] R. Schlinker and R. Amiet. *Helicopter rotor trailing edge noise*. In 7th Aeroacoustics Conference, Palo Alto,CA,U.S.A., October 1981. American Institute of Aeronautics and Astronautics.

[42] Stéphane Moreau and Michel Roger. *Competing Broadband Noise Mechanisms in Low-Speed Axial Fans*. AIAA Journal, 45(1):48–57, January 2007.

[43] Yannick Rozenberg. *Modélisation analytique du bruit aérodynamique à large bande des machines tournantes: utilisation de calculs moyennés de mécanique des fluides*. page 190.

[44] Florian J. Zenger, Gert Herold, Stefan Becker, and Ennes Sarradj. *Sound source localization on an axial fan at different operating points*. Experiments in Fluids, 57(8), August 2016.

[45] Gert Herold, Florian Zenger, and Ennes Sarradj. *Influence of blade skew on axial fan component noise*. International Journal of Aeroacoustics, 16(4-5):418–430, July 2017.

[46] Franck Perot, Stephane Moreau, Min-Suk Kim, Manuel Henner, and Douglas Neal. *Direct aeroacoustics predictions of a low speed axial fan*. In 16th AIAA/CEAS Aeroacoustics Conference, Stockholm, Sweden, June 2010. American Institute of Aeronautics and Astronautics.

[47] Uriel Frisch, B Hasslacher, and Yves Pomeau. *Lattice-Gas Automata for the Navier-Stokes Equation*. Physical review letters, 56:1505–1508, 05 1986.

[48] J. Foss, D. Neal, M. Henner, and S. Moreau. *Evaluating CFD Models of Axial Fans by Comparisons with Phase-Averaged Experimental Data*. May 2001.

[49] Stéphane Moreau and Damiano Casalino. *Aeroacoustic Design of Automotive Engine Cooling Fan Systems*. volume 2, 05 2005.

[50] Julien Christophe, Marlene Sanjosé, Stephane Moreau, Jeroen A. Witteveen, and Gianluca Iaccarino. *Uncertainty quantification of low-speed fan noise*. In 19th AIAA/CEAS Aeroacoustics Conference, Berlin, Germany, May 2013. American Institute of Aeronautics and Astronautics.

[51] Franck Perot and David Freed. *Acoustic absorption of porous materials using LBM*. In 19th AIAA/CEAS Aeroacoustics Conference, Berlin, Germany, May 2013. American Institute of Aeronautics and Astronautics.

[52] Marlène Sanjosé, Dominic Lallier-Daniels, and Stéphane Moreau. *Aeroacoustic Analysis of a Low-Subsonic Axial Fan*. page V001T09A015, 06 2015.

[53] Min-Jun Park and Duck-Joo Lee. *Sources of broadband noise of an automotive cooling fan*. Applied Acoustics, 118:66–75, March 2017.

[54] Samuel Sinayoko, Michael Kingan, and Anurag Agarwal. *On the effect of acceleration on trailing edge noise radiation from rotating blades*. In 19th AIAA/CEAS Aeroacoustics Conference, Berlin, Germany, May 2013. American Institute of Aeronautics and Astronautics.

[55] Franck Perot, Min-Suk Kim, Stéphane Moreau, and M. Henner. *Axial fan noise aeroacoustics predictions and inflow effect on tonal noise using LBM*. 05 2013.

[56] D. Lallier-Daniels, M. Sanjosé, S. Moreau, and M. Piellard. *Aeroacoustic study of an axial engine cooling module using lattice-Boltzmann simulations and the Ffowcs Williams and Hawkings' analogy*. European Journal of Mechanics – B/Fluids, 61:244–254, 2017.

[57] Florian J. Zenger, Andreas Renz, Marcus Becher, and Stefan Becker. *Experimental investigation of the noise emission of axial fans under distorted inflow conditions*. Journal of Sound and Vibration, 383:124–145, November 2016.

[58] Florian Zenger, Gert Herold, and Stefan Becker. *Acoustic Characterization of Forward- and Backward-Skewed Axial Fans Under Increased Inflow Turbulence*. AIAA Journal, 55(4):1241–1250, April 2017.

[59] Julien Christophe, Korcan Kucukcoskun, and Christophe Schram. *Tonal and Broadband sound prediction of a locomotive cooling unit*. In 19th AIAA/CEAS Aeroacoustics Conference, Berlin, Germany, May 2013. American Institute of Aeronautics and Astronautics.

[60] Sabry Allam and Mats Åbom. *Noise Reduction For Automotive Radiator Cooling Fans*. FAN2015 Conference, Lyon, France, 2015.

[61] Seungkyu Lee and J. Stuart Bolton. *The Application of Microperforated Material to Control Axial Fan Noise*. FAN2015 Conference, Lyon, France, 2015.

3

Acoustic investigation of the cooling module at different working conditions

3.1 Introduction

Sound-source localization and directivity measurements are employed in this chapter to study the noise emissions of the cooling module at different operating conditions. The focus is put on the broadband noise which can be attributed to several noise mechanisms according to Section 2.6, namely, turbulence-impingement noise, self-noise, and tip-leakage noise. Turbulence-impingement or leading-edge noise is generated by the interaction of the incoming turbulence with the leading edges of the fan blades [1]. Hence, this noise mechanism is dominant in case of high turbulence intensity passing through the fan [2], but it can be negligible in case of clean inflow conditions [3]. Trailing-edge or self-noise is due to the sudden distortion of the vortical structures born in the turbulent boundary layer with the blade trailing-edge discontinuity [4, 5]. This noise still occurs even with clean inflow conditions since part of the boundary layer of such axial fans is always turbulent [6]. Tip-clearance or tip-leakage noise is produced by recirculating vortical structures that are formed due to the pressure difference between the pressure and the suction sides in the tip region of the blades [7, 8]. In this region, the recirculating flow can reach up to 6 % of the nominal flow rate [9], producing turbulence that interacts with the blade leading and trailing edges, increasing the low-to-mid frequency region of the noise spectrum [10, 11]. It has been found that, in this region, the generated large vortices rotate at a lower speed than the rotor: the frequency of the impact is thus lower than the blade passing frequency (BPF), emitting subharmonic broadband or quasi-tonal noise [7]. Yet, most of the above studies consider the fan alone, flush-mounted on a plenum, and not installed in its cooling module [8, 12]. Noise specifications that any automotive tier-one supplier has to fulfill are however in the latter configuration, which makes the need for reference experimental acoustic data and proper source localization in such a configuration.

Moreover, the effect of the presence of the radiator on the generation and propagation of fan sound sources under real application conditions is not yet fully characterized and understood. There is an aspect related to the absorption of the propagation of acoustic waves passing through

the fine radiator core. In fact, Allam *et al*. [13] tried to exploit this in order to use the heat exchanger as a passive noise control tool, achieving a $5\,\mathrm{dB}$ reduction up to 2-3 kHz, but for a different plate heat exchanger technology. However, while highlighting the importance of considering the masking effect, Rynell *et al*. [14] concluded that, for the truck radiator they studied (similar technology as in the present study), the transmission loss effect was negligible compared to the change in the sound spectrum due to aerodynamic effects. In particular, the broadband sound components were found to be strongly correlated with the coherent turbulent structures in the flow, leading to a reduction of the sound emissions in the full module case, especially at the BPF and harmonics. Christophe *et al.* [15] also studied generic locomotive cooling units with similar fins-and-louvers heat exchangers. They showed that the broadband spectrum is affected by the presence of the radiator, indicating the generation of turbulence through the radiator as the most likely cause. The aerodynamic effect induced by the radiator on the airflow at the fan inlet can have, in fact, several consequences on the dominant sound generation mechanisms. Another relevant study was conducted by Zenger *et al*. [16] in order to understand the effect that a highly distorted flow (they reached a turbulence intensity of up to $40\,\%$) can have on the distribution of sound sources on two types of axial fans. In this case, turbulence grids were designed with the purpose of creating controlled distorted flow conditions. The results showed that the sources have a tendency to distribute on the leading edge of the blade in case there is a strong turbulent interaction with the incoming flow. This has the effect of increasing broadband sound emissions, confirming the outcome of the previous study [17].

On the numerical side, full direct noise simulations of engine cooling modules have appeared with the Lattice Boltzmann Methods (LBM) [8, 12, 18]. In such simulations of the actual experimental set-up, the heat exchanger cores are modeled as equivalent inhomogeneous porous media, which prevents accounting for the possible acoustic diffraction or transmission loss of the cores. Yet, the excellent agreement of the computed noise levels and directivity with measurements in semi-anechoic chambers suggests that the automotive heat exchanger cores are essentially acoustically transparent and transmission losses negligible. Compared with a fan-alone configuration, Lallier-Daniels [19] noticed however that the flow field of a fan in a duct or embedded in a module flat shroud is significantly modified, particularly in the tip region (the dominant noise source in such low-speed fan systems [10]). Moreover, all these conclusions have been drawn at a single-module operating condition.

Therefore, a second goal of the present study is to assess the effect that an actual radiator core can have on the sound emissions of an axial fan operated for different operating points. A microphone-array time-domain technique is implemented, validated, and used in the following work in order to achieve this objective. Directivity measurements at various rpm supplement the source localization and provide additional information about the nature of the noise source. Moreover, this study constitutes an attempt to provide a first clean database on an automotive engine cooling fan working in various configurations, tested complementary in two test facilities.

In the work presented hereafter, Section 3.2 describes the fundamentals of the array-based acoustic source localization. In Section 3.3, we present the setups in which two complementary experimental campaigns in two different anechoic wind tunnels have been carried out, to provide reference acoustical data in well-controlled environments. The implementation and validation of the sound localization technique are discussed in Section 3.4. The single-microphone measurements, directivity measurements, and sound-localization maps for several configurations are outlined and discussed in Section 3.5.

3.2 Acoustic localization methodology

Microphone array methods can be employed in order to localize and quantify the frequency-dependent location and strength of sound sources at different operating points on various configurations. Conventional array-based measurement techniques have been widely used to characterize aeroacoustic sound sources in terms of strength and location on stationary objects. To apply these methods to axial fans, the motion of the fan relative to the microphone array and thus, the Doppler effect, needs to be considered. Both time- and frequency-domain methods have been developed for this purpose.

Sijtsma *et al*. [20] approached this challenge by using a transfer function for a moving monopole source in uniform flow to reconstruct the signal in the time domain and develop an algorithm able to deal with rotating sources, named ROtating Source Identifier (ROSI). They validated the method with rotating whistles and applied it to localize and characterize sound sources on a hovering helicopter rotor and on wind-turbine blades. The capability of this algorithm has been further examined by Oerlemans *et al*. [21] for the investigation of real-scale wind-turbine sound sources. In addition, Sijtsma [22] applied ROSI for the investigation of turbofan engine noise.

Pannert and Maier [23] compensated the motion in the frequency domain through the calculation of the cross-spectral matrix in the rotating frame of reference from stationary data. To apply this method, a constant fan speed is required. A different approach is to arrange the microphones on a ring coaxial to the rotational axis of the fan. Then, the microphone data can be resampled to a virtual array, rotating together with the focus point [24, 25]. This method is called Virtual Rotating Array (VRA) and does not require a constant rotational speed. Zenger *et al*. [26] applied the VRA method to characterize the sources of an axial fan for different operating points, whereas Zenger *et al*. [16] tested the VRA algorithm in forward- and backward-skewed axial fans under distorted inflow conditions. An extension of the VRA technique exploiting arbitrary microphone configurations was recently presented by Jekosch and Sarradj [27], pointing out that the VRA method does not require a specifically-designed circular microphone array to investigate rotating sound sources.

An extensive comparison between VRA and ROSI algorithms has been conducted by Kotán *et al.* [28], highlighting the increased computational cost of ROSI against the VRA method. Nevertheless, both techniques accurately predict the location and the strength of the rotating source. The main advantage of VRA as a frequency-domain method is that deconvolution algorithms can be applied to improve the spatial resolution of the beamformer output. On the other hand, an advantage of the ROSI method is that the alignment of the center of the array with respect to the center of rotation is not required. This aspect turns out to be particularly useful in wind-tunnel experiments with limited space at disposal, or when the center of rotation is masked as in the present module configuration.

There have been studies on localizing sound sources on low-speed cooling fans that employed approaches in both time [29–32] and frequency domain [24, 33, 34]. Nevertheless, all these investigations focused on the fan-alone configuration without the presence of a suction-side radiator. Therefore, in order to obtain further insight into the acoustic phenomena, the coupling between the fan and the radiator is essential to evaluate properly the global emitted noise.

In the present work, the microphone array method described by Sijtsma *et al.* [20] is implemented and validated in order to post-process the measured data. A detailed description of the method is thoroughly explained in [20], only a summary is presented hereafter. The ROSI method constitutes a beamforming algorithm in the time domain able to deal with rotating sources moving with subsonic speed. The beamforming results are calculated on a scanning grid (SG), which is an ensemble of potential sources rotating together with the sound sources of interest. If we assume

a potential source located at the time-dependent position $\boldsymbol{\xi}(t)$ emitting a source signal σ at time τ_e, the sound signal p will be received at the microphone location x at time t. The wave equation for a moving monopole source in a stationary medium is then considered in order to determine the acoustic transfer function between the source signal σ and the measured pressure field p:

$$\frac{1}{c_0}\frac{\partial^2 p}{\partial t^2} - \nabla^2 p = \sigma(t)\delta(\boldsymbol{x} - \boldsymbol{\xi}(t)), \tag{3.1}$$

where c_0 is the speed of sound. The solution of Eq. (3.1) is found following the derivation described in the original work of Sijtsma *et al.* [20] and can be expressed as:

$$p(\boldsymbol{x}, t) = \frac{-\sigma(\tau_e)}{4\pi\{c_0(t-\tau_e) + [\frac{-\boldsymbol{\xi}'(\tau_e)}{c_0}] \cdot [\boldsymbol{x} - \boldsymbol{\xi}(\tau_e)]\}}, \tag{3.2}$$

Hence, it follows that for free-field conditions, the transfer function F from a moving source in $\boldsymbol{\xi}(t)$ to a receiver in $\boldsymbol{x}$, is given by:

$$F(\boldsymbol{x}, \boldsymbol{\xi}(\tau_e), t, \tau_e) = \frac{p(\boldsymbol{x}, t)}{\sigma(\tau_e)} = \frac{-1}{4\pi\{c_0(t-\tau_e) + [\frac{-\boldsymbol{\xi}'(\tau_e)}{c_0}] \cdot [\boldsymbol{x} - \boldsymbol{\xi}(\tau_e)]\}}, \tag{3.3}$$

where $\boldsymbol{\xi}'(\tau_e)$ is the velocity of the moving source at the emission time, whereas the relation between the arrival time t and the emission time τ_e is given by:

$$\Delta t = t - \tau_e = \frac{||\boldsymbol{x} - \boldsymbol{\xi}(\tau_e)||}{c_0}. \tag{3.4}$$

The arrival time vector $(\Delta t + \tau_e)$ at which the recorded pressure signals should be evaluated through Eq. (3.3) does not coincide with the time instants at which the measurement system samples the data. Hence, in order to obtain the proper values of the recorded pressure signals at the desired times, the measured signals are linearly interpolated. The amplitude variation is also taken into account exploiting the transfer function of the potential source. Afterward, the interpolated pressure signals are evaluated at the original uniformly-spaced emission time instants. In this step, the de-dopplerization of the signal is carried out, as proposed by [35, 36] and implemented, for instance, in [37, 38]. Finally, the reconstructed source signal is Fourier-Transformed and the resulting sound pressure level L_p for the investigated point of the SG is obtained. This procedure is repeated for all the points of the SG such that the final source-distribution map can be determined. Hence, each individual sample is time-shifted and amplitude-adjusted depending on the position and on the speed of the source at the emission time in order to reconstruct the emitted source signal from the measured ones.

3.3 Experimental campaigns and setups

The experimental work presented in the following sections took place in two laboratories: at the von Karman Institute for Fluid Dynamics (VKI) and at Université de Sherbrooke (UdeS). The experimental setups and campaigns at VKI and UdeS are hereafter described, separately. Nevertheless, the studied engine cooling module is the same.

3.3.1 Engine cooling module

Experimental investigations are performed on two different samples of the same engine cooling module, designed by the automotive supplier-company Valeo at La Verrière, France. The geometry of the fan, shown in Figure 3.1 (a), consists of 7 forward-skewed blades that are almost equally spaced and have a varying chord and stagger angle. The diameter of the fan is $d_{fan} = 380\,\mathrm{mm}$, the hub-to-tip ratio is 0.37, whereas the gap size between the casing and the rotating L-shaped ring is $6\,\mathrm{mm}$ [39]. The Reynolds number based on the chord at the tip of the blade is approximately 2.45×10^5, stating that the fan is working in the laminar-turbulent transition regime [40]. The Mach number at the blade tip, related to an operational rotational speed of $3400\,\mathrm{rpm}$, is 0.19, and thus, a subsonic incompressible regime can be considered.

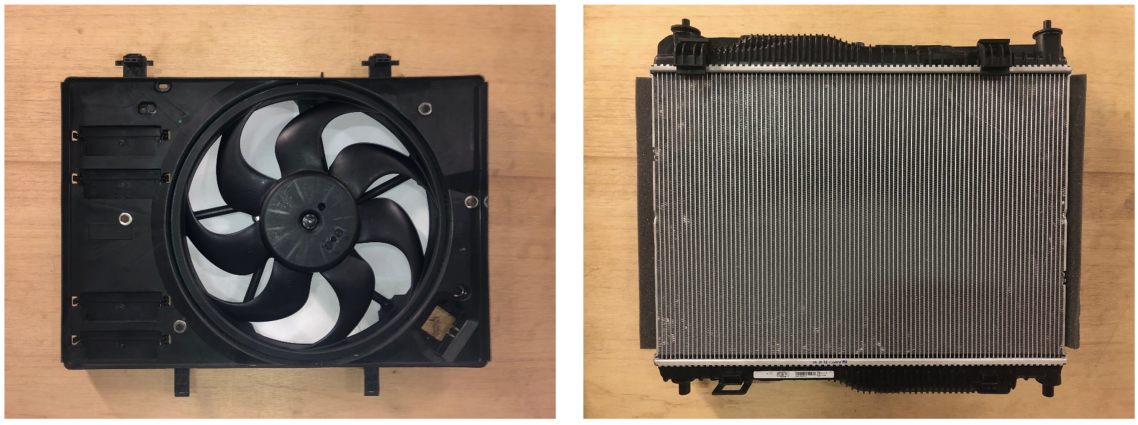

(a) (b)

Figure 3.1: Automotive cooling module installed on the middle wall of the ALCOVES anechoic chamber : (a) Fan Alone -FA- configuration (b) Full Module -FM- configuration.

In Figure 3.1 (b), at VKI, the suction-side radiator is installed in the anechoic chamber by clipping it on the fan shroud displayed in Figure 3.1 (a). Differently, at UdeS, the cooling module is suspended, as detailed in Section 3.3.5. More details regarding the geometrical parameters characterizing the heat exchanger can be found in Table 3.1.

The rotational speed of the automotive fan is evaluated using a diode probe with reflective aluminum tape fixed at the hub of the rotor. The beam emitted by the diode is reflected on the aluminum tape at each fan revolution. Therefore, this trigger per revolution signal is used to track the rotational speed of the fan over time. In addition, the diode signal is acquired synchronously with the microphone data allowing the computation of the angular position of the fan.

3.3.2 VKI ALCOVES anechoic laboratory

The VKI experimental measurements are carried out in the ALCOVES anechoic laboratory, where aerodynamic and aeroacoustic measurements can be conducted simultaneously. This experimental facility is characterized by a cut-off frequency of $200\,\mathrm{Hz}$ [41] and composed of two anechoic rooms separated by a modular wall partition that can accommodate different components such as automotive cooling systems [39] and ducted fans [42]. The flow inside the wind tunnel is driven by an auxiliary fan placed in a downstream circuit, generating a pressure difference across the rooms. To prevent the propagation of the noise emissions upstream towards the test section,

acoustic treatments are included within the pipe in which the external fan is installed. A detailed scheme of the anechoic chamber is illustrated in Figure 3.2.

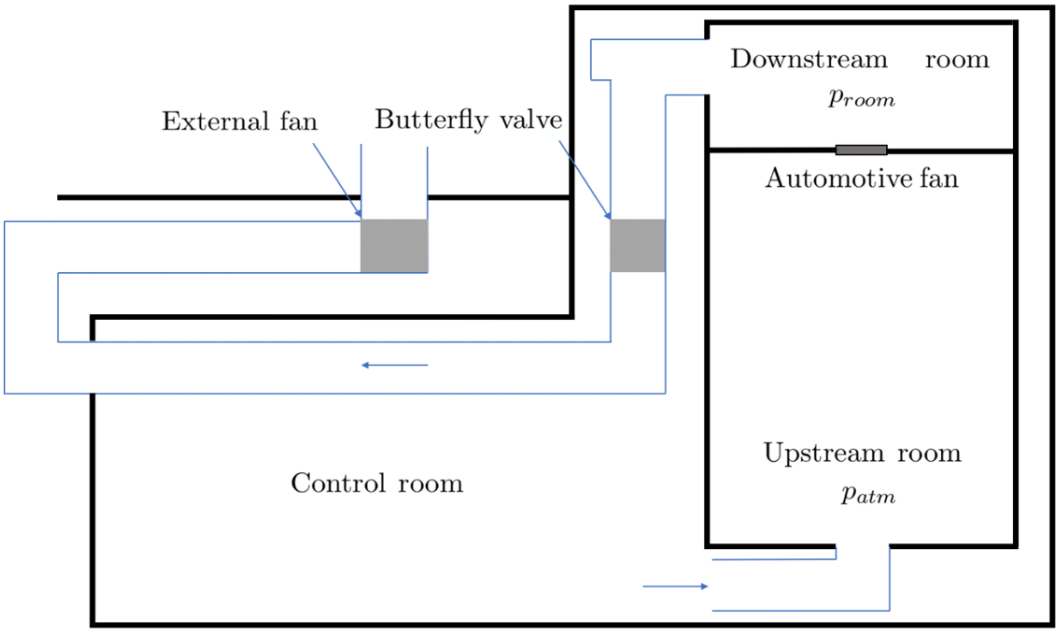

Figure 3.2: ALCOVES anechoic chamber sketch adapted from Dominique et al. [42]

The test chambers are equipped with static sensors permitting the computation of the pressure difference ΔP generated across the partition wall. The air-flow rate Q_m passing through the module is provided by the external auxiliary fan and it is measured according to ISO 5167 [43].

Number of coolant pipes	92	Slat thickness	0.12 mm
Coolant pipe height	385 mm	Space between slats	2.5 mm
Coolant pipe depth	20 mm	Heat exchanger width	558 mm
Coolant pipe width	1.5 mm	Heat exchanger height	385 mm
Space between pipes	4.5 mm	Heat exchanger depth	20 mm

Table 3.1: Geometrical parameters of the heat exchanger.

3.3.3 VKI microphone array

The microphone array considered for the present study at VKI is a planar Dougherty array [44] with 64 microphones distributed over seven logarithmic arms and with a diameter of $D_a = 1.5\,\mathrm{m}$ (see Figure 3.6 (b)). The antenna, shown in Figure 3.3 (b), is characterized by a light and easily transportable structure and is equipped with capacitor-based Knowles electrets (model FG-23329-P07 with a frequency response $\pm 3\,\mathrm{dB}$ and a frequency range of 100 Hz to 10 kHz). The microphone array is installed at a distance of $d_{a-ss} \simeq 2.5\,d_{fan}$, perpendicular to the rotation axis of the fan, on the suction side, as depicted in Figure 3.3 (a). With the present setup, the minimum

resolvable source separation is given by the Rayleigh criterion [45] as:

$$R \simeq d_{a-ss} \tan\left(\frac{1.22\, c_0}{f\, D_a}\right), \tag{3.5}$$

where c_0 is the speed of sound and f is the investigated frequency.

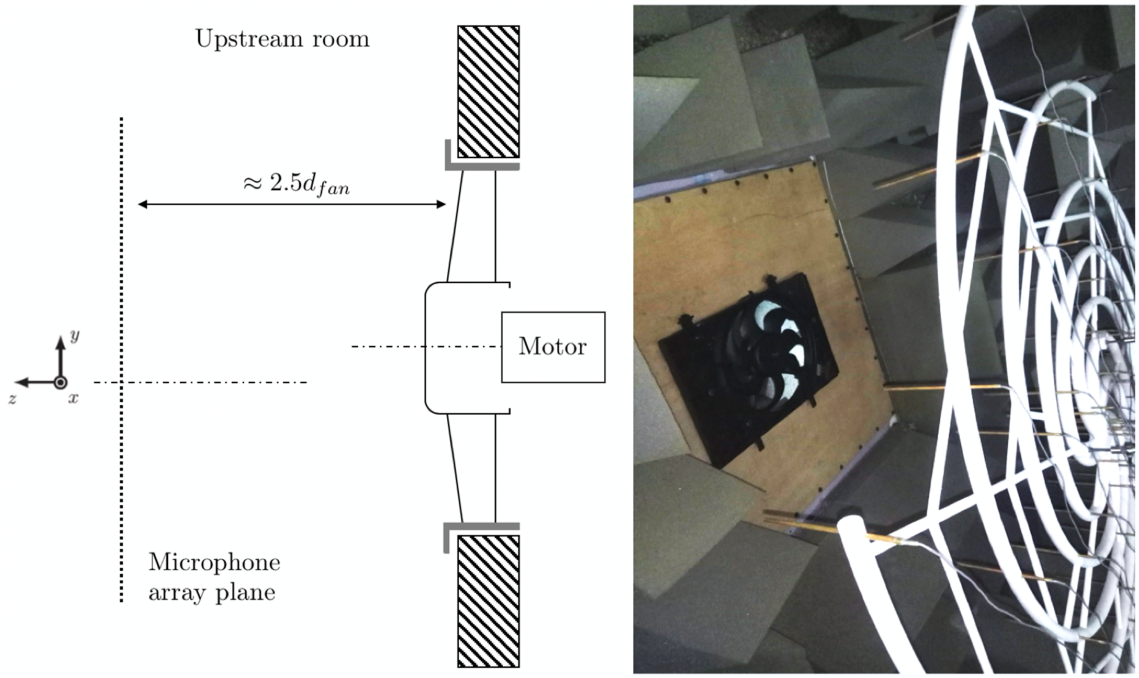

(a) (b)

Figure 3.3: (a) Position of the microphone array in the ALCOVES upstream room with respect to the axial fan. (b) 64 microphones Dougherty array employed for the campaign.

In addition, the calculation of the coordinates of the center of rotation is performed by applying a conventional beamforming method [46] to the acoustic data generated by a loudspeaker installed at the center of the fan and emitting a white noise signal. The position of the monopolar source obtained and displayed in the sound map is taken into account to translate the scanning grid, making it possible for the algorithm to follow the movement of the sources rotating together with the fan. Finally, the data-processing parameters considered to process the experimental data are indicated in Table 3.2.

Measurement time	5 sec	Grid translation	$(x, y) = (0.09\,\mathrm{m}, 0.18\,\mathrm{m})$
Sampling frequency	51.2 kHz	Rectangular grid	$x = \pm 0.25\,\mathrm{m}$, $y = \pm 0.25\,\mathrm{m}$
FFT block size	1024 samples	Grid resolution	0.01 m
FFT window	Hanning, 50 % overlap	Grid points	51×51

Table 3.2: Data-processing parameters of the experimental test case.

3.3.4 VKI performance curves

At VKI, the automotive cooling module is investigated for two configurations: fan alone (FA) and full module (FM). For each of these, three different operating points (OP) are chosen, as shown in Figure 3.4 (a).

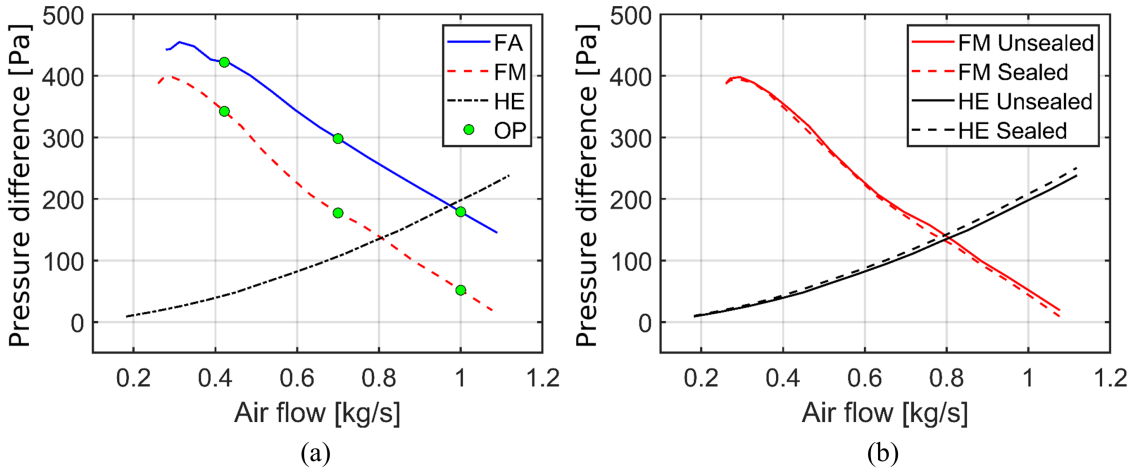

Figure 3.4: Performance curves for the automotive cooling module (a) Chosen unsealed operational points (OP) for the full module (FM) and fan alone (FA) configurations. (b) Effect of sealing the open gap between the casing and the heat exchanger.

The first operating point is set at $q_m = 0.42\,\mathrm{kg\,s^{-1}}$, which is above the stall region in order to avoid possible instabilities and the so-called stall noise appearance [1]. The second operating point is at $q_m = 0.7\,\mathrm{kg\,s^{-1}}$, corresponding to the fan-alone maximum efficiency point. The last, at $q_m = 1\,\mathrm{kg\,s^{-1}}$, is close to the air extraction limit provided by the auxiliary fan. The curves depicted in Figure 3.4 (a) are measured with two static pressure sensors across the lab middle-wall partition. The fan is always run with a quasi-constant rotational speed of 3400 ± 50 rpm. An open gap of approximately $1\,\mathrm{cm}$ is present between the heat exchanger and the fan casing. Hence, part of the air sucked in by the fan might come from this area rather than pass through the heat exchanger. In order to study the influence of this open space over the performance curves, we sealed it and plotted in Figure 3.4 (b) the pressure difference against the mass flow rate for the radiator-and-casing (HE) configuration and for the FM configuration. Since no relevant differences appear between the sealed and unsealed cases, the following study is focused on the unsealed setups, typically used in real applications.

3.3.5 UdeS experimental campaigns

Acoustic directivity and source localization measurements have been conducted on the same engine cooling module (FM) without sealing in the anechoic open-jet wind tunnel at Université de Sherbrooke (UdeS). More details about the wind tunnel can be found in [47]. The module measurements have been carried out in free-field conditions. All results obtained at UdeS are presented with a distance correction corresponding to $2.5\ d_{fan}$ (the fan-microphone array distance at VKI).

3.3.5.1 Directivity setup and acquisition

The arc with a radius of $1.8\,\mathrm{m}$ is instrumented with 13 B&K 1/4" microphones (with a frequency range of $50\,\mathrm{Hz}$ to $10\,\mathrm{kHz}$) and is hanged from the ceiling of the anechoic chamber as shown in Figure 3.5. The microphones are distributed from $0°$ to $180°$ with a step of $\Delta\theta = 15°$ between two consecutive microphones. The hub of the rotor is located at the center of the arc. Microphones 1 and 13 are aligned perpendicularly to the fan plane. The arc is rotated clockwise with respect to its center with a step of $15°$. At each step, the signals from all microphones are recorded for $30\,\mathrm{s}$ with a sampling frequency of $65.536\,\mathrm{kHz}$. The nozzle is covered with foam to minimize reflections and keep the excellent anechoic properties of the chamber. The arc itself has a layer of foam facing the central point. Windscreens are employed on the downstream microphones to minimize the influence of the flow. The directivity tests are conducted at the nominal rotational speed of 3400 rpm. Complementary measurements have been done at 1500 rpm, 2000 rpm, and 2400 rpm. The rotational speed measured with a tachometer is quasi-constant (variation of $\pm 1.5\%$ rpm). Far-field Sound Pressure Levels (SPL) have been obtained with the Welch method (block size of 10480 samples with Hanning window and $50\,\%$ overlap).

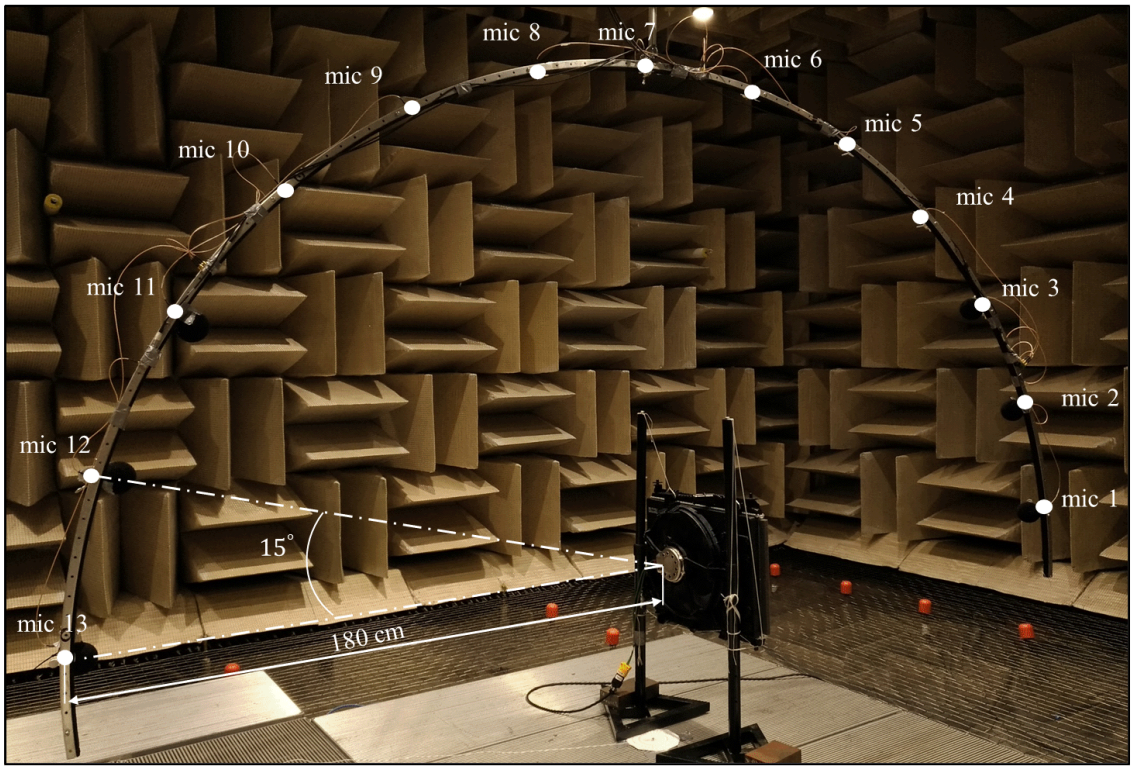

Figure 3.5: Experimental setup for the directivity measurements at UdeS.

3.3.5.2 Source localization setup

An antenna with a diameter of $0.9\,\mathrm{m}$ instrumented with 60 B&K $1/4$" microphones is used for the source localization measurements at UdeS. The microphone array, shown in Figure 3.6 (a), is at the distance of $0.88\,\mathrm{m}$ and faces the heat exchanger. Downstream of the module a tachometer is located to register the rotational speed of the fan. The signals are recorded for $30\,\mathrm{s}$ with a sampling

frequency of 65.536 kHz. Tests have been run at 1500 rpm, 2000 rpm, 2400 rpm and 3400 rpm. Only results at the nominal rpm are presented here.

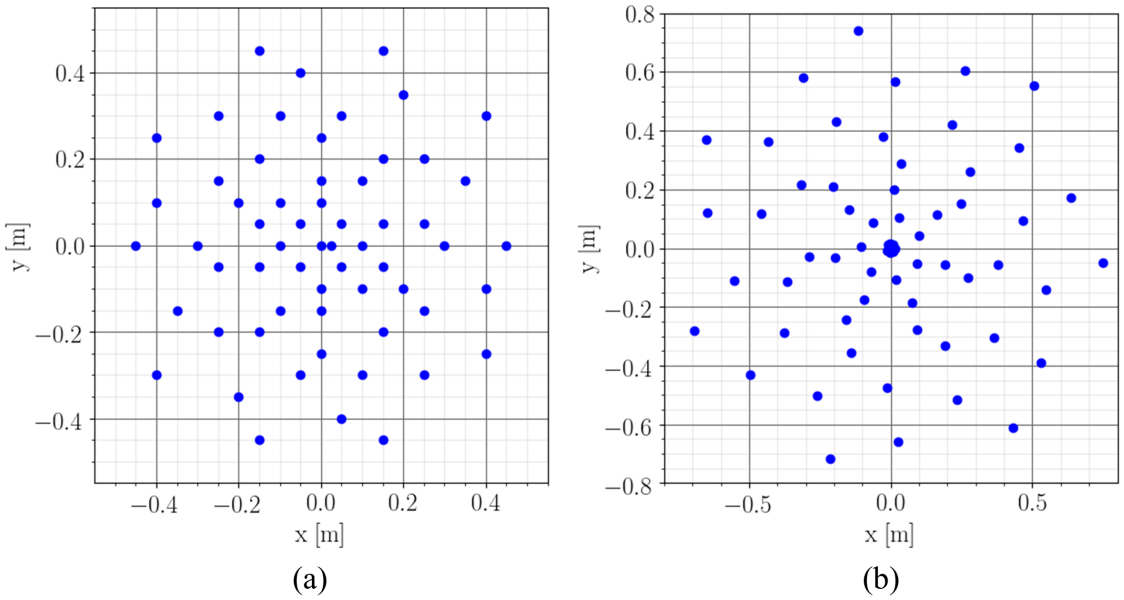

Figure 3.6: (a) 60 microphones array for the source localization measurements at UdeS. (b) 64 electret microphones are shown for the VKI antenna.

Since the microphone array of the UdeS is slightly smaller in diameter with respect to the one installed at VKI (see the distribution of the electrets in Figure 3.6 (b)), the Rayleigh criterion calculated through Eq. (3.5) is equal to 3.66 kHz. As a consequence, the sources are expected to be clearly localized at higher frequencies.

3.4 Implementation and Validation

The ROSI algorithm has been validated through its application to two benchmark datasets featuring simulated rotating monopole sources [48]. Herold *et al.* [49] recently used these datasets to evaluate array method algorithms and their implementations. A tachometer signal has been used to track the rotational rate while the time signals have been generated at 64 microphone positions placed in an equidistant arrangement on a circumference forming an array of aperture $D_a = 1\,\mathrm{m}$. The distance of the array plane to the rotational plane is $z = 0.5\,\mathrm{m}$, whereas the array center is axially aligned with the axis of rotation of the sources, as schematically shown in Figure 3.7.

3.4.1 Synthesized test cases

The first synthesized dataset denoted as subcase A and shown in Figure 3.7 (a), includes one monopolar point source rotating at a radius of $0.25\,\mathrm{m}$ with a constant angular rate of $-1500\,\mathrm{rpm}$, the minus sign indicating a clockwise rotation. The source emits a white noise signal with an amplitude of $94\,\mathrm{dB}$. The second one denoted as subcase B, consists of three uncorrelated point sources rotating in a clockwise direction at the same angular rate that slightly varies over the time around the value of $-1500\,\mathrm{rpm}$ ($\pm 1\%$). In this case, the sources emit white noise at different

intensities. The different relative positions and sound-pressure levels of the sources are displayed in Figure 3.7 (b). In particular, the louder source of $94\,\mathrm{dB}$ and the intermediate one of $91\,\mathrm{dB}$ rotate along a circumference having a radius of $0.25\,\mathrm{m}$, whereas the weaker source of $88\,\mathrm{dB}$ rotates along a circumference having a radius of $0.125\,\mathrm{m}$. The relative angle between the sources on the external circumference is $\phi = 40°$. The challenge of this subcase is to handle the varying angular rate as well as multiple sources with different intensities. The sound levels displayed in Figure 3.7 correspond to the sound-pressure level at $1\,\mathrm{m}$ of distance from the point sources. Finally, the data-processing parameters considered to process the datasets are reported in Table 3.3.

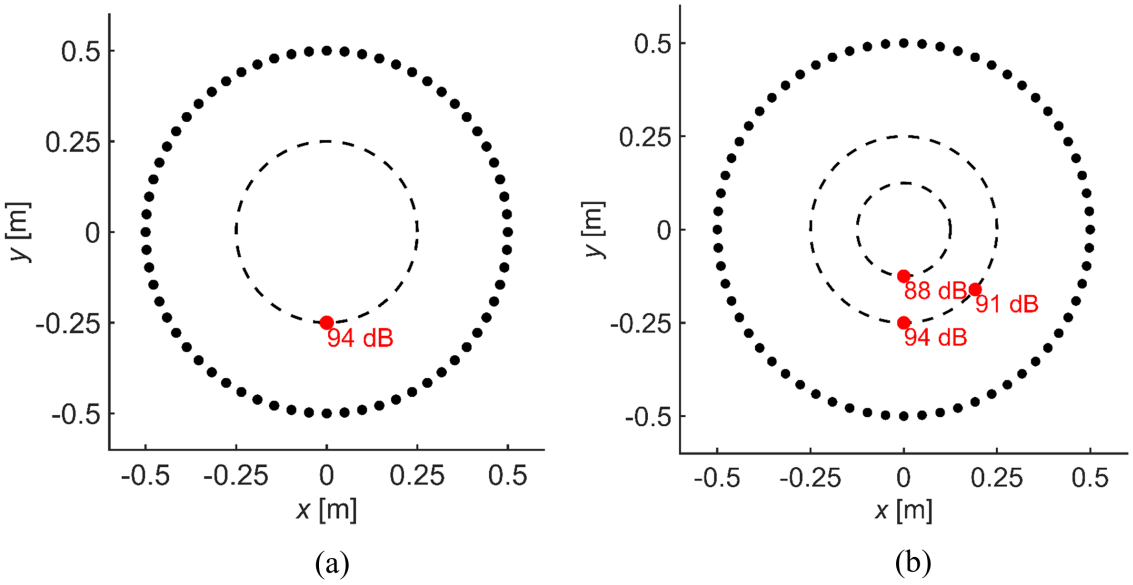

Figure 3.7: Scheme of the benchmark datasets containing the projection of the microphones (black dots) in the x-y plane and the rotating point sources (red dots): (a) one rotating point source with constant angular rate and (b) three rotating point sources at a varying angular rate.

Measurement time	$10\,\mathrm{sec}$	Grid translation	$(x, y) = (0\,\mathrm{m}, 0\,\mathrm{m})$
Sampling frequency	$48\,\mathrm{kHz}$	Rectangular grid	$x = \pm 0.3\,\mathrm{m}$, $y = \pm 0.3\,\mathrm{m}$
FFT block size	1024 samples	Grid resolution	$0.01\,\mathrm{m}$
FFT window	Hanning, $50\,\%$ overlap	Grid points	61×61

Table 3.3: Data-processing parameters of the simulated benchmark cases.

3.4.2 Method validation

The implementation of ROSI has proven to be able to accurately locate and quantify the synthetic rotating sources of the test cases detailed in Section 3.4.1. Figures 3.8 (a) and 3.8 (b) depict the representative sound maps referring to one-third octave frequency band $f_{1/3} = 5\,\mathrm{kHz}$ for the subcases A and B, respectively. The maps are presented using the same dynamic range of $15\,\mathrm{dB}$. For both cases, the positions of the monopolar sources are well-identified and have been successfully retrieved. Moreover, the sound peak levels in subcase B differ by $3\,\mathrm{dB}$ from each other, hinting at

a correct reconstruction of the source amplitude.

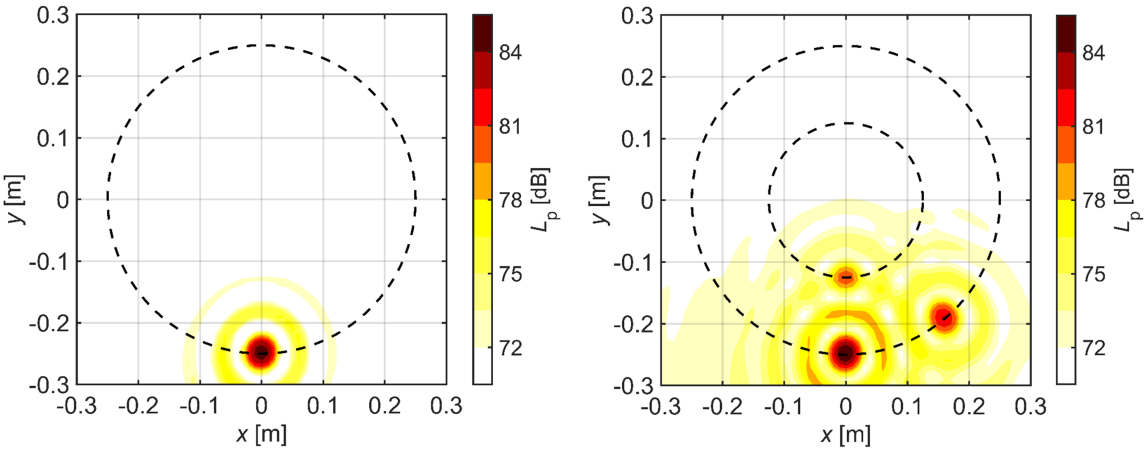

Figure 3.8: ROSI sound maps for $f_{1/3} = 5\,\mathrm{kHz}$ for subcase A corresponding to a monopolar synthetic source rotating at a fixed angular rate (a) and for subcase B corresponding to three monopolar synthetic sources rotating at a varying angular rate (b).

Subsequently, the sound maps have been integrated in order to perform a quantitative analysis of the source-reconstruction performance of the method. The integration is performed by summing the squared pressure levels included within a $1.5\,\mathrm{dB}$ dynamic range from the main peak. Figure 3.9 (a) shows the relative sound-pressure level $\Delta L_{p,1/3}$ for the one-third octave frequency bands ranging from $1\,\mathrm{kHz}$ to $12.5\,\mathrm{kHz}$ for subcase A. The data are referred to a reference pressure of $p_{ref} = 20\,\mu\mathrm{Pa}$. The integrated spectra show a general good agreement with the simulated ones for the investigated frequency range, with a deviation from the expected amplitude that is contained within $\pm 1\,\mathrm{dB}$ for frequencies up to $8\,\mathrm{kHz}$. Above this threshold, the integrated spectra increasingly underestimate the source amplitude level, reaching a difference of $\Delta L_{p,1/3} = -2\,\mathrm{dB}$ at $f_{1/3} = 12.5\,\mathrm{kHz}$. This deviation is probably due to the integration procedure as a wider region surrounding the source peak should be integrated to retrieve the correct level in this case. Figure 3.9 (b) presents the relative sound-pressure levels for the one-third octave frequency bands ranging from $1\,\mathrm{kHz}$ to $12.5\,\mathrm{kHz}$ for subcase B, computed with a reference pressure of $p_{ref} = 20\,\mu\mathrm{Pa}$. Also in this case, the integrated spectra exhibit a fairly good agreement with the simulated ones. Particularly, the spectra for the louder source show a similar trend as the one for subcase A. This result indicates that ROSI is able to correctly reconstruct the source amplitude for a variable angular rate when the information on the angular velocity variation is well documented. Comparable results have also been obtained for the integrated spectra of the intermediate source. In this case, a higher deviation up to $1.8\,\mathrm{dB}$ is seen around $f_{1/3} = 2\,\mathrm{kHz}$. For the weakest source, the sound amplitude reconstruction is found to be less accurate, especially at lower frequencies, where the integrated spectrum overestimates the simulated ones with a maximum $\Delta L_{p,1/3}$ value of almost $4\,\mathrm{dB}$ at $f_{1/3} = 1\,\mathrm{kHz}$. This is mainly due to the difficulty of beamforming to properly isolate non-dominant source contributions. Moreover, the distance between the louder and the weaker source is lower than the minimum resolvable source separation distance given by the Rayleigh criterion in Eq. (3.5), which, for the benchmark simulated setup geometry, corresponds to approximately $0.2\,\mathrm{m}$. Finally, also for subcase B, an underestimation of the correct sound level

up to 2 dB for the first two dominant sources and 4 dB for the third one is visible at higher frequencies.
In general, it can be concluded that the ROSI method successfully detects the sources rotating at constant and varying angular rates while an adequate reconstruction is possible in most of the frequency range.

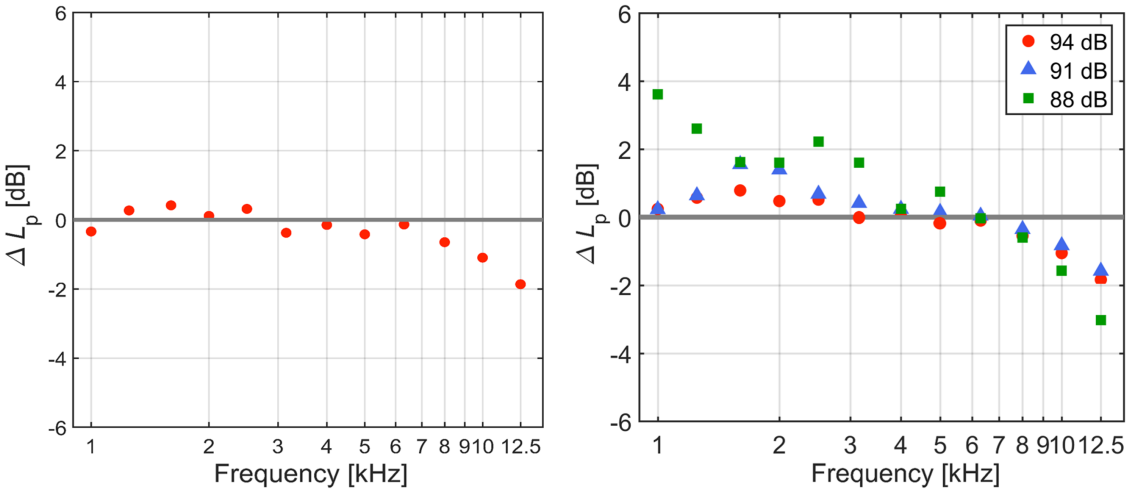

Figure 3.9: Integrated relative spectra for subcase A corresponding to a monopolar synthetic source rotating at a fixed angular rate (a) and for subcase B corresponding to three monopolar synthetic sources rotating with the varying angular rate (b).

3.5 Results and discussion

The following section presents an overview of the acoustic properties of the FA and FM configurations by providing single-microphone measurements and sound-source localization maps. For the latter, a two-dimensional rectangular scanning grid is defined to fully encompass the rotational plane of the fan, with $x = \pm 0.25\,\mathrm{m}$, $y = \pm 0.25\,\mathrm{m}$. The resolution of the scanning grid is set to be $0.01\,\mathrm{m}$ in both directions. A dynamic range of $5\,\mathrm{dB}$ for all the following sound maps is adapted according to the maximum value in the specific map as the upper limit. Moreover, the displayed levels correspond to the sound pressure level at $1\,\mathrm{m}$ distance from the low-speed cooling fan.

3.5.1 Single-microphone measurements

The far-field sound spectra, recorded at VKI by the microphone aligned with the center of the fan working at $q_m = 0.42\,\mathrm{kg\,s^{-1}}$, $0.7\,\mathrm{kg\,s^{-1}}$, and $1\,\mathrm{kg\,s^{-1}}$, are depicted in Figures 3.10 (a), 3.10 (b), and 3.10 (c) respectively. This location corresponds to a specification required by car manufacturers. For all flow-rate cases, the background noise (not reported in the graphs) is negligible compared to the fan sound radiation. Except for the case operating at $q_m = 1\,\mathrm{kg\,s^{-1}}$ above $4\,\mathrm{kHz}$, the fan alone always radiates more noise compared to the full module. Nevertheless, this difference is always less than $3\,\mathrm{dB}$ above $2\,\mathrm{kHz}$. Below this limit, some differences are found around the BPF and harmonics tonal peaks, which are broadened in the fan-alone case. In fact, the subharmonics humps for the fan-alone cases are more prominent. This can be attributed to the fact that

the heat exchanger acts as a flow straightener, breaking down larger vortical structures upstream of the chamber and making the BPF much sharper [14, 50]. Despite this effect, the presence of the heat exchanger does not seem to have a relevant impact on the shape of the spectra for the investigated conditions. This was also clearly observed by Rynell *et al.* [14] on a truck module with a similar heat exchanger technology. Yet, an opposite trend has been recently reported by Czwielong *et al.* [51], which observed larger subharmonic humps and higher tonal peaks in the module case. The present evidence could be mostly explained by the different heat exchanger technology used in this experiment, with larger and fewer tubes and less dense fin and louver arrangement. Consequently, the heater core no longer acts as an efficient turbulence control screen and may actually generate extra-large structures. These have time to develop till the fan inlet as the distance from the heat exchanger core to the fan is also much larger.

In Figure 3.10 (d), the spectrum recorded at VKI for the FM case working at $q_m = 1\,\mathrm{kg\,s^{-1}}$ is compared with the spectrum recorded at UdeS for the FM case working at 3400 rpm in free-field conditions, namely at $\Delta P = 0\,\mathrm{Pa}$. These two operating points are close to each other, as it can be noticed from the performance curve given in Figure 3.4 (a). The spectral shape is globally conserved with overall similar amplitudes, despite small variations at low frequencies mainly due to the different properties of the anechoic chambers, and the appearance of a dip at 7 kHz for the UdeS curve. The latter is an acoustic installation effect, proven to be independent of the axial fan rpm variation, as shown in the following section.

3.5.2 Directivity measurements

The spectra obtained at various rpm during the directivity campaign are presented in Figure 3.11 (a). The shapes of the spectra are similar to each other for all rpm and we can notice three tones. For the case of 3400 rpm the tones corresponding to the first and second BPF are observed around 397 Hz and 793 Hz because of the above slight variation of rotational speed induced by the electrical motor ($\pm$50 rpm). An additional high tone is observed at 280 Hz, which is explained below. At high frequencies, beyond the roll-off at 4 kHz, the features of the spectra such as humps and peaks remain at the same frequencies and are independent of the variation of rpm. The acoustic wavelengths at these frequencies are comparable with the dimensions of the shroud and other components of the module. Therefore, we conclude that this part of the spectra is influenced by the experimental setup.

In Figure 3.11 (b), the SPL normalized by rpm^5 is shown versus the frequency normalized by BPF. The spectra collapse after the 2$^{\text{nd}}$ BPF (2*BPF in the figure), suggesting a dipole noise source. At lower frequencies (corresponding to a Strouhal number based on the tip chord length, St_t, up to 0.6), several tones corresponding to frequencies harmonics of the rotational frequency (5/rev, 9/rev, 12/rev, etc.) are observed. These harmonics can be attributed to the vibration of the module caused by a slight unbalance of the fan. Additional scaling with St_t is depicted in Figure 3.11 (c) for the SPL normalized by rpm^5. A good collapse is observed at Strouhal number around 1 (from 0.6 to 2) and points out that the noise source at the blade tip is chordwise compact at these frequencies. The power 5 is close to the exponent found by Canepa *et al.* [52] for the broadband and tip-leakage noise generated by such automotive engine cooling low-speed fans. Figure 3.11 (d) shows that the normalization with rpm^4 collapses the spectra at Strouhal from 2 to 4 at all rpm, except for the lowest speed. This highlights that the noise source becomes chordwise non-compact at high frequencies or that a different mechanism is responsible for these frequencies. The deviation of the case at 1500 rpm may be caused by some significant contribution of the motor. Surprisingly, a good collapse is also found at low Strouhal numbers up to 0.5, even though it corresponds to the frequency range strongly influenced by vibrations.

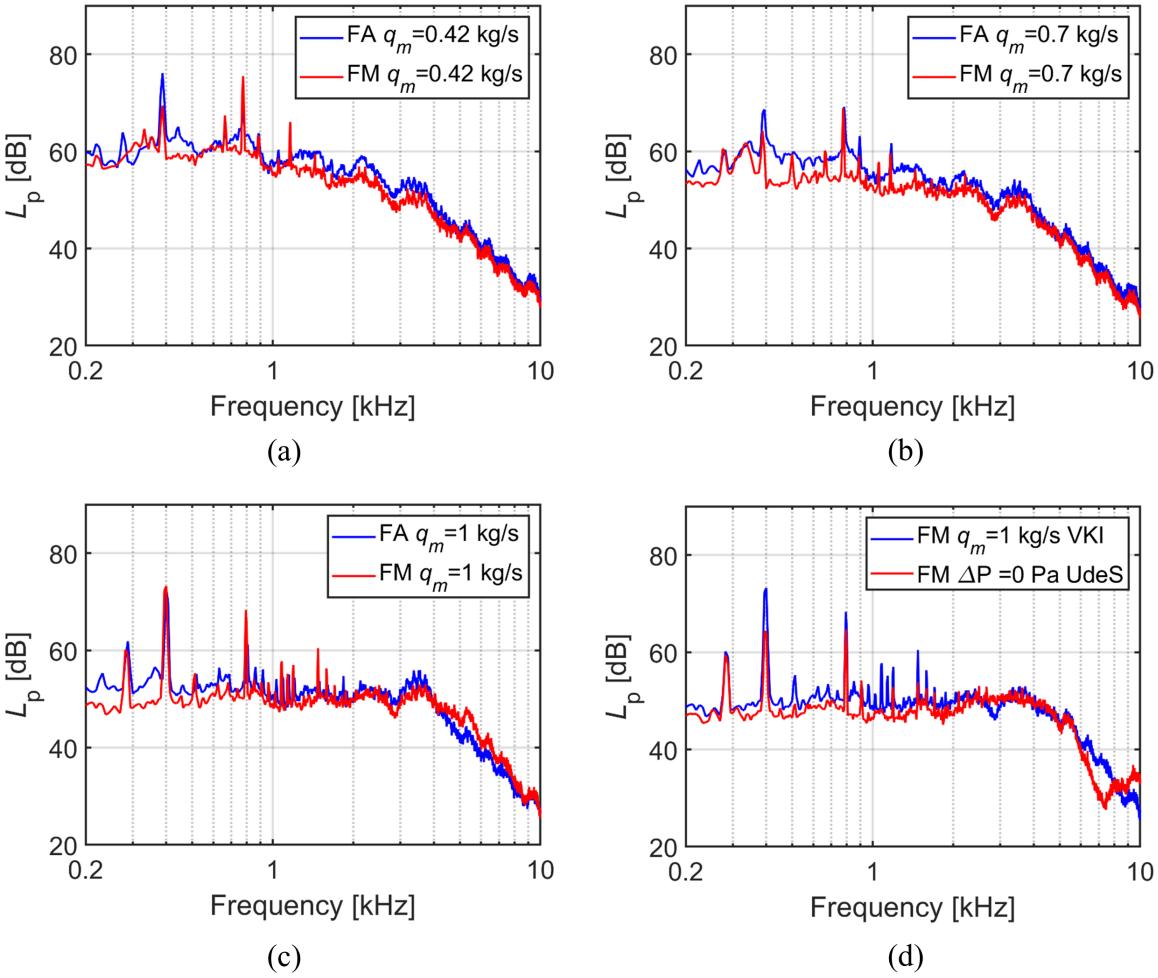

Figure 3.10: Far-field acoustic spectra recorded at VKI by the microphone aligned with the center of the fan at a distance of $2.5d_{fan}$ *of the fan alone (FA) and full module (FM) cases for the low (a), optimal (b), and high (c) airflow working points. The comparison between the FM VKI case at* $1\,\mathrm{kg\,s^{-1}}$ *and the UdeS FM case at* 3400 *rpm is shown in (d). The rotational speed for all the VKI cases is* 3400 ± 50 *rpm.*

In Figure 3.12 the radiation map (frequency versus observation angles) is shown for the arc at $0°$ with the flow direction from $0°$ (microphone 1) to $180°$ (microphone 13). The BPF is observed for all angles and has a higher level in the upstream direction. The harmonic tone at lower frequencies is most pronounced at angles close to the fan axis. It is worth noting that the peak of the 2^{nd} BPF has much higher levels upstream than downstream. At high frequencies beyond $4\,\mathrm{kHz}$, the roll-off appears. Overall, the map is symmetric with respect to $90°$ and presents two lobes of sound radiation, which is another evidence of the dipole source.

3.5.3 Sound-source localization maps and integrated spectra

In this section, the sound-source localization maps carried out at VKI for the FM at $q_m = 1\,\mathrm{kg\,s^{-1}}$ are compared with the ones calculated at UdeS for the FM at $\Delta P = 0\,\mathrm{Pa}$. These operating points are close to each other and so it is possible to confirm the repeatability of the ROSI method implementation by localizing and quantifying the noise sources. In Figure 3.13, the sound maps

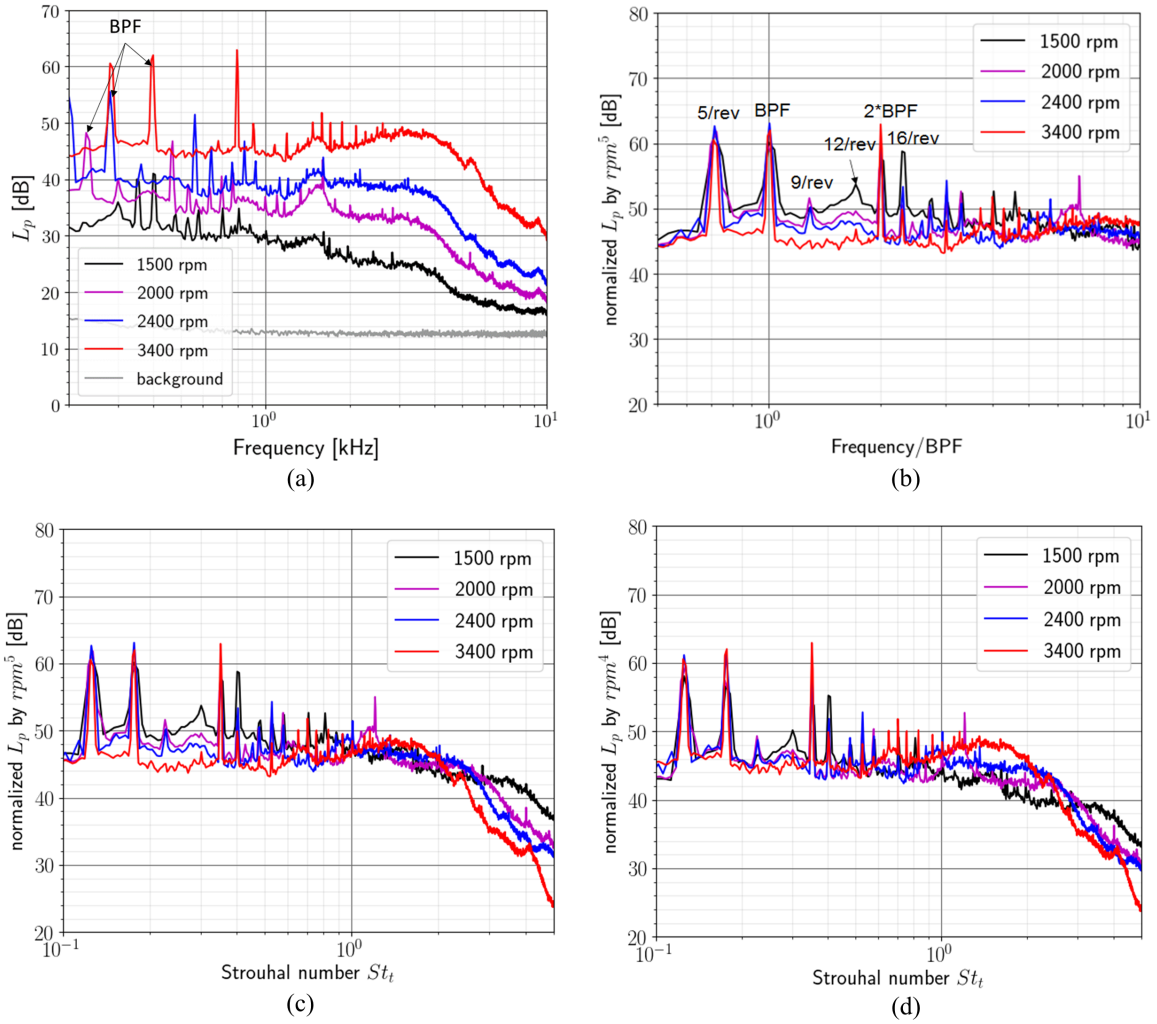

Figure 3.11: Directivity results obtained at UdeS. (a) SPL of the antenna most centered microphone 1 at various rpm. (b) Normalized SPL by rpm^5 versus frequency normalized by BPF. Normalized SPL by rpm^5 (c) and rpm^4(d) versus Strouhal number based on the tip chord.

are depicted for third-octave bands with center frequencies 2.5, 3.15, and 4 kHz.

For frequencies above 3.15 kHz in the VKI case, the maximum L_p appears to be towards the tip of the blade. As frequency increases, a better spatial resolution of the map can be achieved and more details can be observed. In contrast, at 2.5 kHz and below, the identification of the aerodynamic sources for each blade separately is not achievable and the sound sources cannot be attributed to a specific noise mechanism. This shows the limitation of the measurement technique in resolving sound sources at low frequencies. The present evidence can be further examined by the usage of the Rayleigh criterion explained in Section 3.3.3. If the distance between two consecutive blades $R = 0.10$ m is considered as the minimum separation distance of two sources, through Eq. (3.5) the resulting frequency is $f_{min} \approx 2.5$ kHz for the VKI antenna. This result is verified by the VKI beamforming maps in Figure 3.13: at 2.5 kHz as centered frequency, the sound source map is affected by the frequencies which are lower than the f_{min} and the contribution of each blade is not clearly identified. Nevertheless, at 3.15 kHz where all the frequencies of the

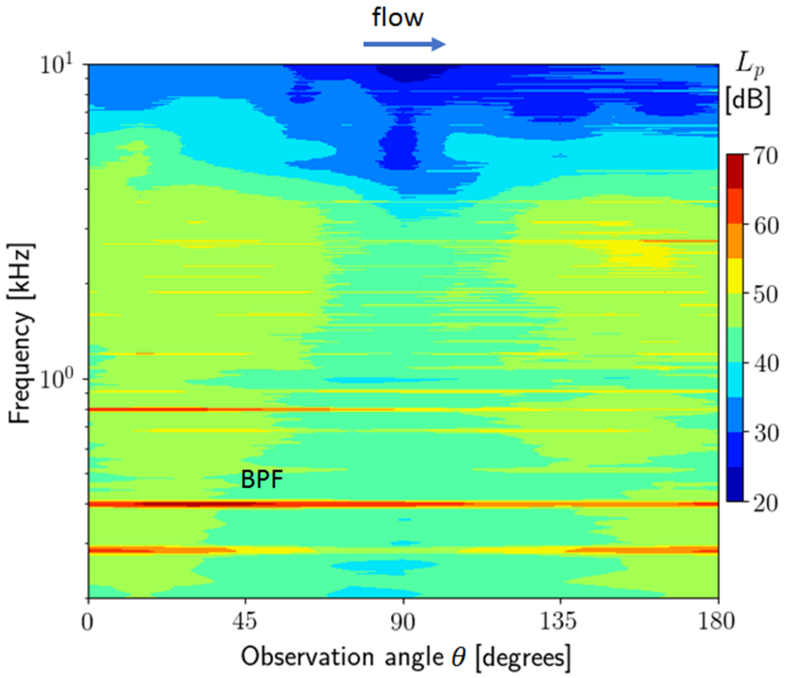

Figure 3.12: Frequency versus observation angle θ map at 3400 *rpm.*

band are above the Rayleigh criterion, sound source spots can be detected for each blade. Similar considerations are made for the UdeS sound maps: in this case, Eq. (3.5) yields a higher frequency of $f_{min} = 3.66\,\mathrm{kHz}$. As a consequence, clean acoustic source separation is carried out only at or above $3.15\,\mathrm{kHz}$. Although for the maps centered at $2.5\,\mathrm{kHz}$ it is hard to infer the azimuthal location of the sources, yet we remark that these are appearing mostly at the mid-span region of the blade. The sound maps at this frequency band for other operating points are not shown here for the sake of conciseness, yet this trend is always observed with and without the heat exchanger. For the studied axial fan, the importance of this blade region in terms of sound emissions was highlighted in [53], especially for frequencies below $3\,\mathrm{kHz}$, where a dominance of the leading-edge noise mechanism was attributed to the high turbulent-kinetic-energy development in such a loaded blade area.

In Figure 3.14, the comparison between the VKI and UdeS cases continues at higher third-octave frequency bands, namely at 5, 6.3, and $8\,\mathrm{kHz}$. For all these cases, the acoustic sources are clearly located at the tip of the blades and, in particular, at the leading edge.

If by comparing the sound maps we can infer the similarity of the source locations for the VKI and UdeS cases, the integrated spectra in Figure 3.15 (a) show quantitatively the amplitude levels with respect to the microphone aligned with the center of the fan. The results are obtained through a summation of the mapped sound pressure levels over the regions where sources with $1.5\,\mathrm{dB}$ dynamic range are included. The dynamic range value can be justified by the fact that spurious sources have to be subtracted in the summation, otherwise, a wrong reconstructed L_p would be calculated. The summation refers to the squared pressure values since the ROSI method assumes the sound sources to be incoherent [20]. As expected, for both VKI and UdeS cases, an erroneous source reconstructed level is found at low frequency. This is due to the poor spatial resolution of the source region that does not allow for proper separation of the different noise contributions coming from the blades, as mentioned in Section 3.3.3. Indeed, the presence of

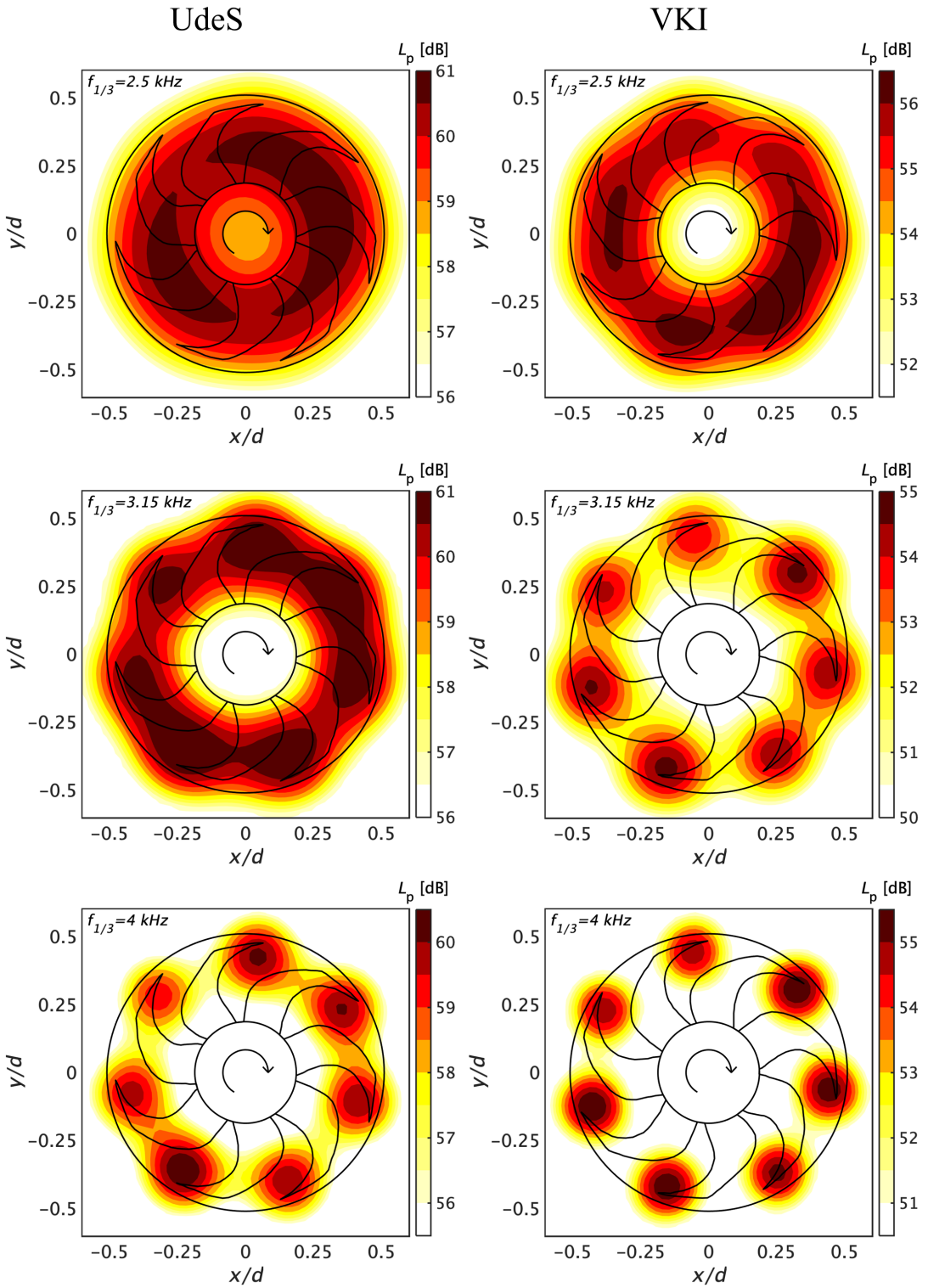

Figure 3.13: Comparison between sound-localization maps at different frequency bands: (left column) sound maps calculated at UdeS for the FM at $\Delta P = 0\,\mathrm{Pa}$, and (right column) sound maps carried out at VKI for the FM at $q_m = 1\,\mathrm{kg\,s^{-1}}$.

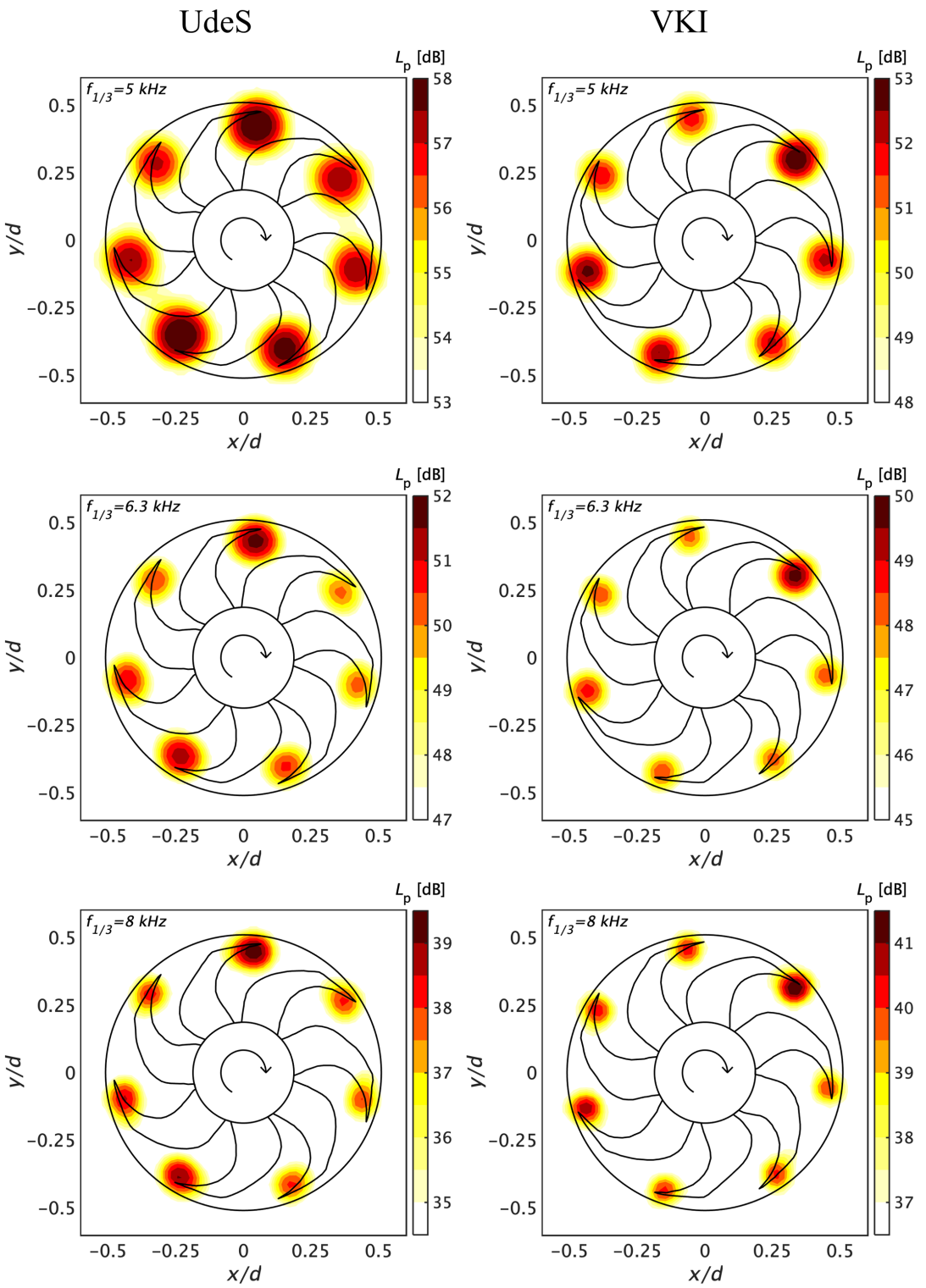

Figure 3.14: Comparison between sound-localization maps at different frequency bands: (left column) sound maps calculated at UdeS for the FM at $\Delta P = 0\,\mathrm{Pa}$, and (right column) sound maps carried out at VKI for the FM at $q_m = 1\,\mathrm{kg\,s^{-1}}$.

overlapping contributions in the integration region leads to an overestimation of the actual sound level that is inversely proportional to the frequency: the lower the frequency, the poorer the spatial resolution and the higher the overestimation. However, for higher frequencies, the algorithm is able to correctly separate the noise contributions and the single-microphone and the ROSI curves exhibit a fairly good agreement for both VKI and UdeS cases. This trend can be further verified from Figure 3.15 (b), where the relative differences on the L_p are depicted for the range between 3.15 to 8 kHz. The VKI maps exhibit a good agreement above 4 kHz, with the lowest difference of about 1 decibel at 6.3 kHz. Although, due to the Rayleigh criterion, UdeS maps still have more than 5 dB of difference at 6.3 kHz, the same trend of VKI maps is followed showing the best agreement (less than 1 dB of difference) at 8 kHz.

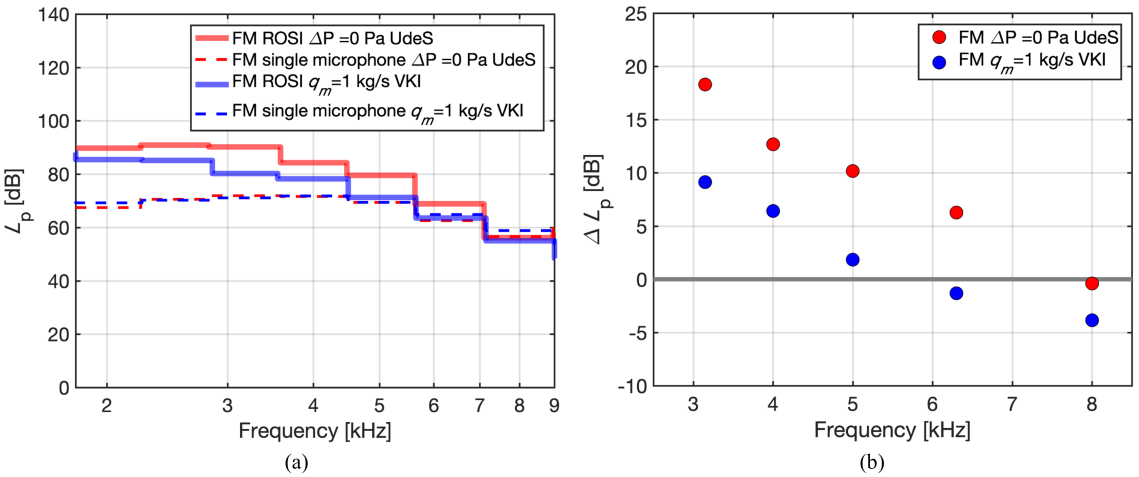

Figure 3.15: Comparisons between the VKI FM-case operating at $q_m = 1\,\mathrm{kg\,s^{-1}}$ and the FM UdeS-case working at $\Delta P = 0\,\mathrm{Pa}$. In (a), the integrated spectra (solid lines) and the single-microphone spectra (dashed lines) are depicted. In (b), the relative differences of the reconstructed L_p by ROSI and the one recorded by the microphone aligned with the center of the fan.

3.5.4 Sound-source localization maps varying the operating conditions

In Figure 3.16, we illustrate the source distribution maps of the reconstructed SPL for the FA and FM configurations at three different volumetric flow rates. These maps are obtained at VKI and for the sake of conciseness, only the ones at 6.3 kHz are shown considering that this is the third-octave frequency band with the best visualization of the results, as highlighted in the previous paragraph. The presence of the radiator for the 3 FM operating points allows for the reconstruction of the acoustic sources, suggesting that the masking effect of the radiator can be neglected. To the authors' knowledge, this work is the first attempt to reconstruct the rotating sound sources through a radiator. To complete the study, the integrated spectra for FA and FM operating under different conditions are shown in Figure 3.17 along with the relative differences of L_p. For all the working conditions, the comparison of the integrated spectra against the single-microphone measurement aligned with the center of the fan is below 5 dB starting from the 5 kHz one-third frequency band. As mentioned in Section 3.1, there are a handful of studies in the literature that use sound source maps to identify the dominant sound generation mechanism in a certain frequency range. Fans with different geometries often lead to a different distribution of sources in the plane of rotation. In particular, the effect of the blade forward or backward curvature is a major

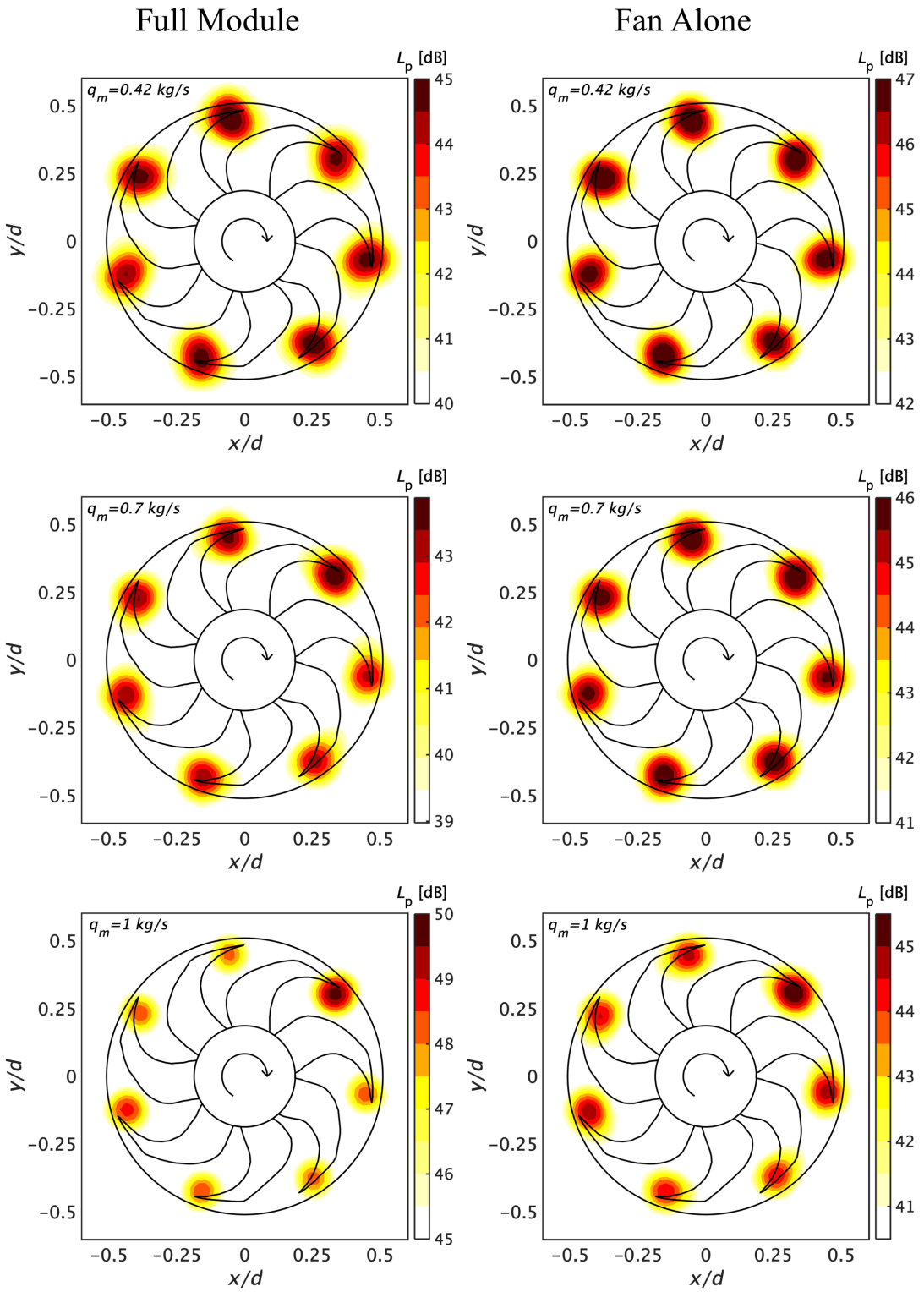

Figure 3.16: Sound-localization maps carried out at VKI at 6.3 kHz *varying the operating condition in a full-module (left column) or fan-alone configuration (right column).*

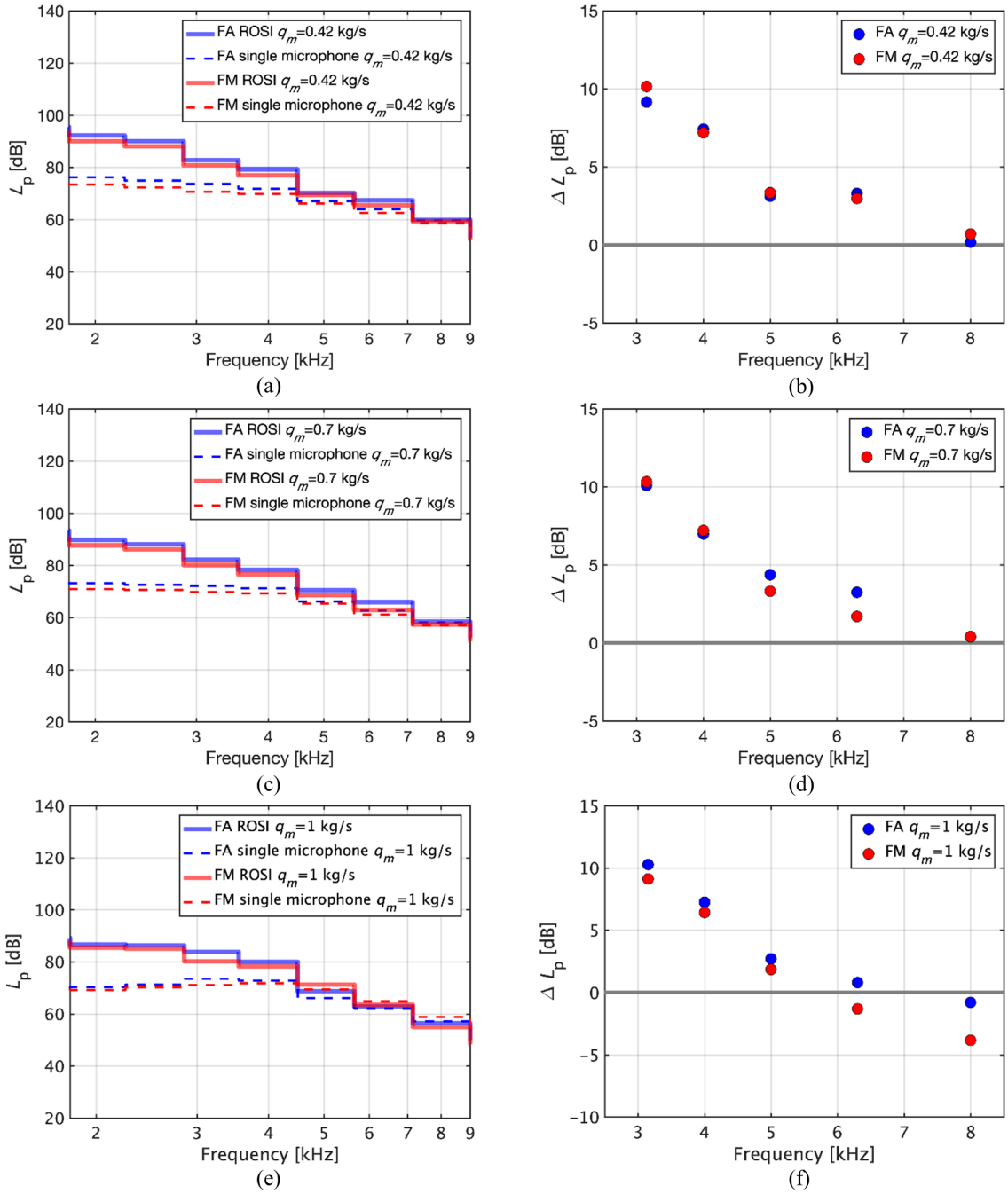

Figure 3.17: The FA and FM integrated spectra (solid lines) and the single-microphone spectra (dashed lines) are compared varying the operating condition. The circles represent the relative differences of the reconstructed L_p by ROSI and the one recorded by the microphone aligned with the center of the fan.

contributor to this difference [26, 34]. Although it is not trivial to make comparisons between fans with different geometry, Zenger et al. [16] demonstrated with a rotating beamforming technique that, for a forward-skewed axial fan, sources distribute (at high frequencies) mainly at the tip of the blades at the leading edge only in the case where the inlet flow conditions are strongly distorted. In contrast, with clean inlet flow conditions, sources still tend to distribute at the tip of the blade, where higher relative velocities are reached, but at the trailing edge. This fact, in agreement with classical studies involving axial fan noise [1, 3], indicates the turbulence-interaction noise as the dominant one under distorted flow conditions, whereas the self-noise is the dominant one under clean inlet conditions. In the present case, above $2.5\,\mathrm{kHz}$, the sources are clearly distributed at the tip of the blade at the leading edge for each tested operating condition, which is also consistent with the study performed on a forward-swept engine cooling fan by Sanjosé and Moreau [54]. Hence, the turbulence-interaction noise appears to be the dominant one in this type of axial fan, at least in the frequency range investigated by the ROSI technique. Nevertheless, as already suggested by the similarity between the frequency spectra in Figure 3.10, the presence of the radiator has no visible effect on the position of the sound sources. This leads one to expect that the turbulence produced downstream of the radiator is either not high or that it is dissipated before interacting with the blades. As a consequence, most of the turbulence is likely produced within the gap between the shroud and the fan, rather than directly coming from the radiator. As Herold et al. [48] found, we can expect a displacement of the sources toward the leading edge of the blade for moderate air flows. For these operating points, the blades are sufficiently loaded such that the recirculation flow at the tip becomes significant. In fact, as pointed out in [9], these plastic-made ventilators can be subjected to significant deformation during rotation that can lead to a flow in the tip regions of the blade equal to $6\,\%$ of the total flow through the fan. This is the case, regardless of the L-shaped ring geometry, designed in order to reduce the recirculation flow in this area of the blade [10]. Thus we infer that this secondary flow is crucial to the generation of the noise not only at low-to-mid frequencies as commonly accepted in the literature but also at high frequencies as the sound-source maps demonstrate.

3.5.5 Acoustic contribution of each blade

The validation of the previous quantitative results gives the possibility to rely on the quantitative estimation of specific parts of the sound-source maps. For this reason, an analysis of the acoustic contribution of each blade is considered in the range of $4\,\mathrm{kHz}$ to $8\,\mathrm{kHz}$ with the same strategy adopted for the calculation of the integrated spectrum (Figure 3.17). For each blade, an integration region with a dynamic range of $1.5\,\mathrm{dB}$ is taken into account. All computed integrated spectra have been compared with a reference one. The latter is computed by dividing the total integrated spectra retrieved in the previous section by the total number of blades ($B = 7$). The division is performed with the squared pressure values.

The relative differences of the integrated spectra between the blades and the reference are illustrated in Figure 3.18. Since it is not possible to observe a significant difference of noise emission among the blades (less than $\pm 1\,\mathrm{dB}$ for the examined frequencies), it can be concluded that each blade contributes to the overall radiated noise in a similar way. This is not a foregone conclusion since the fan blades are not perfectly equally spaced. Furthermore, it would not be possible to infer such a conclusion with standard microphone measurements.

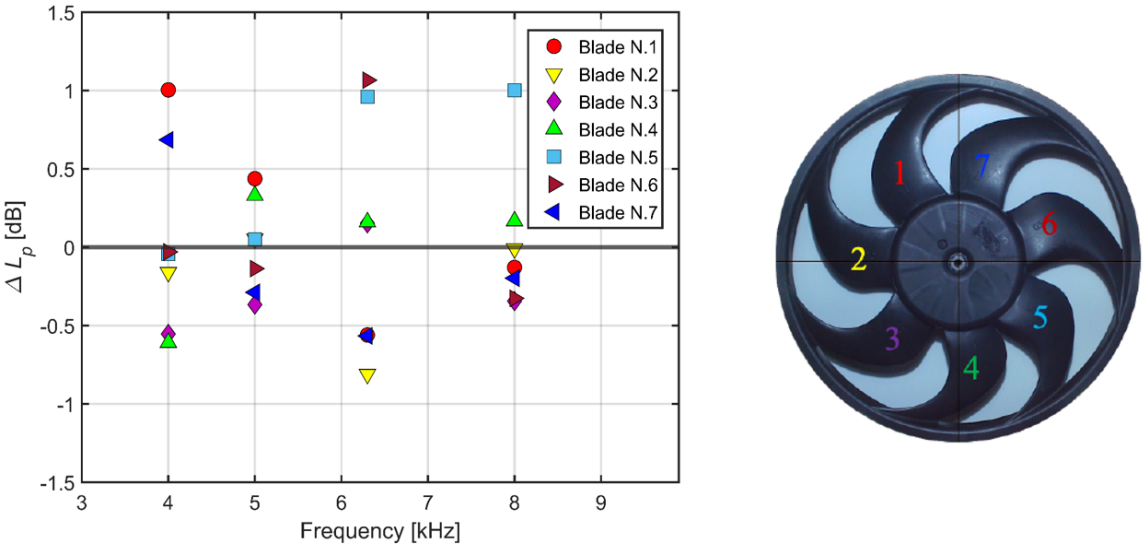

Figure 3.18: Relative differences in sound pressure level for each blade with respect to the reference value $L_{p,ref(1/3)}$ and the numbered blades of the fan.

3.6 Conclusions

In the automotive industry, the engine cooling module is a major contributor to overall automotive noise emissions. To fully characterize the latter in a well-controlled environment, sound-pressure measurements have been performed on the same module in two different anechoic wind tunnels using arrays of microphones, building a unique experimental database on such systems. At UdeS, the module has been tested in free-flow conditions providing directivity data at various rotational speeds. At VKI, measurements on the fan-alone (FA) and on the full module (FM) have further provided narrow-band spectra at different operating conditions. The former case has allowed for some scaling analysis, which has clearly stressed the dipolar nature of the sound emitted by the module and confirmed previous broadband and tip-noise scalings [52]. The latter case has shown the evolution of the SPL with flow rate: the more loaded the fan is, the more broadband the spectrum is with a larger contribution at lower frequencies. This is similar to what is observed in airfoil noise with increasing incidence [55, 56]. This also confirms previously reported sound power measurements in reverberant wind tunnels [10, 57]. The comparison between the fan-alone and the module cases shows that the overall bell shape of the broadband component is similar for the same flow condition, except at lower frequencies around the BPF tones. Indeed, the trend on the tones with the increasing flow rate is similar but their amplitudes and shapes differ. Some line broadening occurs on the fan alone, which is reduced on the module, the heat exchanger acting as a flow straightener or turbulence control screen. For the same free-flow conditions, both facilities yield comparable narrow-band spectra.

Additionally, source localization has been performed on the same module at the nominal speed and free-flow condition in both test facilities. Similar spiral microphone arrays have been used, the VKI one being slightly larger yielding a better resolution at lower frequencies. This joint source localization study has also allowed investigating the influence that the suction-side radiator has on the distribution of sound sources and the transmission of acoustic waves passing through it.

A time-based rotating beamforming technique, ROSI, has been used to localize and quantify the sound sources generated by the low-speed axial cooling fan. The method has been implemented and validated on a database featuring synthetic sources rotating at constant or time-varying speeds, demonstrating in both cases that it can satisfactorily localize and quantify the sources.

In both test facilities, the sound sources are localized at the same position on the module at the tip blade leading edge, making it possible to distinguish the contribution of each blade from the $3.15\,\mathrm{kHz}$ one-third frequency band for the VKI case and $4\,\mathrm{kHz}$ for the UdeS case. This demonstrates the repeatability and robustness of the implemented acoustic technique. Moreover, the presence of the radiator between the antenna and the fan does not prevent the correct reconstruction of the sound sources obtained with the ROSI technique.

At VKI, the method has also been applied to the three operating points in both the FM and FA cases, isolating the sources on the blades from the $3.15\,\mathrm{kHz}$ one-third frequency band. In all cases, the sound sources are always located at the leading edge of the blade tip. Therefore, for this particular engine cooling module, the turbulence-interaction noise generated by the secondary flow in the tip region appears to be the dominant broadband noise mechanism that dominates the noise spectra at all frequencies resolved by ROSI for all studied flow rates. This confirms previously reported sound power predictions as a function of flow rates on a similar forward-swept ring fan that had been tested in a reverberant wind tunnel [10]. Note also that, in the present study, tip noise has primary importance not only at low-to-mid frequencies as generally pointed out in the literature [3], but also at high frequencies.

Finally, regardless of the different operating conditions, the radiator appears to have a negligible influence on sound generation and propagation. Therefore, it can be seen as acoustically transparent with negligible transmission losses as previously shown in LBM simulations.

References

[1] Alain Guédel. *Acoustique des ventilateurs*. PYC Livres, Villeurbanne, France, 1999.

[2] Thomas Carolus, Marc Schneider, and Hauke Reese. *Axial flow fan broad-band noise and prediction*. Journal of sound and vibration, 300(1-2):50–70, 2007.

[3] Stephane Moreau and Michel Roger. *Competing broadband noise mechanisms in low-speed axial fans*. AIAA journal, 45(1):48–57, 2007.

[4] I Jr Sharland. *Sources of noise in axial flow fans*. Journal of Sound and Vibration, 1(3):302–322, 1964.

[5] Michel Roger and Stéphane Moreau. *Broadband self noise from loaded fan blades*. AIAA journal, 42(3):536–544, 2004.

[6] Thomas Carolus. *Ventilatoren-Aerodynamischer Entwurf, Schallvorhersage*. Konstruktion, 2, 2003.

[7] Stéphan Magne, Stéphane Moreau, and Alain Berry. *Subharmonic tonal noise from backflow vortices radiated by a low-speed ring fan in uniform inlet flow*. The Journal of the Acoustical Society of America, 137(1):228–237, 2015.

[8] M. Piellard, B. Coutty, V. Le Goff, F. Pérot, and V. Vidal. *Direct Aeroacoustics Simulation of Automotive Cooling Fan System: Effect of Upstream Geometry on Broadband Noise.* In 20th AIAA/CEAS Aeroacoustics Conference, AIAA 2014-2455 paper, Atlanta, GA, June 2014.

[9] Manuel Henner, Bruno Demory, Mohamed Alaoui, Maxime Laurent, and Benjamin Behey. *Effect of Blade Curvature on Fan Integration in Engine Cooling Module*. Acoustics, 2(4):776–790, October 2020.

[10] Stéphane Moreau and Marlène Sanjosé. *Sub-harmonic broadband humps and tip noise in low-speed ring fans*. The Journal of the Acoustical Society of America, 139(1):118–127, 2016.

[11] Edward Canepa, Andrea Cattanei, Fabio Mazzocut Zecchin, Gabriele Milanese, and Davide Parodi. *An experimental investigation on the tip leakage noise in axial-flow fans with rotating shroud*. Journal of Sound and Vibration, 375:115–131, 2016.

[12] D. Lallier-Daniels, M. Sanjosé, S. Moreau, and M. Piellard. *Aeroacoustic study of an axial engine cooling module using lattice-Boltzmann simulations and the Ffowcs Williams and Hawkings' analogy*. European Journal of Mechanics – B/Fluids, 61:244–254, 2017.

[13] Sabry Allam and Mats Åbom. *Acoustic Modelling and Characterization of Plate Heat Exchangers*. June 2012.

[14] Anders Rynell, Gunilla Efraimsson, Mattias Chevalier, and Mats Abom. *Acoustic characteristics of a heavy duty vehicle cooling module*. Applied Acoustics, 111:67–76, October 2016.

[15] Julien Christophe, Korcan Kucukcoskun, and Christophe Schram. *Tonal and Broadband sound prediction of a locomotive cooling unit*. In 19th AIAA/CEAS Aeroacoustics Conference, Berlin, Germany, May 2013. American Institute of Aeronautics and Astronautics.

[16] Florian Zenger, Gert Herold, and Stefan Becker. *Acoustic characterization of forward-and backward-skewed axial fans under increased inflow turbulence*. AIAA Journal, 55(4):1241–1250, 2017.

[17] Florian J. Zenger, Andreas Renz, Marcus Becher, and Stefan Becker. *Experimental investigation of the noise emission of axial fans under distorted inflow conditions*. Journal of Sound and Vibration, 383:124–145, November 2016.

[18] B. Coutty and S. Moreau. *Aeroacoustic modeling of an automotive engine cooling module*. In 26^{th} International Congress on Noise and Vibration, Montreal, Canada, paper 525, pages Montreal, Canada, 7-1 July 2019.

[19] D. Lallier-Daniels. *Analysis of Tip Leakage Flow Noise Inception in Axial Fans*. PhD thesis, Université de Sherbrooke, Sherbrooke, Canada, 2018.

[20] Pieter Sijtsma, Stefan Oerlemans, and Hermann Holthusen. *Location of rotating sources by phased array measurements*. In 7th AIAA/CEAS Aeroacoustics Conference and Exhibit, page 2167, 2001.

[21] Stefan Oerlemans, Pieter Sijtsma, and B Méndez López. *Location and quantification of noise sources on a wind turbine*. Journal of sound and vibration, 299(4-5):869–883, 2007.

[22] Pieter Sijtsma. *Using phased array beamforming to identify broadband noise sources in a turbofan engine*. International Journal of Aeroacoustics, 9(3):357–374, 2010.

[23] Wolfram Pannert and Christian Maier. *Rotating beamforming–motion-compensation in the frequency domain and application of high-resolution beamforming algorithms*. Journal of Sound and Vibration, 333(7):1899–1912, 2014.

[24] Gert Herold and Ennes Sarradj. *Microphone array method for the characterization of rotating sound sources in axial fans*. Noise Control Engineering Journal, 63(6):546–551, 2015.

[25] Robert Dougherty and Bruce Walker. *Virtual rotating microphone imaging of broadband fan noise*. In 15th AIAA/CEAS Aeroacoustics Conference (30th AIAA Aeroacoustics Conference), page 3121, 2009.

[26] Florian J Zenger, Gert Herold, Stefan Becker, and Ennes Sarradj. *Sound source localization on an axial fan at different operating points*. Experiments in Fluids, 57(8):136, 2016.

[27] Simon Jekosch and Ennes Sarradj. *An Extension of the Virtual Rotating Array Method Using Arbitrary Microphone Configurations for the Localization of Rotating Sound Sources*. In Acoustics, volume 2, pages 330–342. Multidisciplinary Digital Publishing Institute, 2020.

[28] Gábor Kotán, Bence Tóth, and János Vad. *Comparison of the Rotating Source Identifier and the Virtual Rotating Array Method*. Periodica Polytechnica-Mechanical Engineering, 62(4):261–268, 2018.

[29] Olivier Minck, Nicolas Binder, Olivier Cherrier, Lucie Lamotte, and Valérie Pommier-Budinger. *Fan noise analysis using a microphone array*. In Fan 2012 - International Conference on Fan Noise, Technology and Numerical Methods, April, pages 1–9, 2012.

[30] Tamás Benedek and Péter Tóth. *Beamforming measurements of an axial fan in an industrial environment*. Periodica Polytechnica-Mechanical Engineering, 57(2):36–46, 2013.

[31] Tamás Benedek and János Vad. *An industrial onsite methodology for combined acoustic-aerodynamic diagnostics of axial fans, involving the phased array microphone technique*. International Journal of Aeroacoustics, 2016.

[32] Bence Tóth and János Vad. *Algorithmic localisation of noise sources in the tip region of a low-speed axial flow fan*. Journal of Sound and Vibration, 393:425–441, 2017.

[33] Gert Herold and Ennes Sarradj. *Frequency domain deconvolution for rotating sources on an axial fan*. In 6th Berlin Beamforming Conference, February, pages 1–8, 2016.

[34] Gert Herold, Florian Zenger, and Ennes Sarradj. *Influence of blade skew on axial fan component noise*. International Journal of Aeroacoustics, 16(4-5):418–430, 2017.

[35] GP Howell, AJ Bradley, MA McCormick, and JD Brown. *De-dopplerization and acoustic imaging of aircraft flyover noise measurements*. Journal of Sound and Vibration, 105(1):151–167, 1986.

[36] B Barsikow and WF King. *On removing the Doppler frequency shift from array measurements of railway noise*. Journal of Sound Vibration, 120:190–196, 1988.

[37] B Barsikow. *Experiences with various configurations of microphone arrays used to locate sound sources on railway trains operated by the DB AG*. Journal of Sound and Vibration, 193(1):283–293, 1996.

[38] U Michel, J Helbig, B Barsikow, M Hellmig, and M Schüttpelz. *Flyover noise measurements on landing aircraft with a microphone array*. In 4th AIAA/CEAS aeroacoustics conference, page 2336, 1998.

[39] Alessandro Zarri, Julien Christophe, and Christophe F Schram. *Low-Order Aeroacoustic Prediction of Low-Speed Axial Fan Noise*. In 25th AIAA/CEAS Aeroacoustics Conference, page 2760, 2019.

[40] Yongsheng Lian and Wei Shyy. *Laminar-turbulent transition of a low Reynolds number rigid or flexible airfoil*. AIAA journal, 45(7):1501–1513, 2007.

[41] M. Bilka, J. Anthoine, and C. Schram. *Design and evaluation of an aeroacoustic wind tunnel for measurement of axial flow fans*. JASA, 130(6):3788–3796, December 2011.

[42] Joachim Dominique, Julien Christophe, and Christophe Schram. *An experimental multi-ports methodology for fan installation effects investigation*. In 24th AIAA/CEAS Aeroacoustics Conference, page 3926, 2018.

[43] ISO Standard. *ISO 5167:2003, "Measurement of fluid flow by means of pressure differential devices inserted in circular cross-section conduits running full - Parts 1,2,"*. International Organization for Standardization, 2003.

[44] Robert P. Dougherty. *Spiral-shaped Array for Broadband Imaging*, U.S. 5 838 284, Nov. 1998.

[45] Lord Rayleigh. *XXXI. Investigations in optics, with special reference to the spectroscope*. The London, Edinburgh, and Dublin Philosophical Magazine and Journal of Science, 8(49):261–274, 1879.

[46] T. J. Mueller. *Aeroacoustic Measurements*. Springer Berlin, 2002.

[47] Thomas Padois, Paul Laffay, Alexandre Idier, and Stéphane Moreau. *Detailed experimental investigation of the aeroacoustic field around a Controlled-Diffusion airfoil*. In 21st AIAA/CEAS Aeroacoustics Conference, AIAA 2015-2205 paper, Dallas, TX, June 2015.

[48] G. Herold. *Benchmarking Array Analysis Methods: "b11"*. https://www.b-tu.de/fg-akustik/lehre/aktuelles/arraybenchmark, 2017.

[49] Gert Herold, Christof Ocker, Ennes Sarradj, and Wolfram Pannert. *A comparison of microphone array methods for the characterization of rotating sound sources*. In 7th BeBeC, pages 1–12. BeBeC, 2018.

[50] M. Pestana, A. Pereira, E. Salze, J. Thisse, M. Sanjosé, E. Jondeau, P. Souchotte, M. Roger, S. Moreau, J. Regnard, and M. Gruber. *Aeroacoustics of an axial ducted low Mach-number stage: numerical and experimental investigation*. In 23rd AIAA/CEAS Aeroacoustics Conference, AIAA Paper 2017-3215. American Institute of Aeronautics and Astronautics, June 2017.

[51] Felix Czwielong, Florian Kromer, and Stefan Becker. *Experimental investigations of the sound emissions of axial fans under the influence of suction-side exchangers*. In 25th AIAA/CEAS Aeroacoustics Conference, page 2168, 2019.

[52] Edward Canepa, Andrea Cattanei, and Fabio Mazzocut Zecchin. *Scaling properties of the aerodynamic noise generated by low-speed fans*. Journal of Sound and Vibration, 408:291–313, 2017.

[53] Alessandro Zarri, Julien Christophe, Stéphane Moreau, and Christophe Schram. *Influence of Swept Blades on Low-Order Acoustic Prediction for Axial Fans*. Acoustics, 2(4):812–832, 2020.

[54] M. Sanjosé and S. Moreau. *Fast and accurate analytical modeling of broadband noise for a low-speed fan*. Journal of the Acoustical Society of America, 143(5):3103–3113, 2018.

[55] S. Moreau and M. Roger. *Effect of airfoil aerodynamic loading on trailing-edge noise sources*. AIAA journal, 43(1):41–52, 2005.

[56] J. Christophe, J. Anthoine, and S. Moreau. *Trailing Edge Noise of a Controlled-Diffusion Airfoil at Moderate and High Angle of Attack*. In 15th AIAA/CEAS Aeroacoustics Conference, AIAA Paper 2009–3196, May 2009.

[57] R. E. Longhouse. *Noise separation and design considerations for low tip-speed and axial-flow fans*. Journal of Sound and Vibration, 48(4):461–474, 1976.

4

Aerodynamic investigation of the turbulent flow past a radiator

4.1 Introduction

The automotive cooling module is typically composed of a low-speed axial fan preceded by a suction-side radiator, a heat-exchanger used to cool down the car engine (as introduced in Chapter 2). The radiator is composed of flat tubes, where the refrigerant is passing through, and fins and louvers that increase the heat transfer by having more surface exposed to the flow. They also trigger the airflow transition to a turbulent state, enhancing the heat exchange [1]. In Chapter 3, we have shown that the radiator has a low influence on the sound-source localization maps, as well as on the single-microphone spectra. The noise emissions highly depend on the turbulence produced upstream and convected toward the fan inlet, as introduced in Chapter 2. Here, we experimentally investigate the turbulent flow past the radiator with the aim of characterizing the turbulent flow development in real conditions so as to have stronger insight into the kind of turbulence produced by the radiator. If the generated turbulence is supposed to decay downstream of the heat exchanger, cooling module manufacturers cannot locate the fan too far from the radiator outlet because this would substantially reduce its cooling efficiency and also because there is not enough space in the car under-hood compartment. Nevertheless, distancing the ventilators from upstream or downstream obstacles is a common and simple way of mitigating acoustic emissions, often employed in the ventilation industry [2]. As pointed out by Christophe *et al.* [3], there is a lack of understanding about the turbulent features, such as the turbulent kinetic energy (TKE) and the integral length scales, generated by the heat exchanger fine grid. Most of the scientific work involving the study of heat exchangers, both numerical [4–6] and experimental [7, 8], has been focused on the design of the louvers and fins shape in order to optimize the heat transfer and the pressure drop across it. In numerical investigations involving the coupling between the heat exchanger and the fan, the former is typically modeled using a porous medium that induces a pressure drop at the fan inlet [9]. The only relevant previous work regarding the characterization of the flow evolution past radiators found in literature has been carried out in 2019 by Czwielong *et al.* [10]. Here, the authors investigate the acoustic interactions between axial fans and suction-side radia-

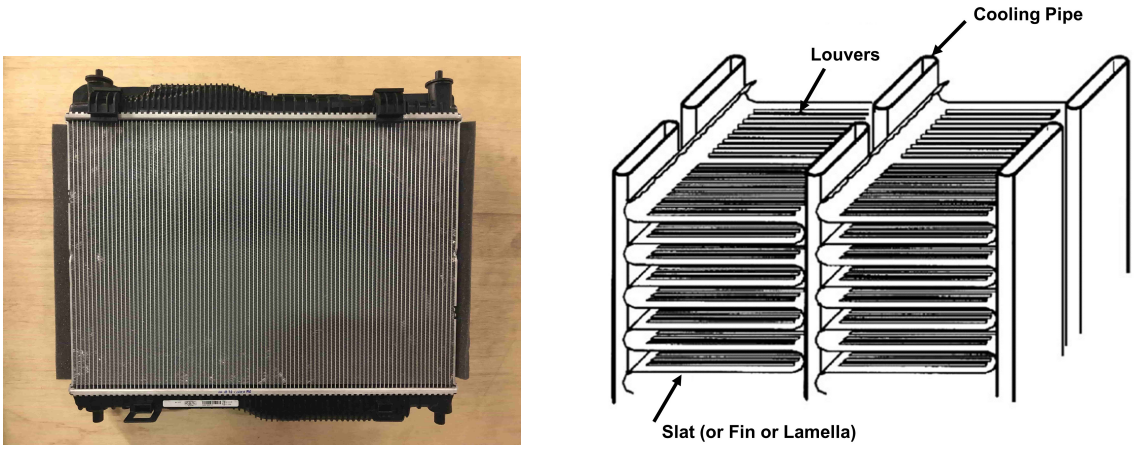

(a) (b)

Figure 4.1: (a) Front view of the automotive heat exchanger produced by the French cooling-systems manufacturer-company Valeo. (b) Adapted from [7], close-up view of the cooling flat tubes, containing the cooling fluid, and of the fins and louvers that are used to increase the heat-transfer efficiency.

tors with 3D anemometry, showing that the heat exchanger affects the flow field upstream of the fan by changing its anisotropic level to a more isotropic one. The clean-flow case presented large vortical structures convected through the casing. Differently, when the 2 radiators with squares and rectangular cross-sections were installed, these acted as flow straighteners, cutting the vortical structures and therefore affecting the overall sound emissions. Moreover, the lack of understanding and real conditions testing was pointed out, which needs to be filled up with simulations and experimental flow visualizations. According to fluid dynamics studies on regular turbulent grid generators [11–13], the flow past the radiator is expected to be anisotropic and non-homogeneous, whereas typically, isotropic and homogeneous turbulence models, such as the von Kármán or the Liepmann model [14, 15], are often employed for turbulence modeling in acoustics. This may lead to less accurate sound predictions if one intends to use them as inputs for semi-analytical noise-predicting models, such as the theory of Amiet for leading-edge noise [16].

4.1.1 Objectives

The aim of the present chapter is to characterize the properties of the flow downstream of an automotive heat exchanger. The latter, provided by the French manufacturing company Valeo, is shown in Figure 4.1 (a). A sketch of the interior structure of the radiator is shown in Figure 4.1 (b): the fine mesh composed of cooling tubes and fins (or lamellas, or slats), acts on the flow similarly to a turbulence-generating grid. Close to the heat exchanger exit a high degree of anisotropy and non-homogeneity is expected, whereas, farther downstream, the energy contained in the large vortical structures is assumed to be transferred to smaller eddies *via* the so-called energy cascade [17], causing the flow to become locally isotropic and homogeneous. Far from the exit, the flow should reach a condition of isotropy and homogeneity, where the turbulence intensity has to decay following a power law. Therefore, the main objectives of this work are hereafter listed:

- To determine the flow anisotropy and non-homogeneity degrees close to the radiator outlet, corresponding to the fan location.

- To define the turbulence creation region and to quantify the experimental turbulence intensity that reaches the fan inlet.

- To assess the applicability of turbulence spectrum models for noise prediction, such as the von Kármán model upstream of the fan location.

In real working conditions, typically, the maximum temperature around the cooling pipes reaches 100 °C[1]. The main effect of the temperature gradient is a change of density in the underhood compartment, even though the Reynolds number based on the fin size is kept within the same order of magnitude as the cold measurements. Test experience shows that the acoustic emissions can be properly captured with cold measurements, also carried out to limit the costs. Hence, the heat exchanger in this work is not operated with coolant liquid and cold measurements will always be considered. In order to carry out these tasks the Stereo Particle Image Velocimetry (S-PIV) [18, 19] has been selected as the most suited experimental technique to implement inside the ALCOVES laboratory at the von Karman Institute for Fluid Dynamics (VKI). The advantage of this technique is the possibility of determining the 3 velocity components on 2D planes, as well as the possibility of analyzing 2D velocity fluctuations spectra, as explained in the following.

The work in this chapter is organized as follows: Section 4.2 describes the methods used to characterize the turbulent flow quantities; in Section 4.3, the S-PIV setup is discussed together with the experimental campaign phases. The uncertainty quantification analysis on the mean velocity components is carried out in Section 4.4. The obtained results are presented and discussed in Section 4.5.

4.2 Turbulence characterization

Most of the fluid flows found in nature or produced in engineering applications are turbulent. The generation of three-dimensional turbulence relies on the vortex-stretching mechanism, which is responsible for the so-called turbulent energy cascade [20]. Large vortical structures, or eddies, are subject to an increase of vorticity in the stretching direction up to a point where the eddie becomes unstable and breaks down in smaller structures. This highly three-dimensional process continues until the turbulent scales are so small that their kinetic energy can be directly converted into heat by viscous effects at a molecular level. This scale is known as the Kolmogorov length scale, defined as $\eta = (\nu^3/\epsilon)^{1/4}$, where ν is the air kinematic viscosity and ϵ is the turbulent kinetic energy dissipation rate. On the other hand, most of the transferring-energy mechanisms from large-scale structures to smaller ones happen to be essentially inviscid. Turbulent flows are highly irregular and of chaotic nature; hence, they are typically investigated with a statistical rather than deterministic approach, based on the average statistics and spectral-energy content of the turbulent structures.

Following the so-called Reynolds decomposition, any flow field can be divided into a mean-field and its fluctuating component around the mean value [21]. The instantaneous streamwise velocity component $u(\mathbf{x}, t)$, typically function of time t and the vectorial space position $\mathbf{x}$, can be expressed as

$$u(\mathbf{x}, t) = U(\mathbf{x}, t) + u'(\mathbf{x}, t), \tag{4.1}$$

where U is the mean velocity component and u' is the fluctuating part. With respect to the investigated case presented in Section 4.3, v is the in-plane crosswise component, whereas w is the

[1] Turbochargers and some other parts in the underhood compartment are above, up to 200 °C.

out-of-plane crosswise component (see Figure 4.8). Hence, the transversal velocity components can be written as:

$$\begin{aligned} v(\mathbf{x},t) &= V(\mathbf{x},t) + v'(\mathbf{x},t), \\ w(\mathbf{x},t) &= W(\mathbf{x},t) + w'(\mathbf{x},t). \end{aligned} \tag{4.2}$$

A statistical mean field can be defined in general, for instance for the streamwise component $U(\mathbf{x},t)$, starting from the number of independent measurements N of one particular variable as:

$$U(\mathbf{x},t) = \lim_{N\to\infty} \frac{1}{N} \sum_{i=1}^{N} u^{(i)}(\mathbf{x},t). \tag{4.3}$$

The root mean square (r.m.s) of a fluctuating component is defined as:

$$u_{rms} = \sqrt{\langle u'^2 \rangle} = \sqrt{\langle (u-U)^2 \rangle}, \tag{4.4}$$

where the $\langle \cdot \rangle$ symbol represents the ensemble average given in Eq. (4.4).

4.2.1 Turbulence intensity

By comparing the turbulence intensity evolution occurring past a heat exchanger with the classical power-law decay past a turbulence-generating grid, we can expect to observe three regions as shown in [12]. In the first part, really close to the grid, large eddies are expected to be highly anisotropic and non-homogeneous, with a generation of turbulent kinetic energy (TKE). In the middle zone, the energy cascade phenomenon transfers the energy to smaller scales, approaching a condition of local isotropy and near-homogeneity. Farther downstream in the third region, the flow is completely isotropic and homogeneous and the smaller scales dissipate the energy through viscous effects. The TKE can be computed by means of the r.m.s. fluctuating velocity components as:

$$k_t = \frac{1}{2} \left(u_{rms}^2 + v_{rms}^2 + w_{rms}^2 \right). \tag{4.5}$$

Exploiting the local mean absolute velocity $|\mathrm{U}|$, we can write the turbulence intensity as:

$$T_q = \frac{\sqrt{\frac{2}{3} k_t}}{|\mathrm{U}|}. \tag{4.6}$$

4.2.2 Homogeneous and isotropic turbulence

Batchelor [22] defines the homogeneous and isotropic turbulence (HIT) as turbulence with the same probability density functions (PDFs) of the different fluctuating velocity components. In general, HIT has the characteristic of having the same statistical properties in each direction and each spatial position. Thus, it has been found a turbulent flow to be nearly homogeneous and isotropic when the PDFs have a Gaussian distribution [23]. In order to have a normal distribution of a statistical quantity α, the skewness of that quantity can be defined as:

$$S_k(\alpha) = \frac{\langle \alpha^3 \rangle}{\langle \alpha^2 \rangle^{3/2}} \approx 0, \tag{4.7}$$

and the kurtosis, or flatness as:

$$K_r(\alpha) = \frac{\langle \alpha^4 \rangle}{\langle \alpha^2 \rangle^2} \approx 3. \tag{4.8}$$

Hearst [23] studied the evolution of these two quantities to infer the homogeneity and isotropy of a flow past a fractal grid. He found that $S_k(u_{rms}) \approx S_k(v_{rms}) \approx 0$, whereas $K_r(u_{rms}) \approx K_r(v_{rms}) \approx 2.95$ in the HIT region. These values were confirmed by previous works on classical grids [12, 24, 25]. In the two following sections, other methods to quantify the non-homogeneity and the anisotropy of a turbulent flow are detailed.

4.2.2.1 Methods to assess non-homogeneous turbulence

Homogeneity is the property of invariance of some given quantity under spatial translations [13]. For instance, the standard deviation of the streamwise fluctuating velocity component in an homogeneous flow has the same value in two separated spatial locations, such that:

$$u_{rms}(x_1, y_1, z_1) = u_{rms}(x_2, y_2, z_2).$$

We are interested in assessing the homogeneity of the flow along the streamwise and transversal planes with respect to the flow direction. As described in [26] for a flow generated by a fractal turbulence grid, a way to evaluate the transverse homogeneity level is to look at the streamwise mean velocity U along the transversal y axis, and at the turbulent intensity $T_q = \langle q^2 \rangle^{1/2} / (3^{1/2} |\mathrm{U}|)$, where $\langle q^2 \rangle = u_{rms}^2 + v_{rms}^2 + w_{rms}^2$ is twice the TKE k_t. These quantities, normalized over each profile by their mean, should be ideally equal to 1 for transversally homogeneous flows; nonetheless, in experimental works intended to generate homogeneous turbulence, variations of 1% for the mean velocity and of 2% for the turbulent intensity are accepted to define the flow as homogeneous (see, for instance, Figure 4 in [24]). To characterize the flow streamwise and transverse homogeneity character, it is possible [23] to show the absence of TKE transfer among the transversal fluctuating components. For this to happen the flow has to be shearless and thus, the ratio w_{rms}^2 / v_{rms}^2 must be ideally equal to 1.

4.2.2.2 Methods to assess anisotropic turbulence

Turbulent flows can be considered isotropic if their statistical point-wise properties are invariant to any axial rotation. The straightforward consequence is that for isotropic turbulence, the standard deviations of the fluctuating velocities are equal to each others:

$$u_{rms}(\mathbf{x}) = v_{rms}(\mathbf{x}) = w_{rms}(\mathbf{x}).$$

Thus, one way to establish the anisotropic character of a given turbulent flow is to look at the ratios of these quantities (u_{rms}/v_{rms}, u_{rms}/w_{rms}, and v_{rms}/w_{rms}) along the downstream direction: a value close to 1 results in a fully isotropic flow. Nevertheless, according to Comte-Bellot and Corrsin [27], typical values in the range of 1.2 to 1.4 for u_{rms}/v_{rms} are accepted to infer the flow isotropy. In classical grid studies [13], to further improve the flow isotropic behavior that can be obtained experimentally, it is possible to add a flow contraction of rate $C \approx 1.27$. This is done in order to reduce the streamwise fluctuating velocity, always the largest because it is fed by the average flow around the bars of the grid, by stretching the vortical structures along the flow direction and thus increasing the crosswise fluctuating components [13].

Another useful tool to get a better insight on the typology of turbulence dominating a particular flow region is the invariant map, also called Lumley Triangle [28, 29]. In order to observe isotropic turbulence, the velocity fluctuations must be invariant to the rotation of the reference axes; in other words, the Reynolds stresses defined as $(\sigma_x, \sigma_y, \sigma_z) = \rho\left(\overline{u'u'}, \overline{v'v'}, \overline{w'w'}\right)$, with ρ being the air density, have to be identical $(\sigma_x = \sigma_y = \sigma_z)$. The non-dimensional form of the anisotropy stress tensor can be defined as:

$$a_{ij} = \frac{\overline{u_i' u_j'}}{2k_t} - \frac{1}{3}\delta_{ij}, \tag{4.9}$$

where δ_{ij} represents the Kronecker delta, whereas k_t is the TKE which is linked to the trace of the Reynolds' stress tensor as $k_t = \overline{u_i' u_i'}/2$. The characteristic equation for any second order symmetric tensor can be written exploiting the Cayley-Hamilton theorem [30]:

$$\sigma^3 - \mathrm{I}\sigma^2 + \mathrm{II}\sigma - \mathrm{III} = 0, \tag{4.10}$$

with σ as the principal stress, whereas I, II, and III are respectively the first, second, and third invariants of the tensor. These are defined for an incompressible flow as:

$$\begin{aligned} \mathrm{I} &= a_{kk} = 0, \\ \mathrm{II} &= a_{ij}a_{ji}/2 = \lambda_1^2 + \lambda_1\lambda_2 + \lambda_2^2, \\ \mathrm{III} &= a_{ij}a_{jn}a_{ni}/3 = -\lambda_1\lambda_2\left(\lambda_1 + \lambda_2\right), \end{aligned} \tag{4.11}$$

where the eigenvalues of the characteristic equation 4.10 are defined as:

$$\lambda_i = \frac{\sigma_i}{2k_t} - \frac{1}{3}, \tag{4.12}$$

exploiting the equality $\lambda_1 + \lambda_2 + \lambda_3 = 0$.

It is possible to generate invariant maps using the eigenvalues or, as in Figure 4.2 and in the following work, to build the invariant map using II and III as coordinates. There are three limiting states for those eigenvalues which define the corners of the invariant maps. Those states are [31]:

- One component or rod-like turbulence: the fluctuations only exist along one axis. In this case the invariants are $\mathrm{II} = -\frac{2}{27}$ and $\mathrm{III} = -\frac{1}{3}$, whereas the eigenvalues are $\lambda_i = [\frac{2}{3}, -\frac{1}{3}, -\frac{1}{3}]$.
- Two components axisymmetric or disk-like turbulence: the fluctuations along those two directions have the same magnitude. The invariants are $\mathrm{II} = \frac{1}{12}$ and $\mathrm{III} = -\frac{1}{108}$, whilst the eigenvalues are $\lambda_i = [\frac{1}{6}, \frac{1}{6}, -\frac{1}{3}]$.
- Isotropic or spherical: fluctuations exist on the 3 directions with the same magnitude. All the three eigenvalues λ_i are equal to zero, as well as $\mathrm{II} = \mathrm{III} = 0$.

The lines that connect the previous limit cases present behaviors that are in between the ones listed above:

- Two-component turbulence, occurring when the invariants respect the equality $\mathrm{II} = 3\big(\frac{1}{27} + \mathrm{III}\big)$, whereas the eigenvalues $\lambda_1 + \lambda_3 = \frac{1}{3}$ and $\lambda_2 = -\frac{1}{3}$.
- Axisymmetric contraction (oblate spheroid), occurring when the invariants are related by $\frac{\mathrm{II}}{3} = \big(-\frac{\mathrm{III}}{2}\big)^{2/3}$, while the eigenvalues are $-\frac{1}{3} < \lambda_1 < 0$ and $0 < \lambda_2 = \lambda_3 < \frac{1}{6}$.
- Axisymmetric expansion (prolate spheroid), occurring when the invariants are related by $\frac{\mathrm{II}}{3} = \big(\frac{\mathrm{III}}{2}\big)^{2/3}$, while the eigenvalues are $0 < \lambda_1 < \frac{1}{3}$ and $-\frac{1}{6} < \lambda_2 = \lambda_3 < 0$.

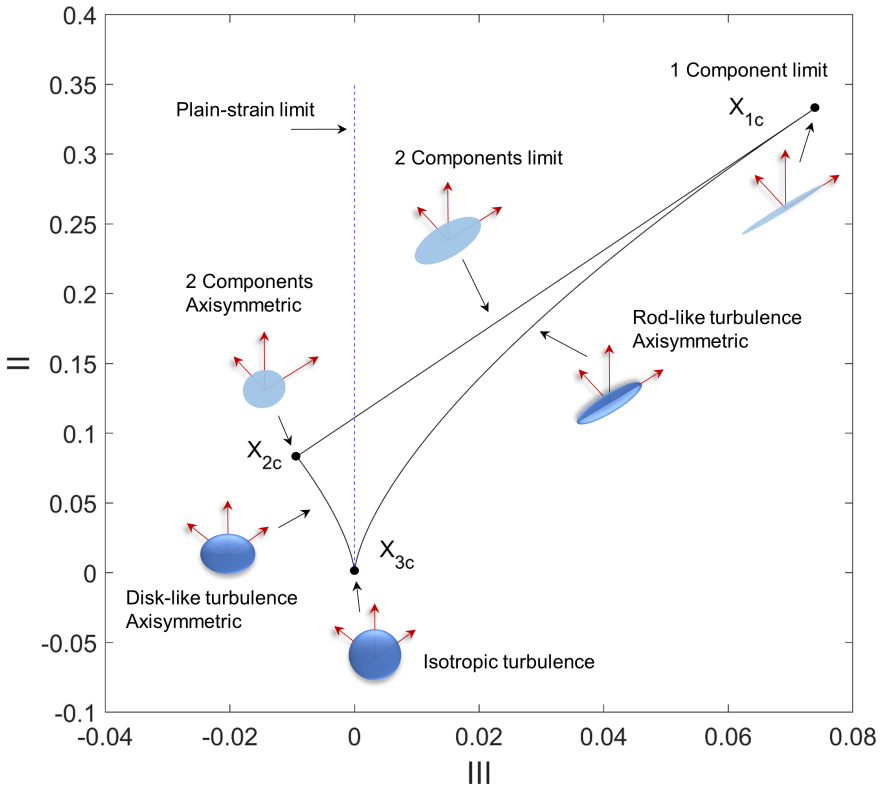

Figure 4.2: Lumley triangle map description. The realizable turbulence states are represented as a function of the invariants II and III.

4.2.3 Turbulent velocity spectrum

To compare with analytical velocity-fluctuations models, as stated in the objectives of Section 4.1.1, we have first to calculate the two-wavenumbers turbulence spectrum. To do that, as proposed in [14], we calculate the spatial 2D-FFT of the velocity field and multiply by its complex conjugate. After that, we obtain the two-dimensional power spectral density by normalizing the result with respect to the spatial resolution. Similar procedures can also be found in [32, 33].

4.2.3.1 Integral length scales

We define the two-points correlation function calculated over a velocity field as [17, 34]:

$$R_{\alpha\alpha}(r_1, r_2) = \frac{\langle \alpha(x,y)\alpha(x+r_1, y+r_2)\rangle}{\langle \alpha(x,y)^2\rangle}, \tag{4.13}$$

where $\alpha = u', v'$, whereas r_1 and r_2 respectively indicate a longitudinal and transversal separations. The integral length scales roughly measure the distances at which the fluctuating velocities are correlated [35]. In general, we can define the integral length scale as:

$$\Lambda_{\alpha,j} = \int_0^{r_0} R_{\alpha\alpha}(r_j)dr, \tag{4.14}$$

with $j = 1, 2$, whereas r_0 is the first zero crossing of the correlation function. Since the extent of the integration is limited in PIV by the size of the velocity field image, we can use the conventional estimate of integrating over a distance at which the correlation function drops below $1/\mathrm{e}^2$, which is consistent with exponential decay and was similarly used by Carter and Coletti [36] (e is the Euler's number).

4.2.3.2 von Kármán spectrum model

The von Kármán spectrum model is commonly used in literature assuming homogeneous and isotropic turbulence [14, 16] to model the turbulent velocity spectrum and it can be written as:

$$\Phi_{ww}\left(K_x, K_y\right) = \frac{4}{9\pi}\frac{u_{rms}^2}{k_e^2}\frac{\bar{K_x}^2 + \bar{K_y}^2}{\left(1 + \bar{K_x}^2 + \bar{K_y}^2\right)^{7/3}}, \tag{4.15}$$

where $\bar{K_x} = K_x/k_e$ and $\bar{K_y} = K_y/k_e$ are, respectively, the dimensionless streamwise wavenumber and the dimensionless crosswise wavenumber. The average wavenumber k_e of the energy-containing eddies is defined as:

$$k_e = \frac{\sqrt{\pi}}{\Lambda}\frac{\Gamma(5/6)}{\Gamma(1/3)}, \tag{4.16}$$

where Λ, in isotropic conditions is equal to $\Lambda_{u,1}$, which is the streamwise integral length scale retrieved integrating the autocorrelation function of u in the x direction.

4.3 Experimental S-PIV campaign

Particle image velocimetry (PIV) is a non-intrusive technique able to provide instantaneous velocity fields over a plane immersed in a flow [37]. Unlike single-point measurement techniques, PIV offers the possibility of investigating continuous spatial structures of the velocity field. Nevertheless, standard PIV only accounts for in-plane velocity components exploiting the projection of the velocity vector and, thus, losing the out-of-plane velocity component information [38]. Especially for three-dimensional flows, planar PIV is affected by an unrecoverable perspective projection error due to the fact that the particle will not just move in a plane parallel to the light sheet, having a velocity component perpendicular to the light-sheet plane. In this work, we do not have *a priori* information about the three-dimensionality of the velocity flow features past the heat exchanger; thus, stereoscopic PIV (or S-PIV) [37–40] is utilized because it yields the three velocity components. This is obtained by exploiting a system based on a pair of cameras that obliquely view the same planar area in the flow region of interest. The second reason that motivates this choice is the two-dimensional turbulent spectrum study, carried out in Section 4.5, that needs the calculation of the 3 velocity components. In the following paragraphs, we discuss the implementation of a stereoscopic PIV setup in the ALCOVES laboratory at VKI (described in Chapter 3), giving details on the used equipment, the experimental campaign phases, and the treatment of the uncertainty.

4.3.1 Radiator and FOV locations

The radiator has been installed on the partition wall, as shown in Figure 4.3 (a), and the airflow provided by the extraction fan has been set to a constant value of $q_m = 0.7\,\mathrm{kg\,s^{-1}}$, corresponding to the nominal flow condition utilized in Chapter 3. The downstream side of the radiator has been painted in matt black to reduce the PIV laser-light reflection. As shown in Figure 4.4 (a),

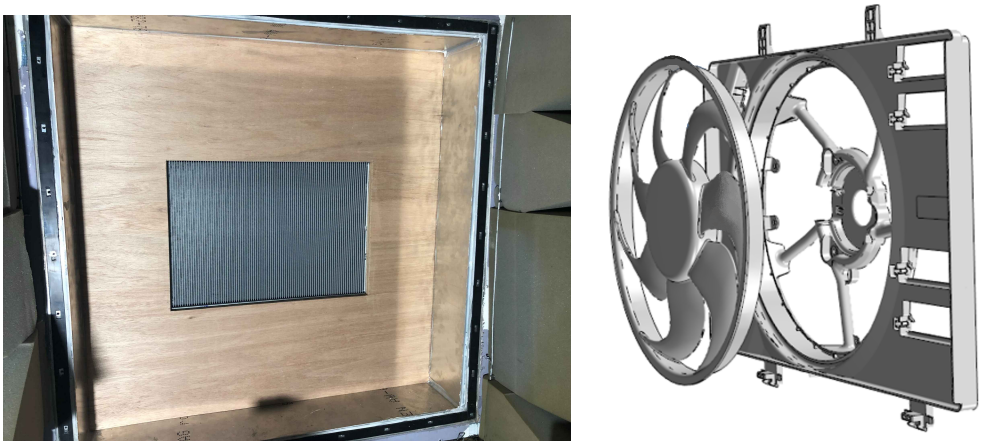

(a) (b)

Figure 4.3: (a) Upstream side of the heat exchanger installed on the partition wall of the ALCOVES laboratory. (b) The circular shape of the fan shroud.

the cooling pipes and the fins are periodically arranged and can be approximated by a grid of isosceles triangles, repeatedly displayed over the radiator surface. The mesh size is defined to be equal to the hydraulic diameter [41] of these triangles as $M = 4A/P = 1.786\,\mathrm{mm}$, where A is the triangle area and P its perimeter. Further specifications of the radiator geometry are given in

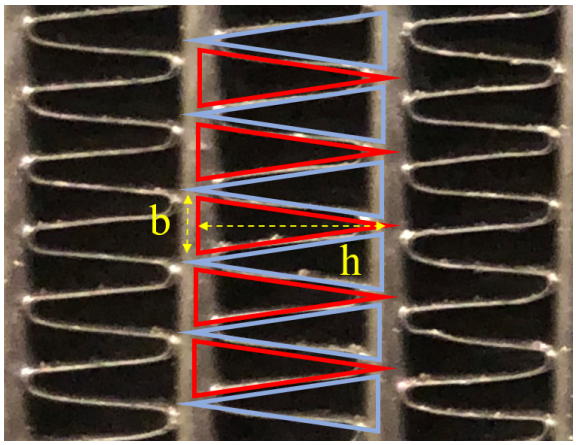

(a)

Number of coolant pipes	92
Coolant pipe width	1.5 mm
Coolant pipe height	385 mm
Coolant pipe depth	20 mm
Space between pipes	4.5 mm
Fin thickness	0.12 mm
Space between fins	2.5 mm
Heat exchanger width	558 mm
Heat exchanger height	385 mm
Heat exchanger depth	20 mm

(b)

Figure 4.4 & Table 4.1: (a) Close-up view of the radiator grid; the mesh-size is defined as the hydraulic diameter of the isosceles triangles of base b and height h. (b) Radiator geometrical parameters.

Table 4.4 (b). In real operating conditions, the flow past the radiator is accelerated through the circular hole of the fan shroud, depicted in Figure 4.3 (b), and this might have an influence on the flow turbulent features before impinging on the blades. In order to replicate this acceleration effect, a circularly-holed wood panel, with a radius of $0.17\,\mathrm{m}$, has been fabricated to have the same open area as the fan shroud. It has been placed at the same downstream distance of $3\,\mathrm{cm}$ from the heat-exchanger outlet as in the cooling module application. Hereafter, two configurations

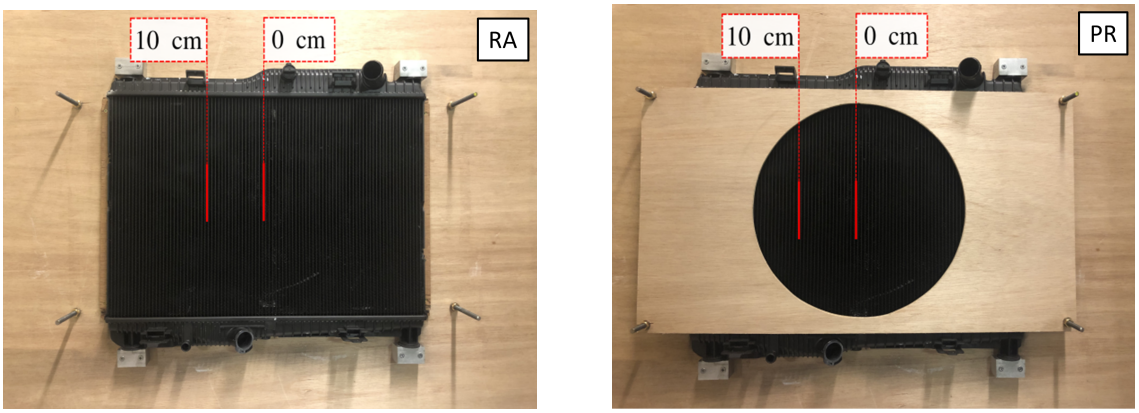

(a) (b)

Figure 4.5: Two different configurations for the cases considered: (a) Radiator alone (RA); (b) Radiator with circularly-holed panel (PR). In each case, the FOV is located in the middle between two following cooling pipes.

are investigated: the radiator-alone (RA) one, shown in Figure 4.5 (a), and the panel-and-radiator (PR) in Figure 4.5 (b). For each configuration, two vertical planes aligned with the cooling pipes are investigated. The first is located at the center of the circular opening of the wood panel, at $z = 0\,\mathrm{cm}$. The second vertical plane has been chosen at $z = 10\,\mathrm{cm}$ from the first plane, namely the maximum distance offering view access for the cameras. In each case, the FOV is located in the middle between two following cooling pipes. We remark that due to the wood panel presence, it would be geometrically impossible to investigate these flow regions with a planar PIV approach, where the camera needs to be located perpendicularly to the flow stream.

4.3.2 Stereo-PIV setup

The S-PIV setup data is acquired with a LaVision PIV system [42] composed of a LaVision 7.2 software installed on a computer with an integrated Programmable Timing Unit (PTU 9). Two Imager Intense digital camera models, shown in Figure 4.6 (a), are utilized to perform double frame acquisitions. The recordings have an image resolution of $1376 \times 1040\,\mathrm{px}^2$ and a pixel size of $6.45\,\mu\mathrm{m}$, with digitalization or gray-scale of 12 bits. Both cameras are equipped with $105\,\mathrm{mm}$ focal length and maximum aperture $f/2.8$ Nikon Micro-NIKKOR objectives, illustrated in Figure 4.6 (b). The used aperture is $f_{\#} = 5.6$, in order to have a shallow depth of focus and to avoid light reflection on the radiator. Perspective-control adapters are used to obtain the Scheimpflug condition [43–45] needed to have the focus all over the FOV. The used laser system is a double cavity Nd:YAG laser with an ICE450 power supply and synchronizer integrated within the computer. The sampling frequency during the acquisition is set to $5\,\mathrm{Hz}$, yielding uncorrelated instantaneous velocity fields. The optical arrangement generating the laser sheet is composed of a spherical lens with a $975\,\mathrm{mm}$ focal length and a cylindrical one with an opening angle of $11.85°$. In addition, a prism of $60\,\mathrm{mm}$ is employed to redirect the laser plane toward the region of interest. As depicted in Figure 4.7[2], a structure made of aluminum Bosch profiles is designed and exploited to hold in place the laser generator and the cameras. This setup made it possible to move

[2]The cameras, laser generator, Scheimpflug adapters, and objectives are unofficial CAD representations drawn with the 3D design software *Sketchup*.

(a) (b)

Figure 4.6: (a) LaVision Imager Intense, (b) Nikon Micro-NIKKOR 105 mm *lens.*

every piece jointly, without having to realign the optical equipment when changing the FOV. The

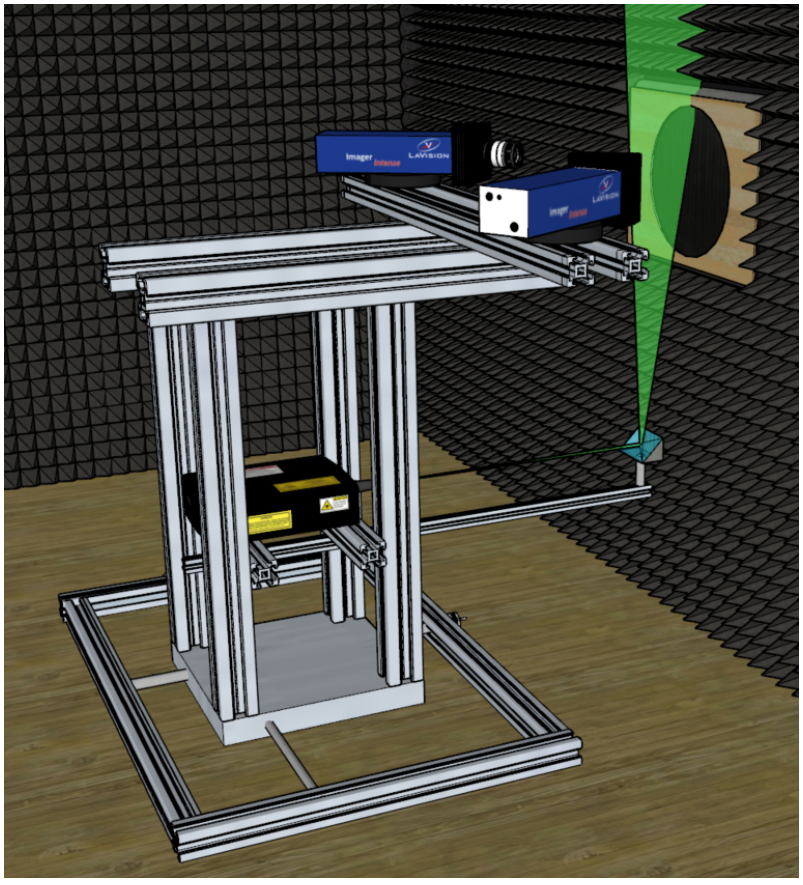

Figure 4.7: 3D representation of the S-PIV Setup inside the ALCOVES anechoic chamber.

seeding particles are produced by an alcohol-based Antari Z-1200 fog generator that, exploiting an upstream buffering area, provides a homogeneous seeding with quasi-constant concentration at the radiator inlet with 1-2 µm mean particle diameter [46, 47]. The alcohol-based smoke has

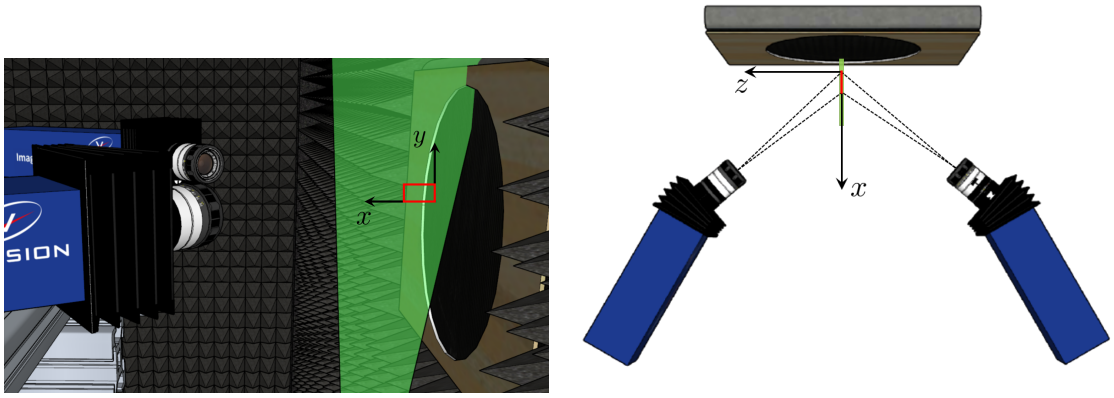

(a) (b)

Figure 4.8: (a) FOV closeup representation over the $x-y$ plane. (b) Top-view sketch of the setup for the $z = 0\,\mathrm{cm}$ configuration.

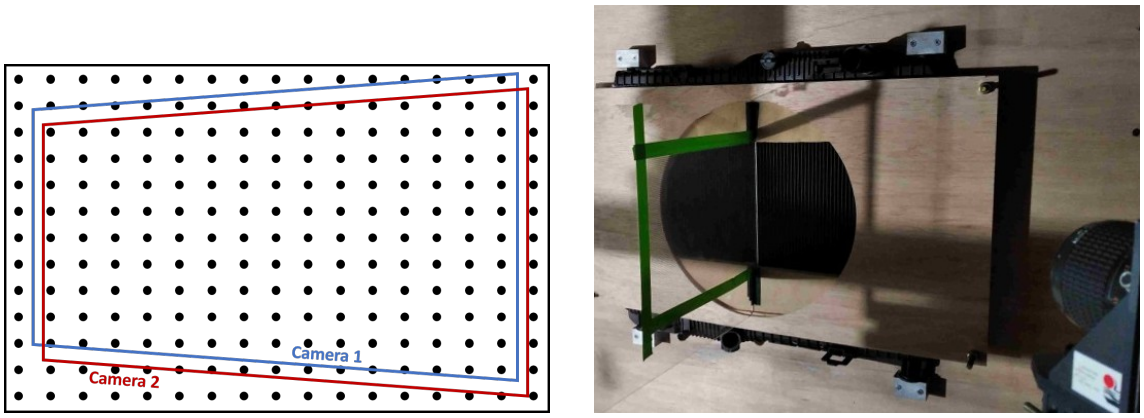

(a) (b)

Figure 4.9: (a) Views of the calibration plate from Camera 1 and Camera 2. (b) Calibration plate installed in the ALCOVES lab.

been preferred to the oil-based one in order to avoid residues within the radiator onto the fins and louvers.

4.3.3 Image acquisition and processing

Four sets of $N_{im} = 900$ uncorrelated images for each of the 4 cases, described in 4.3.1, are acquired. The time interval ΔT of the double-frame exposure is fixed to have about 8 pixels displacement on average. Figures 4.8,(b) show two closeups of the FOV, respectively, from lateral and top views. The FOV is chosen to have a size of $18 \times 34\,\mathrm{mm}^2$. The FOVs are necessarily located $7\,\mathrm{mm}$ downstream from the heat exchanger along the x-axis to avoid laser-light reflections from the metallic grid.

Davis 8.4 calibration procedure [48] of the two cameras has been implemented, with no need to measure distances or angles. This step is crucial for two reasons: to determine the pixel-to-

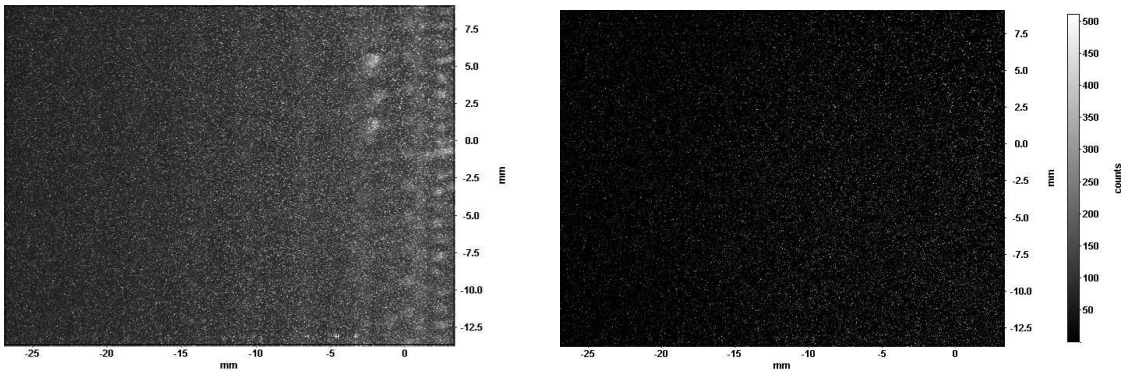

(a) (b)

Figure 4.10: Raw image example, where the radiator outlet is on the right: (a) before background removal, (b) after background removal.

mm image scale and to allow the stereoscopic reconstruction of the out-of-plane component. In Figure 4.9a, a calibration plate with an array of black circles is mounted perpendicular to the radiator on a Plexiglas panel to enable both cameras, located on opposite sides of the panel, to focus on the calibration plate (see Figure 4.9b). Thanks to a sliding mechanism of cranks, the S-PIV setup is designed to translate along the Z-axis (refer to Figure 4.8). This ensured that three views could be acquired, as required by the calibration procedure, each one separated by $0.5\,\mathrm{mm}$ from the other (at $z = -0.5, 0,$ and $0.5\,\mathrm{mm}$, respectively), avoiding moving the plate during the calibration procedure. Although small rotational errors can be corrected by the self-calibration procedure (see Section 4.4), care is taken to ensure that the plane of the plate remains perpendicular to the light sheet. A 3^{rd} order polynomial fitting is used to fit the marks found in each image. The average deviation to marks obtained is quite good, about $0.3\,\mathrm{px}$ for each camera. The obtained digital resolution is $45.25\,\mathrm{px\,mm^{-1}}$. As one can observe in Figure 4.10 (a), the traces of the radiator fins can be noticed in the background, due to the laser-sheet reflections. Hence, the first image-processing action is to clean up the raw images by removing their average. This procedure is quite effective because the fins do not move with the flow: the background-less image can be seen in Figure 4.10 (b). Afterward, the images are processed with a multi-pass cross-correlation technique [49], with $24\,\mathrm{px} \times 24\,\mathrm{px}$ as the interrogation window size of the final step and a 50% of overlap. Hence, we achieve a spatial resolution of $0.266\,\mathrm{mm} \times 0.266\,\mathrm{mm}$, with a vector spacing of $0.133\,\mathrm{mm} \times 0.133\,\mathrm{mm}$. An average of 6 to 8 particles per interrogation window is preserved, as suggested in [50].

4.4 Uncertainty quantification

In stereo-PIV, uncertainty quantification is still a subject of research and development, as shown by the recent work of Sciacchitano [51]. We can address the study first by distinguishing systematic from random sources of uncertainty. In stereo-PIV, the systematic uncertainties to consider are typically the peak locking, the calibration errors, and the particle-slip error. The random uncertainties are dominated by the planar-PIV uncertainty and the errors due to the convergence of the statistical quantities.

4.4.1 Peak-locking uncertainty

Peak locking is a bias error source in PIV [52] and is the tendency of the measured particle displacement and location to be biased toward integer values. It occurs typically when the produced particle images have less than one-pixel diameter [53]. To keep this error source to a minimal level, the particles have 2-3 px diameter in this work. The negligible effect of the peak lock is further confirmed by keeping the peak-lock indicator below 0.1, as suggested in the Davis 8.4 manual [42].

4.4.2 Calibration uncertainty

As discussed in Section 4.3.3, in stereo-PIV the correctness of the calibration procedure is an essential prerequisite in order to properly reconstruct the three velocity components. A major difficulty of this procedure is to perfectly align the calibration plate and the laser sheet. In order to ensure this, the so-called self-calibration method has been developed by Wieneke [54] and utilized here. This method has proven to accurately calculate the mapping functions even in cases when the calibration plate is quite far away or tilted relative to the light sheet. Although in the present case the calibration procedure shows to be already accurate, the self-calibration scheme is advisable in any case to check the calibration and improve its accuracy [54]. This self-calibration technique consists of computing a disparity vector map on the real particle images by cross-correlating the images from cameras 1 and 2 in order to estimate if the laser-sheet plane coincides with the calibration plate. This allows eliminating potential bias errors in the vector calculation due to laser-sheet misalignment. Once the scheme is applied within the Davis 8.4 environment, the negligible remaining disparity of 0.05 mm is achieved in all datasets.

4.4.3 Particle-slip uncertainty

Particle-slip error is the systematic tendency of the particle to experience a certain lag with respect to the velocity changes of the flow [55]. The effectiveness of a seeding particle to behave as a fluid particle is determined by its smallness and density in relation to the fluid under investigation. Air particle tracers are usually much heavier than air itself and their Reynolds number is low. A reasonable simplification for high-density ratios is to consider only the effect of viscosity and inertia in the particle equation of motion [56]. In such a case, if one wants to study the harmonic response of a spherical particle subjected to the flow oscillations, the ratio of amplitude oscillation can be modeled:

$$\frac{U_p}{U_f} = \frac{1}{\sqrt{1 + 4\pi^2 {S_t}^2}}, \tag{4.17}$$

where U_p is the particle velocity, U_f is the flow velocity, whereas $S_t = \tau_v / t_c$ is the Stokes number, t_c being the characteristic time over which the flow experiences variations. The time lag τ_v represents an estimation of the time that the particle needs to adapt its velocity to a sudden change of the flow velocity. It can be written as:

$$\tau_v = \frac{\rho_p d_p^2}{18\mu},$$

where ρ_p and d_p are respectively, the density and the diameter of the particle, whereas μ is the air viscosity coefficient. We can define the relative error estimation as:

$$E_r(U_p/U_f) = \frac{U_p - U_f}{U_f}, \tag{4.18}$$

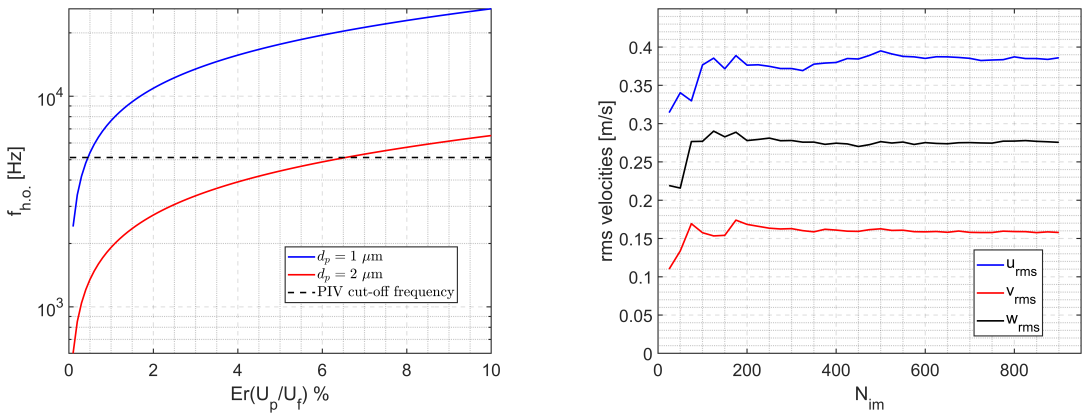

Figure 4.11: (a) Harmonic-oscillating frequency as a function of the modulation error for particles of 1 *and* $2\,\mu\mathrm{m}$ *diameters. (b) Statistical convergence of the turbulent root-mean-square velocity components against the number of images.*

which can be related through Eq. (4.17) to the harmonic-oscillating frequency $f_{h.o.} = S_t/\tau_v$. This quantity is shown in Figure 4.11 (a) as a function of the relative error $E_r(U_p/U_f)$ for two-particle diameters of $1\,\mu\mathrm{m}$ and $2\,\mu\mathrm{m}$. In this work, we achieve a spatial resolution of $0.266\,\mathrm{mm}$. If this is transformed into the frequency domain by using Taylor's hypothesis, with U_c as the convective velocity, the maximum measured frequency according to the Nyqvist criteria is $5122\,\mathrm{Hz}$. As a consequence, for $1\,\mu\mathrm{m}$-diameter particles, we have 1% bias error at the cut-off frequency due to the particle-slip phenomenon, whereas 6.25% bias error is estimated for $2\,\mu\mathrm{m}$-diameter particles. These are reasonably acceptable uncertainty values for this application, considering that the particles have an average diameter of $1\,\mu\mathrm{m}$.

4.4.4 Planar-PIV uncertainty

The systematic uncertainties previously discussed are proved to be negligible, and so the instantaneous quantities carried out with stereo-PIV are more sensitive to the planar uncertainty estimates [57]. The built-in direct *a posteriori* method implemented in Davis 8.4 and utilized in this work for planar PIV uncertainty estimation is the so-called Correlation Statistics method, developed by Wieneke [58]. Exploiting the reached convergence of the multi-pass PIV algorithm [59], this method evaluates the contribution of each pixel to the asymmetry of the correlation peak, and associates such asymmetry with the uncertainty of the measured displacement [51]. Further details of the implementation and derivation of the method can be found in the original paper [58]. Hence, the instantaneous planar-PIV uncertainties are calculated and propagated in order to obtain the planar-PIV uncertainties of the mean velocity components. This is carried out by dividing the uncertainties by $\sqrt{N_{im}}$ [60]. These uncertainties correspond to $\pm 0.5\%U$, $\pm 0.4\%V$, and $\pm 1.9\%W$.

4.4.5 Statistical convergence uncertainty

For statistical quantities such as the mean velocity components, an additional part of random uncertainty is due to the lack of statistical convergence caused by the finite number of images. The

mean flow velocity estimated from N_{im} images can be written, for instance for the streamwise component, as $U \pm z_c \sigma_U / \sqrt{N_{im}}$ [61]. Here, σ_U is the standard deviation of the streamwise component, whilst $z_c = 1.96$ is the confidence critical value in order to have a confidence level of 95% [62]. Thus, in this work, the uncertainties due to the finite sample size associated with the mean velocities are $\pm 0.8\% U$, $\pm 7.8\% V$, and $\pm 3.6\% W$. Especially for the crosswise components, the relatively high uncertainties can be explained by the fact that the actual flow fluctuations are comparable with the mean component value in amplitude. Typically, when this happens, the uncertainty of statistical quantities is dominated by the finite sample size rather than the random instantaneous uncertainties [60]. Nevertheless, we can look at the peak-to-peak variation of the velocity fluctuations r.m.s. in Figure 4.11 (b), where these are plotted against the number of samples. For illustrative purposes, only one representative point in a set of images is used to show convergence of r.m.s. velocities. Utilizing 600 samples instead of 900 leads to a convergence error always lower than 1.5%. Therefore, the available sample size of 900 images is large enough to have sufficiently converged statistical quantities.

4.5 Aerodynamic results

In this section, we discuss the aerodynamic results for the 4 FOVs analyzed, respectively, for the radiator-alone (RA) and panel-and-radiator (PR) cases, as defined in Figure 4.5. A reference velocity $U_0 = 2.715\,\mathrm{m\,s^{-1}}$ is used in the following to scale the velocity and the TKE fields. This has been defined as $U_0 = \frac{q_m}{\rho A_0}$, where $A_0 = 0.215\,\mathrm{m^2}$ is the area of the heat exchanger, whereas the airflow is equal to $q_m = 0.7\,\mathrm{kg\,s^{-1}}$, and the density $\rho = 1.2\,\mathrm{m^3\,kg^{-1}}$.

4.5.1 Isocontours of mean quantities

Figure 4.12 shows the average streamwise velocity fields for the 4 analyzed FOVs, normalized with respect to the reference velocity U_0. The stream moves from left to right and the radiator outlet is located at $x/M \approx -3.9$. The circularly-holed panel is located at a downstream distance of $x/M = 12$, i.e., in the same position in which the fan is located in the complete cooling system. In all FOVs, one can see the jets generated by the radiator grid fins downstream. The acceleration of the airflow in the streamwise direction can be observed in the PR cases, due to the presence of the panel, which narrows the area through which the flow is forced to pass. In all the studied cases, the streamwise velocity is always positive, so we can rule out large recirculation areas where the flow returns to the radiator. We can observe that the jets are affected by the shape of the radiator fins which, under real application conditions, may have a slightly modified geometry due to wear and debris of the working environment. The in-plane crosswise velocity fields are shown in Figure 4.13. The order of magnitude of this average velocity is in all the studied cases much lower than the average streamwise velocity, remaining below $7.5\% U$. Indeed, the flow in this direction seems to oscillate around the null value. However, in the case PR $z = 10\,\mathrm{cm}$ a general pattern can be discerned as the presence of the holed panel at distance $x/M = 12$ causes a rapid change in the vertical direction of V. Fin jets are also present in the mean fields of the out-of-plane crosswise velocity, as illustrated in Figure 4.14. Generally, W also exhibits values rather lower than those of the streamwise velocity and thus we can conclude that the mean velocity field generated by the radiator is not highly three-dimensional, preserving a strong streamwise momentum, even immediately after the radiator exit. However, the PR $z = 10\,\mathrm{cm}$ case is an exception since the presence of the holed panel deflects the flow toward the center of the radiator, with a velocity W reaching about 25% of U. This acceleration, as well as for the other two

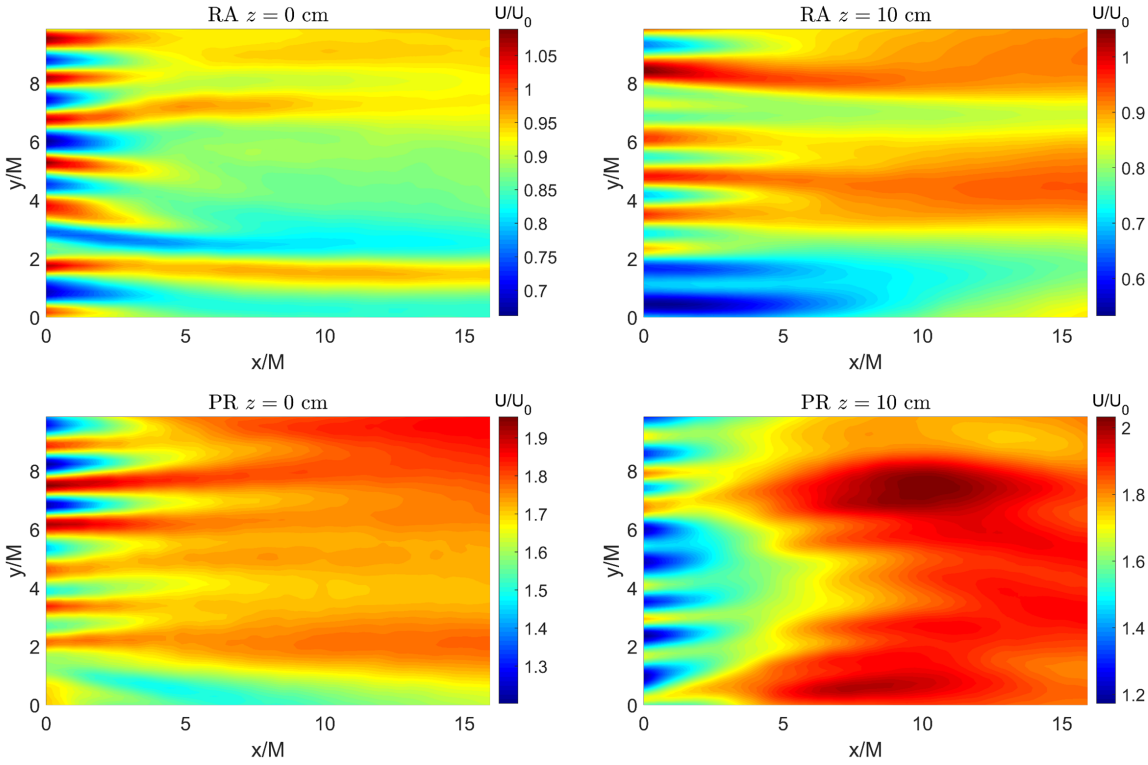

Figure 4.12: Streamwise average velocity fields were obtained with stereo-PIV for the radiator-alone (RA) and the panel-and-radiator (PR) cases. The fan would be located at $x/M = 12$.

average velocities, appears to cancel out the fin jets. It is interesting to observe in Figure 4.15 that the areas of turbulent kinetic energy production appear at the fin jets where the velocity is greatest. Thereafter, the TKE is rapidly attenuated. Finally, it can be noticed that the cases with the panel present values one order of magnitude higher than the cases with the radiator alone. This indicates a correlation between higher TKE production and higher flow velocity.

4.5.2 Mean velocity and turbulence intensity horizontal cuts

The mean (time-averaged) streamwise velocity profiles of the investigated FOVs are compared in Figure 4.16 (a). In the dashed line the horizontal cuts are shown, all of them obtained at $y/M = 5$. The horizontal velocity profiles, averaged along the y-axis, are shown in solid lines. It can be seen that the curves for the two cases without the holed panel, present a linear trend with a slight slope tending to the reference velocity value U_0 farther downstream. The cases with the panel, on the other hand, present a higher average velocity, as already noted when analyzing the average velocity fields. The PR $z = 0\,\mathrm{cm}$ case, after a short acceleration, presents a slightly increasing linear trend, whereas the PR $z = 10\,\mathrm{cm}$ case is affected by the proximity of the panel, which accelerates the streamwise flow to a downstream distance equal to $x/M = 8$. Similar conclusions can be drawn by looking at the crosswise components, shown in Figures 4.16 (b) and (c). It is interesting to observe the strong acceleration that these two components undergo in the case PR $z = 10\,\mathrm{cm}$. Except for this case, the fact that V and W have values particularly close to zero justifies the relatively high uncertainty values obtained in Section 4.4. In Figure 4.16 (d), we can observe the evolution of the turbulence intensity T_q as a function of the distance from the radiator. In all the

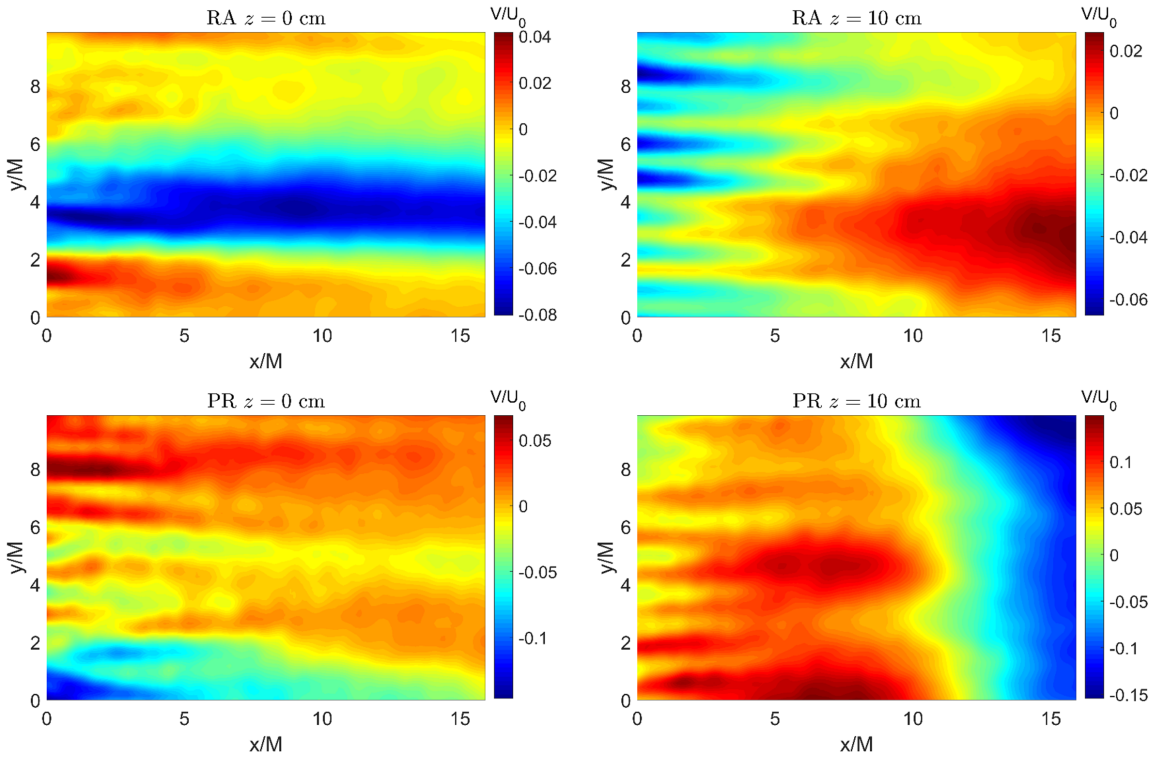

Figure 4.13: In-plane crosswise average velocity fields were obtained with stereo-PIV for the radiator-alone (RA) and the panel-and-radiator (PR) cases. The fan would be located at $x/M = 12$.

analyzed cases, the zone of maximum production is located at about $x/M = 0$. Nevertheless, the turbulence decay is very different in the four analyzed cases. This differentiates the case of turbulence produced by the radiator from that produced by classical turbulence grids, where it is instead possible to identify a power law that uniquely predicts the decay rate [21]. We can observe that at $x/M = 0$, the maximum peak of turbulence intensity production does not reach 15%. At the same time, in each analyzed case, $T_q < 6\%$ at $x/M = 12$, the position where the fan would be located. Hence, the turbulence intensity produced by the radiator does not reach the high levels found for instance in [63], and this can explain the small influence that the radiator has on the sound localization maps and noise spectra obtained in Section 3.5.4 [3].

4.5.3 Flow isotropy and homogeneity assessment

In the following paragraphs, the checks introduced in Section 4.2.2 in order to assess the flow anisotropy and non-homogeneity levels are analyzed.

4.5.3.1 Fluctuating velocity ratios evolution

In Figures 4.17 (a), (b), and (c) the ratios of velocity fluctuations as functions of downstream distance are depicted, respectively, u_{rms}/v_{rms}, u_{rms}/w_{rms}, and w_{rms}/v_{rms}. Again, the dashed lines are horizontal cuts at a height of $y/M = 5$, whereas the solid lines represent the transverse

[3] This, together with the fact that the tip-leakage noise appears to be the dominant noise mechanism characterizing the sound maps of Section 3.5.4.

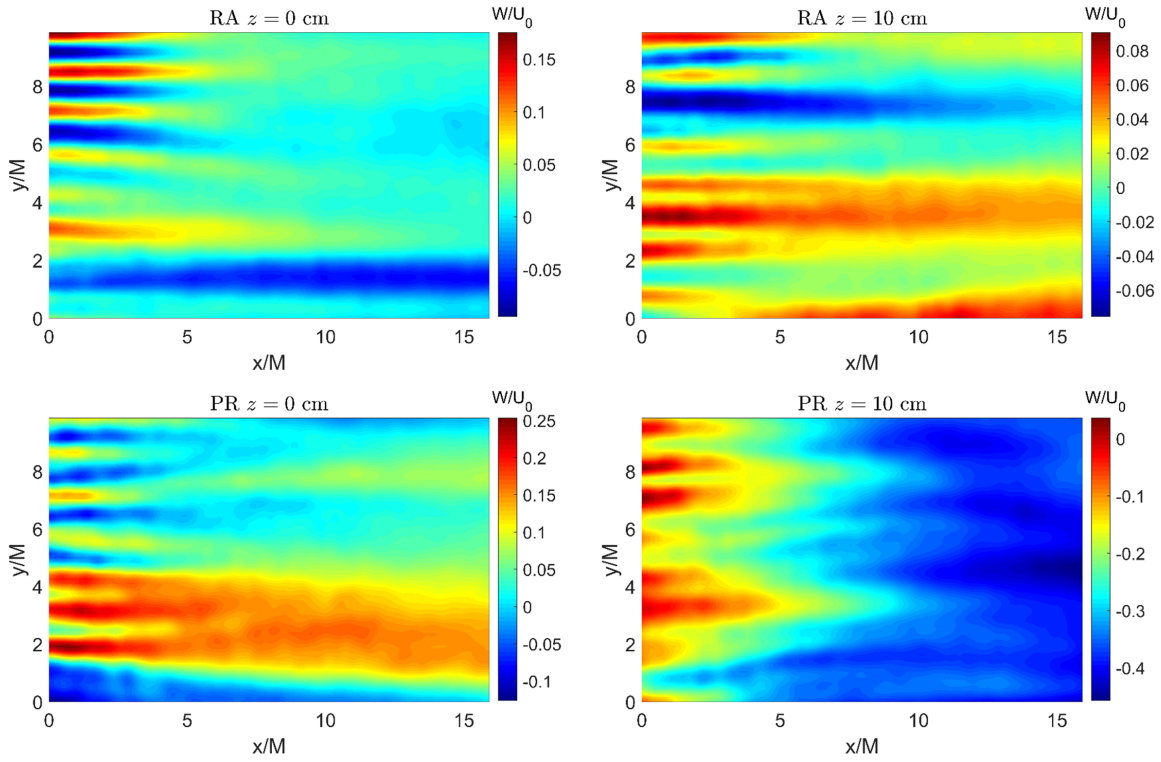

Figure 4.14: Out-of-plane crosswise average velocity fields were obtained with stereo-PIV for the 4 *studied FOVs. The fan would be located at* $x/M = 12$.

average of the horizontal cuts. Recalling that values of the u_{rms}/v_{rms} ratio in the range of 1.2 and 1.4 are sufficient in the literature to conclude on the isotropy of the flow [27], we remark a general tendency of the flow toward an isotropic behavior for all cases considered. We can see from the evolution of the ratios u_{rms}/v_{rms} and u_{rms}/w_{rms} that it is the PR cases that show values closer to unity. Indeed, a classical method of producing isotropic turbulence in the laboratory is to impose an acceleration of the flow after the turbulence grid *via* a circular contraction [21]. The case RA $z = 10\,\mathrm{cm}$ turns out to be the one furthest from the isotropy condition, reaching average values near $u_{rms}/v_{rms} \approx 1.6$. However, although an average trend toward the isotropic state is noticeable, just by looking at the unaveraged horizontal cuts, it is not possible to conclude on the achieved isotropy of the flow, as these quantities still exhibit oscillations away from the radiator outlet. Probably, the isotropy state is reached farther downstream of the radiator.

4.5.3.2 Skewness and kurtosis evolution

As a way to confirm the overall trend toward isotropy, the skewness and kurtosis of u_{rms} in the case RA $z = 0\,\mathrm{cm}$ are shown in Figures 4.17 (d). Without loss of generality, the skewness and kurtosis of the other components and for the other FOVs are not reported here since they exhibit very similar behavior to that shown in Figure 4.17 (d). To have a quasi-normal distribution of the velocity probability density function, and thus have isotropic flow behavior, $S_k(u_{rms}) = 0 \pm 1$ and $K_r(u_{rms}) = 3 \pm 1$ [64]. In the case of profiles averaged along the transverse direction, $S_k(u_{rms}) = -0.2$ and $K_r(u_{rms}) = 3.2$ in the area where the fan would be located. However, it is possible to compare the values obtained in this work with those achieved in studies with

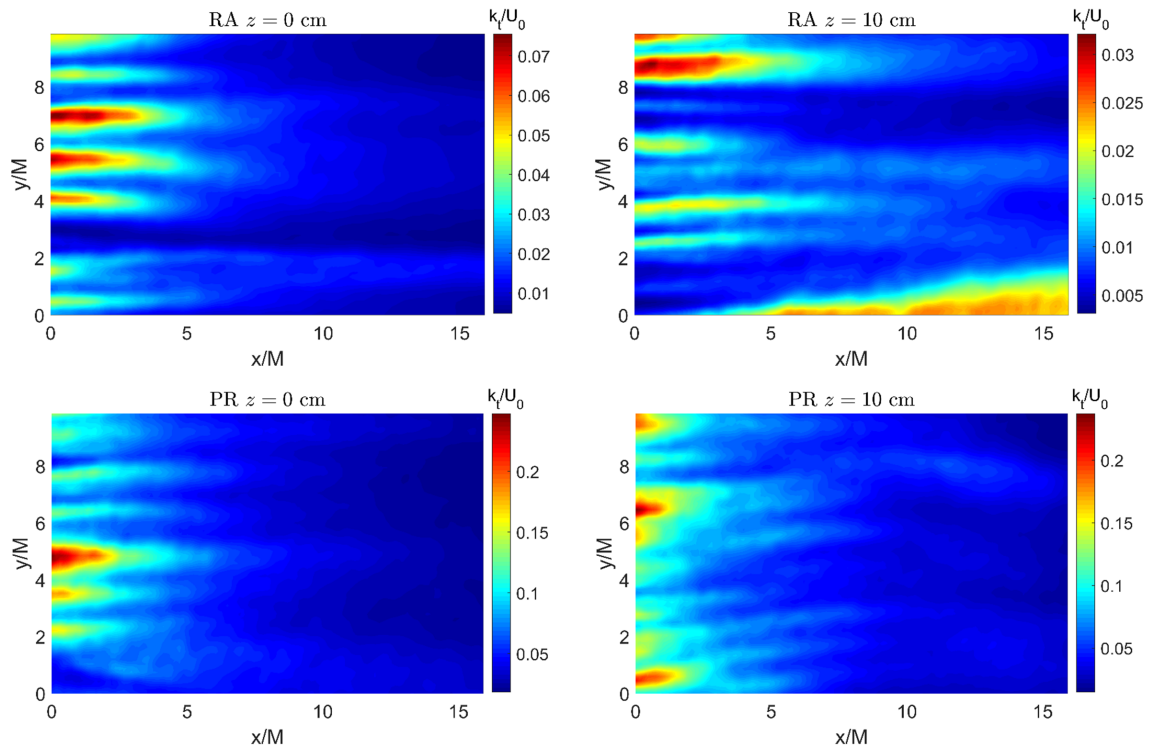

Figure 4.15: Average turbulent kinetic energy fields were obtained with stereo-PIV for the radiator-alone (RA) and the panel-and-radiator (PR) cases. The fan would be located at $x/M = 12$.

classical [12] or fractal [26] turbulence grids, where a state of full isotropic turbulence is actually attained. In the first case, values of $S_k(u_{rms}) = 0.01$ are obtained. In the second case, values of approximately $S_k(u_{rms}) = 0.02$ and $K_r(u_{rms}) = 2.95$ are reached. Hence we can once again conclude that in the 4 FOVs considered, the flow tends toward the isotropic turbulent state, without having yet fully reached it in the region where the fan inlet would be located.

4.5.3.3 Invariant maps

To more accurately describe the type of turbulence produced by the radiator, Lumley triangles [65] are illustrated in Figure 4.18 for the two cases at $z = 0\,\mathrm{cm}$. Three vertical positions along the direction of flow are chosen, respectively at $x/M = 0.58$, 8.45, and 16.75. For each position, 30 measuring points populate the invariant maps. Regardless of the presence of the panel, moving away from the radiator we observe a migration from the central area of the invariant maps toward the two states of axisymmetric and isotropic turbulence. In particular, in the case with the panel, the measurement points away from the radiator outlet cluster markedly toward the isotropic zone. In the two cases at $z = 10\,\mathrm{cm}$ shown in Figure 4.19, the measurement points move notably toward the rod-like axisymmetric turbulence zone to the right of the invariant map. In this area, the fluctuation magnitude in one spatial direction is larger than in the other two spatial directions. A similar result is obtained by Czwielong *et al.* [10]. Again, the effect of the presence of the panel is to reduce the importance of the dominant fluctuating component, moving the measurement points toward the isotropic turbulence state.

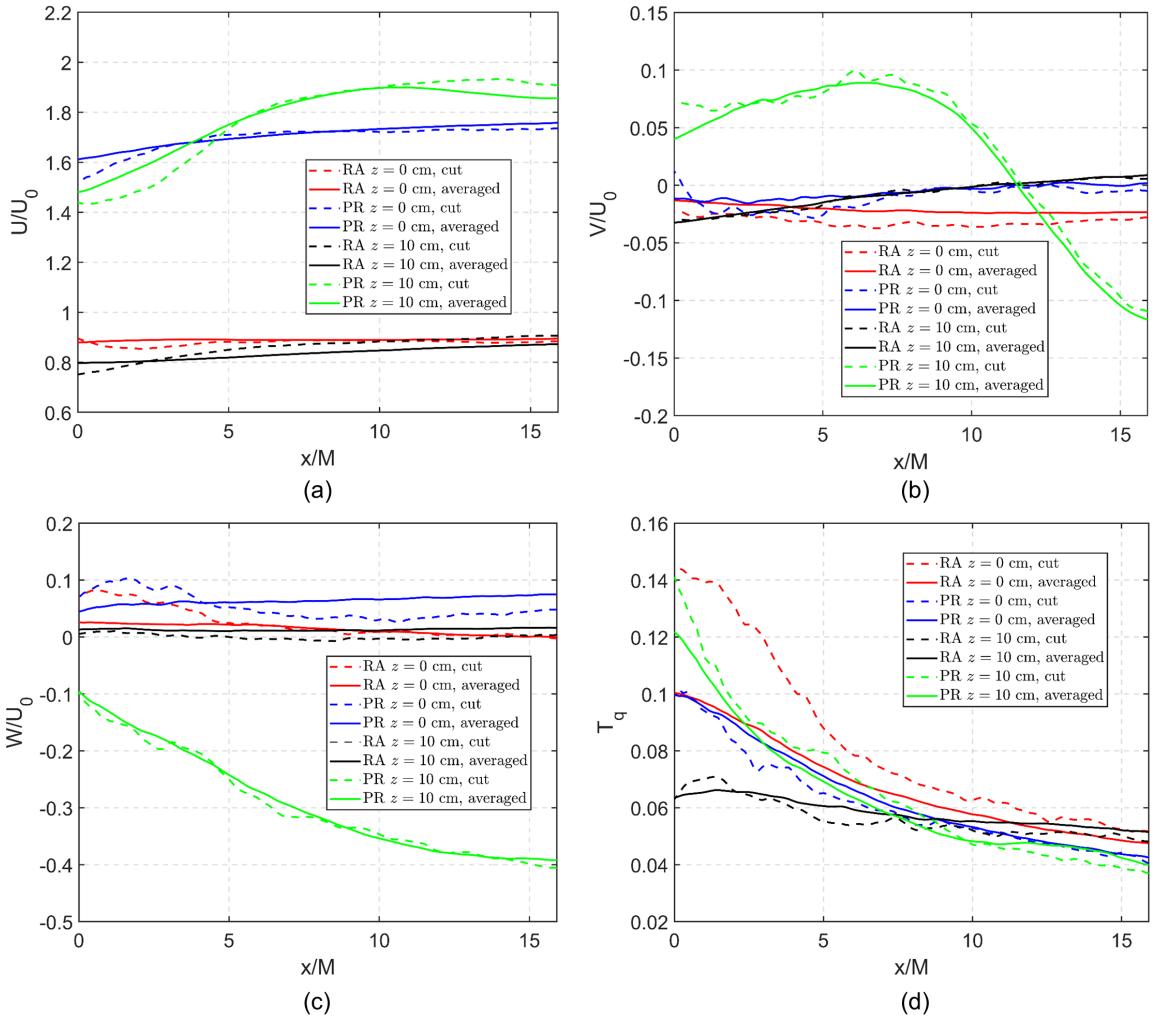

Figure 4.16: Horizontal cuts of the mean streamwise velocity (a), of the in-plane crosswise mean velocity (b), of the out-of-plane crosswise mean velocity (c), and of the turbulence intensity (d). Dashed lines are the horizontal cuts at $y/M = 5$, whereas solid lines are the vertical mean of all horizontal cuts.

4.5.3.4 Transverse velocity and turbulent-intensity profiles

Without loss of generality, in Figure 4.20, we study the non-homogeneous character of the turbulence produced by the radiator alone at $z = 0\,\mathrm{cm}$. The other FOVs are not reported since they yield similar values to the case under study. In particular, the presence of the panel does not appear to have an ameliorative effect on the turbulence homogeneity state. Figure 4.20 (a), reports the streamwise average velocity profile $U(y)$ on three vertical cuts, respectively at $x/M = 0$, 8, and 16, each normalized with respect to its own vertical average velocity U^{va}. At $x/M = 16$, the jets produced by the radiator fins are clearly visible, creating a sinusoidal-like pattern. Farther downstream, the peak-to-peak distance is about $\pm 10\%$ relative to U^{va}. Similarly, in Figure 4.20 (b), 3 vertical cuts of the turbulence intensity are shown, each normalized with respect to its average vertical value T_q^{va}. The difference in turbulence intensity at a distance of $x/M = 16$, with respect to the average vertical value, reaches $30\% T_q^{\mathrm{va}}$. These values are far from being able to consider the flow homogeneous in the transverse direction. In fact, looking at studies made

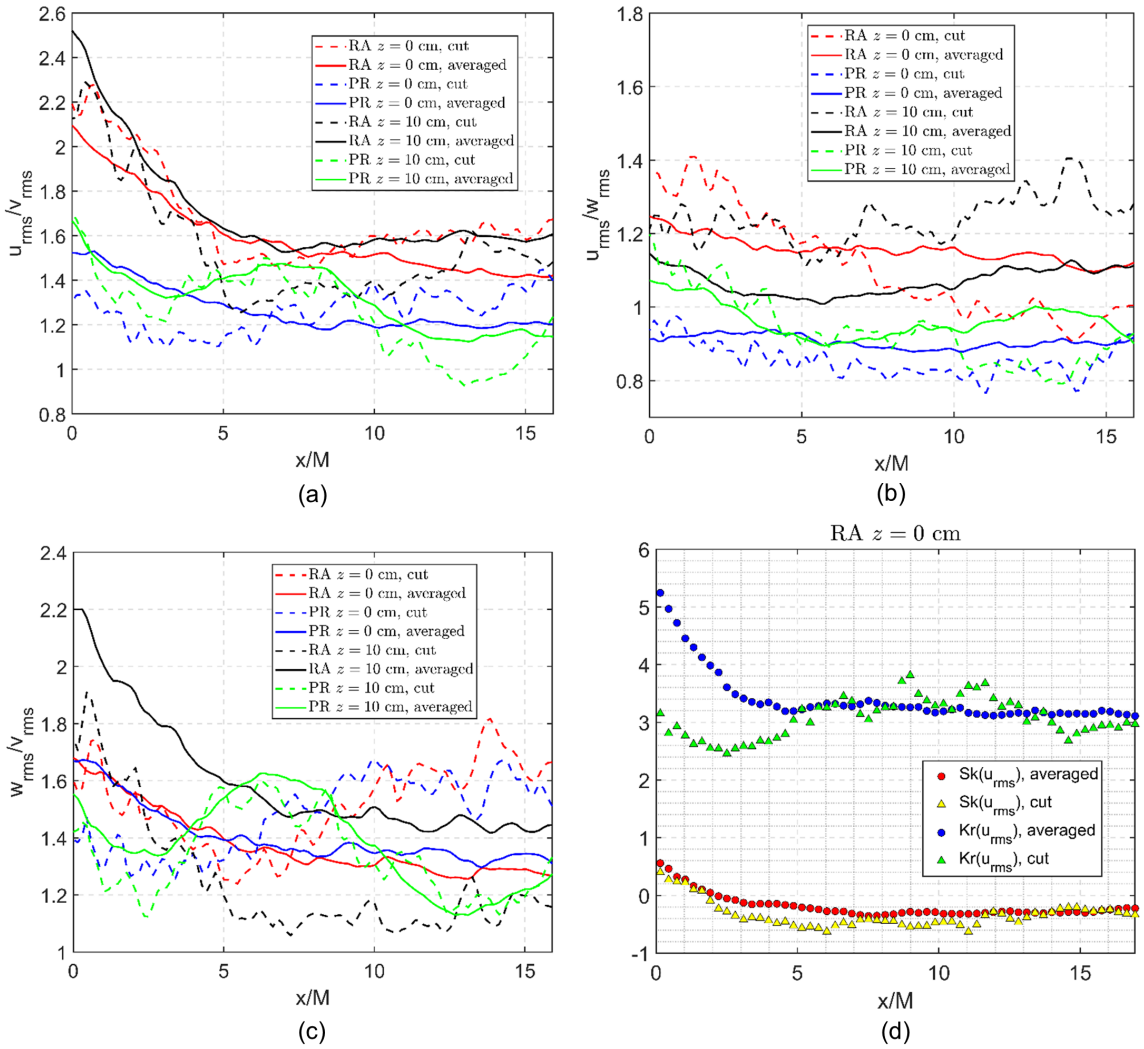

Figure 4.17: The root-mean-square velocity ratios are reported for the 4 studied FOVs in (a), (b), and (c). Dashed lines are the horizontal cuts at $y/M = 5$, whereas solid lines are the vertical mean of all horizontal cuts. In (d), the skewness and kurtosis of u_{rms} are reported for the RA $z = 0\,\mathrm{cm}$ case. The triangles represent the horizontal cut values at $y/M = 5$, whereas the circles depict the mean of all the horizontal cuts.

on fractal turbulence grids [26], the flow becomes homogeneous only over 20 times the mesh size, where we have $U(y)$ constant within $\pm 1\%$, whereas $T_q(y)$ reaches values of $\pm 3.5\%$. We can therefore conclude that although the flow may be reaching a transversely homogeneous state farther downstream, at a distance of $x/M = 12$, it is still transversely inhomogeneous.

4.5.4 Autocorrelations and integral length scales

We report a snapshot of the out-of-plane velocity in Figure 4.21 (a) in order to show the square area in the black dashed line that is chosen to conduct the analysis concerning the two-dimensional turbulence spectra. For each of the four investigated FOVs, this square area is always centered in

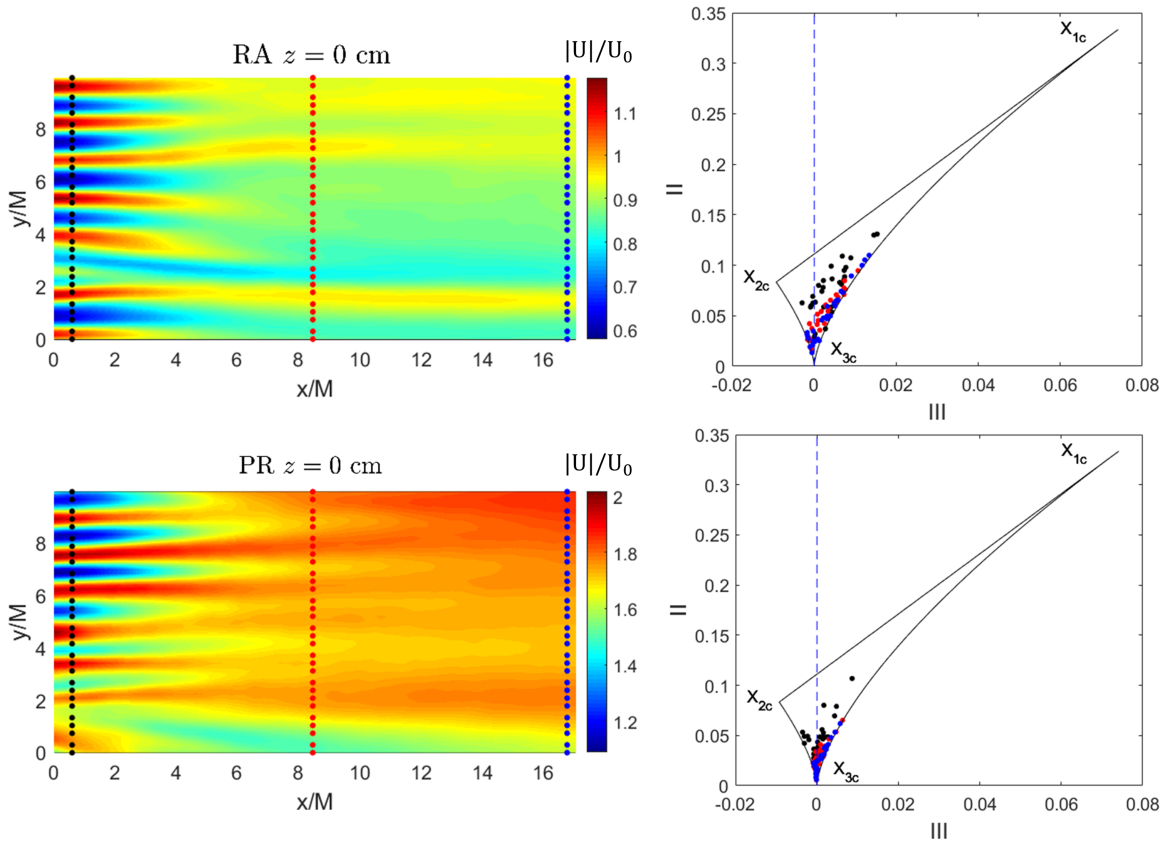

Figure 4.18: Three vertical locations at $x/M = 0.58$, 8.45, and 16.75 are chosen moving downstream from the radiator. The measuring points represented by circular symbols in black, red, and blue, are utilized to build the invariant maps on the right, for the cases at $z = 0\,\mathrm{cm}$.

$x/M = 12$, $y/M = 5$, and has a size of $4M$. This area is chosen in order to conduct the analysis at a distance from the radiator around which the fan is located. In the following analysis regarding the autocorrelation functions, we only show the RA $z = 0\,\mathrm{cm}$ case although similar studies and considerations have been made for the other 3 FOVs. The contour map of the autocorrelation function of the streamwise velocity R_{uu} is shown in Figure 4.21 (c). We can observe that the autocorrelation peak is well defined in the center of the map by the concentric ellipsoidal shapes. We can confirm the degree of anisotropy of the flow since, in a fully isotropic case, the ellipsoids must have the longest side aligned with the ξ/M axis and an aspect ratio equal to 2. Similarly, it can be noted that the autocorrelation function of the in-plane crosswise velocity R_{vv} also exhibits an anisotropic state since the ellipsoids are not aligned along the ν/M axis. In Figure 4.21 (b), cuts of the autocorrelation functions are performed along $\xi/M = 0$ and $\nu/M = 0$. We note that $R_{uu}(\nu = 0)$ is the only cut that does not reach zero before the spatial limit of the square area defined in Figure 4.21 (a). This motivates defining the integral length scales with an integration up to the value r_0 corresponding to the potential decay $1/\mathrm{e}^2$, as defined in Section 4.2.3.1. This approach, defined in [36], yielded negligible errors on the computation of the integral length scales reaching r_0 and allows for the estimation of $\Lambda_{u,1}$. In this case of relevant anisotropy, Carter and Coletti [36] pointed out that it is ambiguous to define the streamwise integral length scale simply as the integration of R_{uu} along $\nu/M = 0$. They rather suggest defining the streamwise length scale as

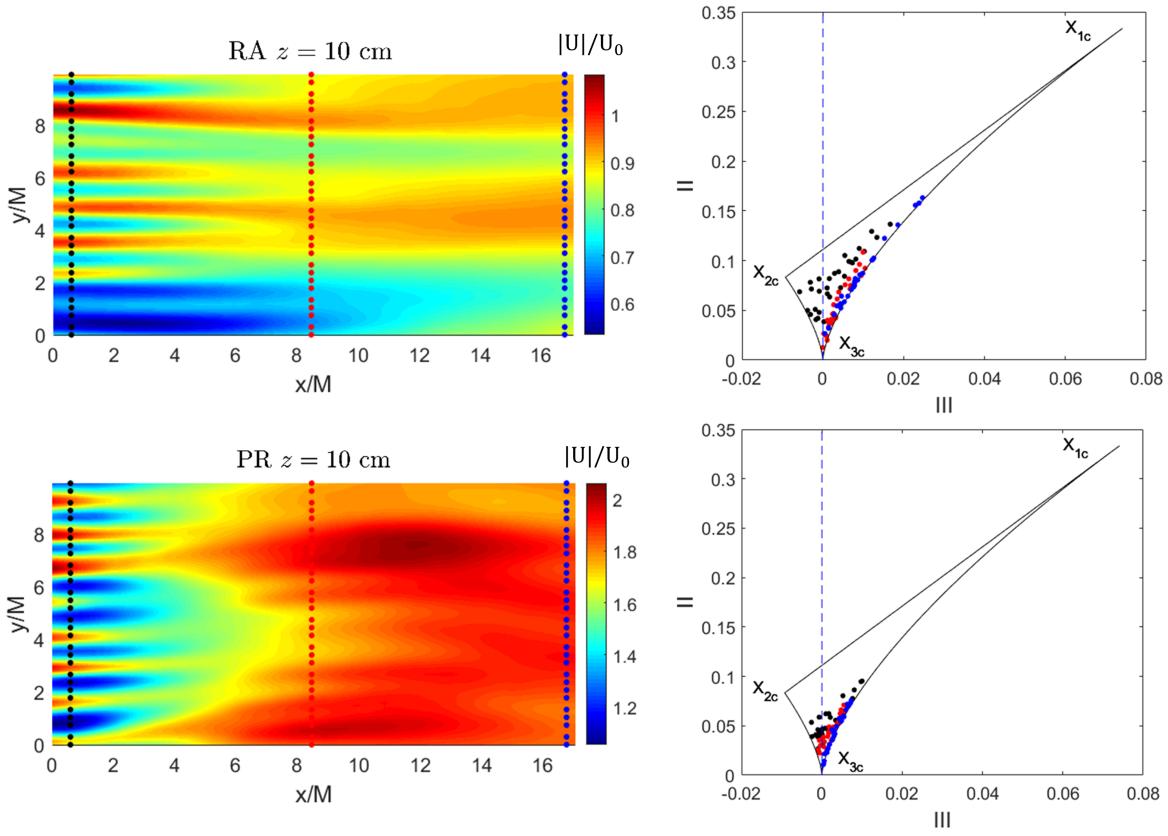

Figure 4.19: Three vertical locations at $x/M = 0.58$, 8.45, and 16.75 are chosen moving downstream from the radiator. The measuring points represented by circular symbols in black, red, and blue, are utilized to build the invariant maps on the right, for the cases at $z = 10\,\mathrm{cm}$.

$\Lambda_u = \sqrt{\Lambda_{u,1}\Lambda_{u,2}}$. This solution is also used in this work to define the in-plane crosswise velocity $\Lambda_v = \sqrt{\Lambda_{v,1}\Lambda_{v,2}}$. Ultimately, we define the integral length scale to be used in the calculation of the von Kármán spectrum in Eq. (4.15) as proposed for example by Hearst [23]: $\Lambda = (\Lambda_u + \Lambda_v)/2$.

4.5.5 Comparison with the von Kármán turbulence model

In this section, we intend to study the applicability of the von Kármán turbulence model on the studied FOVs. In Figure 4.22, the comparison between the two-dimensional experimental turbulence spectra and the von Kármán turbulence model defined in Eq. (4.15) is presented for the four FOVs analyzed. The agreement in the RA $z = 0$, $10\,\mathrm{cm}$ and PR $z = 0\,\mathrm{cm}$ cases is reasonable at low wavenumbers, where the highest energy content is found. The PR $z = 10\,\mathrm{cm}$ case presents an underestimation of the von Kármán model with respect to the experimental spectrum $\Phi_{ww}^{Exp}(K_x, K_y)$ at low wavenumbers (see Figure 4.22 (d)). This can be explained by the considerable acceleration that the out-of-plane crosswise component receives as a result of the proximity of the holed panel. In order to improve the match at high frequencies, an exponential correction to the turbulence model is proposed, following the work of Moreau and Roger [66]. This correction is needed for physical consistency, as explained by Pao [67]. For this reason, this will be referred to as the von Kármán-Pao model. Dealing with two-dimensional turbulence spectra, we multiply the von Kármán spectrum given in Eq. (4.15) by the exponential correc-

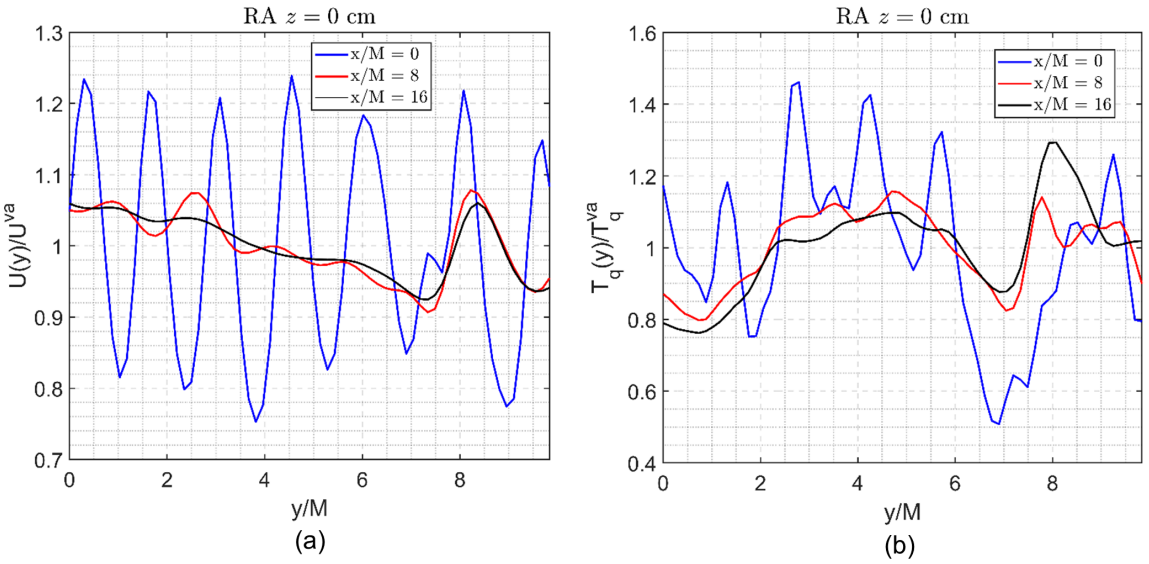

Figure 4.20: Three vertical locations are chosen at $x/M = 0$, 8, and 16 to plot the mean streamwise velocity $U(y)$ and the turbulence intensity $T_q(y)$ against the y-axis. These quantities are normalized by the vertical mean of each profile.

tion $\exp\left(-\beta_c \bar{K}_x\right) \cdot \exp\left(-\beta_c \bar{K}_y\right)$, where the coefficient $\beta_c = 12 \cdot 10^{-3}$ has been tuned in the considered case to match the experimental spectrum decay. In Figure 4.23 (a) it can be observed for the RA $z = 0\,\mathrm{cm}$ case that Pao's correction improves the high-wavenumber matching[4]. This is further noticeable by performing 3 cuts along the transversal wavenumber, respectively at $K_y = 408,\ 2042,\ 8170\,\mathrm{rad\,m^{-1}}$, as shown in Figure 4.23 (b). Here, we can remark both the acceptable approximation of the von Kármán at low frequencies and the improvement that the Pao's correction allows at high frequencies. Hence, the von Kármán model seems to fairly well approximate the two-dimensional turbulence spectra considered, despite the fact that the flow exhibits a non-negligible degree of anisotropy and transversal non-homogeneity. Nevertheless, as far as acoustic modeling is concerned, this approximation is acceptable only if it yields small discrepancies when the model is used as input to predict the far-field noise. For this reason, in the following section, these discrepancies between the modeled and the measured turbulent spectra are estimated.

4.5.6 Error evaluation related to the von Kármán model use

In this section, the aim is to estimate the error made in using the corrected von Kármán-Pao model instead of the turbulence spectrum measured in Section 4.5.5. This is done in order to make explicit what influence the modeling of the turbulence spectrum has on the acoustic prediction. For this purpose, we rewrite Eq. 2.19 that models the turbulence-interaction noise according to Amiet's theory [16]:

$$S_{pp}^{LE}(\mathbf{x}, \omega) = \left(\frac{\rho_0 k_a c z}{2 S_0^2}\right)^2 \pi U_0 \frac{L}{2} \left|\mathcal{L}^{LE}\left(x, K_x, K_y\right)\right|^2 \Phi_{ww}\left(K_x, K_y\right). \tag{4.19}$$

[4]The other cases are not shown, but present a similar response to the 2D spectrum correction.

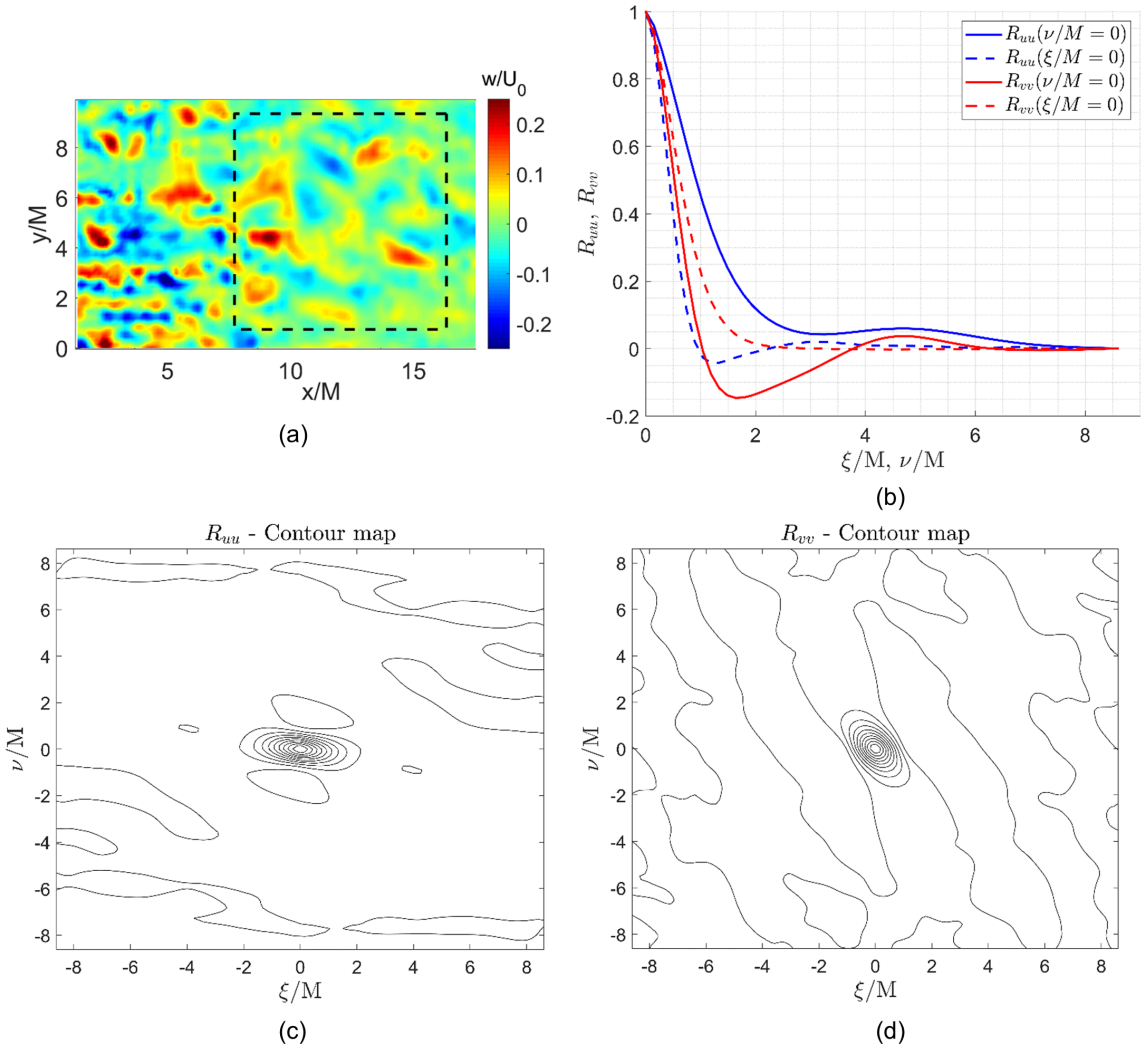

Figure 4.21: (a) Out-of-plane crosswise velocity snapshot with the square box (dashed black line) where the 2D analysis is carried out. (b) Autocorrelations R_{uu} and R_{vv} cuts along the normalized axes ξ/M and ν/M. (c) and (d): autocorrelation functions contour maps for R_{uu} and R_{vv}, respectively.

First, it can be noted that it is not possible to apply this equation directly to the case under investigation since rotating FOVs would be required to provide the upwash velocity fluctuations upstream of the blade leading edge and along the blade curvature (see the strip approach used in Chapter 5 for more details). However, the only FOVs on which the turbulence spectrum has been measured are those shown in Figure 4.5. Nevertheless, a linear dependence can be seen in Eq. 4.19 between the far-field noise S_{pp}^{LE} and the 2D turbulence spectrum Φ_{ww}. In fact, the other terms on the right-hand side of Eq. 4.19 depend on listener position, blade geometry, and flow velocity, but are all independent of the turbulence spectrum. Assuming invariance with respect to the rotation of the latter, it is possible to study the difference in sound pressure level expressed as:

$$\Delta L_p = 10 \log_{10}(\Phi_{ww}^{Pao}/\Phi_{ww}^{Exp}), \tag{4.20}$$

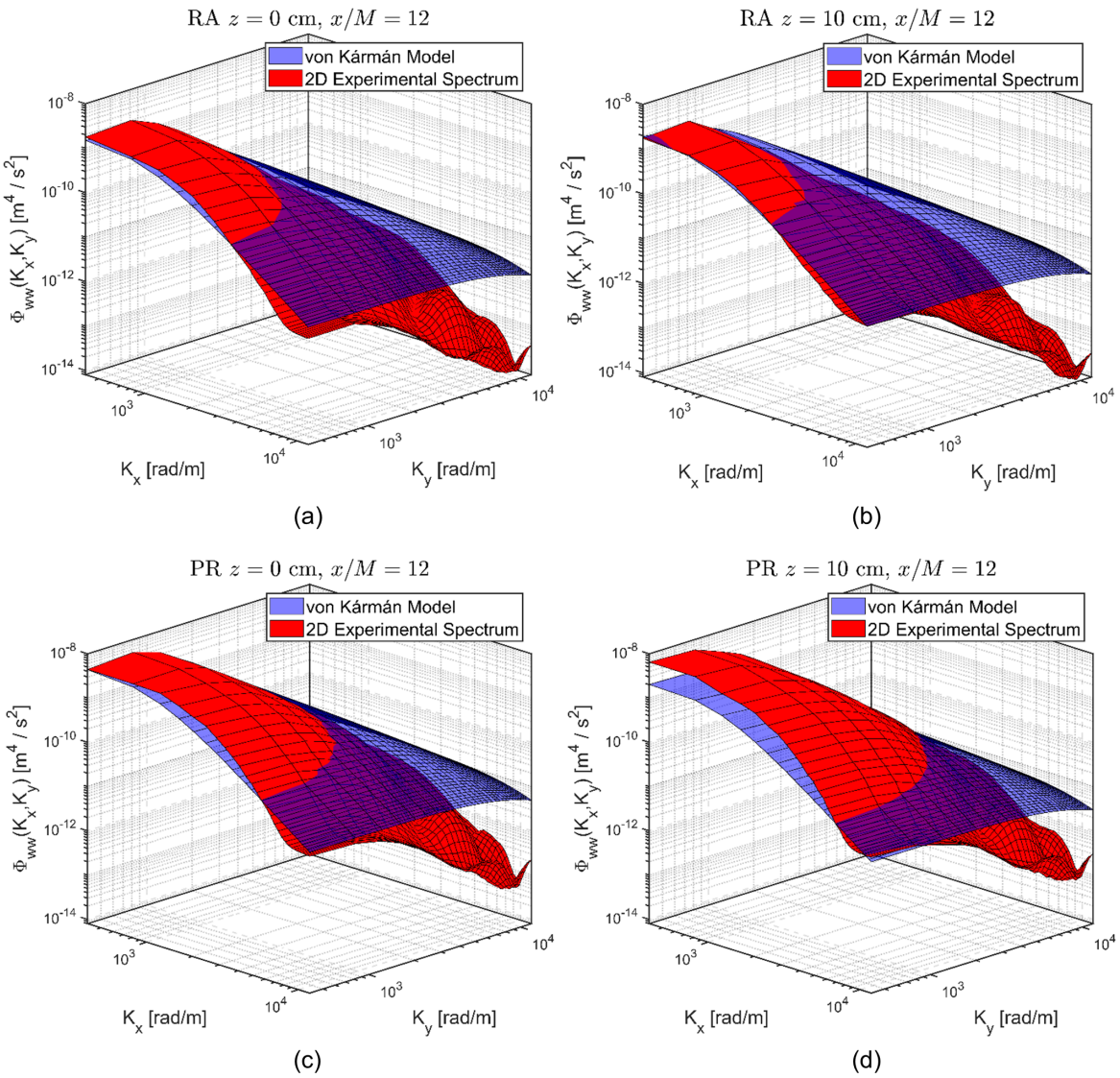

Figure 4.22: 2D experimental turbulent spectra compared with the von Kármán turbulence model for the 4 *analyzed FOVs.*

where Φ_{ww}^{Pao} represents the von Kármán model to which the exponential correction of Pao has been applied, as indicated in Section 4.5.5.

In Figure 4.24 (a), the RA $z = 0\,\mathrm{cm}$ case is illustrated[5] by defining three cuts along the transversal wavenumber, respectively at $K_y = 408, 2042, 8170\,\mathrm{rad\,m^{-1}}$.
It can be observed that up to $K_x = 7000\,\mathrm{rad\,m^{-1}}$, the two curves at lower wavenumbers are contained in the range $\Delta L_p = \pm\,3\,\mathrm{dB}$. Only the case $K_y = 8170\,\mathrm{rad\,m^{-1}}$ diverges earlier at medium frequencies. Thus, we can state that the von Kármán-Pao model approximates the measured turbulence spectrum fairly well ($\pm\,3\,\mathrm{dB}$) at low and medium frequencies, i.e., in the case

[5]The cases at RA $z = 10\,\mathrm{cm}$ and PR $z = 0\,\mathrm{cm}$ are not reported since analogous considerations can be drawn from the one under consideration in Figure 4.24 (a).

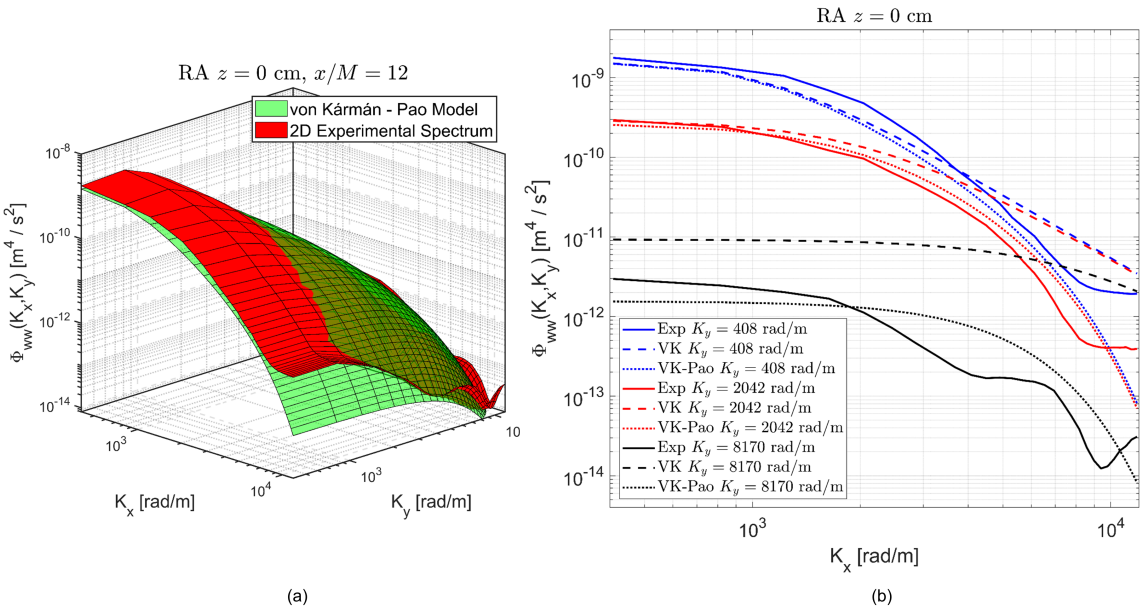

Figure 4.23: (a) Pao's correction applied to the two-wavenumber von Kármán spectrum. (b) 2D turbulent spectrum compared with the von Kármán model for 3 constant longitudinal wavenumbers.

where the wavenumbers are below about $7000\,\mathrm{rad\,m^{-1}}$. In addition, we can see in Figure 4.24 (b) the PR case $z = 10\,\mathrm{cm}$, i.e., where the FOV is in the vicinity of the circularly-holed panel. Here, even the lowest wavenumber curve $K_y = 408\,\mathrm{rad\,m^{-1}}$, which represents the part of the spectrum with the highest energy content (as can be noticed in Figure 4.22), shows a difference of $-5\,\mathrm{dB}$ at $K_x = 400\,\mathrm{rad\,m^{-1}}$, which becomes worse at medium frequencies. Consequently, in this specific case where the flow undergoes high shear with non-negligible acceleration along the out-of-plane direction, as illustrated in Figure 4.14 (d), the von Kármán model must be applied with caution.

4.6 Conclusions

In this chapter, we employed the stereo-PIV technique in order to analyze the airflow developing downstream of an automotive radiator. This was done in order to characterize the type of turbulence produced, quantify the turbulence intensity level at the fan inlet, and also verify the applicability of the von Kármán turbulence model frequently used in leading-edge noise prediction models. The stereo-PIV experimental campaign was carried out in the ALCOVES laboratory of the VKI, where the radiator was mounted and the airflow through it was provided by an external fan [68]. A circularly-holed panel was manufactured in order to replicate the area contraction caused by the fan casing past the radiator, which forces the flow to accelerate. Four FOVs of size $18 \times 34\,\mathrm{mm^2}$ were analyzed at two positions with (PR) or without (RA) the holed panel: at the center of the radiator, i.e. $z = 0\,\mathrm{cm}$, and laterally, up to where optical access was possible for the PIV cameras, i.e. $z = 10\,\mathrm{cm}$. The uncertainty analysis concerning the mean velocities calculated by stereo-PIV was conducted by splitting the uncertainty due to systematic and random errors, the latter dominating over the former. These, for the three mean velocity components, are equal to $\pm 1.3\%U$, $\pm 8.2\%V$, and $\pm 5.5\%W$.

The averaged velocity field analysis showed that the radiator fins create jets that often reach the downstream location where the fan would be. In addition, the flow is essentially streamwise and

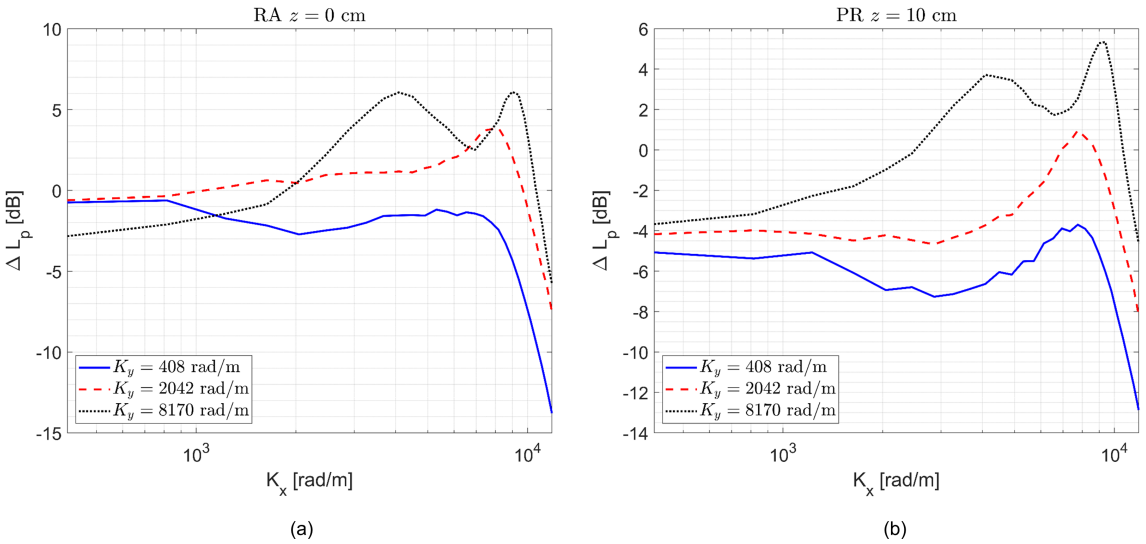

Figure 4.24: Difference of L_p due to the use of the von Kármán-Pao model with respect to the measured turbulence spectrum. Three K_y cuts are chosen for the RA $z = 0\,\mathrm{cm}$ case (a), and for the PR $z = 10\,\mathrm{cm}$ case (b).

there are no areas of significant recirculation. An exception is made by the case with the holed panel at $z = 10\,\mathrm{cm}$. Here the flow is deflected toward the center of the radiator due to the presence of the panel while maintaining strong momentum along the x-axis. It can be seen that the areas of higher TKE production are located at the fastest jets of the radiator. However, they dissipate very quickly. We found that the turbulence intensity produced immediately downstream of the radiator never exceeds 15% and is never greater than 6% at a distance of $x/M = 12$. Thus, we can affirm that the turbulence produced by the radiator does not reach very high levels (as found in [63]) and dissipates farther at the fan inlet. This can justify the little influence that the radiator has on the far-field noise, as discussed in Chapter 3. By analyzing the relationships between the root-mean-square velocity fluctuations, as well as the study of skewness and kurtosis, we can conclude that although there is a tendency of the flow toward isotropy, this is not achieved at a downstream distance of $x/M = 12$. In particular, the study of invariant maps yields information about the type of turbulence to be found. In fact, moving away from the radiator outlet, the turbulence evolves toward the axisymmetric (especially the rod-like one, similarly to what is found in [10]) and isotropic states. We can also observe that the presence of the panel accelerates the shift toward isotropy. Regarding the transverse direction, from the study carried out on the mean velocity and vertical turbulence intensity profiles, it can be concluded that the flow remains quite non-homogeneous. It is also interesting to investigate the applicability of the von Kármán model, which is widely used in the study of turbulence-interaction noise [69], by comparing it with the two-wavenumber turbulence spectrum experimentally obtained from the velocity fluctuation fields. The results indicate that although the flow is not completely isotropic and homogeneous, the von Kármán model describes the spatial turbulence spectrum quite well, especially at low wavenumbers, where there is the largest energy contribution. Moreover, applying the exponential Pao's correction improved the approximation at high wavenumbers [66]. However, the approximation gets worse in the case where the flow experiences acceleration and high shear. In such cases, the model must be applied cautiously. Future investigations should be aimed at studying turbulence with the presence of rotating blades, which may lead to an installation effect with the radiator that was neglected in this

study. Also, since the airflow analyzed here is cold, it would be interesting to investigate the effect of the thermal gradient due to engine heat dissipation on the flow past the radiator.

References

[1] F. N. Beauvais. *An Aerodynamic Look at Automotive Radiators*. February 1965.

[2] Alain Guédel. *Acoustique des ventilateurs*. Villeurbanne, France, 1999. PYC Livres.

[3] Julien Christophe, Korcan Kucukcoskun, and Christophe Schram. *Tonal and Broadband sound prediction of a locomotive cooling unit*. In 19th AIAA/CEAS Aeroacoustics Conference, Berlin, Germany, May 2013. American Institute of Aeronautics and Astronautics.

[4] A. Achaichia and T.A. Cowell. *Heat transfer and pressure drop characteristics of flat tube and louvered plate fin surfaces*. Experimental Thermal and Fluid Science, 1(2):147–157, April 1988.

[5] Hiechan Kang, Hyeonsik Oh, Minkyoo Lee, Anthony M Jacobi, and Jin Ho Kim. *Air-Side Heat Transfer Performance of Louver Fin and Multi-Tube Heat Exchanger for Fuel-Cell Cooling Application*. 2012.

[6] Monica Balcau and Liviu Scurtu. *Design and CFD Simulation of an Automotive Air Heat Exchanger*. In Ilie Dumitru, Dinu Covaciu, Laurențiu Racila, and Adrian Rosca, editors, The 30th SIAR International Congress of Automotive and Transport Engineering, pages 502–507. Springer International Publishing, Cham, 2020.

[7] Hiroshi Aoki, Tsutomu Shinagawa, and Kazuhiko Suga. *An experimental study of the local heat transfer characteristics in automotive louvered fins*. Experimental Thermal and Fluid Science, 2(3):293–300, July 1989.

[8] Ralph L Webb and Paul Trauger. *Flow Structure in the Louvered Fin Heat Exchanger Geometry*.

[9] Manuel Henner, Bruno Demory, Mohamed Alaoui, Maxime Laurent, and Benjamin Behey. *Effect of Blade Curvature on Fan Integration in Engine Cooling Module*. Acoustics, 2(4):776–790, October 2020.

[10] Felix Czwielong, Florian Krömer, and Stefan Becker. *Experimental investigations of the sound emission of axial fans under the influence of suction-side heat exchangers*. In 25th AIAA/CEAS Aeroacoustics Conference, Delft, The Netherlands, May 2019. American Institute of Aeronautics and Astronautics.

[11] Mohamed Gad-El-Hak and Stanley Corrsin. *Measurements of the nearly isotropic turbulence behind a uniform jet grid*. Journal of Fluid Mechanics, 62(1):115–143, January 1974.

[12] Mohsen S. Mohamed and John C. Larue. *The decay power law in grid-generated turbulence*. Journal of Fluid Mechanics, 219(-1):195, October 1990.

[13] Christophe Bailly and Geneviève Comte-Bellot. *Turbulence*. 04 2015.

[14] J. Christophe. *Application of hybrid methods to high frequency aeroacoustics*. PhD thesis, Université libre de Bruxelles, 2011.

[15] Marlène Sanjosé and Stéphane Moreau. *Fast and accurate analytical modeling of broadband noise for a low-speed fan*. The Journal of the Acoustical Society of America, 143(5):3103–3113, May 2018.

[16] R.K. Amiet. *Acoustic radiation from an airfoil in a turbulent stream*. Journal of Sound and Vibration, 41(4):407 – 420, 1975.

[17] Stephen B. Pope. *Turbulent Flows*. Cambridge University Press, 2000.

[18] M. Gaydon, M. Raffel, C. Willert, M. Rosengarten, and J. Kompenhans. *Hybrid stereoscopic particle image velocimetry*. Experiments in Fluids, 23(4):331–334, August 1997.

[19] C. J. Kähler and J. Kompenhans. *Fundamentals of multiple plane stereo particle image velocimetry*. Experiments in Fluids, 29(1):S070–S077, December 2000.

[20] A. Tsinober. *Turbulence: The Legacy of A. N. Kolmogorov. By U. FRISCH. Cambridge University Press, 1995. 296 pp. ISBN 0 521 45713 0. £15.95.* Journal of Fluid Mechanics, 317:407–410, 1996.

[21] Christophe Bailly and Geneviève Comte-Bellot. *Turbulence*. Experimental Fluid Mechanics. Springer International Publishing, Cham, 2015.

[22] G. K. Batchelor. *The theory of homogeneous turbulence*. Press Syndicate of the University of Cambridge, 1953.

[23] Robert Jason Hearst. *Fractal, Classical, and Active Grid Turbulence: From Production to Decay*.

[24] P.-å. Krogstad and P. A. Davidson. *Freely decaying, homogeneous turbulence generated by multi-scale grids*. Journal of Fluid Mechanics, 680:417–434, August 2011.

[25] Juan C. Isaza, Ricardo Salazar, and Zellman Warhaft. *On grid-generated turbulence in the near- and far field regions*. Journal of Fluid Mechanics, 753:402–426, August 2014.

[26] R. J. Hearst and P. Lavoie. *Decay of turbulence generated by a square-fractal-element grid*. Journal of Fluid Mechanics, 741:567–584, February 2014.

[27] Geneviéve Comte-Bellot and Stanley Corrsin. *The use of a contraction to improve the isotropy of grid-generated turbulence*. Journal of Fluid Mechanics, 25(4):657–682, 1966.

[28] John L. Lumley. *Stochastic Tools in Turbulence*. In Applied Mathematics and Mechanics, volume 12. Elsevier, 1970.

[29] John L. Lumley. *Computational modelling of turbulent flow*. 18:123–179, 1978.

[30] A. J. Simonsen and P.-å. Krogstad. *Turbulent stress invariant analysis: Clarification of existing terminology*. Physics of Fluids, 17(8):088103, August 2005.

[31] M Emory and Iaccarino. *Visualizing turbulence anisotropy in the spatial domain with componentality contours*. 2014.

[32] M. Piirto, H. Ihalainen, H. Eloranta, and P. Saarenrinne. *2D spectral and turbulence length scale estimation with PIV*. Journal of Visualization, 4(1):39–49, March 2001.

[33] Leandro de Santana. *Semi-analytical Methodologies for Airfoil Noise Prediction*. PhD thesis, KU Leuven, 2015.

[34] Stefano Discetti, Isaac B Ziskin, Tommaso Astarita, Ronald J Adrian, and Kathy P Prestridge. *PIV measurements of anisotropy and inhomogeneity in decaying fractal generated turbulence*. Fluid Dynamics Research, 45(6):061401, December 2013.

[35] Hooman Amiri Hazaveh. *Experimental Investigation of the turbulent near wake flow field of multiscale/fractal grids. Ph.D. Thesis*.

[36] Douglas W. Carter and Filippo Coletti. *Scale-to-scale anisotropy in homogeneous turbulence*. Journal of Fluid Mechanics, 827:250–284, September 2017.

[37] Markus Raffel, Christian E. Willert, Fulvio Scarano, Christian J. Kähler, Steve T. Wereley, and Jürgen Kompenhans. *Particle Image Velocimetry*. Springer International Publishing, Cham, 2018.

[38] Christian Willert. *Stereoscopic digital particle image velocimetry for application in wind tunnel flows*. Measurement Science and Technology, 8(12):1465–1479, December 1997.

[39] J. Westerweel and F. T. M. Nieuwstadt. *Performance tests on 3-dimensional velocity measurements with a two-camera digital particle-image velocimeter*. In Laser Anemometry - Advances and Applications 1991, volume 1, pages 349–355, January 1991.

[40] B. Wieneke. *Stereo-PIV using self-calibration on particle images*. Experiments in Fluids, 39(2):267–280, August 2005.

[41] Frank M White. *Fluid mechanics*. 2017.

[42] LaVision GmbH Göttingen. *Product-Manual for DaVis 8.4, "FlowMaster"*. Göttingen, Germany, 2017.

[43] H. Royer and M. Stanislas. *Stereoscopic and holographic approaches to get the third velocity component in PIV*. 1996.

[44] K D Hinsch. *Three-dimensional particle velocimetry*. Measurement Science and Technology, 6(6):742–753, jun 1995.

[45] Ajay K. Prasad and Kirk Jensen. *Scheimpflug stereocamera for particle image velocimetry in liquid flows*. Appl. Opt., 34(30):7092–7099, Oct 1995.

[46] E. Kit, I. Wygnanski, D. Friedman, O. Krivonosova, and D. Zhilenko. *On the periodically excited plane turbulent mixing layer, emanating from a jagged partition*. Journal of Fluid Mechanics, 589:479–507, October 2007.

[47] A. Darisse, J. Lemay, and A. Benaïssa. *Investigation of passive scalar mixing in a turbulent free jet using simultaneous LDV and cold wire measurements*. International Journal of Heat and Fluid Flow, 44:284–292, December 2013.

[48] LaVision GmbH Göttingen. *Product-Manual for DaVis 8.4, "Imagining Tools"*. Göttingen, Germany, 2017.

[49] F. Scarano and M. L. Riethmuller. *Advances in iterative multigrid PIV image processing*. Experiments in Fluids, 29(7):S051–S060, December 2000.

[50] Christian J. Kähler, Sven Scharnowski, and Christian Cierpka. *On the resolution limit of digital particle image velocimetry*. Experiments in Fluids, 52(6):1629–1639, June 2012.

[51] A Sciacchitano. *Uncertainty quantification in particle image velocimetry*. Measurement Science and Technology, 30(9), September 2019.

[52] Dirk Michaelis, Douglas R Neal, and Bernhard Wieneke. *Peak-locking reduction for particle image velocimetry*. Measurement Science and Technology, 27(10):104005, sep 2016.

[53] Ajay Prasad, Ronald Adrian, Chris Landreth, and P. Offutt. *Effect of resolution on the speed and accuracy of particle image velocimetry interrogation*. Experiments in Fluids, 13:105–116, 06 1992.

[54] Bernhard Wieneke. *Stereo-PIV using self-calibration on particle images*. Experiments in Fluids, 39:267–280, 08 2005.

[55] Clayton T. Crowe, John D. Schwarzkopf, Martin Sommerfeld, and Yutaka Tsuji. *Multiphase Flows with Droplets and Particles*. CRC Press, 0 edition, August 2011.

[56] A Melling. *Tracer particles and seeding for particle image velocimetry*. Measurement Science and Technology, 8(12):1406–1416, dec 1997.

[57] Sayantan Bhattacharya, John J Charonko, and Pavlos P Vlachos. *Stereo-particle image velocimetry uncertainty quantification*. Measurement Science and Technology, 28(1):015301, January 2017.

[58] Bernhard Wieneke. *PIV uncertainty quantification from correlation statistics*. Measurement Science and Technology, 26(7), jun 2015.

[59] F Scarano. *Iterative image deformation methods in PIV*. Measurement Science and Technology, 13(1):R1–R19, nov 2001.

[60] Andrea Sciacchitano and Bernhard Wieneke. *PIV uncertainty propagation*. Measurement Science and Technology, 27(8):084006, jun 2016.

[61] Ian Grant and Edward H. Owens. *Confidence interval estimates in PIV measurements of turbulent flows*. Applied Optics, 29(10):1400, April 1990.

[62] J.F. Kenney and E.S. Keeping. *Mathematics of Statistics*. Van Nostrand, 1959.

[63] Florian Zenger, Gert Herold, and Stefan Becker. *Acoustic Characterization of Forward- and Backward-Skewed Axial Fans Under Increased Inflow Turbulence*. AIAA Journal, 55(4):1241–1250, April 2017.

[64] Paul Mallery Darren George. *IBM SPSS Statistics 23 Step by Step: A Simple Guide and Reference*. Routledge, 14 edition, 2016.

[65] John L. Lumley and Gary R. Newman. *The return to isotropy of homogeneous turbulence*. Journal of Fluid Mechanics, 82(1):161–178, 1977.

[66] Stéphane Moreau and Michel Roger. *Competing Broadband Noise Mechanisms in Low-Speed Axial Fans*. AIAA Journal, 45(1):48–57, January 2007.

[67] Yih-Ho Pao. *Structure of Turbulent Velocity and Scalar Fields at Large Wavenumbers*. Physics of Fluids, 8(6):1063, 1965.

[68] M. Bilka, J. Anthoine, and C. Schram. *Design and evaluation of an aeroacoustic wind tunnel for measurement of axial flow fans*. The Journal of the Acoustical Society of America, 130(6):3788–3796, December 2011.

[69] Alessandro Zarri, Julien Christophe, Stéphane Moreau, and Christophe Schram. *Influence of Swept Blades on Low-Order Acoustic Prediction for Axial Fans*. Acoustics, 2(4):812–832, November 2020.

5

Sweep-angle effect on low-order acoustic prediction

5.1 Introduction

In the automotive field, tier 1 suppliers are interested in including the acoustic study within the pre-design optimization cycles of the future cooling modules. To this end, hybrid low-order approaches are typically preferred for two reasons: firstly, they are less time-consuming with respect to high-order techniques; secondly, they do not require detailed geometries, often unknown in the early industrial development phases. The aim of this chapter is to develop a low-order noise prediction methodology, coupling inexpensive CFD techniques, such as steady RANS, in order to determine the source field, with semi-analytical methods to propagate the sound waves to the far-field [1]. The second goal of this work is to assess the importance of the blade sweep angle for the proposed prediction methodology. In fact, utilizing curved (or swept) blades is considered a classical technique in order to mitigate the far-field emissions as well as to enhance the aerodynamic efficiency [2]; for this reason, backward-swept and forward-swept propellers are often employed in the field [3]. Several noise-generating mechanisms of tonal and broadband nature occur in this application [4] and among the most influencing ones, we distinguish the turbulence-interaction or leading-edge noise and the trailing-edge or self-noise mechanism [5]. Following the semi-analytical works carried out in [1, 6–8] for the previous two broadband mechanisms, we intend to implement semi-analytical methods, based on Amiet's airfoil noise theory [9, 10], able to take into account the effect of having swept leading- and trailing-edges. Although these methodologies were already proven to accurately model the noise emitted by static swept airfoils, no application to low-speed rotating blades has been carried out so far including sweep, in order to predict the overall emitted broadband sound. Nevertheless, the work of Roger et al. [7] aimed at modeling tonal noise emissions by Contra-Rotating Open Rotors (CRORs) and was instrumental in deriving the set of equations hereafter adapted to model the leading-edge noise for low-speed cooling fans. The third goal of this chapter is to carry out a sensitivity study in order to understand better the influence of some of the several parameters characterizing the application of Amiet's theory for trailing- and leading-edge noise prediction. In order to model the former, several semi-empirical

wall-pressure models have been proposed in the literature [11], but few studies were carried out to assess their validity for rotating blades' sound emissions, especially in automotive low-speed fans [1, 12]. Moreover, for these applications, the Corcos' model [13] is generally employed [14] to estimate the spanwise integral length scale l_y. Nevertheless, as pointed out in [6], having skewed blade edges may lead to a different redistribution of the spectral energy over the chordwise and spanwise wavenumbers, ultimately yielding a wrong estimation of l_y. To overcome this problem, the Generalized Corcos' Model proposed by Caiazzo et al. [15] is implemented following the work of Grasso et al. [6], and several combinations of the Butterworth-filter order coefficients are examined in Section 5.5.4. Regarding the turbulent impingement noise, no guidelines are present in literature about the upstream location at which one has to collect the CFD information to feed Amiet's airfoil theory: a location is chosen in this work by examining the overall emitted sound as a function of the leading-edge upstream distance.

The limitations of the methodology proposed hereafter mainly consist in the lack of modeling of sound-source mechanisms governed by large vortical structures that are relevant sources in the low-frequency range and that require higher-order CFD methods to be simulated. For these cooling modules, in fact, the secondary flow passing through the gap between the ring and the shroud can reach 6% of the nominal flow rate [16]. As shown by an unsteady detached-eddy computation of the same fan depicted in Figure 5.1, the Q-criterion technique depicts complex vortical structures developing all around the rotating ring. This suggests the presence of large coherent eddies that are not captured by steady calculations and that are probably responsible for the typical subharmonic humps characterizing the low-frequency spectrum, as discussed in [17, 18]. Other secondary structures can be localized at the blade cusp regions near the hub, as shown in [19]. This work remains focused on the turbulence impingement and self-noise which are contributing to most of the broadband content from the middle to high frequencies. The chapter is organized as follows: Section 5.2 presents the experimental setup where acoustic measurements were acquired at the von Karman Institute for Fluid Dynamics, as described in [12], as well as the installed automotive fan with its geometry and characteristics; in Section 5.3 the numerical simulation, based on steady RANS, is detailed with a focus on the extraction parameters needed to feed the acoustic methodology; the latter is discussed in Section 5.4, describing the strip-theory approach followed by the inclusion of the sweep angle in Amiet's airfoil theory; finally, Section 5.5 illustrates the far-field acoustic results, involving a parametric study and highlighting the importance of taking into account the sweep-angle effects.

5.2 Experimental setup

The cooling module has been mounted in the ALCOVES anechoic chamber in a fan-alone configuration, as depicted in Figure 5.2 (a), and its far-field sound spectrum has been measured for the fan nominal working condition at a one-meter distance, aligned with the center of the fan. The laboratory has been designed by Bilka et al. [20] to have a low turbulence level at the inlet and an acoustic cut-off frequency of $150\,\mathrm{Hz}$. Further details regarding the ALCOVES laboratory are given in Chapter 3.

The fan has 7-unequally-spaced blades that are forward skewed, with high sweep-angle values particularly at the tip of the blades. The sweep angle, defined as the angle between the radius and the local tangent to the blade curvature, at the leading edge, reaches very high values of about 70 degrees at the tip of the blade. A slower increase of up to about 50 degrees is attained by the trailing-edge curvature at the blade tip. The hub diameter is $142\,\mathrm{mm}$, whereas the total diameter consists of $380\,\mathrm{mm}$. The operating condition of this rotor is a rotational speed of 3400 rpm with

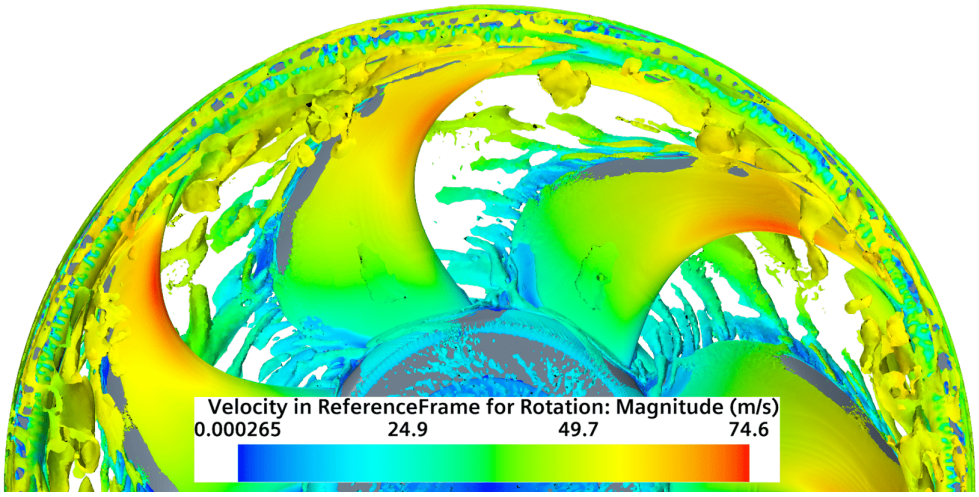

Figure 5.1: The relative velocity is plotted for an unsteady DES computation onto the isosurface obtained with the Q-criterion technique; large vortical structures are depicted in particular close to the ring and in the trailing-edge recirculating region near the hub (the fan rotation is clockwise).

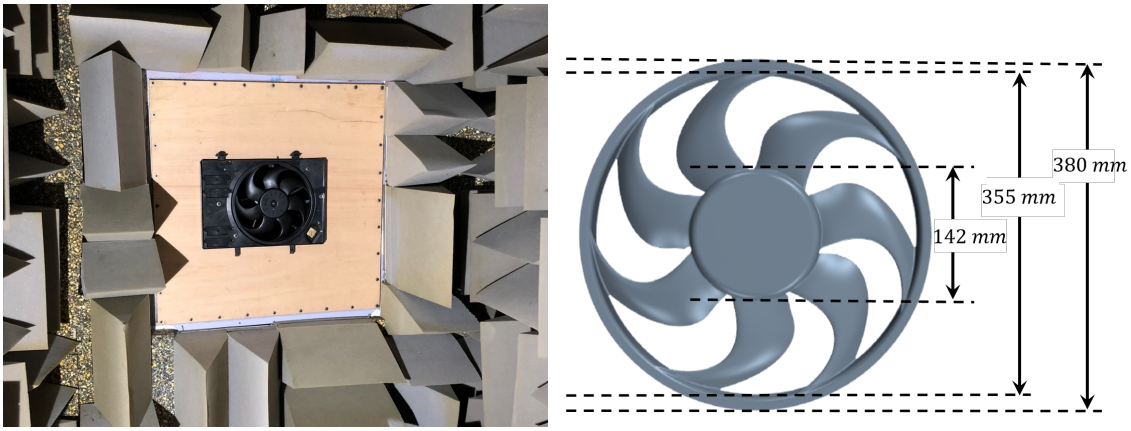

(a) (b)

Figure 5.2: (a) ALCOVES anechoic chamber: upstream room with fan-alone configuration. (b) Suction-side 3D CAD model of the Valeo forward-skewed fan employed in the steady RANS simulation.

a volumetric flow rate of $3400\,\mathrm{m^3\,h^{-1}}$. The Reynolds number based on the chord at the tip of the blade is 2.45×10^5, stating that the fan is working in the laminar-turbulent transition region [21]. The Mach number at the tip, related to a rotational speed of 3400 rpm, is 0.19, and thus, the incompressible regime can be considered.

5.3 Numerical simulation of the low-speed fan

CFD computations are carried out with STAR-CCM+ Version 15.04. As illustrated in Figure 5.3, three computational domains are considered: the mass flow inlet, the moving reference frame (MRF) with a rotational velocity of 3400 rpm defined where the fan is settled, and the pressure

outlet.

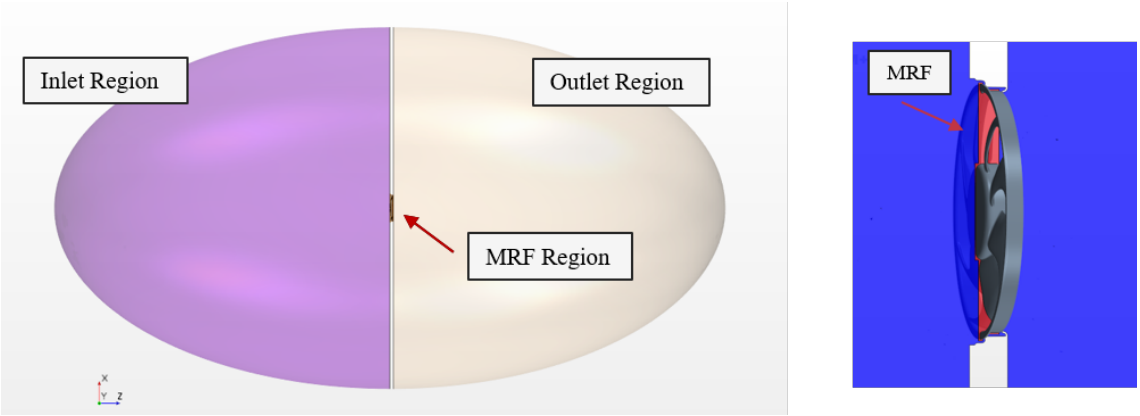

Figure 5.3: The 3 regions of the computational domain are represented on the left, whereas a close-up of the moving reference frame (MRF) where the fan is located as shown on the right.

Both inlet and outlet regions are conceived large enough to have fairly low influence on the MRF region, as well as to allow free-field atmospheric conditions as outlet boundary conditions. A polyhedral mesh of approximately 25 million cells has been created similar to what has been done by Henner et al. [22]. A section of the mesh over the plane normal to the Y axis is shown in Figure 5.4: the wake refinements are remarked in the outlet region on the right.

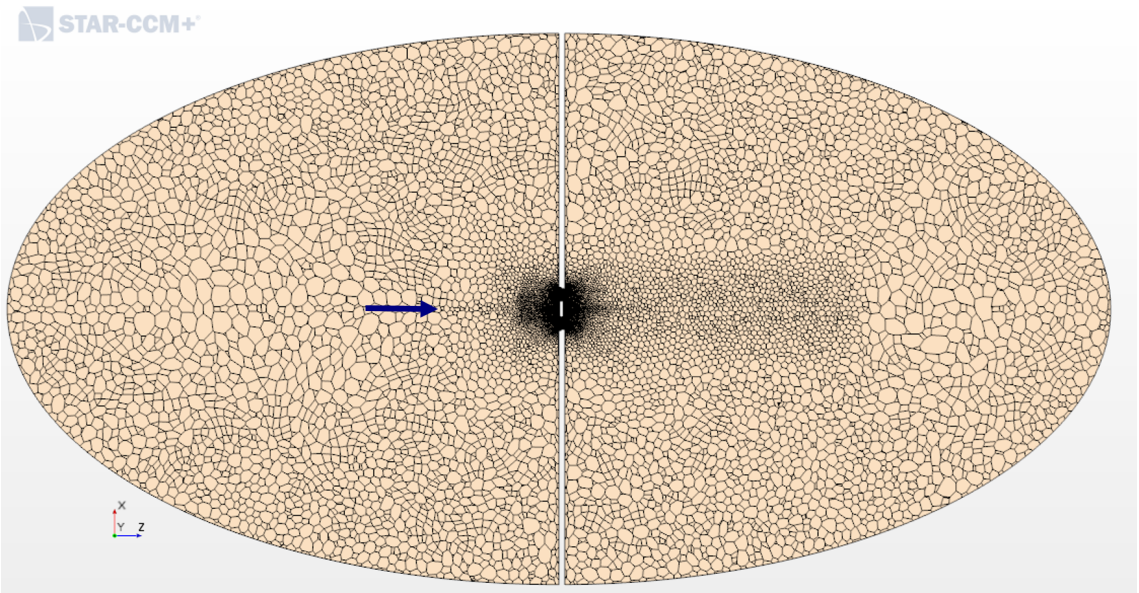

Figure 5.4: Polyhedral mesh section over the plane normal to the Y axis.

Figure 5.5 shows a close-up of the meshed area of the MRF region: small cells are visible especially around the blades. A mesh independence study has been performed varying the refinements over the fan surfaces, as well as in the wake region. Steady RANS are considered in this work as an acceptable compromise between computational cost and accuracy in describing the flow features. As in [16], the SST $k-\omega$ turbulence model has been chosen in order to re-

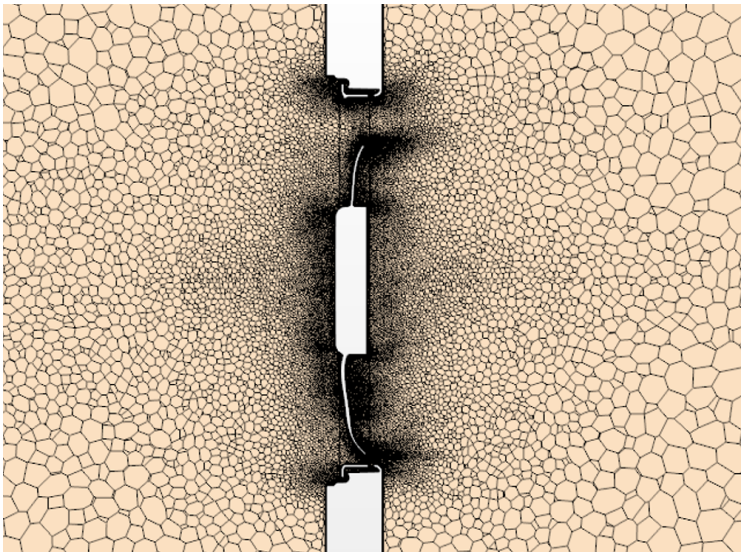

Figure 5.5: Close-up visualization over the fine polyhedral mesh of the MRF region.

solve the boundary-layer features close to the walls: $y+ \approx 1$ values are obtained in every region. A similar simulation strategy, despite the use of an unsteady approach, in that case, can be found in [16] where the analyzed forward-skewed fan is a slightly bigger sample of the same rotor family produced by Valeo.

The seven blades present similar aerodynamic properties, where at the tip the highest values of mean velocities are observed in Figure 5.6 (a). Moreover, the pressure load on the fan suction side presents similar distribution over the blades, with higher values at their leading-edge tip, as Figure 5.6 (b) shows. For these reasons, only one blade has been used for the following acoustic results. This assumption could not be done in advance because the blades are not equally spaced. The typical radial development of the wake at nominal conditions, consistently with [16], is shown in Figure 5.7 (a), whereas the cylindrical cut in Figure 5.7 (b) confirms the azimuthal axial symmetry of the wake. The relative-velocity scalar field around iso-radius cuts of the blades is also displayed in Figure 5.8. In each case, at the hub, mid-span, and tip regions, the flow appears to be fairly attached along the airfoil suction line, allowing the use of the semi-empirical wall-pressure models explained in Section 5.4, not suited when the flow is highly separated.

5.3.1 Inlet turbulence

In order to feed the leading-edge noise formulation with the RANS-based parameters (turbulence kinetic energy k_t, specific rate of dissipation ω_t, and mean relative or entrainment velocity U_0), point-wise locations upstream of the blade leading-edge line are defined. Two quantities are related to the turbulent $k_t - \omega_t$ STT model parameters, illustrated by defining the radial normalized distance y/L_B: the turbulent length scale Λ_f in Figure 5.9 (a) and the mean square of the velocity fluctuations $\overline{u^2}$, in Figure 5.9 (b). The former influences the slopes and the roll-off frequency location of the turbulent velocity fluctuations spectrum and is defined as:

$$\Lambda_f = \frac{B_t k_t^{1/2}}{\omega_t C_\mu}, \tag{5.1}$$

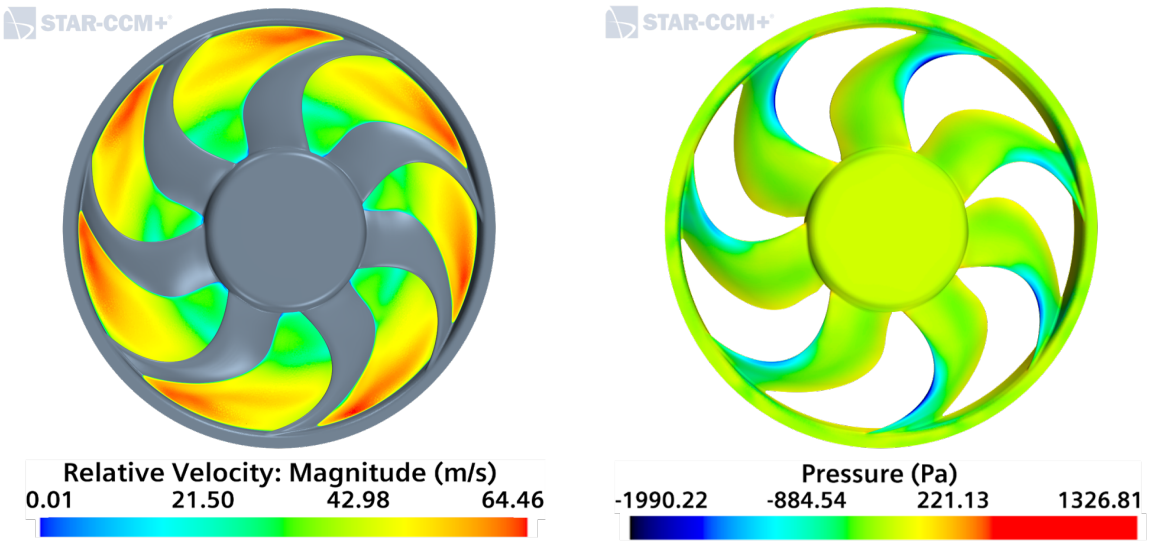

(a) (b)

Figure 5.6: The RANS-based numerical results show similar azimuthal features over the 7 non-equally-distributed fan blades, making it possible to deal with them separately: in (a), the relative velocity is illustrated on a plane normal to the fan rotating axis, showing higher velocities at the blade trailing-edge tips; in (b), the distribution of pressure indicates that the most loaded zones are the blade leading-edge tips.

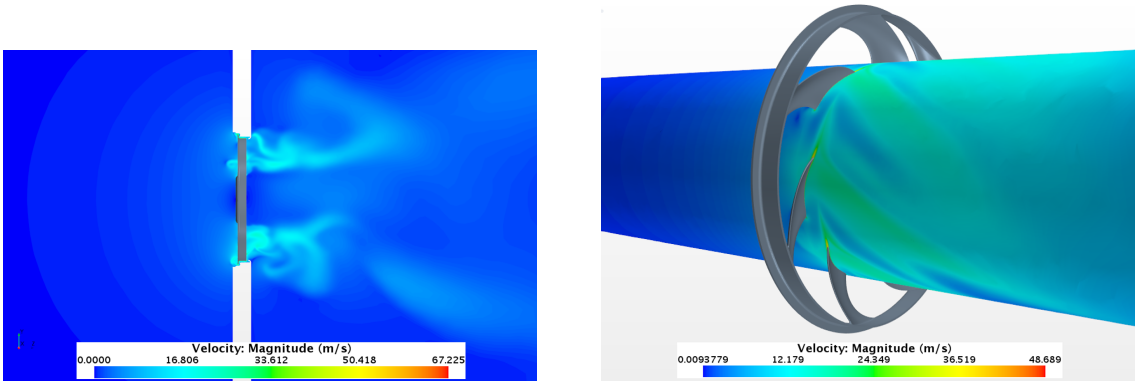

(a) (b)

Figure 5.7: Scalar field of the velocity magnitude obtained with RANS simulation: (a) Planar section showing the MRF region with its radial wake. (b) The cylindrical section along the Z-axis.

with the empirical constant $B_t = 0.4$ given in [23] and $C_\mu = 0.09$ given in [24]. The amplitude of the spectrum of the velocity fluctuations (see Section 5.4.2) is mostly affected by $\overline{u^2}$, directly linked to the turbulent kinetic energy as $\overline{u^2} = \frac{2}{3}k_t$. In Figure 5.9 (a), it is worth noticing that $\overline{u^2}$ reaches a peak in the range $0.15 < y/L_B < 0.45$ and then it starts to grow again while approaching the tip of the blade. Similar trends have been found in the RMS velocity components of Figure 10 in [19].

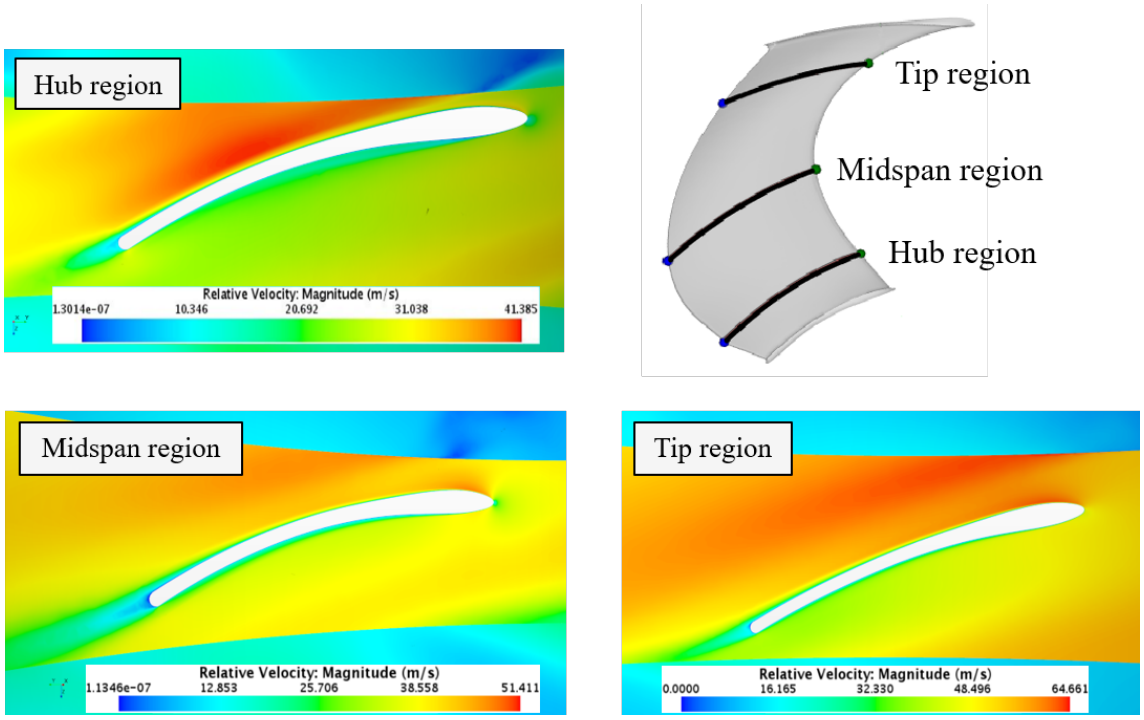

Figure 5.8: Relative velocity at 3 iso-radial cuts along the blade span.

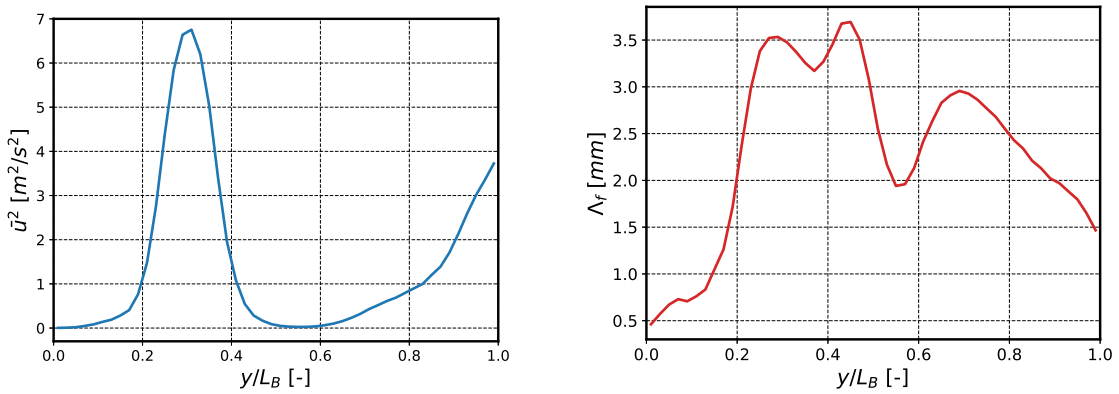

(a) (b)

Figure 5.9: Inlet turbulence parameters are extracted from the steady-RANS computation upstream of the blade leading-edge line (at 12% of the chord, as motivated in Section 5.5.2) and depicted as functions of the spanwise normalized distance y/L_B: in (a), the mean square of the velocity fluctuations $\overline{u^2}$ is depicted; in (b), the characteristic length scale of the turbulent eddies Λ_f is illustrated.

5.3.2 Boundary-layer parameters

The steady-RANS simulation provides a statistically converged solution of the velocity field around the fan blades. We are interested in extracting the trailing-edge velocity boundary layers at several spanwise locations in order to implement the strip-theory approach presented in Section 5.4.

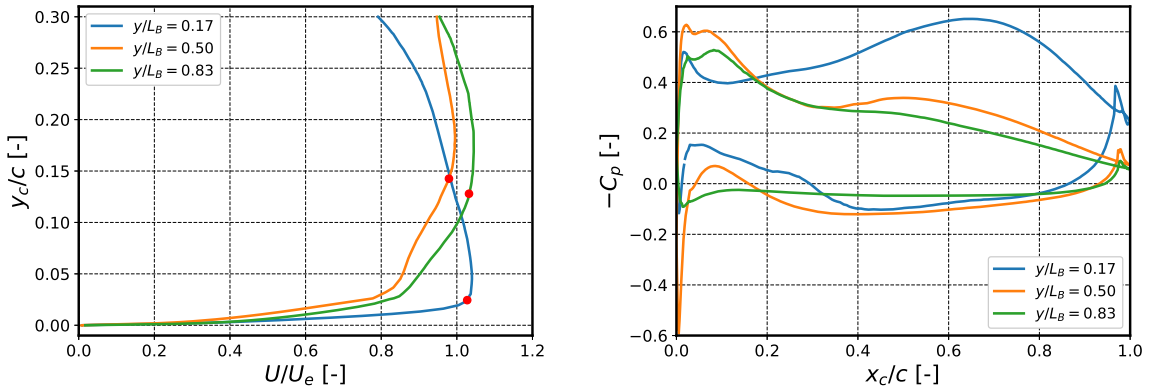

(a) (b)

Figure 5.10: Three isoradial cuts are plotted at 3 spanwise locations y/L_B: (a) the boundary-layer velocity profiles are depicted as functions of the non-dimensional boundary-layer distance y_c/c with the red dots corresponding to the boundary layer thickness δ; (b) the negative pressure coefficient C_p is plotted as a function of the chordwise nondimensional coordinate x_c/c.

By so doing, it is possible to estimate the boundary-layer parameters to model the trailing-edge wall-pressure spectra. For automotive forward-skewed fans as the one considered in this work, it is not trivial to define an external boundary-layer velocity U_e because secondary flows, especially at the blade tip and hub regions as well as flow separation zones can easily occur. For three spanwise locations illustrated in Figure 5.10 (a), the boundary-layer thickness δ (shown with red dots) has been defined at the location normal to the blade corresponding to (U_e). The external velocity has been calculated with two methods, the first one consisting of using the boundary-layer maximum velocity, such that $U_e = 0.99U_{max}$. To ensure the validity of the previous assumption, the total pressure boundary-layer profiles are calculated so that U_e is found at the location where the total pressure reaches its maximum, similarly to what has been done in [1]. The previous methods lead to the same external velocity values and thus, the latter has been used in the following investigations. We define the displacement and momentum thicknesses, respectively as δ^* and θ, by integrating the velocity over the boundary-layer thickness:

$$\delta^* = \int_0^\delta \left(1 - \frac{U(y)}{U_e}\right) dy, \tag{5.2}$$

$$\theta = \int_0^\delta \frac{U(y)}{U_e}\left(1 - \frac{U(y)}{U_e}\right) dy. \tag{5.3}$$

The pressure coefficient C_p at three spanwise locations is plotted as a function of the chordwise coordinate (where $x_c/c = 0$ at the leading-edge point) and is defined as:

$$C_p = \frac{p - p_\infty}{\frac{1}{2}\rho_\infty U_0^2}, \tag{5.4}$$

with $U_0 = r\Omega$ as the local entrainment velocity, whereas p_∞ and ρ_∞ are the laboratory pressure and air density, respectively. One can notice that we are in the presence of adverse pressure gradients on the blade suction side in the trailing-edge regions ($x_c/c > 0.8$) and therefore semi-empirical wall-pressure models that take them into account are implemented and discussed in Section 5.4.5.

5.4 Noise prediction methodology

An extension of Amiet's theory to rotating blades, initially developed by Schlinker and Amiet [25] and subsequently by Rozenberg et al. [8], is firstly proposed in order to take into account leading-edge and trailing-edge noise mechanisms. Following the work of Sanjosé and Moreau [1], the two sound-mechanism models present consistent similarities but will be treated separately when implementing Amiet's airfoil theory with or without taking into account the sweep-angle effect.

5.4.1 Noise emitted by rotating blades

To deal with spanwise-varying conditions, the fan blade is subdivided into strips (or segments) through isoradial cuts such that each strip encounters its own flow condition. The overall radiated fan noise is calculated as the sum of the sounds individually emitted by each strip to which the single-airfoil theory is applied, assuming that the circular motion can be approximated by an equivalent local translation. The relative motion between the listener and the source is afterward considered by including a Doppler frequency-shift factor and taking into account all the azimuthal blade locations as shown in Figure 5.11 (a) and expressed by Eq. (5.5). For a given listener angular frequency ω, the fan radiated noise is calculated as:

$$S_{pp}(\mathbf{x},\omega) = \frac{B}{2\pi}\int_0^{2\pi}\left(\frac{\omega_e(\Psi)}{\omega}\right)^2 S_{pp}^{\Psi}\left(\mathbf{y},\omega_e\right)d\Psi, \tag{5.5}$$

where $\mathbf{x}$ is the vectorial listener's position, whereas $\mathbf{y}$ is the source location; B represents the number of the blades, $\omega_e(\Psi)$ is the source emitted frequency for a given azimuthal position expressed by the angle $\Psi = \Omega t$, as depicted in Figure 5.11 (a). The Doppler factor has to be squared as proven by Sinayoko et al. [26] and for low-Mach number is given by the relation:

$$\frac{\omega_e(\Psi)}{\omega} = 1 + M_r \sin\Psi \sin\Theta, \tag{5.6}$$

in which M_r is the Mach number of the source relative to the fluid. The term $S_{pp}^{\Psi}(\mathbf{y},\omega_e)$ of Eq. (5.6) is obtained from the single-airfoil theory as the sum of the trailing-edge and leading-edge noise contributions such that $S_{pp}^{\Psi} = S_{pp}^{TE} + S_{pp}^{LE}$, discussed in the next paragraphs.

5.4.2 Leading-edge noise formulation

Based on the classical Amiet's analytical gust-airfoil interaction noise model [9], Roger et al. [7] extended the formulation to account for swept blades in order to predict tonal noise emitted by CRORs. In the following work, these developments are used to predict broadband sound sources as carried out for an isolated airfoil in the work of Giez et al. [27]. The sweep angle is defined as the angle between the fan radius line and the line locally tangent to the edge of the blade, as depicted in Figure 5.11 (b). A local reference frame (x, y, z) is defined, with the x axis parallel to the flow direction $U_0 = \Omega R$ (with the fan angular rotation Ω), the z axis perpendicular to the blade-strip plane and the y axis orthogonal to the previous two, pointing at the center of rotation. A second local reference frame (x', y', z) is obtained with a clockwise rotation around the z axis by the sweep angle ψ; the y' axis is now laying on the leading edge of the blade segment. We specify that Figure 5.11 (b) depicts the case where the reference frames are centered on the trailing-edge, valid for the TE noise formulation discussed later. For the LE formulation, the only difference is that the reference frames are located at the center of the strip, as Figure 5.12 illustrates. The chord c and

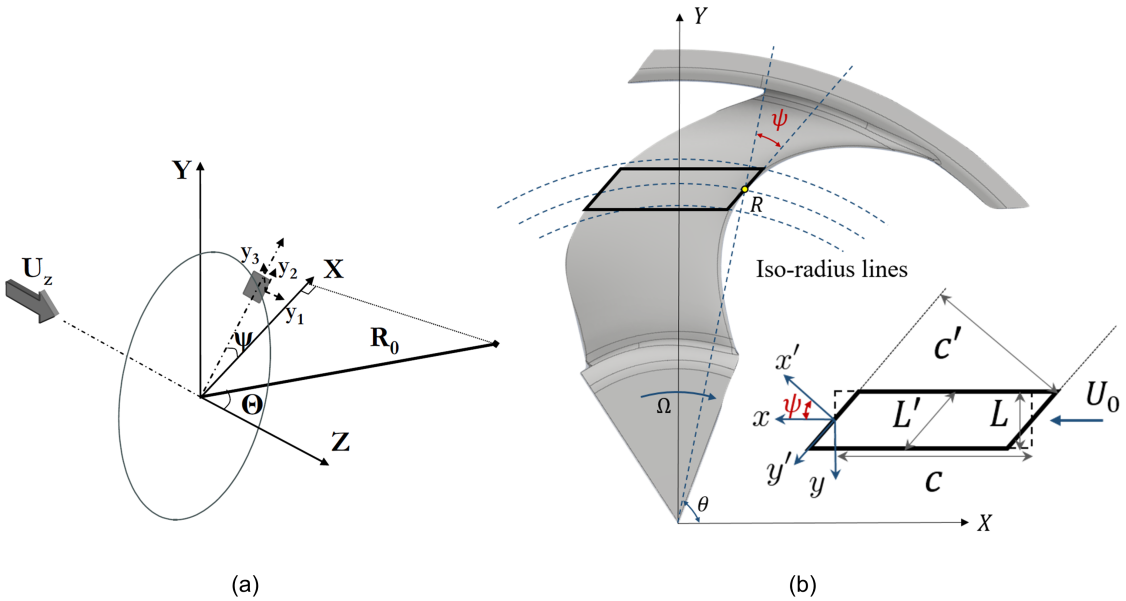

Figure 5.11: (a) From [8], rotating local airfoil reference frame. The fixed reference frame $\mathbf{x} = (X, Y, Z)$ *defines the observer's position. (b) Sweep-angle definition over the leading edge of the fan blade; the rotated local reference frame* (x', y', z) *is determined.*

span L of the blade segment are equivalently indicated in the same figure, as well as the rotated chord $c' = c\cos(\psi)$, parallel to x', and the rotated span $L' = L/\cos(\psi)$, parallel to y'. To have further information about the following formulation, the interested reader can refer to [7, 28, 29]. We define the acoustic wavenumber $k_a = \frac{\omega}{c_0}$ and the observer corrected distance S_0 to take into account the convection effects as:

$$S_0^2 = \beta_y^2 X_o^2 + \beta_x^2 Y_o^2 + \beta_0^2 Z_o^2, \quad \text{where} \quad \beta_{y,x,0} = \sqrt{1 - \left(\frac{U_{y,x,0}}{c_0}\right)^2}, \tag{5.7}$$

where (X_o, Y_o, Z_o) must refer to the rotated reference frame (x', y', z). Eq. (5.7) introduces the velocity component $U_x = \frac{U_0}{\cos\psi}$ perpendicular to the swept leading edge and the one parallel to it $U_y = \frac{U_0}{\sin\psi}$. The turbulence is assumed to be isotropic, frozen, and expanded into harmonics gusts. We write the power-spectral density (PSD) of the far-field acoustic pressure for a fluid with the speed of sound c_0 and the density ρ_0, with the assumption of large aspect ratio on the full blade span. This not only yields a simpler mathematical expression of the PSD reported in Eq. (5.8), but it is the only one that converges with the number of the strips. This was discussed in the Ph.D. thesis of Rozenberg (see Section 4.4.5 in [30]) and confirmed by Christophe et al. [31]. We write the PSD of the far-field sound as:

$$S_{pp}^{LE}(\mathbf{x}, \omega) = \left(\frac{\rho_0 \omega b' Z_o}{c_0 S_0^2}\right)^2 2\pi U_x \frac{L'}{2} \Phi_{ww}\left(\overline{K_x'}, \overline{K_y'}\right) \left|\mathcal{L}^{LE}\left(X_o, K_x', K_y'\right)\right|^2, \tag{5.8}$$

where $b' = c'/2$ and K_y' is the only involved gust, which can be verified to be always supercritical, as stated in [28], and is expressed as [6, 27]:

$$K_y' = \frac{k_a}{\beta_0^2}\left(\frac{\beta_x^2 Y_o}{S_0} - \frac{U_y}{c_0}\right). \tag{5.9}$$

Given the dispersion equation $\mathbf{U_0} \cdot \mathbf{K} = U_x K'_x + U_y K'_y$, the x'-wavenumber is defined as:

$$K'_x = \frac{\omega - K'_y U_y}{U_x}. \tag{5.10}$$

The mathematically-derived aeroacoustic wavenumber term $\mathcal{L}^{LE}$ does not consider the contribution of the trailing-edge back-scattering derived in [14], which is typically much smaller if compared to the main contribution:

$$\mathcal{L}^{LE} = -\frac{e^{-i\Theta_2}}{\pi}\sqrt{\frac{2}{\left(\overline{K'_x} + \beta_x^2\kappa\right)\Theta_1}}E\left[2\Theta_1\right]. \tag{5.11}$$

We define the parameter κ as:

$$\kappa^2 = \mu^2 - \frac{\overline{K'_y}^2}{\beta_x^2}, \quad \text{with} \quad \mu = \frac{\overline{K'_x} U_x}{c_0 \beta_x^2},$$

where $\overline{K'_x}$ and $\overline{K'_y}$ are the dimensionless wavenumbers; $E[-]$ is the Fresnel integral, whereas Θ_1 and Θ_2 can be can be written [7, 27, 29]:

$$\Theta_1 = \left(\kappa - M_x^2\overline{K'_x}/\beta_x^2\right) + b\left\{\tan\psi K'_y - \frac{k_a}{\beta_0^2 S_0}\left[\beta_y^2 X_o - S_0\frac{U_x}{c_0} + \tan\psi\left(\beta_x^2 Y_o - S_0\frac{U_y}{c_0}\right)\right]\right\},$$

$$\Theta_2 = \Theta_1 + \left(\frac{U_1^2\overline{K'_x}}{c_0^2\beta_x^2} - \kappa\right) - \pi/4.$$

The von Kármán's and Liepmann's spectrum models, assuming homogeneous isotropic turbulence, are used to calculate the two-wavenumber spectrum $\Phi_{ww}(K'_x, K'_y)$, analogously to what has been done in [1, 32]. Starting off from the steady RANS extracted data of Section 5.3, we can write the von Kármán's model spectrum as:

$$\Phi_{ww}^{VK}\left(K'_x, K'_y\right) = \frac{4}{9\pi}\frac{\overline{u^2}}{k_e^2}\frac{\hat{K'_x}^2 + \hat{K'_y}^2}{\left(1 + \hat{K'_x}^2 + \hat{K'_y}^2\right)^{7/3}}, \tag{5.12}$$

whereas, using the Liepmann's model spectrum:

$$\Phi_{ww}^{LM}\left(K'_x, K'_y\right) = \frac{3\overline{u^2}\Lambda_f^4\left(K'^2_x + K'^2_y\right)}{4\pi\left(1 + \Lambda_f^2\left(K'^2_x + K'^2_y\right)\right)^{5/2}}, \tag{5.13}$$

with $\overline{u^2}$ as the mean square of the velocity fluctuations, which is directly related to the RANS scalar turbulent kinetic energy k_t as: $\overline{u^2} = \frac{2}{3}k_t$.

The average wavenumber of the energy-containing eddies k_e in Eq. (5.14) is defined as:

$$k_e = \frac{\sqrt{\pi}}{\Lambda_f}\frac{\Gamma(5/6)}{\Gamma(1/3)}, \tag{5.14}$$

where the turbulent length scales Λ_f has been defined in Eq. (5.1).

5.4.3 Trailing-edge noise formulation

According to the original derivation by Amiet [10], afterward extended by Roger and Moreau in [14], the inclusion of the sweep-angle effect for the trailing-edge noise modeling, in this work, followed the recent work of Grasso et al. [6]. The PSD of the far-field noise for the large aspect ratio is given as:

$$S_{pp}^{TE}(\mathbf{x},\omega) = \left(\frac{\omega\cos\psi b' Z_o}{2\pi c_0 S_0^2}\right)^2 \pi L' \left|\mathcal{L}\left(\overline{K}_c', \overline{K}_y'\right)\right|^2 \Pi_0\left(\omega, \overline{K}_y'\right). \tag{5.15}$$

Consistently with the leading-edge formulation in the previous section, the main contribution of the aeroacoustic transfer function is written:

$$\mathcal{L}^{TE} = -\frac{\mathrm{e}^{2\mathrm{i}C/\cos\psi}}{\mathrm{i}C}\left\{(1+\mathrm{i})\mathrm{e}^{-2\mathrm{i}C/\cos\psi}\sqrt{\frac{2B}{\cos\psi}}\mathrm{ES}^*\left[\frac{2(B-C)}{\cos\psi}\right] + \right.$$
$$\left. - (1+\mathrm{i})\mathrm{E}^*\left[\frac{2B}{\cos\psi}\right] + 1 - \mathrm{e}^{-2\mathrm{i}C/\cos\psi}\right\}, \tag{5.16}$$

where the mathematical expressions of the functions $E^*[-]$ and $ES[-]$, both closely related to the Fresnel integral, are given for instance in [6]. The parameters B and C can be written as:

$$B = \left(\alpha\overline{K}_c' + \mu\frac{U_x}{c_0} + \kappa\right)\cos\psi,$$

$$C = \alpha\overline{K}_x'\cos\psi + \overline{K}_y'\sin\psi - \frac{\overline{k_a}}{\beta_0^2}\left(\frac{\beta_y^2 X_o\cos\psi}{S_0} + \frac{\beta_x^2 Y_o\sin\psi}{S_0} - \frac{U_0}{c_0}\right).$$

The $\overline{K_y'}$ term is given by Eq. (5.9), whilst the rotated convective wavenumber is shown in Eq. (5.17):

$$K_c' = \frac{\omega}{U_c\cos\psi} - K_y'\tan\psi, \tag{5.17}$$

assuming the frozen turbulence hypothesis can be applied such that the convective velocity is determined as $U_c = U_0/\alpha$, with $\alpha = 1.43$. In order to compare with far-field experimental results, as described in the original work of Amiet [10], Eq. (5.8) and Eq. (5.15) have to be multiplied by a factor $b_w = 2\pi$ needed to convert to a 1 Hz bandwidth. As indicated by [33], there is no need to multiply Eq. (5.15) by 2 to convert to a single-sided frequency spectrum, as done in [14], because all the wall-pressure models hereafter utilized are already single-sided. Nonetheless, Eq. (5.15) is further multiplied by 2 in order to account for the pressure and suction sides. According to [10], this factor of 2 should be used only for cases where two identical boundary layers are encountered on the pressure and suction sides. Even though with control diffusion airfoils the suction side is typically radiating more than the pressure side [1], the latter cannot be neglected in advance in view of the similar boundary-layer thicknesses. Nonetheless, no semi-empirical wall-spectrum model has been conceived to account specifically for favorable pressure gradients that we notice on the pressure-side trailing-edge region, as illustrated in Figure 5.4 (b). Hence, this 2 factor is used to be conservative about the emitted trailing-edge noise, yielding to a global multiplication factor of 4π.

5.4.4 Generalized Corcos' model

In Amiet's classical formulation, the separation of frequency and wavenumber variables of the Corcos' model [13] is assumed in order to write the wall-pressure PSD $\Pi_0(\omega, K_y)$ of Eq. (5.15) as:

$$\Pi_0(\omega, K_y) = \int_{-\infty}^{+\infty} \Pi(k_x, K_y, \omega)\, dk_x = \frac{1}{\pi}\varphi_{pp}(\omega) l_y(\omega/U_c, K_y), \tag{5.18}$$

where the complete frequency-wavenumbers wall-pressure power-spectral density $\Pi(k_x, K_y, \omega)$ is given by:

$$\Pi(k_x, k_y, \omega) = \varphi_{pp}(\omega) \frac{\frac{1}{\pi\alpha_\omega}}{1 + \left(\frac{k_x - k_\omega}{\alpha_\omega}\right)^2} \frac{\frac{1}{\pi\beta_\omega}}{1 + \left(\frac{k_y}{\beta_\omega}\right)^2}, \tag{5.19}$$

with $k_\omega = \omega/U_c$, $\alpha_\omega = \alpha_x\omega/U_c$ and $\beta_\omega = \beta_y\omega/U_c$. The coefficients $\alpha_x = 0.1$ and $\beta_y = 1/1.47$ are chosen within intervals suited for smooth rigid walls [15]. The spanwise correlation length $l_y(\omega/U_c, K_y)$ in Eq. (5.18) is obtained after integrating over k_x as in [14]:

$$l_y(\omega, K_y) = \frac{k_\omega/b_c}{K_y^2 + (k_\omega/b_c)^2}, \tag{5.20}$$

with b_c as a constant. Even though the mathematical simplicity of Eq. (5.20) is appealing, taking into account a skewed gust may lead to a wrong estimation of the spectral energy distribution on the streamwise and spanwise rotated wavenumbers. To overcome this problem, Grasso et al. [6] implemented the Generalized Corcos' model firstly developed in [15]. As introduced in the latter work, the Lorentzian functions originally utilized in the Corcos' model to describe the two spatial correlation lengths, are interpreted as Butterworth filters of orders $m = 1$ and $n = 1$. Thus, in the general case, Eq. (5.19) can be modified as:

$$\Pi(k_x, k_y, \omega) = \varphi_{pp}(\omega) \frac{\frac{n\sin(\pi/2n)}{\pi\alpha_\omega}}{1 + \left(\frac{k_x - k_\omega}{\alpha_\omega}\right)^{2n}} \frac{\frac{m\sin(\pi/2m)}{\pi\beta_\omega}}{1 + \left(\frac{k_y}{\beta_\omega}\right)^{2m}}. \tag{5.21}$$

Caiazzo et al. [15] intended this generalization to correct the low-wavenumber behavior that is causing the original Corcos' model to overestimate the contribution of the subconvective streamwise wavenumber range to a given angular frequency ω. The filter order coefficients m and n can be seen as free parameters to be adjusted in order to better approximate the experimental wall-pressure spectrum. When introducing the rotated streamwise and spanwise wavenumbers, a coupling between the coherence lengths appears:

$$\Pi(k'_x, k'_y, \omega) = \varphi_{pp}(\omega) \frac{\frac{n\sin(\pi/2n)}{\pi\alpha_\omega}}{1 + \left(\frac{k'_x\cos\psi + k'_y\sin\psi - k_\omega}{\alpha_\omega}\right)^{2n}} \frac{\frac{m\sin(\pi/2m)}{\pi\beta_\omega}}{1 + \left(\frac{-k'_x\sin\psi + k'_y\cos\psi}{\beta_\omega}\right)^{2m}}. \tag{5.22}$$

Nevertheless, the analytical integration over k'_x is still possible, but rather cumbersome, and it was performed by Grasso et al. [6] for a combination set of m and n order coefficients, by using the open-access software named Sage Math. The aim was to calculate a different spanwise correlation length l_y for each couple of m and n with the limit case of Eq. (5.19) when $m = 1$, $n = 1$. These derivations have been implemented in the following methodology in order to clarify their influence on the far-field radiated sound.

5.4.5 Semi-empirical wall-pressure models

As a closure to Eq. (5.15), semi-empirical models have been implemented to calculate the frequency-dependent part of the wall-pressure spectrum (WPS) $\phi(\omega)$. Originally proposed by Lee [11] and based on the work of Goody [34], a universal formulation can be used to describe the shape of $\phi(\omega)$ and expressed as:

$$\frac{\phi_{pp}}{\phi^*} = \frac{a(\omega^*)^b}{[i(\omega^*)^c + d]^e + [fR_T^g\omega^*]^h}, \tag{5.23}$$

where the parameters $a-h$ are set to modify the shape of the spectra according to the chosen model (more details on the effect of each coefficient can be found in [11, 35]), the rescaled wall-pressure spectrum and the circular frequency ϕ^* and ω^*, respectively; finally, R_T is the time-scale ratio which accounts for Reynolds number effects. Three different models will be considered hereafter, Goody's model that is suited to zero-pressure gradient profiles, Rozenberg's model that is tuned to take into account adverse-pressure gradient profiles, and Lee's model that is based on the previous two and can be applied in both cases.

5.4.5.1 Goody's model

Goody's model is based on the work of Chase [36] and Howe [37] and it is often taken as a reference model to compare with more recent ones [11]. The overlap region was extended by introducing the time-scale ratio, defined as the ratio of the outer time scale to the inner time scale as:

$$R_T = (\delta/U_e)/(\nu/u_\tau^2), \tag{5.24}$$

with the kinematic viscosity ν and the friction velocity u_τ. The angular frequency is scaled by $\omega^* = \delta/U_e$, whereas the wall-pressure spectrum model is scaled by $\phi^* = \tau_w^2\delta/U_e$, with τ_w as the wall-shear stress (directly related to the friction velocity as $u_\tau = \sqrt{\tau_w/\rho_\infty}$), which is estimated in the following sections applying the general method proposed by Bradshaw and Ferriss in [38]. The coefficients given in Eq. (5.23) for the Goody's model are $a = 3.0$, $b = 2$, $c = 0.75$, $d = 0.5$, $e = 3.7$, $f = 1.1$, $g = -0.57$, $h = 7.0$, and $i = 1.0$.

5.4.5.2 Rozenberg's model

In order to account for adverse pressure gradient flows, Rozenberg et al. [39] developed a model basing it on Goody's. The frequency is scaled by $\omega^* = \delta^*/U_e$, whereas the wall-pressure spectrum normalization is defined as $\phi^* = \tau_{max}^2\delta^*/U_e$, where the boundary-layer maximum wall-shear stress was introduced. Nevertheless, in this work τ_w has been employed instead, as suggested by Lee [11]. Other three parameters are determined to characterize the effect of the adverse pressure gradient: Zagarola-Smits' parameter $\Delta_* = \delta/\delta^*$ [40], Clauser's equilibrium parameter [41] $\beta_c = (\theta/\tau_w)\,(dp/dx)$, and Coles' wake parameter [42] Π. The latter is estimated using the empirical formula given by Durbin and Reif in [43], $\Pi = 0.8(\beta_c + 0.5)^{3/4}$. The other parameters in section 5.4.5 are defined as:

- $a = [2.82\Delta_*^2\left(6.13\Delta_*^{-0.75} + d\right)^e]\,[4.2\,(\Pi/\Delta_*) + 1]$,
- $b = 2.0$,
- $c = 0.75$,
- $d = 4.76\,(1.4/\Delta_*)^{0.75}\,[0.375e - 1]$,

- $e = 3.7 + 1.5\beta_c$,
- $f = 8.8$,
- $g = -0.57$,
- $h = \min\left(3, 19/\sqrt{R_T}\right) + 7$,
- $i = 4.76$.

One may notice that here, unlike Goody's model, the parameters have to be determined as functions of the pressure gradient dp/dx, which is directly provided by the RANS computation at the blade wall and it is rotated to follow the isoradial curvature of the blade suction side.

5.4.5.3 Lee's model

Lee [11] recently proposed a model to extend the validity of Rozenberg's model to low and high-pressure gradient flows, as well as to higher β_c values, for extensive applications. Most of the parameters used for Rozenberg's model are kept the same with some exceptions discussed hereafter. First, the spectrum is scaled by the wall-shear stress τ_w, rather than using the maximum shear stress τ_{max} over the boundary-layer length. To correct the higher amplitudes for low and middle frequencies predicted by Rozenberg's model in low-pressure gradient flows, the parameter d is modified as $d = \max(1.0, 1.5d)$ if $\beta_c < 0.5$. The parameter a is adjusted as $a = \max(1, (0.25\beta_c - 0.52)a)$. To compensate for the rapid decay rate encountered in Rozenberg's model for zero and low-pressure gradient flows, the parameter h is modified as follows:

$$h = \min\left(5.35, 0.139 + 3.1043\beta_c, 19/\sqrt{R_T}\right) + 7, \tag{5.25}$$

whereas the following expression has to be used if $h = 12.35$:

$$h = \min\left(3, 19/\sqrt{R_T}\right) + 7. \tag{5.26}$$

5.5 Acoustic far-field results

The implementation of the single-airfoil Amiet's analytical formulations including the sweep-angle effect has been compared and validated with the work of Giez et al. [27] for the LE noise case, and with the work of Grasso et al. [6] for the TE noise case. The strip-theory approach is illustrated in Figure 5.12 (a) for the LE noise case, where 10 blade strips have been generated together with their local reference frames at the center of the segments performing equidistant cuts along the radius line. An improvement taking into account the sweep angle is shown in Figure 5.12 (b), where the leading-edges of the blade planes are now locally parallel to the forward-skewed curvature of the blade. A similar approach has been implemented to carry out the blade segments for the TE formulation as shown in Figure 5.13. Nevertheless, for this specific case, the blade segments are obtained by subdividing the TE line into equidistant cuts. In fact, when the blade is divided into evenly distributed segments over the radius, a systematic underestimation of about 2 dB in the far-field noise is observed due to the fact that the strips would have a too-short span. On the contrary, one can notice in Figure 5.13 (b) that the trailing-edge line is completely covered using this distribution of the isoradial strips. A convergence study was carried out in order to establish the minimum number of strips to acceptably discretize the noise emissions along the

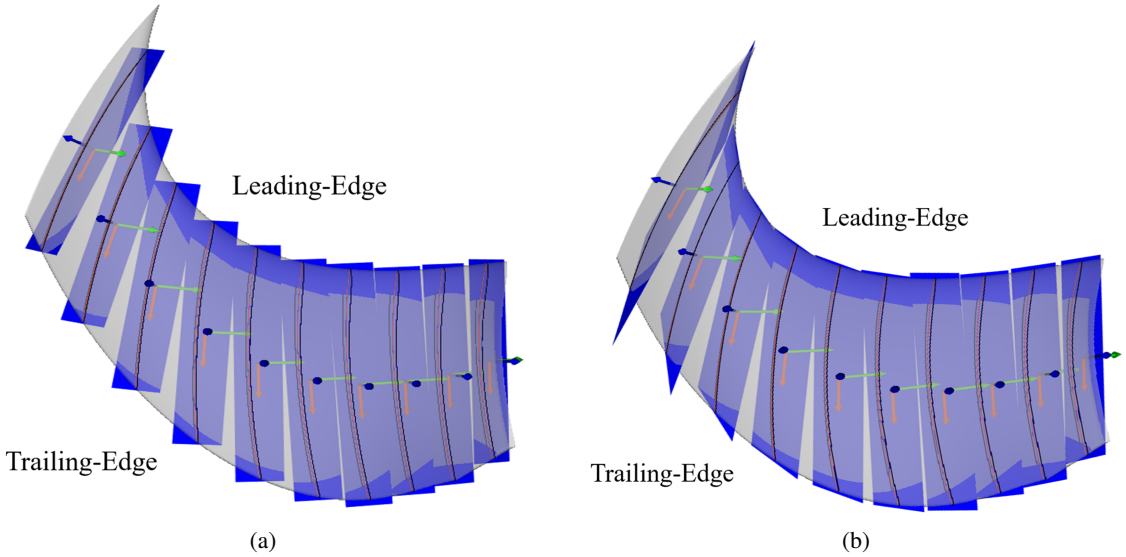

Figure 5.12: For the leading-edge case, the blade is divided into 10 segments: in (a), a classical unswept leading-edge formulation can be used; in (b), the effect of the sweep is evaluated with blade strips which have locally parallel leading-edges, following the blade forward-skewed curvature.

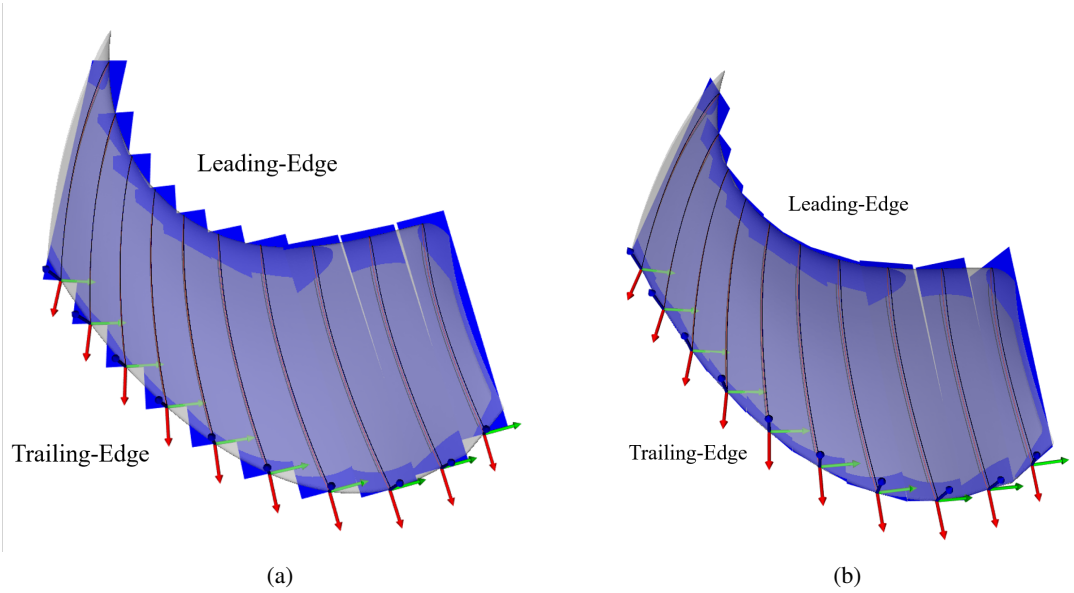

Figure 5.13: For the trailing-edge case, the blade is divided into 10 *segments: in (a), a classical unswept trailing-edge formulation can be used; in (b), the effect of the sweep is evaluated with blade strips which have locally parallel trailing-edges, following the blade forward-skewed curvature.*

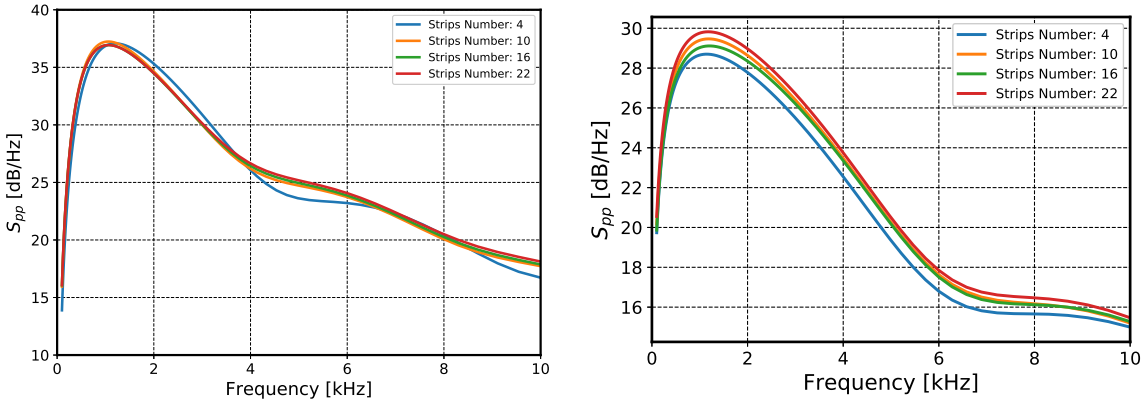

Figure 5.14: Convergence study on the number of strips to use in order to acceptably discretize the noise sources on the blade span: (a) leading-edge noise prediction case, (b) trailing-edge noise prediction case.

blade span. For both sound mechanisms, the blade is finally cut in 16 strips: this value is kept throughout the study. While for the LE case, illustrated in Figure 5.14 (a), the convergence is quite fast, for the TE case in Figure 5.14 (b) small differences up to about 1 dB are depicted between the 16 and 22 strips cases. This is due to the 3D discretization of the blade as well as to the distribution of the strips over the most emitting areas.

5.5.1 Noise distribution over the strips

For the two noise mechanisms, the unswept classical Amiet's formulations [9, 10] are retrieved as a limit case where $\psi = 0$. In Figure 5.15, the LE and TE noise methodologies are compared with respect to the unswept Amiet's formulation. Three strips are reported with a respective distance from the hub of y/L_B. In Figure 5.15, one can generally notice that closer to the tip, the far-field sound predicted by the unswept approach is higher, due to the radial linear increase of the relative velocity. The effect of the sweep is to reduce, mainly in amplitude, the PSD of each strip. We mention that at $y/L_B = 0.22$, the local blade sweep is near 0, and therefore the unswept (UN) and swept (SW) formulations give very close results.

For the LE case, depicted in Figure 5.15 (a), the unswept formulation shows higher PSD values nearer the tip and beyond 1.9 kHz. Nevertheless, for the swept formulation, the strip at $y/L_B = 0.22$ is seen to be louder than the one at $y/L_B = 0.59$ throughout all frequencies. For low to middle frequencies, this can be explained by the high values of $\overline{u^2}$, which are found in the range $0.15 < y/L_B < 0.45$, as depicted in Figure 5.9 (a). In fact, the mean square of the velocity fluctuations is directly linked to the turbulent kinetic energy content found in the RANS simulation and depicted in Figure 5.16 (a). This increase of k_t has been found in other studies with similar fans, as Figure 9 in [19] illustrates. Particularly at the tip of the blade, where the curvature reaches around 70 degrees, considering the sweep angle leads to a substantial decrease of the emitted noise and, therefore, the strip at $y/L_B = 0.22$ turns out to be the dominant one. This is an important result because it shows that we cannot assume in advance that the tip of the blade is the most emitting one just in view of the higher relative velocities. Thus, only considering the unswept classical Amiet's formulation can lead to this erroneous conclusion. Analogously for

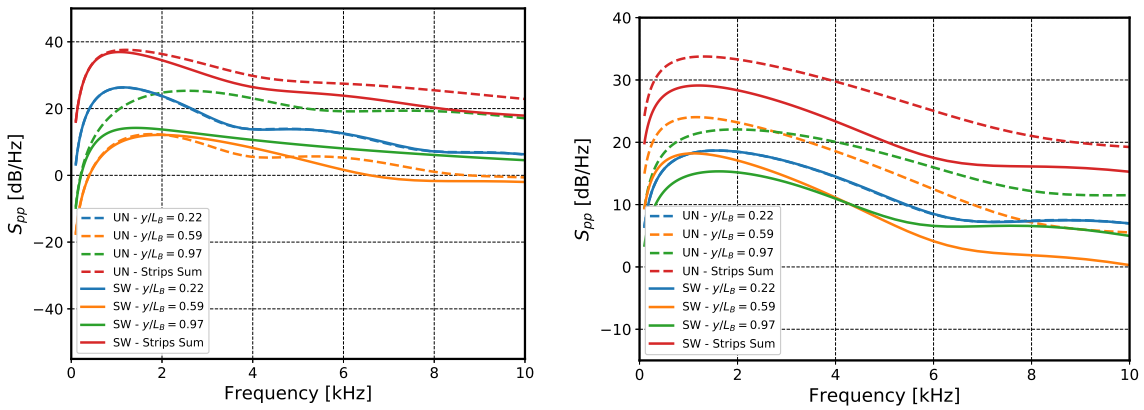

(a) (b)

Figure 5.15: Far-field sound power-spectral density (PSD) distribution over the blade span. The dashed curves represent the classical Amiet's theory, whilst the solid ones take into account the varying sweep-angle: (a) leading-edge noise prediction case, (b) trailing-edge noise prediction case.

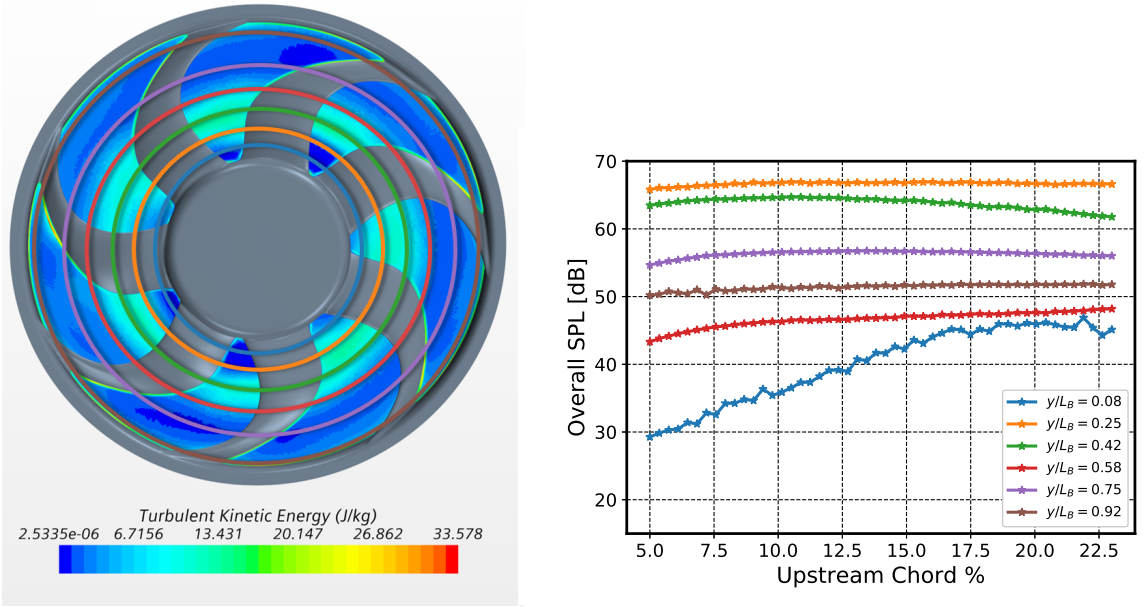

(a) (b)

Figure 5.16: The turbulent kinetic energy content is shown in (a); colored concentric circles represent the isoradial locations at which the blade is cut in order to study the overall SPL of the strips shown in (b). Here, the overall SPL is depicted against the upstream chord distance from the leading-edge point.

the TE noise, the most emitting strip is at $y/L_B = 0.22$, in the range where the C_p reaches its peak, as depicted in Figure 5.10 (b).

5.5.2 Leading-edge upstream extraction location

It is not trivial to define the upstream chord distance at which the RANS data $\overline{u^2}$ and Λ_f should be extracted in order to feed the turbulence models. In Figure 5.16 (b), six strips are used for the SW LE sound case. On the x-axis the upstream chord percentage distance from the LE is defined, whereas, on the y-axis, the overall SPL has been calculated as the integral of the strip PSD over the frequency spectrum. Once again, one can notice that the most emitting strips are the ones in the $0.15 < y/L_B < 0.45$ interval, whilst the overall SPL curve of the strip closer to the tip is substantially reduced by the local high sweep angle. Except for the least emitting strip near the fan hub, the overall SPL of the remaining curves converges to a plateau between 10% and 15% of the chord upstream. For this reason, a value of 12% is used for the following results. On the other hand, for the TE formulation case, the boundary layers are extracted at 85% of the chord, as done in [1].

5.5.3 LE and TE noise comparison with experimental PSD

The acoustic far-field predicted results are compared in Figure 5.17 with the measured spectrum of the fan at its nominal operating condition. The sound has been measured at $1\,\mathrm{m}$ distance from the fan suction side (in the upstream anechoic chamber), with the microphone aligned with the fan center of rotation. The experimental sound curve presents tonal contributions, particularly at the blade-passing frequency (around $400\,\mathrm{Hz}$) and its harmonics not accounted for in the prediction methodology. When including the sweep-angle effect, the LE noise mechanism appears to be relevant throughout the whole frequency spectrum, while still being comparable to the TE noise around $3.75\,\mathrm{kHz}$ and at very high frequencies. This is in agreement with the rotating beamforming result, on the same automotive fan, at the same working condition investigated by Amoiridis et al. [44] (see Figure 13), as well as with the results of Herold et al. [3]. The unswept behavior is fairly similar to the one computed in Figure 10 by Sanjose and Moreau in [1], on a similar but less forward-skewed automotive fan (H380EC1). We can affirm that the sum of the LE and TE sound mechanisms for the swept formulation is in fairly good agreement with the experimental curve, especially at high frequency, resulting in a better description of the noise emission with respect to the unswept classical Amiet's formulation. The unswept case overpredicts the radiated noise in this frequency range. As expected, the methodology is not suited to model the sound spectrum for very low frequencies; in this region, most of the radiated sound is generated by subharmonic coherent vortical structures convected upstream within the gap between the fan shroud and the rotating ring [17, 18]. Secondary flows with more broadband behavior as well as recirculation bubbles under the trailing-edge pressure side of the blade can also take place in the tip and near the hub regions [19], but their modeling would require higher-order CFD inputs to feed the semi-analytical models.

5.5.4 Sensitivity study

In Figure 5.17, the von Kármán's model, Lee's model, and the original Corcos' model with $m = 1$ and $n = 1$ have been used to delineate the far-field results. Nevertheless, it is interesting to investigate which of the models proposed in Section 5.4 provides the best comparison with respect to the experimental far-field acoustics. Figure 5.18 (a) shows that among the three semi-empirical wall-pressure models, Lee's and Rozenberg's better compare with respect to Goody's, the latter giving a PSD reduction of up to $3\,\mathrm{dB}$. This is expected as Goody's model does not account for the effect of adverse pressure gradients developing on the blades, and consequently underpredicts the low frequencies. This is consistent with the results reported by Sanjose and

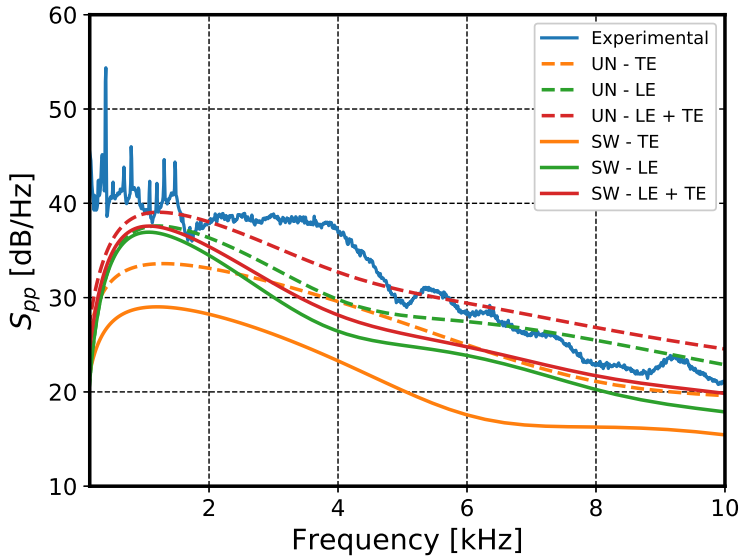

Figure 5.17: PSD of the far-field emitted sound by the fan at its nominal working point: the solid red line representing the sum of trailing-edge (TE) and leading-edge (LE) noise contributions for the swept case (SW) is in fairly good agreement with the experimental curve in solid blue, especially at high frequency, resulting into a better description of the noise emission with respect to the unswept (UN) classical Amiet's formulation shown in dashed line. In this plot, Lee's model and Corcos' model with $m = 1$ and $n = 1$ are employed for the TE noise prediction, whilst the von Kármán's model is used for the LE noise prediction.

Moreau on the H380EC1 fan [1]. A negligible shift in frequency is encountered when employing von Kármán's or Liepmann's models for the LE noise prediction, also in agreement with [1, 45]. Several combinations of Butterworth-filter orders have been tested in Figure 5.18 (b), appearing to have a negligible effect on the TE noise prediction, with a relative difference of less than $1\,\mathrm{dB}$.

5.6 Conclusions

We implemented a semi-analytical methodology, based on Amiet's theory, to predict the leading-edge and the trailing-edge noise mechanisms for an automotive fan with forward-skewed blades. The aim of the present work was to extend the low-order noise prediction methodology developed in [12], exploiting the same near-field steady RANS computation and comparing the results with the experimental ones. The blades have been divided into strips through isoradius cuts where the single-airfoil Amiet's theory has been implemented, taking into account the local sweep angles for the leading and trailing edges separately.

The overall effect of considering swept blades with respect to the classical Amiet's formulations is a reduction of the predicted noise for both sound mechanisms and throughout the entire frequency spectrum. This mitigating effect is particularly efficient at the blade tip, where the highest values of local sweep angles are reached. In fact, the most emitting strips are found to be the ones within the interval $0.15 < y/L_B < 0.45$. A crucial consideration is that neglecting sweep effects can lead to the erroneous conclusion that the dominant strips are the ones at the tip of the blade, due to higher relative velocities, whereas in that area the forward curvature mitigates substantially the noise emission. Considering the sweep-angle effects also allows us to discern the

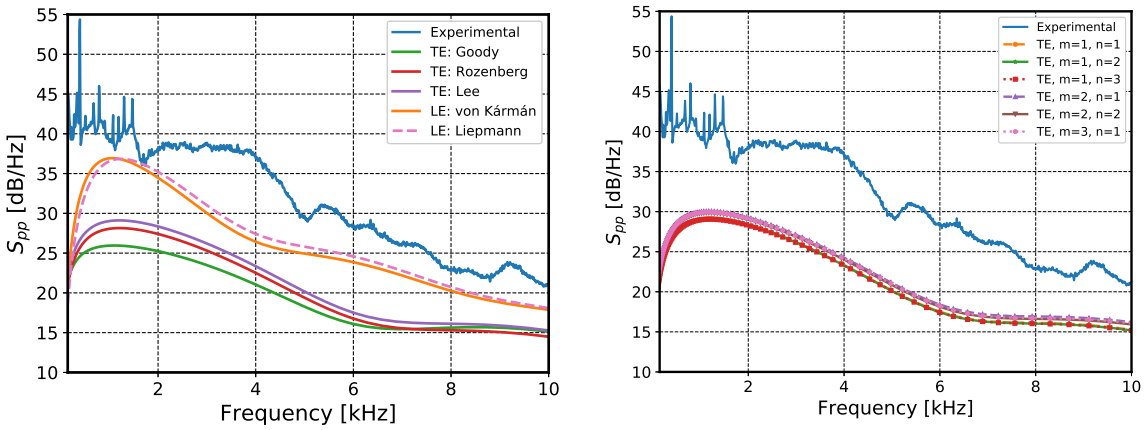

(a) (b)

Figure 5.18: A parametric study is proposed for the SW case by comparing the predicted results with the measured ones: in (a), 3 semi-empirical wall-pressure models Lee's, Rozenberg's, and Goody's are compared for the TE case; 2 turbulence velocity fluctuations models: von Kármán's and Liepmann's are compared for the LE case. In (b), several combinations of the Corcos' order coefficients m and n are tested out.

relative importance between the LE and TE noise mechanisms, the former being globally dominant but comparable to the latter around $3.75\,\mathrm{kHz}$ and at very high frequencies, in agreement with [1, 3, 44].

A sensitivity analysis complements this work by studying three of the modeling key parameters. Firstly, the correct location at which one has to extract the CFD information to feed the LE noise model is proposed to be at 12% of the chord, upstream of the leading-edge location. Secondly, the semi-empirical models that account for adverse pressure gradient flows are the best at comparing with the experimental results in agreement with [19]; specifically, Lee's model exhibits the best trend. Thirdly, the relatively new Generalized Corcos's model was implemented to calculate the spanwise integral length scale with a formulation that accounts for the coupled influence of the skewed wavenumbers on the spectral energy. Even though further investigations are required, the Butterworth-filter order coefficients seem to have a negligible influence on the far-field noise prediction.

References

[1] Marlène Sanjosé and Stéphane Moreau. *Fast and accurate analytical modeling of broadband noise for a low-speed fan*. The Journal of the Acoustical Society of America, 143(5):3103–3113, May 2018.

[2] F. B. Metzger and C. Rohrbach. *Benefits of blade sweep for advanced turboprops*. Journal of Propulsion and Power, 2(6):534–540, November 1986.

[3] Gert Herold, Florian Zenger, and Ennes Sarradj. *Influence of blade skew on axial fan component noise*. International Journal of Aeroacoustics, 16(4-5):418–430, July 2017.

[4] Stéphane Moreau and Michel Roger. *Competing Broadband Noise Mechanisms in Low-Speed Axial Fans*. AIAA Journal, 45(1):48–57, January 2007.

[5] Michel Roger, Stephane Moreau, and Alain Guedel. *Broadband fan noise prediction using single-airfoil theory*. Noise Control Engineering Journal, 54(1), January 2006.

[6] Gabriele Grasso, Michel Roger, and Stéphane Moreau. *Effect of sweep angle and of wall-pressure statistics on the free-field directivity of airfoil trailing-edge noise*. In 25th AIAA/CEAS Aeroacoustics Conference, Delft, The Netherlands, May 2019.

[7] Michel Roger, Christophe Schram, and Stéphane Moreau. *On vortex–airfoil interaction noise including span-end effects, with application to open-rotor aeroacoustics*. Journal of Sound and Vibration, 333(1):283–306, January 2014.

[8] Yannick Rozenberg, Michel Roger, and Stéphane Moreau. *Rotating Blade Trailing-Edge Noise: Experimental Validation of Analytical Model*. AIAA Journal, 48(5):951–962, May 2010.

[9] R.K. Amiet. *Acoustic radiation from an airfoil in a turbulent stream*. Journal of Sound and Vibration, 41(4):407–420, August 1975.

[10] R.K. Amiet. *Noise due to turbulent flow past a trailing edge*. Journal of Sound and Vibration, 47(3):387–393, August 1976.

[11] S. Lee. *Empirical Wall-Pressure Spectral Modeling for Zero and Adverse Pressure Gradient Flows*. AIAA Journal, 56(5):1818–1829, May 2018.

[12] Alessandro Zarri, Julien Christophe, and Christophe F Schram. *Low-Order Aeroacoustic Prediction of Low-Speed Axial Fan Noise*. In 25th AIAA/CEAS Aeroacoustics Conference, page 2760, 2019.

[13] G. M. Corcos. *The structure of the turbulent pressure field in boundary-layer flows*. Journal of Fluid Mechanics, 18:353–379, 1964.

[14] Michel Roger and Stéphane Moreau. *Back-scattering correction and further extensions of Amiet's trailing-edge noise model. Part 1: theory*. Journal of Sound and Vibration, 286(3):477–506, September 2005.

[15] A. Caiazzo, R. D'Amico, and W. Desmet. *A Generalized Corcos model for modelling turbulent boundary layer wall pressure fluctuations*. Journal of Sound and Vibration, 372:192–210, June 2016.

[16] Manuel Henner, Bruno Demory, Mohamed Alaoui, Maxime Laurent, and Benjamin Behey. *Effect of Blade Curvature on Fan Integration in Engine Cooling Module*. Acoustics, 2(4):776–790, October 2020.

[17] Stéphan Magne, Stéphane Moreau, and Alain Berry. *Subharmonic tonal noise from backflow vortices radiated by a low-speed ring fan in uniform inlet flow*. The Journal of the Acoustical Society of America, 137(1):228–237, January 2015.

[18] Stéphane Moreau and Marlène Sanjosé. *Sub-harmonic broadband humps and tip noise in low-speed ring fans*. The Journal of the Acoustical Society of America, 139(1):118–127, January 2016.

[19] M. Sanjosé, D. Lallier-Daniels, and S. Moreau. *Aeroacoustic Analysis of a Low-Subsonic Axial Fan*. In Volume 1: Aircraft Engine; Fans and Blowers; Marine, Montreal, Quebec, Canada, June 2015. ASME.

[20] M. Bilka, J. Anthoine, and C. Schram. *Design and evaluation of an aeroacoustic wind tunnel for measurement of axial flow fans*. The Journal of the Acoustical Society of America, 130(6):3788–3796, December 2011.

[21] Yongsheng Lian and Wei Shyy. *Laminar-Turbulent Transition of a Low Reynolds Number Rigid or Flexible Airfoil*. AIAA Journal, 45(7):1501–1513, July 2007.

[22] M. Henner, B. Demory, F. Franquelin, Y. Beddadi, and Z. Zhang. *Test Rig Effect on Performance Measurement for Low Loaded Large Diameter Fan for Automotive Application*. In Volume 1A: Aircraft Engine; Fans and Blowers, Düsseldorf, Germany, June 2014. American Society of Mechanical Engineers.

[23] Katepalli R. Sreenivasan. *On the universality of the Kolmogorov constant*. Physics of Fluids, 7(11):2778–2784, November 1995.

[24] H. K. Versteeg and W. Malalasekera. *An introduction to computational fluid dynamics: the finite volume method*. Pearson Education Ltd, Harlow, England ; New York, 2nd ed edition, 2007.

[25] R. Schlinker and R. Amiet. *Helicopter rotor trailing edge noise*. In 7th Aeroacoustics Conference, Palo Alto,CA,U.S.A., October 1981. AIAA.

[26] S. Sinayoko, M. Kingan, and A. Agarwal. *Trailing edge noise theory for rotating blades in uniform flow*. Proceedings of the Royal Society A: Mathematical, Physical and Engineering Sciences, 469(2157), September 2013.

[27] Justine Giez, Laurence Vion, Michel Roger, and Stephane Moreau. *Effect of the Edge-and-Tip Vortex on Airfoil Selfnoise and Turbulence Impingement Noise*. In 22nd AIAA/CEAS Aeroacoustics Conference, Lyon, May 2016. AIAA.

[28] Stéphane Moreau and Michel Roger. *Advanced noise modeling for future propulsion systems*. International Journal of Aeroacoustics, 17(6-8):576–599, November 2018.

[29] Michel Roger and Arnulfo Carazo. *Blade-Geometry Considerations in Analytical Gust-Airfoil Interaction Noise Models*. In 16th AIAA/CEAS Aeroacoustics Conference, Stockholm, Sweden, June 2010.

[30] Yannick Rozenberg. *Modélisation analytique du bruit aérodynamique à large bande des machines tournantes: utilisation de calculs moyennés de mécanique des fluides*. PhD thesis, École Centrale de Lyon, 2007.

[31] J. Christophe, J. Anthoine, and S. Moreau. *Amiet's Theory in Spanwise-Varying Flow Conditions*. AIAA Journal, 47(3):788–790, March 2009.

[32] Julien Christophe. *Application of Hybrid Methods to High Frequency Aeroacoustics*. PhD Thesis, ULB - VKI, 2011.

[33] Kevin Volkmer and Thomas Carolus. *Correction: Aeroacoustic airfoil shape optimization utilizing semi-empirical models for trailing edge noise prediction*. In 2018 AIAA/CEAS Aeroacoustics Conference, Atlanta, Georgia, June 2018. American Institute of Aeronautics and Astronautics.

[34] Michael Goody. *Empirical Spectral Model of Surface Pressure Fluctuations*. AIAA Journal, 42(9):1788–1794, September 2004.

[35] Yakut Cansev Küçükosman, Julien Christophe, and Christophe Schram. *Trailing edge noise prediction based on wall pressure spectrum models for NACA0012 airfoil*. Journal of Wind Engineering and Industrial Aerodynamics, 175:305–316, April 2018.

[36] D M Chase. *Turbulent Boundary Layer Wall Pressure*. Journal of Sound and Vibration, 70(1):29–67, 1980.

[37] M. S. Howe. *Acoustics of Fluid-Structure Interactions*. Cambridge University Press, 1 edition, August 1998.

[38] P. Bradshaw and D. H. Ferriss. *Applications of a General Method of Calculating Turbulent Shear Layers*. Journal of Basic Engineering, 94(2):345–351, June 1972.

[39] Yannick Rozenberg, Gilles Robert, and Stéphane Moreau. *Wall-Pressure Spectral Model Including the Adverse Pressure Gradient Effects*. AIAA Journal, 50(10):2168–2179, October 2012.

[40] Mark V. Zagarola and Alexander J. Smits. *Mean-flow scaling of turbulent pipe flow*. Journal of Fluid Mechanics, 373:33–79, October 1998.

[41] Francis H. Clauser. *Turbulent Boundary Layers in Adverse Pressure Gradients*. Journal of the Aeronautical Sciences, 21(2):91–108, February 1954.

[42] Donald Coles. *The law of the wake in the turbulent boundary layer*. Journal of Fluid Mechanics, 1(2):191–226, July 1956.

[43] P. A. Durbin and B. A. Pettersson Reif. *Statistical Theory and Modeling for Turbulent Flows*. John Wiley & Sons, Ltd.

[44] Orestis Amoiridis, Alessandro Zarri, Riccardo Zamponi, Julien Christophe, Christophe F. Schram, Gyuzel Yakhina, and Stephane Moreau. *Experimental Analysis of the Sound Radiated by an Automotive Cooling Module Working at Different Operational Conditions*. In AIAA AVIATION 2020 FORUM, VIRTUAL EVENT, June 2020. American Institute of Aeronautics and Astronautics.

[45] Sébastien Guérin, Carolin Kissner, Pascal Seeler, Ricardo Blázquez, Pedro Carrasco Laraña, Hélène de Laborderie, Danny Lewis, Paruchuri Chaitanya, Cyril Polacsek, and Johan Thisse. *ACAT1 Benchmark of RANS-Informed Analytical Methods for Fan Broadband Noise Prediction: Part II—Influence of the Acoustic Models*. Acoustics, 2(3):617–649, August 2020.

6
General conclusions

The work presented in this manuscript is aimed at studying the noise emitted by automotive cooling modules, which are among the vehicle components with the loudest noise emissions under conditions such as stopping at traffic lights or due to rush hour traffic. Several experimental, numerical, and analytical techniques were employed in order to isolate, quantify, and simulate the dominant broadband sound generation mechanisms. The whole study involved a cooling module manufactured by the French company Valeo, consisting of a radiator or heat exchanger clamped to the suction side of a low-speed axial fan. The first is constituted of a dense core of cooling pipes, with fins and louvers that increase the heat exchange between the vehicle engine and the surrounding environment. The second is composed of 7 unevenly spaced blades, curved or swept in the direction of rotation and joined together by a spinning L-shaped ring. This automotive module, which continues to be widely used on the road, was chosen because we were interested in studying a case as close as possible to real working conditions. In particular, we directed our interest toward the effect that the presence of the radiator plays on the sound sources occurring on the fan blades. In fact, in the literature, it was noted that there was no clarity on this installation effect, since in some studies the presence of the radiator increases the sound emissions with respect to the fan-alone case (as a result of the turbulence produced and the onset of turbulence-interaction noise), whereas in other investigations the radiator seems to reduce the noise produced (as a result of the chopping of large eddies that reach the fan-alone case). To this end, two experimental campaigns in two different anechoic laboratories were conducted: at the von Karman Institute for Fluid Dynamics, in Belgium, and at the Université de Sherbrooke, in Canada. After implementing and validating a time-based beamforming algorithm for rotational sound source identification (ROSI), we applied it to the study of three working conditions (low, nominal, and high-flow rate) of the cooling module, with and without the radiator, in the ALCOVES lab at VKI. Instead, in the Canadian laboratory, we repeated the study of the ROSI algorithm in the conditions at $\Delta P = 0$ (very similar to the high-flow rate studied at VKI), complementing it with directivity and velocity-scaling analysis of the SPL. The results clearly showed that, for the frequencies where ROSI can distinguish the contribution of each blade (above the limit imposed by the Rayleigh criterion) on the sound-localization maps, the sources are always located at the tip of the blades at the leading edge, regardless of the fan operating condition and whether the upstream radiator is present or

not. Consequently, the dominant mechanism of sound production does not appear to be originating from the turbulent flow generated by the radiator. The latter also allows the reconstruction of sound sources despite being located between the fan and the microphone array, demonstrating negligible transmission loss, even at high frequencies. The present evidence leads one to believe that it is in the tip gap between the rotating ring and the fan casing where the turbulent flow responsible for the dominant sound sources is originated. This validates existing high-fidelity LBM/VLES studies that have simulated the far-field noise with and without the radiator, albeit the geometry of the latter has always been modeled by porous media to limit the computational cost. The two experimental campaigns mentioned above have also confirmed the use of rotating beamforming algorithms as a valuable tool for acoustic source analysis in these applications and have allowed for the creation of a database that includes fan studies under various conditions, which may be useful for tier-one suppliers during their design phases and for validating high-fidelity aeroacoustic simulations.

The research described so far, however, prevents investigating the characteristics of the turbulent flow that is produced downstream of the radiator. Hence, a second experimental campaign based on stereo-PIV was carried out at VKI to assess the turbulence intensity production and dissipation, as well as the non-homogeneity and anisotropy levels of the flow past the radiator. To reproduce the effect of the contraction of the flow streamlines due to the fan casing, a circularly-holed wood panel was mounted downstream of the heat exchanger. For both instances, with and without the panel (RA and PR, respectively), two fields of view were studied, namely at the center of the heat exchanger ($z = 0$ cm) and laterally ($z = 10$ cm), near the circular hole. Several methods to quantify the level of non-homogeneity and anisotropy were used. The findings indicate that, in the region where the downstream fan would be located ($x/M = 12$), the flow is far from being homogeneous in the transverse direction. This is caused by the wakes of the radiator fins that can extend to large distances downstream (beyond the FOV studied). The flow in this region does not yet exhibit isotropic behavior although an evolution towards this state is clear, particularly when, due to the presence of the panel, the flow is accelerated. When observing the turbulence intensity trend downstream of the radiator, we can distinguish a generation zone followed by a decay. This does not follow a specific power law as widely documented in studies of turbulence decay produced by classical turbulence grids. However, the turbulence intensity decreases below 6% at $x/M = 12$, for each velocity field under examination. Comparing these values with previous studies, we noticed that the upstream conditions of the fan have to attain much higher turbulence intensities to have a notable impact on the noise spectrum. This occurs especially in cases where radiators have larger gaps between their cooling pipes, in contrast to the dense core of the radiator under investigation, which rather acts as a chopper of large vortical structures. However, as the turbulence produced by the radiator arriving at the fan inlet is not negligible, we verified whether the von Kármán turbulence model, which assumes isotropy and homogeneity, was still applicable in the present case (which we recall being fairly inhomogeneous and anisotropic). This comparison is made possible because, by means of the three velocity components computed with stereo-PIV, one can calculate the experimental two-dimensional turbulent spectrum and compare it with the von Kármán model. The latter is based on the experimental integral length scale obtained from the two-dimensional correlation functions. The results show that the von Kármán model approximates the experimental turbulence spectrum reasonably well but care must be taken to apply it when the flow undergoes a rapid acceleration such as that due to the contraction imposed by the panel.

The last part of the manuscript is devoted to the low-order simulation of the noise emitted by the fan alone. A computational domain reproducing the nominal working condition of the fan was

created, replicating the real labyrinth gap geometry. The purpose of this work was to investigate the effect of blade sweep on noise generation. This was done by appropriately extending and implementing Amiet's theory in order to model leading-edge and trailing-edge noise. The results indicate that the effect of the sweep angle is to mitigate noise emissions considerably, especially at the blade tip where the relative velocity is greater as is the sweep angle. This proved to be a key parameter that should be taken into account if the low-order methodology is to be included in pre-design industrial optimization phases. Despite the simulation presenting a clean inflow condition, in agreement with the experimental results obtained from the experimental sound localization maps discussed above, the leading edge of the blade is shown to be the area with the highest sound emissions. The effect of the analytical sweep model, however, is to show as dominant the blade section at about one-third of the blade span from the hub (especially at frequencies around $1000\,\mathrm{Hz}$). Although the contribution of the blade tip becomes relevant also for the analytical results at higher frequencies, the experimental maps clearly show that at those frequencies the blade tip is the most dominant region. This apparent inconsistency is still being investigated but is likely due to the three factors listed here. The CFD approach used is steady and, although the turbulent kinetic energy increase is modeled within the ring gap region, it does not account for the large periodic turbulent eddies that develop here. In fact, previous studies have shown that smaller structures that are re-ingested by the impeller come to form precisely from the ripping of the larger ones. Secondly, the sweep considered is the geometric one; however, the streamlines at the blade tip might present radial components that can vary the aerodynamic angle between the flow and the blade curvature, yielding a diverse mitigation effect induced by the sweep angle. Finally, the simulation does not take into account the significant deformation to which the fan is subject when the blades are loaded (umbrella effect). Because of this, the gap widens and favors the production of turbulent structures, as well documented in previous studies.

6.1 Perspectives

- The experimental study involving the implementation of the rotating beamforming algorithm has only considered one forward-skewed fan. It would be interesting to extend the database to backward-skewed and un-skewed ones to verify if the position of the sound sources moves to the trailing edge when increasing the airflow. At the same time, testing a less dense heat exchanger could modify substantially the locations of the sources.

- More advance frequency-based rotating beamforming techniques could be implemented in order to access acceptable resolution, i.e., having a clear separation of the sources, even at lower frequencies. In fact, in this case, it would be possible to apply frequency-based deconvolution or inverse methods to extend the dynamic range and resolution of the resulting sound map. Nevertheless, from preliminary studies, we observed that around $2000\,\mathrm{Hz}$ the sound sources appear to cluster around a region in the middle of the blade. This would be in agreement with the low-order prediction methodology from which a clear contribution of this region was simulated when accounting for the sweep effect.

- An unsteady low-order approach could be attempted to capture the large periodic eddies that wrap around the fan blade. This could be used as an input for a rotating dipole formulation based on the Ffowcs-Williams and Hawkings analogy, in order to capture the discrete frequency peaks. Nevertheless, most of the energy content produced within the gap would be still unknown. Likely, before modeling analytically this unsteady three-dimensional flow, one should investigate experimentally (for instance with phase-locked PIV), and numer-

ically with high-fidelity methods, the temporal and spatial evolution of these geometry-dependent vortical structures.

- During the stereo-PIV campaign concerning the characterization of the turbulent flow past the radiator, only cold measurements have been performed, neglecting the effect of the temperature gradient of the cooling pipes when operated to refrigerate the car engine. It would be of interest to operate the heat exchanger in a hot environment to analyze the temperature effects on the fin wakes and on their dissipation.

- Passive mitigation methodologies could be applied to the fan and its environment in order to reduce the noise emissions. In particular, to minimize the ring gap, a second non-rotating ring could be installed on the fan inlet to prevent the eddies to be convected upstream and re-ingested. To break the coherence of the recirculating zone around the fan tip, it would be also possible to install fins on the ring. Another promising mitigation technique, that was already proven to work very efficiently on steady airfoils and on wind turbines, is the installation of serrated edges. This could be local, involving for instance the leading edge of the blade tip, after tuning the serrations according to the turbulent eddies that originate within the ring gap. Finally, micro-perforated plates may be included in the core of the radiator. In this case, the noise emitted by the fan would be absorbed along its propagation path through the radiator. A multi-physical analysis would be the first step in order to investigate also the perforation ability to dissipate heat and likely an optimized solution would need to be found to cool the engine and mitigate the sound. To this end, the fundamentals of MPPs modeling are given in appendix A.

A

Micro-perforated plates modeling review

This section is aimed at describing the modeling of the micro-perforated plates (MPPs) employed as a sound-absorbing material. This work was part of an early literature analysis aimed at understanding the sound mitigation properties offered by the micro-perforated plates. An example of their implementation is given by the work of Allam and Åbom [1] regarding the noise reduction of an automotive radiator cooling fan achieved with the use of MPPs, showing the potential of this technology when applied to rotational cooling machinery. In the following sections, the MPPs will be firstly described from their physical point of view and then, the classical modeling methodologies will be discussed along with the main problems which are still subject to investigation.

A.1 MPPs physical description

Perforated plates are plates on the surface of which orifices of generic shape, typically slits or circular holes, are engraved. As in porous or fibrous materials, the aim is to convert acoustic energy into heat. This is carried out by the friction between the oscillating air particles against the internal and external parts of the holes, as well as by exploiting the resonance properties of the backing cavity [2]. Therefore, to employ them as useful sound-absorbing materials, the oscillating viscous boundary layers (Stokes layers) have to fill up almost completely the volume of the holes. This is obtained by keeping the dimensionless Shear number k approximately equal to 1. To define k, a relation between the hole characteristic dimension $d/2$ with respect to the viscous boundary layer thickness $\sqrt{\nu/\omega}$ can be written as $k = d\sqrt{\omega/4\nu}$, where the kinematic viscosity of the acoustic medium ν and the angular frequency of the sound excitation ω are present. Hence, micro-perforated plates with tens of thousands of sub-millimeter orifices are required and they need to have a porosity σ, defined as the open area with respect to the plate surface ratio, in the order of 1%. This is instrumental in increasing the particle velocity level within the orifice, in order to have a more efficient viscous dissipation. Generally, the thickness t of an MPP is normally chosen so that the ratio t/d is kept in the order of 1.

A.2 MPPs modeling

As Maa stated in [3], an MPP is defined as a surface with controlled complex impedance Z_{MPP} where the real part, called resistance R_{MPP}, has to be constant (frequency-independent), whereas the imaginary part, the reactance M_{MPP}, has to be small enough such that:

$$Z_{MPP} = R_{MPP} + j\omega M_{MPP} \approx \rho c,$$

being ρc the characteristic impedance of the air, with the density ρ and the speed of sound c. The viscous effects are represented by the acoustic resistance, whereas the reactance represents the air inertia to be moved by the acoustic waves. The absorption peak is therefore perfectly retrieved when the imaginary part is ideally equal to zero, whereas the resistance is equal to the air characteristic impedance, at that particular frequency. This is required so that the maximum amount of acoustical energy can enter the orifice without encountering a jump of impedance. To control at which frequency the absorption peak appears, it is possible to tune the air cavity depth L_c, such that behavior similar to a Helmholtz resonator is achieved. Nevertheless, a classical resonator reaches good sound mitigation only at its resonance frequency, since the viscous effects are negligible. Instead, for the MPPs, the absorption range has a broadband spectrum due to the dissipation mechanisms within and near the orifices. To further enlarge the absorption range, one may consider adopting multi-layer MPPs, as well as subdivide the backed air cavity, for instance, with honey-combs, in order to increase the local reaction to the acoustic waves [4]. Nevertheless, only single-layer with air cavity are considered hereafter.

A.3 Dissipation mechanisms

When one considers the acoustical impedance of a micro-perforated plate, different dissipation mechanisms have to be taken into account: the thermal effects, the radiation, the viscosity, the flow interaction, and the non-linearity due to high sound levels. The first two can be neglected as stated in [2] and later confirmed [5]. Hereafter, we introduce the remaining ones.

A.4 Internal viscous contribution

The contributions given by viscosity to the MPP transfer impedance can be separately considered as internal and external parts. The first one is due to the oscillating viscous boundary layers inside the orifice volume. From the theory of sound propagation in tubes, developed by Rayleigh [6] and simplified by Crandall [7] for short tubes, the equation of air motion inside a single cylindrical orifice is given by:

$$j\omega\rho u - \frac{\nu}{r}\frac{\partial}{\partial r}\left(r\frac{\partial}{\partial r}u\right) = \frac{\Delta p}{t}, \tag{A.1}$$

being Δp the sound pressure difference between the ends of the tube, u the particle velocity, and r the hole radius. The solution can be written defining the single-hole impedance Z_1 as the ratio between Δu and the cross-sectional averaged velocity $\overline{u}$ as:

$$Z_1 = \frac{\Delta p}{\overline{u}} = j\omega\rho t\left[1 - \frac{2}{k\sqrt{-j}}\frac{J_1(k\sqrt{-j})}{J_0(k\sqrt{-j})}\right]^{-1}, \tag{A.2}$$

where J_0 and J_1 are the Bessel functions of the first kind of zero and first order respectively. Eq. (A.2) can be easily normalized by the air characteristic impedance and extended to the MPPs

relative acoustic impedance by dividing it by the porosity:

$$z_{\text{in}} = \frac{j\omega t}{\sigma c}\left[1 - \frac{2}{k\sqrt{-j}}\frac{J_1(k\sqrt{-j})}{J_0(k\sqrt{-j})}\right]^{-1}, \tag{A.3}$$

being z_{in} the relative acoustic impedance due to internal viscous effects. A similar solution for slit-shaped perforated plates has been derived by Allard [8], but it is not here reported, for the sake of simplicity. For circular-shaped holes, Maa [2] derived the following expression for the internal resistance r_{in} of an orifice invested by a perpendicularly incident sound wave:

$$r_{in} = \frac{32\nu}{\sigma\rho c}\frac{t}{d^2}\sqrt{1 + \frac{k^2}{32}},$$

whereas the reactance part can be written as:

$$m_{in} = \frac{t}{\sigma c}\left(1 + \frac{1}{\sqrt{1 + \frac{k^2}{2}}}\right). \tag{A.4}$$

A.5 External viscous contribution

Since thin plates are studied, the external shape-dependent viscous dissipation developing on the orifice ends has to be modeled. Ingard [9] suggested that from the power dissipation occurring to oscillating air motion on an infinite plane surface S, approximately given by:

$$W_\nu = \frac{1}{2}\int_S R_S \left|U_S\right|^2 dS, \tag{A.5}$$

with U_S as the tangential velocity amplitude, the "surface resistance" can be expressed as:

$$R_S = \frac{1}{2}(2\mu\rho\omega)^{\frac{1}{2}}, \tag{A.6}$$

being μ the dynamic viscosity. A motion of air mass occurs next to the orifice edges and therefore, a contribution to the reactance has been theoretically calculated by Crandall [7] and Sivian for circular holes [10] as $\delta = 8d/3\pi$. Globally, the external contribution to the relative impedance for an MPP can be written as:

$$z_{ex} = \frac{\alpha 2 R_S}{\sigma\rho c} + j\frac{\delta\omega}{\sigma c}, \tag{A.7}$$

where $\alpha = 2$ for rounded orifice ends and $\alpha = 4$ for sharp ones [11]. Nevertheless, as Ingard based his end-correction coefficient derivation on plane surfaces when the curvature radius of the perforation edge is small, this formulation should be corrected. To solve this, a numerical model in 2D axisymmetric coordinates has been developed by Bolton and Kim [12] and generalized, for circular perforations in the linear regime, by Muttalip *et al.* [13]. In that work, different circular edge profiles were studied such as square, chamfered, inverse-chamfered, and their linear combinations. It is shown that, while the plate thickness has a negligible effect on the end-correction coefficients, α and δ strongly depend on the edge profile and on the k number, thus they are frequency-dependent. For instance, for the square-edge profile case, which is comparable to theory, asymptotic values are found with increasing k as $\alpha = 1.70$ and $\delta = 1.54$. For chamfered profile, both α and k have higher values since the internal-hole friction region is reduced, considering the same plate thickness. Therefore, according to [13], the two coefficients can be expressed as functions of k and the edge-profile by fitting the experimental results.

A.6 Non-linear contribution

Non-linear dissipation effects occur when the acoustic particle velocity within the orifice reaches high values due to moderate to high sound intensity levels [14]. In this condition, flow separation and vortices appear on the hole edges in a free-jet configuration, becoming a relevant part of the acoustic resistance. In fact, the developed vorticity is alimented by converting the acoustic field energy. Even the reactance is decreased and, although this process is not fully understood [11, 15], this is likely due to the turbulent-jet breaking apart the slug of mass present in and around the orifice region. An interesting conclusion is reported in the work of Leung *et al.* [16], since they noticed how the vortices are typically shed upstream and downstream of the orifice, but they are shed only downstream when a bias flow is present. To understand when the non-linear formation of vortices starts, the study can be based on the Strouhal number [17]:

$$S_r = \frac{\omega d}{|\overline{u}|}. \tag{A.8}$$

If $S_r \gg 1$, the vortices do not normally appear since the particle displacement is smaller than the hole diameter and thus, the system is linear and no other contribution is added to the impedance. If $Sr \ll 1$, the non-linear turbulent jet is totally developed; for this case, Cummings and Eversman [18], assuming quasi-steady behavior, derived the particle velocity from the Bernoulli equation. With the assumption of negligible downstream pressure past the orifice, the upstream acoustic pressure amplitude is given by:

$$|p_{up}| \approx \rho \, |u_h|^2 \, \frac{1 - \sigma^2 C_\nu^2}{2 C_\nu^2}, \tag{A.9}$$

where $|u_h|$ is the amplitude peak of the velocity within the hole, whereas C_ν is the vena-contracta factor, which is geometry-dependent and, for sharp edges, is $C_\nu \approx 0.7$. Moreover, due to MPPs low porosity levels, the term $\sigma^2 C_\nu^2 \approx 0$. For these reasons, the initially proposed formula by Ingard and Ising [19] is applicable to sharp-edges, leading to the resistance non-linear contribution:

$$r_{n-l} = \frac{|u_h|}{\sigma c}. \tag{A.10}$$

For the reactance part, an empirical formula has been proposed by Maa [14] to be multiplied to the end correction term: $\delta \left(1 + r_{n-l}\right)^{-1}$. Nevertheless, these relations are valid when the behavior is fully non-linear, i.e., $Sr \gg 1$. To fulfill the transition regime between linearity and non-linearity, Temiz *et al.* [17] provided correction functions for resistance and reactance, which are strongly dependent on the Shear and the Strouhal numbers and can be used for practical MPPs design. It is important to highlight though, that these terms are dependent also on the kind of perforation. In fact, as shown by Temiz *et al.* [20], for the chamfer-edge profiles the non-linear resistance contribution is decreased by around 50% compared to square-edge profiles.

A.7 Flow-interaction contribution

For rotational machinery applications, it is also important to take into account the impedance contribution due to the presence of a tangential flow parallel to the MPP plane referred to as grazing flow. The acoustic resistance, according to the work of Åbom and Allam [21], a term proportional to the Mach number M of the grazing flow has to be added: $\beta M/\sigma$, being $\beta = 0.15$

for MPPs with circular holes. Guo *et al.* [11] showed that it depends on the slit orientation for slit-edge perforations. Furthermore, the presence of the flow blows away the air mass at the orifice ends; for this reason, the mass end correction has to be corrected. The relation between the mass end correction with no flow δ and the one with the grazing flow δ_g is given by Rice [22] as:

$$\delta_g = \frac{\delta}{1 + \alpha_g M^3}, \tag{A.11}$$

being $\alpha_g = 305$, although further analysis showed that a factor of 6-7 has to be multiplied to a_g for the tested MPPs [12].

A.8 MPP absorbing coefficient and cavity-length depth

For normal acoustic incidence, the absorption coefficient α_{MPP} of a micro-perforated plate with a backed cavity, is given in [2] as:

$$\alpha_{MPP} = \frac{4r}{(1+r)^2 + \left(\omega m - \cot\left(\omega L_c/c\right)\right)^2}, \tag{A.12}$$

where the relative acoustic resistance of the cavity is $-\cot(\omega l/c)$. The maximum value of α_{MPP} is $-\cot(\omega l/c)$, occurring at the resonance frequency f_0 for which:

$$\omega_0 m - \cot\left(\frac{\omega_0 L_c}{c}\right) = 0, \tag{A.13}$$

with $f_0 = \frac{\omega_0}{2\pi}$. In a practical application context, from the solution of Eq. (A.13), the cavity length L_c can be deduced in order to tune the MPP at the resonance frequency:

$$\frac{L_c}{\lambda_0} = \frac{1}{2\pi}\cot^{-1}\left(\omega_0 m\right), \tag{A.14}$$

where $\lambda_0 = c/f_0$ is wavelength corresponding to the resonance frequency. The resistance r and reactance m parts of the relative transfer acoustic impedance of an MPP with circular square-edge orifices, can be finally written collecting the previously derived contributions of viscous, flow-interaction, and non-linear effects, as:

$$\left.\begin{aligned} r &= \frac{1}{\rho\sigma c}\left(32\nu\frac{t}{d^2}\sqrt{1+\frac{k^2}{32}} + 2\alpha R_S + |u_h|\,\rho + \beta M\rho\sigma c\right), \\ m &= \frac{t}{\sigma c}\left(t\left(1+\frac{1}{\sqrt{1+\frac{k^2}{2}}}\right) + \frac{\delta\omega\left(1+r_{n-l}\right)^{-1}}{1+\alpha_g M^3}\right). \end{aligned}\right\} \tag{A.15}$$

A.9 Conclusions

The micro-perforated plates have been studied because they are a promising sound mitigation technology to be applied to automotive low-speed cooling fans. In fact, within the hood of cars, for instance, clean, durable, not-cumbersome, temperature, and moist resistant solutions are desirable. The dissipation effects, including viscosity, flow interaction, and non-linearity occurring on

MPPs have been analyzed and modeled. Hence, guidelines have been traced for designing a new MPP prototype tuned to absorb parts of a typical sound spectrum emitted by low-speed cooling fans. Nevertheless, many parameters contribute to the calculation of the MPP transfer acoustic impedance, as well as the absorption coefficient. For this reason, an optimization technique will be likely needed to find the most suitable solution.

References

[1] Sabry Allam and Mats Åbom. *Noise Reduction for Automotive Radiator Cooling Fans*. Conference Paper Fan2015, Lyon, 2015.

[2] Dah-You Maa. *Potential of microperforated panel absorber*. J. Acoust. Soc. Am., vol. 104, no. 5, pp. 2861–2866, 1998.

[3] Hai-An Zhou, Xiao-Ming Wang, and Yu-Lin Mei. *Theoretical analysis of the sound absorption characteristics of periodically stiffened micro-perforated plates*. Acta Mechanica Sinica, 30(5):714–726, October 2014.

[4] S. Allam and M. Åbom. *A New Type of Muffler Based on Microperforated Tubes*. Journal of Vibration and Acoustics, 133(3):031005, June 2011.

[5] Thomas Herdtle and J Stuart Bolton. *Effect of Thermal Losses and Fluid-Structure Interaction on the Transfer Impedance of Microperforated Films*. page 24, Presentation at NoiseCon 2014, Purdue Univerity, U.S.A, 2014.

[6] John Rayleigh. *The Theory of Sound 2 Volume Set*. Cambridge University Press, 08 Cambridge, UK, 2011.

[7] I. B. Crandall. *Theory of Vibrating Systems and Sound*. Nature, 120(3024):544–544, October 1927.

[8] J.-F. Allard and Noureddine Atalla. *Propagation of sound in porous media: modelling sound absorbing materials*. Wiley, Hoboken, N.J, 2nd ed edition, 2009.

[9] Uno Ingard. *On the Theory and Design of Acoustic Resonators*. The Journal of the Acoustical Society of America, 25(6):1037–1061, November 1953.

[10] L J Sivian. *Acoustic Impedance of Small Orifices*. Journal of the Acoustical Society ofAmerica, Vol. 7, 1935.

[11] Sabry Allam, Ying Guo, and Mats Abom. *Acoustical Study of Micro- Perforated Plates for Vehicle Applications*. 05 2009.

[12] J Stuart Bolton and Nicholas Kim. *Use of CFD to Calculate the Dynamic Resistive End Correction for Microperforated Materials*.

[13] Muttalip Aşkın Temiz, Ines Lopez Arteaga, Gunilla Efraimsson, Mats Åbom, and Avraham Hirschberg. *The influence of edge geometry on end-correction coefficients in micro perforated plates*. The Journal of the Acoustical Society of America, 138(6), December 2015.

[14] D. Y. Maa. *Micro-perforated panel at high sound intensity*. Proceedings of Internoise 1994, vol. 94, pp. 1511–1514, Yokohama, Japan, 1994.

[15] K K Ahuja and R I Gaeta. *Active Control of Liner impedance by Varying Perforate Orifice Geometry*. 2000.

[16] Randolph Leung, R.M.C. So, M. Wang, and X. Li. *Induct orifice and its effect on sound absorption*. Journal of Sound and Vibration - J SOUND VIB, 299, 02 2007.

[17] Muttalip Temiz, Ines Lopez Arteaga, Gunilla Efraimsson, Mats Abom, and Avraham Hirschberg. *Acoustic end correction in micro-perforated plates - Revisited*. volume 2, 07 2014.

[18] A. Cummings and W. Eversman. *High amplitude acoustic transmission through duct terminations: Theory*. Journal of Sound and Vibration, 91(4), December 1983.

[19] Uno Ingard and Hartmut Ising. *Acoustic Nonlinearity of an Orifice*. The Journal of the Acoustical Society of America, 42(1), July 1967.

[20] Muttalip Aşkın Temiz, Jonathan Tournadre, Ines Lopez Arteaga, and Avraham Hirschberg. *Non-linear acoustic transfer impedance of micro-perforated plates with circular orifices*. Journal of Sound and Vibration, 366, March 2016.

[21] Sabry Allam and Mats Åbom. *Experimental Characterization of Acoustic Liners with Extended Reaction*. In 14th AIAA/CEAS Aeroacoustics Conference (29th AIAA Aeroacoustics Conference), Vancouver, British Columbia, Canada, May 2008. American Institute of Aeronautics and Astronautics.

[22] E j Rice, C E Feiler, and L W Acker. *Acoustic and aerodynamic performance of a 6-foot diameter fan for turbofan engines III performance with noise suppressors*.